



University of Studies of Naples “Federico II”

Department of Industrial Engineering - Aerospace Section
Doctorate School in Industrial Engineering
Ph.D. Course in Aerospace, Naval and Quality Engineering
XXVIII cycle

**Structural Health Monitoring (SHM) systems
in aircraft: wing damage detection employing
guided waves techniques**

The Chairman of the Ph.D. School:

Prof. Luigi De Luca

Research Supervisors:

Prof. Leonardo Lecce

Prof. Fabrizio Ricci

Dr. Eng. Ernesto Monaco

Candidate:

Eng. Natalino Daniele Boffa

March 2016

*“Everything must be made as simple as possible.
But not simpler.”*

Albert Einstein

Index

- Abstract 7
- ACKNOWLEDGEMENTS 9
- Chapter 1- Structural Health Monitoring 10
 - 1.1 Introduction 10
 - 1.2 Structural health monitoring in composite structures..... 11
 - Operational evaluation 14
 - Data acquisition 14
 - Feature extraction..... 14
 - Classification 14
 - 1.3 Classifications 15
 - 1.4 NDT Techniques 17
 - 1.5 Major technology gaps 18
 - 1.6 Review of Existing Structural Health Monitoring Technologies 19
 - 1.7 Non-destructive evaluation in composite materials 20
 - 1.7.1. Visual inspection 20
 - 1.7.2. Ultrasonic inspection 20
 - 1.7.3. Acoustic emission..... 21
 - 1.7.4. Eddy current methods 21
 - 1.7.5. Radiography and Thermography 22
 - 1.7.6. Electrical resistance and conductivity 22
 - 1.7.7. Strain gauge methods..... 23
 - 1.8 SHM Cost-Benefits Analysis..... 24
 - 1.8.1 Costs definition 25
 - 1.8.2 Benefit 25
 - 1.8.3 Designing for cost/benefit optimization 26
 - 1.8.4 Study case scenario: fuselage SHM system cost saving analysis..... 27
 - 1.9 Thesis objective and scope 29
 - 1.10 References 31

Chapter 2 - Ultrasonic guided waves	35
2.1 Introduction	35
2.2 Fundamentals of Lamb wave	36
2.3 Generation of Lamb waves	39
2.3.1. Actuator/sensor for Lamb waves	39
2.3.2. Ultrasonic probe	39
2.3.3. Laser	39
2.3.4. Piezoelectric element	40
2.3.5. Interdigital transducer	40
2.3.6. Optical fiber	41
2.4 Ultrasonic Guided Waves Inspection	41
2.5 UGW Signal processing for damage detection	43
2.6 References	44
Chapter 3 - Structural Health Monitoring System Design and Testing	47
3.1 Introduction	47
3.2 Sensor technology	50
3.2.1. Sensors bonding procedures	51
3.3 Laboratory device actuation and sensing technology	52
3.3.1 Acquisition System	52
3.3.2 Power amplifier	53
3.3.3 Signal generator	53
3.3.4 Data storage	54
3.4. Signal acquisition	55
3.4.1 Choice of excitation signal	55
3.5 Signal Acquisition Parameters (Sampling Frequency, Windowing...)	58
3.5.1 Time of flight (TOF)	58
3.5.2 Central Frequency	59
3.5.3 Amplitude	59
3.6 Signal analysis	60
3.6.1 Signal analysis technique aimed at damage patterns extraction (STFT, Wavelet, Damage Indices...)	60

3.6.2	Damage Index (DI) Approach.....	60
3.6.3	STFT Approach.....	62
3.6.4	Pitch catch and pulse echo technique	63
3.7	Damage scenario	64
3.8	Guided waves based SHM methodologies	67
3.8.1	Damage patterns definition	68
3.9	Signal algorithm evolution	70
3.9.1	Preliminary damage analysis software	71
3.9.2	Matlab damage analysis code testing	74
3.9.3	LabVIEW damage analysis code design and testing	76
3.10	Numerical modeling approaches for SHM system design.....	84
3.10.1	Composite flat panel model	85
3.10.2	Composite stiffened panel model	87
3.11	Statistical evaluation of experimental noise: threshold value definition	92
3.12	Tomographic analysis.....	99
3.12	References	105
Chapter 4 -	SHM System Implementation on a Full Wing Ground Demonstrator.....	107
4.1	Introduction	107
4.2	Full Scale Ground Test Wing Demonstrator experimental investigations	108
4.2.1	Static tests	110
4.2.2	Fatigue Test.....	112
4.2.3	Ground Test Demonstrator SHM experimental tests setup.....	113
4.3	Data Acquisition System (DAQ)	116
4.3.1	DAQ Hardware	118
4.3.2	DAQ Data Storage.....	119
4.4	Damage scenario	121
4.4.1	Ground test demonstrator impact survey	123
4.4.2	LWP calibration impacts NDT inspection	124
4.4.3	LWP scheduled impacts NDT inspection	125
4.5	SHM system data acquisition	129

4.6 Guided wave based Graphic User Interface (GUI)	131
4.6.1 Signal analysis GUI sub interface	132
4.6.2 Material Characterization GUI sub interface	139
4.6.3 GUI results	141
4.7 References	145
Conclusions	146
Appendix - Infrared thermography and ultrasonics in carbon epoxy materials	148
I. Introduction	148
II. Techniques overview	149
III. Experimental investigation	150
IV. Impact tests	151
V. Non-destructive evaluation with lock-in thermography	153
VI. Non-destructive evaluation with ultrasonic phased array.....	157
VII. Data comparison and discussion.....	160
VIII. References.....	162

Abstract

About 3 billion people every year use air transport to realize their business and leisure needs, whereas about 5 trillion euros worth of goods are transported by air. And these figures are on the rise: annual passengers are expected to reach over 6 billion by 2030, according to current projections.

As the number of flights increases, pollution and noise from air travel impose significant challenges on the industry. This is why airlines, aircraft manufacturers, and researchers are constantly searching for new ways to make their planes lighter, with increased aerodynamic performance, achieving at the same time greater fuel efficiency and thereby reduce the environmental footprint of air travel.

Moreover, there is a large inventory of aircraft structures in operation throughout Europe and the world that are undergoing continuous degradation through aging. This number is increasing by around 5% every year, resulting in significant negative impact on the economy of many nations.

From this point of view, modern maintenance scenarios, where the inspection of the structure is carried out only when needed, are a topic on which airlines, aircraft manufacturers and scientific community have been spending big effort during the last two decades.

Increasing emphasis on the integrity of critical structures such as aircraft creates an urgent need to monitor structures in situ and in real-time and detect damage at an early stage to prevent catastrophic failure.

Recent advances in sensing technologies along with current developments in computation and communications have resulted in a significant interest in developing structural health monitoring (SHM) technologies that can be integrated seamlessly into the structures as a built-in diagnosis system.

Nowadays, the degradation of critical structural components is controlled through careful and expensive regularly scheduled inspections in an effort to reduce their risk of failure. An SHM system able to interrogate a structural sub-component with accuracy and reliability of a traditional NDT technique would allow to substitute the actual two-level inspection approach, based on visual inspection followed eventually by NDT analysis, with a single-level inspection highly automated based on sensors that are permanently and not invasively installed on the structure to monitor.

Using distributed sensors to monitor the physical condition of in-service structures becomes feasible if sensor signals can be interpreted accurately and rapidly to reflect the in situ condition of the structures through real-time data processing.

The research conducted in this doctoral thesis fits into this context and, in particular is part of a wider European project, coordinated by Airbus, called SARISTU (Smart Intelligent Aircraft Structures). SARISTU main purpose is the study of structural integration of smart, multifunctional materials throughout the life cycle of the aeronautical product. To achieve this goal, the technologies examined, for an integrated approach to smart structures for

aeronautical use, consist of structures self-sentient, nanotechnology, multi-functional materials with shape memory or editable shape. In this sense, the ultrasonic research community has studied guided waves for nondestructive evaluation of plate-like structures for several decades.

The doctoral thesis provides a detailed description of the implementation of methodologies and technologies based on ultrasonic guided waves for Structural Health Monitoring (SHM) on wing structural elements made of composite materials for BVID or hidden flaws detection.

The developed methodologies have been first technologically integrated and applied on small scale structural elements, unstiffened and stiffened plates. Subsequently the SHM system was integrated on a full scale wing box demonstrator in order to perform the delamination detection. The implemented SHM system is capable to control a network of surface mounted piezoelectric transducers, to perform Electromechanical Impedance measurement at each transducer, to check the reliability as well as the bonding strength, and to perform an active guided wave screening.

In particular, at the end of the work, a technological solution is presented based on a switching matrix able to control at least 160 transducers, and where 4 transducers at a time can be used to screen the structure, with a significant cost saving and with no loss of SHM capabilities.

The main issues that will be described here include: methodologies, methodologies integration and assessment, experimental and numerical damage detection results and SHM system platform implementation.

ACKNOWLEDGEMENTS

This Doctoral Thesis was written at the Division of Aerospace Engineering, Department of Industrial Engineering at the Federico II University (UNINA) under the supervision of Professors Leonardo Lecce, Fabrizio Ricci and Ernesto Monaco.

I am indeed grateful to my supervisors for my academic career opportunity, for creating a positive working environment, for their availability, comprehension and friendship.

In particular, my heartfelt thanks go to Professors Ernesto Monaco and Fabrizio Ricci, I could not ask for better mentors, I owe them much for all of their superior guidance over the years. Their leadership consistently challenged me to be a better engineer and provided the right determination to achieve my goals.

Tanks to Dr Carosena Meola for her teachings, support and involvement in interesting activities and discussions.

A special thanks to SARISTU project partners, in particular to: Alessandro Marzani (Bologna University), Nicola Testoni (Bologna University), Luca De Marchi (Bologna University), Mihail Lilov (Fraunhofer Institute), Koen Van Den Abeele (Katholieke Universiteit Leuven), Alfonso Apicella (Alenia Aermacchi), Felice Menafro (Alenia Aermacchi).

Thanks to the Chairman of the Ph.D. School Prof. Luigi De Luca for his help, availability and comprehension in the various vicissitudes of my doctoral studies.

Thanks to personal in Aerospace Engineering Division for their help, friendship and human support.

Thanks to all my former colleagues and collaborations partners. Special thanks go to PhD studentes/Post-Docs at the Aerospace Section of the Department of Industrial Engineering: Marco Di Palma, Giuseppe Petrone, Leandro Maio, Marco Magnifico, Marco Barile, Vittorio Memmolo, Angelo De Fenza, Vincenzo D'Alessandro and Simone Boccardi for being a good and supportive friends, for their enthusiasm, hard work and excellent collaboration. It has been my great privilege to be a member of their research group. Thanks to all undergraduates and graduates that worked and that are now working at Aerospace Division.

Great thanks to my dear friends for their endless support: Andrea C., Piergiorgio, Nicola, Ninni, Marco, Vissia, Giuseppe, Simona, Adriano, Annamaria, Daniele, Daniela, Pietro, Diego, Clairet, Andrea A., Laura V., Francesca, Carla, Laura, Federico, Fabio, Sabrina, Marilisa, Giosué and the little ones Michele, Noemi, Giulia and Frida.

Greatest gratitude to my family, especially for my mother Lina, my father Lorenzo and my brother Stefano for being there and supporting me in all kind of ways you could ever imaging.

Finally, I dedicate this thesis to my beloved Elena. You are always there and provide me with your affection. I love you!

I also love aircrafts because they are symbols of freedom, power, connection, teamwork and hope.

Napoli, March 2016

Natalino Daniele Boffa

Chapter 1

Structural Health Monitoring

1.1 Introduction

The use of composite components in the aerospace field is increasing gradually due to the opportunities they present for weight reduction. In addition to their high specific stiffness and strength, other advantages include their superior fatigue performance, their improved thermal and electrical conductivity and the possibility to integrate sensors or actuators [1]. Due to the composition complexity of a composite material, its final properties do not depend only on the properties of component materials (matrices, reinforcements, fillers and additives). A combination of parameters affects the design with composite materials, including the number of layers, the material combinations, ply directions and fabrication method [3]. The most common method to build these materials is the autoclave processing that provides high performance composite structures. A variety of other methods are available nowadays, e.g. Resin Transfer Molding (RTM) and Liquid Resin Infusion (LRI) methods.

Most efficient use of advanced composites in aerospace is in applications with highly loaded parts, areas susceptible to corrosion and in applications with high fatigue loads (launcher structures, primary / secondary structures, antenna reflectors, equipment structures, solar array substrates, fasteners and inserts). Also in the aeronautical field, they are used in air frames, wing spars, spoilers, tail-plane structures, fuel tanks, drop tanks, bulkheads, flooring, helicopter rotor blades, propellers, and structural components, pressured gas containers, nose and landing gear doors, fairings, air distribution ducts, seat components, access panels, and so forth. Many modern light aircraft are being increasingly designed to contain as much lightweight composite material as possible.

Unlike metals, composite materials are inhomogeneous and anisotropic and failure does not always occur by the propagation of a single macroscopic crack. Fiber breakage and matrix cracking, debonding, transverse-ply cracking, and delamination, occur sometimes independently and sometimes interactively, and the predominance of one or other may be strongly affected by both materials variables and testing/service conditions [4] [5] [6].

The timely damage diagnosis and characterization in structures before failure is vitally important in the aeronautical sector, where the structural integrity must be constantly ensured [2]. All structural components of a commercial aircraft are inspected at regular intervals using different evaluation techniques that are expensive, complicated, and costly. Currently, the service intervals are obtained statistically by taking into account the probability of failure. These methods are called predictive maintenance since repairs and overhauls are preprogrammed.

If continuous structure monitoring tools were available, predictive methods could be changed to the methods based on the assessment of real condition of the structure and the revisions could be made when and where they are necessary.

Continuous monitoring of the location of the damage and the level of its severity enables implementing this strategy, which would save both direct maintenance costs and time spent on each revision. Moreover, the criteria used to minimize the weight of aircraft result in an increased use of composite materials. However, these materials have anisotropic mechanical properties, which seriously complicate the inspection process.

Many flaw types, such as, barely visible delaminations, detachment between layers, fiber breakage, or porosity may result in a serious loss of strength. All these defects could be monitored with structural health monitoring (SHM) techniques and systems, which would additionally permit for increasing the use of composite materials and using all their advantages. One of the main advantages would be significant savings in fuel and the corresponding decrease in CO₂ and NO_x emissions.

Structural testing of aircraft elements is generally a complex, costly, and time-consuming process. Typical primary components fatigue tests of aircraft structures usually last between one and two years. In addition, this process must be interrupted periodically to check the structure integrity, usually using nondestructive methods that increase more and more the total duration of the process.

Therefore, the development of systems that simplify and reduce the currently used techniques and the cost of them has to be considered [1].

1.2 Structural health monitoring in composite structures

“Structural Health Monitoring (SHM) aims to give, at every moment during the life of a structure, a diagnosis of the “state” of the constituent materials, of the different parts, and of the full assembly of these parts constituting the structure as a whole” [7]. Or, alternatively, SHM is defined as “the use of in-situ, nondestructive sensing and analysis of structural characteristics, including the structural response, for detecting changes that may indicate damage or degradation” [8]. A recent alternative definition of SHM by NASA is Fault Management, which is defined as “the operational capability of a system to contain, prevent, detect, diagnose, respond to, and recover from conditions that may interfere with nominal mission operations” [9].

Most commonly Structural health monitoring is a multidisciplinary process of implementing a strategy for damage identification in a way that nondestructive testing becomes an integral part of the structure. This process involves the definition of potential damage scenarios for a structure, the observation of the structure over a period of time using periodically spaced measurements, the extraction of damage sensitive parameters (features) from these measurements and the analysis of these features to determine the current state of health of the structure (classification). The output of this process are periodically updated information regarding the ability of the structure to perform its intended function in consideration of the applied loadings, aging and degradation resulting from the operational environments.

In contrast to conventional nondestructive testing techniques that are operated offline during maintenance, structural health monitoring techniques can be operated off-line as well as on-line. On-line refers, in this case, to the monitoring during operation of the system or structure. The structural health monitoring technique is part of the on-board systems. Sensors are permanently attached (surface sensors) or embedded (integrated sensors) in the structure. As a result, information on the structural state is available at arbitrary times.

Many definitions have been proposed to describe damage, health and structural monitoring. In general, health is defined as the ability to function and maintain the structural integrity during the entire life of a structure. Damage can be defined as a material, structural or functional failure, or as a change in physical parameters, such as mass, stiffness or damping. Monitoring is the process of structural diagnosis and prognosis [10]. SHM is considered as the observation of a system over time based on periodically sampled response measurements from a sensor network, the extraction of features sensitive to damage and the analysis of these features, in order to define the health system's structural condition [11]. It consists a very important tool for the current and future design, analysis and maintenance of engineering structures [12].

The SHM target is to ensure that the safety of a structure is maintained during its lifetime. The main objective is to be able to replace conventional testing methods with continuous monitoring systems to provide real time data and information about the structural integrity. The purpose of SHM is to preserve system functionality, or, stated differently, to control state variables within an acceptable range, in the presence of current or predicted future failures. Figure 1.1 illustrates the SHM objectives. In effect, SHM can improve understanding, characterization, and prediction of effects associated with failure that threaten the structural safety. In addition, it can offer fault tolerance to component/subsystem/system-level and offer the potential to reduce cost associated with maintenance to assure structural safety [13]. With the use of an ideal in-situ SHM, its components would operate continuously without any regularly scheduled maintenance until the SHM system reported that a repair is necessary. For this reason, all the subsystems need to interact effectively in order reliable results to be obtained [14].



Figure 1.1: SHM objectives diagram

Figure 1.2 illustrates the principle and main organization of a typical SHM system. The definition of the integrity monitoring system is based on the type of physical phenomenon that causes the damage. The damage is monitored by the sensor network and the data (recorded by same type of sensors by multiplexing or merged by several types of sensors) are sent to the acquisition and storage subsystem. The output of the integrity monitoring system combined with previously registered information, is used to create diagnosis. Usage monitoring aims to measure the inputs as well as the structural responses before any damage. The information derived from the integrity monitoring subsystem in combination with the data of the usage monitoring subsystem and the knowledge based on damage mechanics and behavior laws, lead to the prognosis and health management of the structure and of the full system [7].

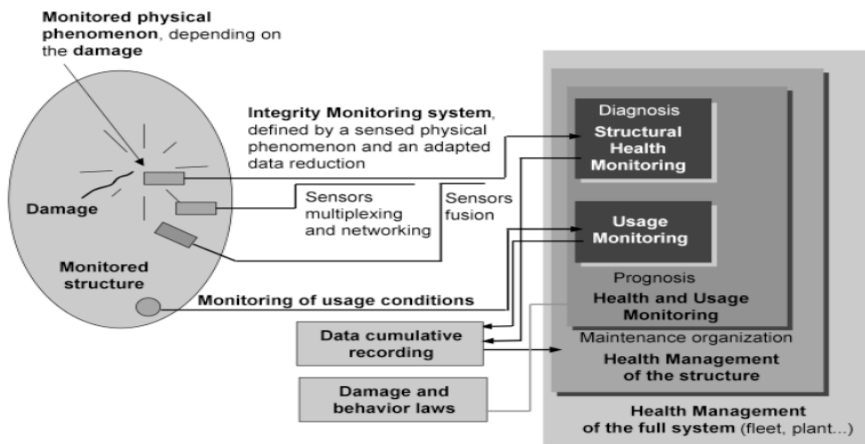


Figure 1.2: Principle and organization of a SHM system [6]

The present thesis focuses on the diagnostic part of the structural health monitoring process, which can be divided into a four-step process (Figure 1.3) [15]:

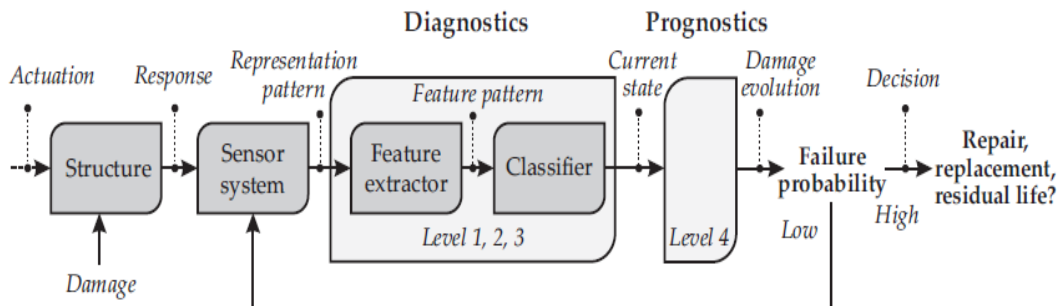


Figure 1.3 The multidisciplinary structural health monitoring process.

Operational evaluation

Operational evaluation answers questions regarding the implementation of the structural health monitoring system, such as possible failure modes, operational and environmental conditions and data acquisition related limitations.

Data acquisition

This step defines the data acquisition in terms of the quantities to be measured, the type and quantity of sensors to be used, the locations where these sensors are to be placed and the hardware to be used. Moreover, it defines the data fusion and cleansing, which is the determination of which data is necessary and useful in the feature extraction process.

Feature extraction

Feature extraction is the process of identifying damage sensitive parameters from measured data. These damage features are defined in the time, frequency or modal domain. Information reduction and condensation is also of concern for a large quantity of data, particularly if comparisons of many measurements over the service life of the structure are required.

Classification

The last step is concerned with the implementation of algorithms that operate on the extracted features to distinguish between the damaged and the undamaged structural state and to quantify the damage state of the structure. Statistical methods are used to establish the feature's sensitivity to damage and to prevent false damage identification.

An ideal robust damage identification scheme should be able to: detect damage at a very early stage, locate the damage within the sensor resolution being used, provide some estimate of the extent or severity of the damage and predict the remaining useful life of the structural component in which damage has been identified, all independently from changes

in the operational and environmental conditions. The method should also be well suited to automation, and should be independent of human judgement and ability.

1.3 Classifications

Damage identification methods can be classified in different ways. This section summarizes the most important classifications used in this thesis.

Performance levels: A performance based classification of the damage identification methods was introduced by Rytter [16]. Rytter defined four levels of damage identification:

- Level 1: Verification of the *presence* of damage in a structure.
- Level 2: Determination of the *location* of the damage.
- Level 3: Estimation of the *extent / severity* of the damage.
- Level 4: Prediction of the *remaining service life* of the structure.

Some researchers [17, 18] included the determination of the type of damage (characterization) as an additional step between level 2 and 3. Levels 1 to 3 are related to the damage *diagnosis*, while level 4 is concerned with the damage *prognosis*. Higher levels generally represent an increasing degree of complexity and a greater need for mathematical models. Generally, a level 4 prediction requires a fracture mechanics and fatigue life analysis based on structural and damage models to predict the evolution of the damage [15].

Model and non-model based approach: The second classification distinguishes two approaches, namely *model* and *non-model* based damage identification methods.

In a non-model based method the results are compared with the results of a reference measurement performed prior to setting the structure in service. Deviances in the damage sensitive parameters are used to identify damage. In a model based technique the response is compared with some form of model. This can either be an analytical or a numerical (e.g. finite element) model.

Advantages of model based techniques are that these could well be extended to provide information about the severity of the detected damage and can be used to account for environmental or operational variations (e.g. temperature, boundary conditions). On the contrary, it is rather difficult to obtain an accurate model representation of complex (composite) structures. Moreover, the computational costs can limit the applicability for in situ monitoring.

Local and global methods: Damage identification techniques are usually classified as *local* or *global* [19]. This classification is based on the relative size of the area that can be inspected at once by the method with respect to the overall dimensions of the structure. The local methods concentrate on a part of the structure and are usually considered to be more sensitive than the global methods. They are capable of detecting small damages such as cracks, but their application requires a prior knowledge of the location of the damaged area. The global methods can analyze a relatively large area at once, but the resolution is,

however, rather limited. As a consequence, only relatively severe damage cases can be identified.

Baseline and non-baseline: One of the fundamental axioms of Structural Health Monitoring proposed by Worden, et al. [20] reads that the assessment of damage requires a comparison between two system states.

Technique	Ref.	Inspection area	Inspection mode	Structure accessibility
Electric, magnetic and electromagnetic				
Electrical conductivity testing	[16, 17]	Local/global	Off-/on-line	Not required
Magnetic particle testing	[18, 19]	Local	Off-line	Required
Eddy current testing	[18, 20]	Local	Off-line	Required
Radiography (X-ray)	[18, 21]	Local	Off-line	Required
Infrared thermography	[18, 22]	Local/global	Off-line	Required
Mechanic, dynamic				
(Quasi-) static	[23]	Local	Off-/on-line	Not required
Structural vibrations and acoustics	[24, 25]	Local/global	Off-/on-line	Not required
Electro-mechanical impedance	[26, 27]	Local/global	Off-/on-line	Not required
Acoustic emission	[18, 28]	Local/global	On-line	Not required
Acousto-ultrasonics	[29, 30]	Local/global	Off-/on-line	Not required
Ultrasonic testing	[18]	Local	Off-line	Required
Optical				
Shearography	[31, 32]	Local	Off-line	Required
Visual inspection	[5, 18]	Local/global	Off-line	Required

Table 1.1: An overview of the most commonly used nondestructive testing (NDT) techniques.

The response of a structure measured at an earlier stage is usually utilized as a baseline to distinguish between the damaged and undamaged state. For model based methods, this baseline can also be obtained from a model (e.g. finite element model). Other researchers [21, 22] also propose methods that do not require a baseline to classify the structure as damaged or undamaged. This might be interpreted as not requiring a comparison of system states. It can be argued that this discrepancy is a matter of terminology. Non-baseline methods still compare two states, but instead of utilizing a baseline measurement they rely on an assumed normal behavior (e.g. a smooth pattern or a linear-elastic response) of the structure. The system is in this case classified as damaged when the response deviates from the norm.

1.4 NDT Techniques

A wide range of nondestructive testing techniques can be employed for damage identification purposes. An overview of the most commonly used nondestructive testing techniques and their characteristics has been presented in the previous Table 1.1. The majority of these techniques can only be applied when the structure is not in operation ('off-line') and readily accessible. Consequently, only a few of these techniques are suitable to be applied in a health monitoring environment.

Technology	Frequency range [Hz] ¹	Actuation approach	Sensitivity to damage	Ease of data interpretation	Applicability for SHM
Structural vibration and acoustics	10^0 – 10^4	active/passive	■ ■ □ □ □	■ ■ ■ ■ □	■ ■ ■ ■ □
Electro-mechanical impedance	10^3 – 10^5	active	■ ■ ■ □ □	■ ■ ■ □ □	■ ■ ■ ■ □
Acoustic emission	10^4 – 10^6	passive	■ ■ ■ ■ □	■ ■ □ □ □	■ ■ ■ □ □
Acousto-ultrasonics	10^4 – 10^6	active	■ ■ ■ ■ □	■ □ □ □ □	■ ■ ■ ■ □
Ultrasonic testing	10^5 – 10^7	active	■ ■ ■ ■ ■	■ ■ □ □ □	■ □ □ □ □

¹ Typical frequency range at which the technology is operating.

Table 1.2 An overview of the dynamics based nondestructive testing (NDT) technologies.

As part of this selection, the technologies based on electrical conductivity are generally limited to conductive materials. The (quasi-) static techniques are of lower interest because of a rather low sensitivity to damage compared to the dynamics based techniques. The dynamics based techniques are applicable to a wide range of structures and are therefore considered to be a promising group of technologies for structural health monitoring.

Table 1.2 provides a detailed comparison of each technique performances. The low frequency *structural vibration* (SV) and *electromechanical impedance* (EMI) techniques primarily rely on standing wave patterns, while the higher frequency *acoustic emission* (AE), *acousto-ultrasonics* (AU) and *ultrasonic testing* (UT) utilize traveling wave characteristics.

The former group of methods provides data that is relatively easy to interpret. More complex structures can be analyzed with these methods and a relatively large area can be explored at once. The frequency range, and hence the resolution, is however limited [19]. As a consequence, only relatively severe damage such as delaminations can be identified. The methods in the latter group are usually considered to be more sensitive. They are capable of detecting small damage such as cracks [23]. For that reason, these wave propagations based technologies are increasingly being explored for aircraft applications [24, 25]. The downside is the more complex interpretation of the data, in particular in case of non-flat or complex (composite) structures [26]. The rating for the sensitivity is linked

to the operational frequency range [20], while the other aspects are ranked according to the available literature. It should be noted that these ratings are rather subjective. The intention here is, however, to give an impression of the relative strengths and weaknesses rather than to condemn techniques.

1.5 Major technology gaps

Although many structural health monitoring techniques have been proposed in the literature, there are still numerous difficulties in the practical application of these approaches. The most important technical issues that need to be resolved before structural health monitoring technologies can make the transition from a research topic to actual practice are summarized below.

• **Complex composite structures**

The applications to composite structures are to a large extent limited to relatively simple composite beams and plates with mainly well-defined or artificial damage scenarios. The complexity of the components and the wide variety of potential damage scenarios hampers the application of structural health monitoring to more complex composite structures. Therefore, research should be focused on the application to composite structures such as stiffened panels and torsion boxes, as well as realistic damage scenarios.

• **Selection damage feature and classifier**

Damage identification aims to uniquely identify damage at an early stage with a minimum of false positive results. For this purpose, an enormous amount of damage features and (statistical) classifiers are addressed in the literature with a varying level of success. None of the methods solves all problems in all structures. The development and selection of damage sensitive features and classifiers that provide a high detection probability without getting false alarms is therefore one of the key challenges for structural health monitoring.

• **High performance level**

Current health monitoring approaches are often capable to detect (level 1) and localize (level 2) damage, but are limited in their ability to estimate the type or extent/severity (level 3) of the damage accurately. Damage severity assessment is an important requirement for the analysis of the damage evolution and the prediction of the remaining lifetime (level 4). The evolution towards a high performance level is considered as an important step forward in the development of autonomous monitoring of the integrity of structures.

• **Integrated sensors and network**

A structural health monitoring system requires an integrated sensor system. The design and implementation of these systems involve numerous challenges. These challenges range from the selection of the optimal position and number of sensors and the monitoring of failure or debonding of a sensor to the data transmission and the supply or harvesting of

power. Consequently, a large part of the research in the field of structural health monitoring is dedicated to the development of sensor systems.

- **Operational and environmental variability**

A large obstacle for the practical application of structural health monitoring technologies is the dependency of damage parameters on the operational and environmental conditions, such as temperature, humidity, loads and boundary conditions. Changes in these conditions can mask or magnify the effects that are resulting from the damage. Methods should have the ability to separate the damage related effects from those that are coming from changes in environmental conditions. A wide variety of methods, comprising statistical techniques and model based methods, are presented in the literature to compensate for these variations, but confidence in these methods is lacking.

In addition to the technical issues described above, there are other nontechnical issues that must be addressed before structural health monitoring technologies can make the transition to actual application. These issues include, for example, convincing operators, engineers and authorities of the potentials of the technology as well as the certification of the technologies. More detailed discussions on this topic are provided by Boller [27] and Farrar et al. [28].

1.6 Review of Existing Structural Health Monitoring Technologies

Due to the potential cost savings offered by its realization, there has been much interest in the field of SHM recently across many different application domains. Ensuring the continued service ability of infrastructure (such as vehicles, bridges and buildings) is a significant challenge that globally has attracted attention to SHM [29, 30]. Pipeline inspection has been an active research field, driven partly by very significant interest in developing the technology for the oil and gas industry [31,32]. In the aerospace industry, several application areas have garnered significant interest. Rapid inspection of satellite structures for pre-launch verification has made use of SHM/NDE technologies [33, 34]. Chia et al. presented work toward developing smart hangar technology, where noncontact measurements would be used to inspect aircraft structures [35]. Advanced composite materials have generated substantial interest in the research community due primarily to their increased usage in both military and commercial aircraft. Next-generation marine vessels are also adopting composite materials and for similar reasons there exists a need for capable monitoring systems [36].

Many different sensing methodologies have been deployed for these various applications in order to generate the data necessary for SHM. Vibration-based SHM is a vast field based on monitoring the dynamic response of structures to a variety of inputs. There are many methods based upon strain measurements, which can be sensed by conventional gauges or other techniques [37].

The development of these techniques has been pushed forward especially by the aerospace industry where composites are used in many critical applications and testing is vital. Some of the most important nondestructive techniques include Ultrasonics, Eddy Current methods, Acoustic Emission and Radiography, Thermography, Strain Gauge methods, Visual Inspection and Electrical resistance and conductivity methods [38].

A brief overview of the major nondestructive techniques, including their advantages and disadvantages, will be presented in the following section 1.7.

1.7 Non-destructive evaluation in composite materials

1.7.1. Visual inspection

Visual inspection is the natural form of evaluating structural integrity of material components. It is the standard method for detecting damage and assessing deterioration in most structures and is the oldest and most common damage inspection technique applied in aircraft service. Visual inspection (general or even more detailed one) by the unassisted eye (without the use of microscopy) is very limited particularly in composite materials and especially when damage occurs inside the laminate. Detailed information about delaminations in composites and micro-cracks in metallic elements can be provided by microscopy but only in laboratory conditions. Large areas need to be scanned rapidly without removal of individual components, minimizing the disruption of the structure's operation. Recent trends in this technique include various illumination techniques that allow improving inspection capability [10, 25, 39].

1.7.2. Ultrasonic inspection

Ultrasonic inspection is based on various properties of ultrasonic waves propagating in monitored structures. It utilizes wave attenuation, reflection, scattering, wave mode conversion and many other physical phenomena. Ultrasonic testing is the most widely used and most powerful procedure for inspecting fiber reinforced composites for internal defects. Fundamentally a probe with a piezoelectric crystal transmits ultrasonic pulses into the specimen and whenever a change in material acoustic impedance occurs the pulses are reflected back and received by the same or another crystal. Appropriate instrumentation can display the information in various ways. These techniques are referred as A, B and C-scans. The "A" refers to a single point measurement, the "B" scan measures along a single line and the "C" scan is collection of B-scans forming a surface contour plot. The C-scan has become common practice in industry specifically with the introduction of composite materials. A common technique is immersion testing where the transducer is coupled to the specimen with water. Contact testing is also possible where the probe is placed on the specimen with a viscous gel couplant being used between the probe and specimen.

Careful attention to detail in ultrasonic testing can result in the identification of very small cracks, disbonds, voids or inclusions in aerospace hardware that could be detrimental to

mission performance. New ultrasonic technologies are enhancing the accuracy, speed, and cost effectiveness of this method of nondestructive testing. By use of advanced transducers, a better data collection, via many signal gates, is possible and, with the aid of advanced digital signal processing, the new C-scan tests have become a very effective NDT tool for composite structures.

However, in general, this method is highly sensitive to small surface and deep flaws in the material. Various disadvantages related to coupling and scanning requirements appear. Additionally, the scanning time for C-scan is quite significant. The size and the cost of the whole equipment is also a limitation [10, 40, 41, 42].

1.7.3. Acoustic emission

All materials have a certain level of elasticity and plasticity before they finally fracture. Due to the application of external forces a certain level can be exceeded and this results in fracture of the material. Acoustic emission (AE, sometimes called stress wave emission) is the term used to describe the resulting acoustic stress waves when energy is released rapidly due to the occurrence of micro structural changes in a material. AE technology involves the use of ultrasonic transducers (20KHz - 1MHz) to listen for the sounds of failure occurring in materials and structures. Crack growth due to fatigue, hydrogen embrittlement, stress corrosion, and creep can be detected and located by the use of AE technology. In addition, high pressure leaks can also be detected and located. Fiber breakage, matrix cracking, and delamination are ways that produce AE signals when stress is applied to a composite component. A number of specific signal features are used for damage detection and location. Acoustic Emission monitoring has gained a lot of attention because it provides real-time information on damage progression inside the structure. AE technology has many applications in the NDT for structural integrity of composite materials and structures [10, 43, 44, 45].

1.7.4. Eddy current methods

The eddy current technique (ECT) is a very important monitoring technology used in the aerospace field. This technique is the third most commonly used for in-service aircraft inspection next to visual and ultrasonic inspections. By this method, changes in electromagnetic impedance due to material defects are detected. A probe, which is in fact a coil, is excited with sinusoidal alternating current to induce closed loops of current in the material. The closed loops are called eddy currents and are distorted due to material defects. Eddy currents are circular and oriented perpendicular to the direction of the applied magnetic field. The electrical conductivity, magnetic permeability, geometry and homogeneity of the test object, all affects the induced currents. The ECT is very useful for the detection of service induced cracks due to fatigue or stress corrosion.

ECT is a fast, reliable, and cost effective NDT method for inspecting also irregularly shaped conductive materials. It has also the advantage of being automatic. With proper

equipment and skilled test technician readout is instantaneous. The main drawback is that it needs an electrically conductive material, which is not always the case with composites. Other main disadvantage is that they require a large amount of power and that the data they produce are among the most complicated to interpret which makes damage detection difficult. In addition, this method requires extensive calibration before any characterization of defects can be done [46, 10, 47, 48].

1.7.5. Radiography and Thermography

Radiography is one of the oldest and widely used NDT methods. Radiographic techniques use many forms of γ -rays or X-rays for the material scanning. A radiograph is a photographic record produced by the transmission of Electromagnetic radiation such as X-rays or γ -rays through an object onto a film. When film is exposed to the specific light an invisible change is produced in film emulsion, known as a 'latent image'. The exposed areas become darker when the film is immersed. After development the film is rinsed, placed into a fixing bath and then washed. At the end, it is dried in order to be handled for interpretation and record.

Thermography uses the thermal conductivity and emissivity of material defects. The surface monitored radiate energy at wavelengths corresponding to their temperature. In "Lock-in" thermographic evaluation of materials, such as fiber reinforced composites, a sinusoidal thermal wave is directed at the surface of a specimen. Part of the wave penetrates into the specimen and will reflect from internal defects. The reflected wave will interfere with the surface wave. Changes in phase and amplitude of the surface interference pattern will enable defect characteristics to be determined. The thermographic image can still show the general shape of the defect but its characteristics are not as clearly defined as by ultrasonic C-scan. Thermography offers a technique for broad area inspection that, once a defect location has been identified, can be used in conjunction with localized detection techniques. This has the potential to significantly reduce the inspection time. The principle disadvantage associated with thermography is its depth penetration [10, 49, 50].

1.7.6. Electrical resistance and conductivity

The ability of carbon fibers to conduct electricity has resulted in the electrical resistance to be utilized as a parameter for in situ damage detection of composite laminates. The basic theory of using electrical resistance for damage detection is that delamination or breakage of a fiber results in a decrease in the electrical conductivity in the damaged area leading to resistance or voltage change. In order to measure the electrical resistance, a pair of electrodes has to be attached to the composite and the contact with the carbon fiber is necessary. Electrical conductivity mapping is based on the same principle as electrical resistance. The fibers are the sensors due to their ability to conduct electricity. Electrical conductivity mapping maps the structure's electrical resistivity. Two of the electrodes are used to input a voltage into the specimen. The potential difference is then measured by the

other electrodes. With the use of different combinations of input electrodes in different sequences, information can be recorded and analyzed in order to extract resistivity distributions within the specimen. The damage is indicated by areas of low resistivity. Further work has to be done in this emerging field, but the technique is promising [51, 52].

1.7.7. Strain gauge methods

Since 1940, the resistance strain gauges have been the most powerful tool in the area of experimental stress analysis. They are very common in a variety of applications for monitoring material deformations, both internally and externally. Currently, strain gauge methods are the most typical way to monitor damage in composite materials on in-service vehicle.

A voltage applied across a foil gauge measures strain by the resistance change due to deformation. Strain gages provide very accurate strain readings and the results are easy to be interpreted. They are relatively small, light with low cost. Strain gages can monitor local strain to detect time-history overloads and deformations. In most applications, they are mounted on the surface.

The physical environment of the strain gauge is a crucial parameter that has to be considered in gauge selection and protective coating. Due to their relatively high surface area and to the fact that protective coatings are necessary, electrical resistance strain gauges have not found wide acceptance for embedment into laminated composite materials.

A main disadvantage to this technique is that the results from a single gauge can only cover a small area of the surface accurately, so a large quantity of them would be necessary to monitor an entire vehicle, yielding a complex system with many wires. In order to avoid this situation, the gauges can only be placed in a few select predicted problem areas. Lately, optical fibers have been introduced to overcome the apparent shortcomings of conventional strain gauges [53, 54, 55].

A summary of the advantages and disadvantages of the existing SDT techniques is given in Table 1.3.

Method	Advantages	Disadvantages	SHM Potential
Visual Inspection	<ul style="list-style-type: none"> - Inexpensive equipment - Simple procedure - Simple to implement 	<ul style="list-style-type: none"> - Only surface damage - Only large areas - No data analysis 	Currently none
Ultrasonics	<ul style="list-style-type: none"> - Portable - Sensitive to small damage - Quick scan of large area 	<ul style="list-style-type: none"> - Very expensive equipment - Complex results - Specialized system for operation 	Location based on ultrasonic waves

Acoustic emission	<ul style="list-style-type: none"> - Real time monitoring - Applied to structures with limited access - Covers long distances 	<ul style="list-style-type: none"> - Emissions can be very weak - Sometimes hard to detect due to background noise 	Damage detection and localization. Successfully used in many engineering areas
Eddy current methods	<ul style="list-style-type: none"> - Simple to implement -Do not require expensive equipment 	<ul style="list-style-type: none"> - Require large amount of power - Complicated data to interpret - Extensive calibration 	Detection of damage and corrosion. Third most commonly used method in aircraft inspection
Radiography	<ul style="list-style-type: none"> - Capable of internal damage detection - Permanent record of results - Simple procedure 	<ul style="list-style-type: none"> - Expensive equipment - Expensive to implement - Time consuming 	Detection of internal damage growth and propagation
Electrical conductivity	<ul style="list-style-type: none"> - Simple to implement - Low cost 	<ul style="list-style-type: none"> - Requires a lot of electrodes 	Promising technique in detecting damages
Strain gauge method	<ul style="list-style-type: none"> - Surface mounted - Simple procedure - Portable 	<ul style="list-style-type: none"> - Expensive equipment - Expensive to implement 	Lightweight. Low power required for operation

Table 1.3: Overview of NDT techniques

1.8 SHM Cost-Benefits Analysis

Requirements for structural health monitoring, in the last decades, have rapidly increased, and these requirements have stimulated many new developments in various sensing technologies. Having passed the stage of scientific or technical curiosity, SHM is now entering its adulthood and systems need to clearly demonstrate their economic benefits as well. Owners and engineers are no longer satisfied with the general benefits of SHM such

as “reducing risk”, “improving knowledge” and “verifying hypotheses”, and need to provide justification from an economic point of view, clearly defining the cost-effectiveness of a SHM system. As with any commercial market, the relationship between the cost of a product and the perceived benefit for the buyers, is a central concept for the SHM industry as well. There are several scientific studies [57] showing how the correct implementation of SHM can have a positive impact on the live-cycle-cost of a structure, and therefore presents a positive cost/benefit ratio.

Commercial experiences and a commercial perspectives proposing SHM systems have allowed to identify several scenarios, where immediate, near-term and long-term cost savings exceed the SHM system cost confirming the benefits of its implementation.

In the following, before a study case scenario analysis, a cost/benefit analysis is presented.

1.8.1 Costs definition

SHM costs definition is not always easy mostly because some hidden costs can sometimes be difficult to estimate a-priori. The main costs, that are associated with the implementation of an SHM system, are usually divided in Immediate costs/capital investments and Operational costs.

Immediate costs/capital investments:

- SHM design costs, including integration with the structure’s design;
- Hardware costs (sensors, cables, data acquisition, data management hardware, communication hardware);
- Installation costs, including integration with building schedule, configuration and commissioning;
- Costs for installation reporting, as-built documentation, system manuals;

Operational costs:

- System maintenance, spare parts, consumables, energy, communication costs;
- Data management costs;
- Data analysis, interpretation and reporting costs.

1.8.2 Benefit

The SHM system benefits can be subdivided into two main categories: hard benefits and soft benefits. Hard benefits include benefits that can be economically quantified, such as immediate/deferred cost savings or increased value. Soft benefits include intangible benefits that the owner of a SHM system perceives and for which is ready to pay a price, but that cannot be directly quantified. Soft benefits include image, prestige, adherence to standards or trends or reduction of perceived risk. Some benefits are a mix of hard and soft benefits. For example, a reduction of risk could lead to a savings in insurance cost and increase in safety, therefore creating both a hard benefit (decrease of costs) and a soft benefit (peace of mind).

Then the implementation of an SHM system can be considered a capital investment and therefore increases the total value of a structure. However, as for most investments, value is not simply measured by the implementation cost but also by its future capacity to generate profits.

1.8.3 Designing for cost/benefit optimization

The designing and implementing of a cost-effective SHM System is a process that must be carried out following a logical sequence of analysis steps and decisions. Below the main steps that have proven, over the years, how to achieve an integrated structural health monitoring systems that respond to the needs of all parties involved in the design, construction and operation of structures of all kinds.

Step 1: Identify structures needing monitoring

This step might seem trivial, but is indeed a very important first step. Before considering a structural health monitoring system, it is important to consider if a specific structure will really benefit from it.

Step 2: Risk / Uncertainty / Opportunity analysis

The SHM system designer, the design engineers or the engineers in charge of the structural assessment and the owner, must jointly identify the risks, uncertainties and opportunities associated with the specific structure and their probability. The risk analysis will lead to a list of possible events and degradations that can possibly affect the structure. The uncertainty list includes all unanswered questions about the structural conditions and performance. Examples of uncertainties include the performance of the construction materials (e.g. the E modulus or the thermal expansion coefficient of a composite), the magnitude of loads or the correspondence between the calculated and the real strain levels. The opportunity list includes all parameters and performance indicators that might be better than expected or assumed. The result of this step is a list of risks that must be addressed by the SHM system.

Step 3: Responses

For each of the retained risk, uncertainty and opportunity, it is fundamental to associate one or several responses that can be observed directly or indirectly. For example, corrosion produces a chemical change, but also a section loss. The inaccuracy of the Finite Element Model produces a difference in the response between the structure and the model. At this stage, it is also useful to roughly quantify the expected responses. This is very important to select sensors with the appropriate specifications. It is also possible to determine which responses are easily and efficiently observed by a periodic visual inspection and others that may require instrumentation. The physical locations where these responses are expected, or will appear at their maximum, also need to be established. The output of this step is a list of responses that need to be detected and measured, their estimated amplitudes and their locations.

Step 4: Design SHM system and select appropriate sensors

The goal is now to select the sensors that have the appropriate specifications to sense the expected responses and are appropriate for installation in the specific environmental conditions and under the technical constraints found in the structure [56]. Often makes sense to include sensors based on different technologies, to increase the system redundancy and complementarily. On the other hand, having too many data acquisition systems will increase the system cost and complexity, so a good balance is required. The result of this step is a design document, including a list of sensors, installation and cable plans, installation procedure and schedule, as well as a budget.

Step 5: Installation and Calibration

Installation of all systems must adhere to the supplier's specifications. The result of this step is an as-built plan of the SHM system, a system manual and a calibration report.

Step 6: Data Acquisition and Management

This is the operational part of the process. The data is acquired and stored in a database, with appropriate backup and access authorizations. Documentation of all interventions on the structure and on the system is also important in this phase. The result of this step is a database of measurements and a log of events.

Step 7: Data Assessment

By analyzing the responses of the structure, the engineer will be able to identify if any of the foreseen risks and degradations have materialized. At this step the owner will also establish procedures to respond to the detection of any degradation. The analysis of the data might prompt further investigation, including inspection, testing or installation of additional sensors. The output of this step is a series of alerts, warnings and periodic reports.

1.8.4 Study case scenario: fuselage SHM system cost saving analysis

In the following the SHM system implementation cost saving analysis for a typical door surround (cargo or passenger door) airplane with an investigation area of about 7 m². The estimation is based on the assumption that the design life goal (DFG) of a fuselage is typically 100k flight hour (FH). The main items related to costs can be summarized as:

Inspection costs - It is assumed that both non-visible and visible impact damage sizes are within the allowable size. For these damage a detailed NDT inspection is required by a L2 inspector for which it can be estimated a cost of about 40k€, including aircraft on ground (AoG) and inspection costs.

Weight estimate – Sensors 3 kg, electronics 7 kg, cables and others 16 kg for a total of 26 kg per door.

Weight costs - The costs associated with the SHM system incremental weight is 0.07€ per flight hour and kilogram. No maintenance costs are associated with the SHM system (assumption).

Sensor installation costs – The sensors installation costs can vary depending on how sensor are bonded. If they are bonded on the cured structure the cost is about 26k€ per door surround (worst case), requiring about 200 man hours (MH). If they are co-bonded the installation cost can be reduced by a factor 10, then 8k€ per door surround. The overall cost for 4 doors is 104k€ and 32 k€, respectively.

Sensors cost – 12k€ per door, the cost for 4 doors is 48k€.

Damage occurrence – about 10^3 damages are expected in 500k FH, then $2 \cdot 10^{-3}$ occurrences per FH. About 75% of these damages occur at door surround ($2 \cdot 10^{-3}$ per FH) and 80% of these damages have a dent depth within 0.3mm and 1.3mm, then $1.1 \cdot 10^{-3}$ occurrences per FH.

For a composite structure it is possible to assume that for a damage dent $d < 0.3\text{mm}$ damages are not visible, for $0.3 < d < 1.3$ are visible but within the allowable size and for $d > 1.3\text{mm}$ are visible and produce a non-allowable damage. Concluding, damage occurrence that requires inspection is $1.1 \cdot 10^{-3}$ per FH.

In the following Figure 1.4 the damage occurrences are reported, in terms type of event occurrence frequency. For a narrow body (NB) fuselage with a 1-hour flight duration, we have 1 event every 4600 FH, that is considerably less than the value considered (1.1 every 1000 FH).

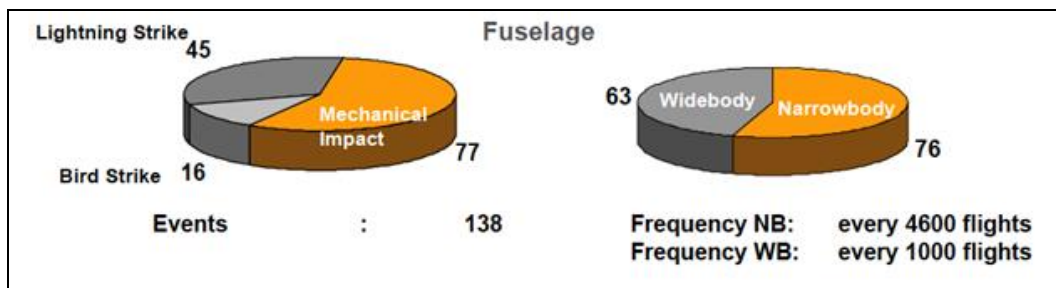


Figure 1.4: damage occurrences on wide body (WB) and narrow body (NB) composite fuselages (source Lufthansa Technik)

Therefore, taking into account the assumptions and estimates set out above:

- **for a non sensorized fuselage** the number of damage occurrence, in 100k FH, will be $1.1 \cdot 10^{-3} \times 100 \cdot 10^3 = 110$ damages. With an inspection cost of 40k€, the total cost for inspections in 100k FH will be 4M€.
- **an SHM sensorized fuselage will cost:** Weight: 0.07€ (per kg per FH) $\times 26\text{kg} \times 4$ (doors) $\times 100 \cdot 10^3$ FH = 728k€; Sensors installation 26 k€ (worst case, per door) $\times 4$ (doors) = 104k€; Sensors 12k€/door $\times 4$ doors = 48k€

The total costs for a sensorized fuselage will be 0.876M€. The cost saving in comparison with the not sensorized fuselage will be $4\text{M€} - 0.876\text{k€} = 3.1\text{M€}$.

1.9 Thesis objective and scope

The development of a structural health monitoring strategy involves multidisciplinary research challenges, as was shown in the previous sections. Figure 1.5 schematically illustrates the associated multidisciplinary framework. This framework comprises four components (i.e. structure, damage identification method, damage scenario, actuation and sensing technology). The characteristics of these components are closely interconnected and together they define the performance of the structural health monitoring strategy. Ideally, a strategy combines a high probability of detection and a high performance level with a low number of false positives. The success of a damage identification strategy is, however, dependent on the actual structure and on the damage scenario that is considered. The selection of the most suitable approach is, therefore, far from straightforward and is finally a matter of compromise. This gives rise to the development of a dedicated tool that can be used to design a damage identification strategy depending on the type of structure and on the potential threats. Design recommendations and guidelines are required for each scenario to assist in the development of such a tool. This thesis is dedicated to the identification of damage in composite skin-stiffener structures. Skin-stiffener structures are widely used in nearly all aircraft wing and fuselage designs. Stiffeners are used to increase the bending stiffness of the component without a severe weight penalty. A primary failure mode for these structures is delamination damage of skin and debonding at the connection between skin and stiffener. Impacts near these connections can lead to local skin-stringer separation. This is a safety-critical failure mode, because it can significantly affect the structural performance of the component while remaining invisible from the outer surface. Skin-stiffener structures are therefore considered as a good candidate for health monitoring. The structural ultrasonic, guided wave based, health monitoring approaches are considered in the present work. These methods are based on the concept that the dynamic behavior of a structure can change if damage occurs. The motivation is twofold: firstly, because they do not require, once assembled, the structure to be readily accessible. Secondly, because these low frequency methods provide data that is relatively easy to interpret. This allows opportunities to analyze more complex structures, such as the skin-stiffener structures.

The identification of barely visible impact damage sets the lower bound for the capabilities of the approach. In summary, the objective of the research presented is: the development of methodologies aimed at the damage detection, localization and characterization and at the SHM implementation on typical composite wing components based on guided waves.

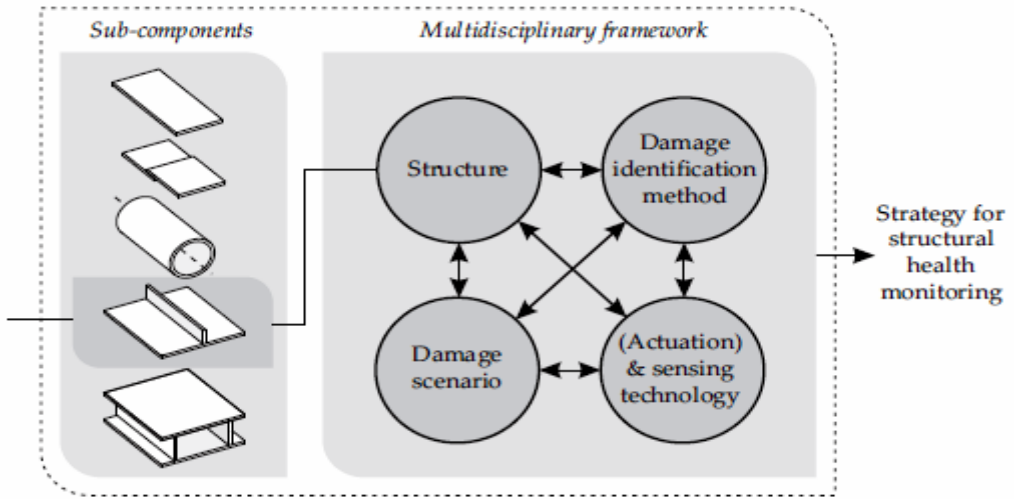


Figure 1.5 - The multidisciplinary framework for the design of a structural health monitoring system.

1.10 References

1. Smart Intelligent Aircraft Structures (SARISTU), Proceedings of the Final Project Conference - Piet Christof Wölcken • Michael Papadopoulos Editors
2. R Zhu, G L Huang and F G Yuan, Fast damage imaging using the time-reversal technique in the frequency–wavenumber domain, SMART MATERIALS AND STRUCTURES 22 (2013) 075028 (11pp), doi:10.1088/0964-1726/22/7/075028
3. N. D. Boffa, L. Lecce, E. Monaco, F. Ricci, Application of the beam-forming technique for damage detection in composite plate - American Society of Mechanical Engineers, Noise Control and Acoustics Division (Publication) NCAD - pp. 489-495 - August 2012
4. Harris, B. Engineering Composite Materials. The Institute of Materials, London, 1999.
5. Razi, H., Ward, S. Principles for Achieving Damage Tolerant Primary Composite Aircraft Structures. In 11th DoD/FAA/NASA Conference On Fibrous Composites in StructuralDesign. Fort Worth, 1996.
6. Voyiadjis, G.Z. Damage and interfacial debonding in composites. Elsevier, 1996.
7. Balageas, D. Introduction to Structural Health Monitoring. In D. Balageas, C.P. Fritzen, A.Guemes, ed., Structural Health Monitoring. ISTE Ltd, London, 2006.
8. Housner, G.W., Bergman, L.A., Caughey, T.K., Chassiakos, A.G., Claus, R.O., Masri, S.F. Structural control: Past, Present and Future. In Journal of Engineering Mechanics. ASCE, 123(9), 897-971, 1997.
9. Johnson, S.B., Gormley, T., Kessler, S., Mott, C., Patterson-Hine, A., Reichard, K., Scandura, P. System Health Management with Aerospace Applications. John Wiley & Sons Ltd, West Sussex, United Kingdom, 2011.
10. W.Staszewski, C.Boller, G.Tomlinson, ed., Health Monitoring of Aerospace Structures. John Wiley & Sons Inc. , West Sussex, England, 2004.
11. Laboratory, Los Alamos National. A Review of Structural Health Monitoring Literature: 1996-2001. Report, LA-13976-MS, California, 2003.
12. Bisby, L.A., Briglio, M.B. An Introduction to Structural Health Monitoring. SAMCO Final Report F10, 2005.
13. Srivastava, A.N., Mah, R.W., Meyer, C. Integrated Vehicle Health Management "Automated detection, diagnosis, prognosis to enable mitigation of adverse events". NASA Technical Plan, Version 2.03, 2009.
14. Kessler, S.S., Spearing, S.M., Atalla, M.J., Cesnin, C.E.S., Soutis, C. Structural Health Monitoring in Composite Materials using Frequency Response Methods. In Composites, Part B. 33, 87-95, 2002.
15. C.R. Farrar, H. Sohn, F.M. Hemez, M.C. Anderson, M.T. Bement, P.J. Cornwell, S.W. Doebling, J.F. Schultze, N. Lieven, and A.N. Robertson. Damage prognosis: current 16 Chapter 1. Introduction status and future needs. Technical report, Los Alamos National Laboratory, Los Alamos, NM, 2001.

16. A. Rytter. Vibration based inspection of civil engineering structures. Ph.D. thesis, Aalborg University, 1993.
17. H. Sohn, C.R. Farrar, F.M. Hemez, D.D. Shunk, D. Stinemans, and B.R. Nadler. A review of structural health monitoring literature: 1996-2001. Technical report, Los Alamos National Laboratory, Los Alamos, NM, 2003.
18. K. Worden and J.M. Dulieu-Barton. An overview of intelligent fault detection in systems and structures. *Structural Health Monitoring*, 3(1):85, 2004.
19. C.-P. Fritzen and P. Kraemer. Self-diagnosis of smart structures based on dynamical properties. *Mechanical Systems and Signal Processing*, 23(6):1830–1845, 2009.
20. K. Worden, C.R. Farrar, G. Manson, and G. Park. The fundamental axioms of structural health monitoring. *Proceedings of the Royal Society A: Mathematical, Physical and Engineering Sciences*, 463(2082):1639–1664, 2007.
21. E.S. Sazonov, P. Klinkhachorn, U.B. Halabe, and H. V.S. GangaRao. Non-baseline detection of small damages from changes in strain energy mode shapes. *Nondestructive Testing And Evaluation*, 18(3-4):91–107, 2003.
22. S. Park, C. Lee, and H. Sohn. Reference-free crack detection using transfer impedances. *Journal of Sound and Vibration*, 329(12):2337–2348, 2010.
23. A. Raghavan and C.E.S. Cesnik. Review of guided-wave structural health monitoring. *The Shock and Vibration Digest*, 39(2):91–114, 2007.
24. W.J. Staszewski, S. Mahzan, and R. Traynor. Health monitoring of aerospace composite structures – Active and passive approach. *Composites Science and Technology*, 69(11-12):1678–1685, 2009.
25. K. Diamanti and C. Soutis. Structural health monitoring techniques for aircraft composite structures. *Progress in Aerospace Sciences*, 46(8):342–352, 2010.
26. R.P. Dalton, P. Cawley, and M.J.S. Lowe. The potential of guided waves for monitoring large areas of metallic aircraft fuselage structure. *Journal of Nondestructive Evaluation*, 20(1), 2001.
27. C. Boller. Structural health monitoring – Its association and use. In W. Ostachowicz and J.A. Güemes, editors, *New Trends in Structural Health Monitoring*, volume 542 of CISM International Centre for Mechanical Sciences, Chapter 1, pages 1–79. Springer Vienna, 2013.
28. C.R. Farrar and K. Worden. An introduction to structural health monitoring. *Philosophical Transactions of the Royal Society A: Mathematical, Physical and Engineering Sciences*, 365(1851):303–15, 2007.
29. P.C. Chang, A. Flatau, S.C. Liu, Review Paper: Health Monitoring of Civil Infrastructure, *Structural Health Monitoring*. 2, 3; 2003, 257–267.
30. J. Ou, H. Li, Structural Health Monitoring in mainland China: Review and Future Trends, *Structural Health Monitoring*. 9, 3; 2010, 219–231.

31. J. Davies, P. Cawley, The application of synthetic focusing for imaging crack-like defects in pipelines using guided waves, *IEEE Transactions on Ultrasonics, Ferroelectrics and Frequency Control*. 56, 4; 2009, 759–771.
32. J.-R. Lee, S.Y. Chong, H. Jeong, C.-W. Kong, A time-of-flight mapping method for laser ultrasound guided in a pipe and its application to wall thinning visualization, *NDT & E International*. 44, 8; 2011, 680–691.
33. A. Zagrai, D. Doyle, B. Arritt, Embedded nonlinear ultrasonics for structural health monitoring of satellite joints, *Proc. SPIE*, 6935, 2008, San Diego, CA.
34. Z. Mao, M. Todd, A structural transmissibility measurements-based approach for system damage detection, *Proc. SPIE*, 7650, 2010, San Diego, CA.
35. C.C. Chia, J.-R. Lee, C.-Y. Park, H.-M. Jeong, Laser ultrasonic anomalous wave propagation imaging method with adjacent wave subtraction: Application to actual damages in composite wing, *Optics & Laser Technology*. 44, 2; 2012, 428–440.
36. R. Do, C. Haynes, M. Todd, W. Gregory, C. Key, Efficient Detection Methods on a Composite Plate with Interior Embedded Fiber Optic Sensors via Impact Test, *Proc. International Workshop on Structural Health Monitoring*, 2013, Stanford University.
37. N. Takeda, S. Minakuchi, T. Nadabe, Distributed Strain Monitoring for Damage Evolution in CFRP Bolted Structures with Embedded Optical Fibers, *Key Engineering Materials*. 558, 2013, 252–259.
38. J.S. Hall, J.E. Michaels, A model-based approach to dispersion and parameter estimation for ultrasonic guided waves, *The Journal of the Acoustical Society of America*. 127, 2; 2010, 920–930.
39. Speckmann, H. Focal point for SHM - Structural Health Monitoring, Bremen, IMRBPB Meeting, Airbus, 2007.
40. NASA. Ultrasonic Testing of Aerospace Materials. In *Preferred Reliability Practices*, 1999.
41. Djordjevic, B.B. Nondestructive Test Technology for the Composites. In *10th International Conference of the Slovenian Society for Non-Destructive Testing*. Ljubljana, Slovenia, 2009.
42. Workman, G., Walker, J., Lansing, M. Acoustic Method for Damage Sensing in Composite Materials. In *NASA-CR-196538*. 1994.
43. Loutas, T.H., Sotiriades, G., Kostopoulos, V. On the application of Wavelet Transform of AE signals from composite materials. In *European Working Group on Acoustic Emission Conference*. 2004.
44. Gardiner, D.S., Pearson, L.H. Acoustic Emission Monitoring of Composite Damage Occuring under Static and Impact Loading. In *Experimental Techniques*. 9(11), 22-28, Wiley, 2008.
45. Cole, P.T. Using Acoustic Emission (AE) To Locate and Identify Defects in Composite Structures. In *Composite Structures*. 3, 59-267, 1985.

46. Regez, B., Krishnaswamy, S. Nondestructive Evaluation of Structures. Encyclopedia of Aerospace Engineering, 2010.
47. NASA. Eddy Current Testing of Aerospace Materials. In Preferred Reliability Practices. 1999.
48. Bray, D.E., Stanley, R. Nondestructive Evaluation. McGraw-Hill Inc., 1989.
49. Krishnapillai, M., Jones, R., Marshall, I.H., Bannister, M., Rajic, N. Thermography as a tool for damage assessment. In Composite Structures. 67, 149-155, 2005.
50. Baldev, R., Jayakumar, T., Thavasimuthu, M. Practical Non-Destructive Testing. Woodhead Publishing Limited, Cambridge, England, 2002.
51. Shen, L., Liaw, B.M., Delale, F., Chung, J.H. Modeling and Analysis of the Electrical Resistance Measurement of Carbon Fiber Polymer - Matrix Composites. In Composite Science and Technology. 67 (11-12), 2513-2520, 2006.
52. Seo, D.C., Lee J.L. Damage Detection of CFRP Laminates using Electrical Resistance Measurement and Neural Network. In Composite Structures. 47, 525-530, 1999.
53. Karbhari, V.M., Kaiser, H., Navada, R., Ghosh, K., Lee, L. Methods for Detecting Defects in Composite Rehabilitated Concrete Structures. Oregon Department of Transportation Research Unit, Oregon, 2005.
54. Walter, P.L. Strain gage instrumentation. In Piersol, A.G., Paez, T.L., ed., Harris' Shock and Vibration Handbook. McGraw - Hill Companies Inc., United States, 2002.
55. Starr, G.E. Basic Strain Gage Characteristic. In Hannah, R.L., Reed, S.E., ed., Strain Gage Users' Handbook. Chapman & Hall, London, 1994.
56. Glisic, B. and Inaudi, D. (2003) Components of structural monitoring process and selection of monitoring system, PT 6th International Symposium on Field Measurements in GeoMechanics (FMGM 2003), Oslo, Norway, 755-761.
57. Radojicic, A., Bailey, S. and Brühwiler, E. (1999) Consideration of the serviceability limit state in a time dependant probabilistic cost model, Application of Statistics and Probability, Balkema, Rotterdam, Netherlands, Vol.2, 605-612.

Chapter 2

Ultrasonic guided waves

2.1 Introduction

Discovered by Horace Lamb in 1917, Lamb waves can exist in plate-like thin plate with parallel free boundaries. A comprehensive theory for such a wave was established by Mindlin in 1950 [1], in parallel with experimental work conducted by Schoch in 1952 and Frederick in 1962 [2]. The development of such a topic was driven essentially by its applications in medical industry during World War II. Subsequently in 1961, Worlton [3] introduced Lamb waves as a means of damage detection. All these pilot studies established the fundamentals of the utilization of Lamb waves as a prominent non-destructive evaluation (NDE) tool. With a high susceptibility to interference on a propagation path, e.g. damage or a boundary, Lamb waves can travel over a long distance even in materials with a high attenuation ratio, such as carbon fiber-reinforced composites, and thus a broad area can be quickly examined. The entire thickness of the laminate can also be interrogated by various Lamb modes, affording the possibility of detecting internal damage as well as that on surface. In general, a Lamb wave-based damage detection approach features the ability to inspect large structures while retaining coating and insulation, e.g. a pipe system under water; the ability to inspect the entire cross sectional area of a structure (100% coverage over a fairly long length); the lack of need for complicated and expensive insertion/rotation devices, and for device motion during inspection; excellent sensitivity to multiple defects with high precision of identification; and low energy consumption and great cost-effectiveness [4]. At a sophisticated level, a Lamb wave-based identification should hierarchically perform, with increasing levels of difficulty, qualitative indication of the occurrence of damage; quantitative assessment of the position of damage; quantitative estimation of the severity of damage; and prediction of structural safety, e.g. residual service life [5]. However, the propagation of Lamb waves in anisotropic viscoelastic media is notoriously complicated. With a very fast velocity, waves reflected from boundaries may easily conceal damage-scattered components in the signals. To ensure precision, the structure under inspection may have to be relatively large, and with a relatively small area for detection. Multiple wave modes usually exist, and their dispersive properties throughout the thickness of the medium are not identical, even for the same mode but in

different frequency scopes. For its sophistication in damage detection for advanced composites, substantial efforts have been directed to Lamb wave study, especially in the past decade. There is no shortage of achievements for Lamb wave-based identification techniques.

2.2 Fundamentals of Lamb wave

Lamb waves, made up of a superposition of longitudinal and shear modes, are available in a thin plate, and their propagation characteristics vary with entry angle, excitation and structural geometry. A Lamb mode can be either symmetric or anti-symmetric (Figure 2.1), formulated by:

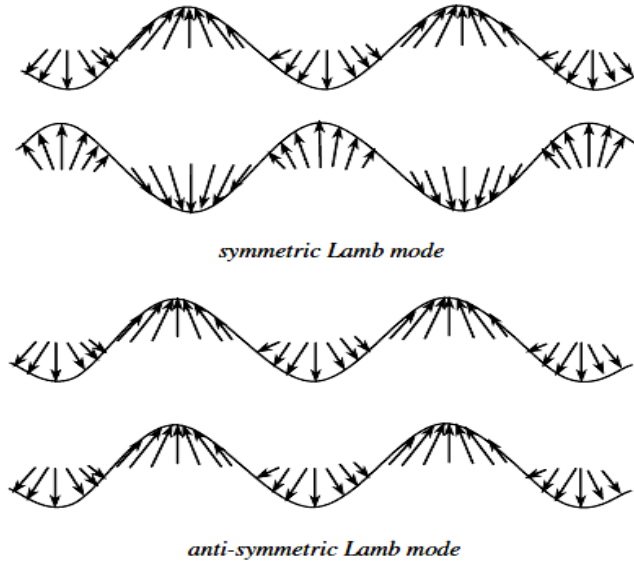


Figure 2.1: Zero order symmetric and antisymmetric Lamb waves modes.

$$\left\{ \begin{array}{l} \frac{\tanh(pd)}{\tanh(qd)} = -\frac{(\xi^2 - q^2)^2}{4\xi^2 pq} \quad \text{Symmetric modes (S)} \\ \frac{\tanh(pd)}{\tanh(qd)} = -\frac{4\xi^2 pq}{(\xi^2 - q^2)^2} \quad \text{Antisymmetric modes (A)} \end{array} \right. \quad (2.1)$$

$$p^2 = \frac{\omega^2}{c_L^2} - k^2, \quad q^2 = \frac{\omega^2}{c_T^2} - k^2 \quad \text{and} \quad k = \omega / c_p$$

where h , k , c_L , c_T , c_p , ω are the plate thickness, wavenumber, velocities of longitudinal and transverse modes, phase velocity and wave circular frequency, respectively. Eq. (2.1),

correlating the propagation velocity with its frequency, implies that Lamb waves, regardless of mode, are dispersive (velocity is dependent on frequency) (see Figure 2.2). By considering the velocity of Lamb waves packets traveling in the plate, it is possible to introduce the group velocity c_g which is linked to phase velocity through the relation:

$$c_g = \frac{\partial \omega}{\partial c_{ph}} \quad \text{or even} \quad c_g = \frac{c_{ph}}{1 - \frac{\omega}{c_{ph}} \frac{\partial c_{ph}}{\partial \omega}} \quad (2.2)$$

In addition to Lamb modes, a transverse (shear) motion, different from normal shear waves (vertical shear mode), was detected between layers of laminate by Love in 1911. This observation has also been confirmed by finite element simulation [6] and experimental study [7]. Perpendicular to the plane of wave travel (see Figure 2.3), such a mode was accordingly named the shear horizontal (SH) mode (Love wave) [8]. In some identification schemes [9, 10], Love mode is employed together with Lamb modes.

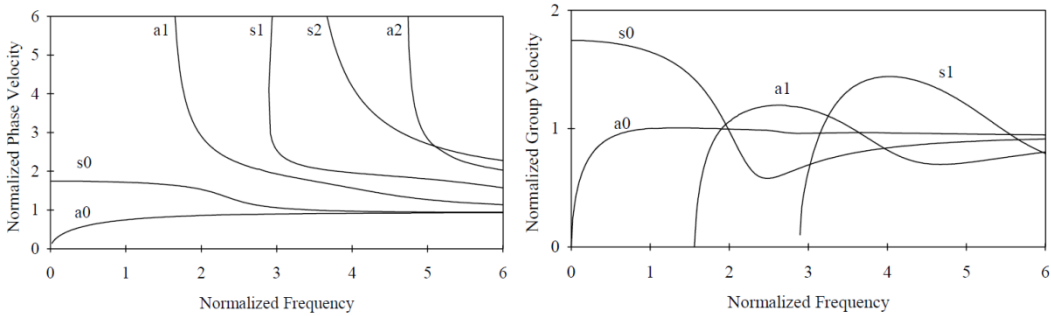


Figure 2.2: Dispersion curves for an aluminum plate, lowest order solutions. Normalizing velocity: shear velocity c_s ; normalizing frequency: $\xi_S \cdot d$, with $\xi_S = \omega/c_s$.

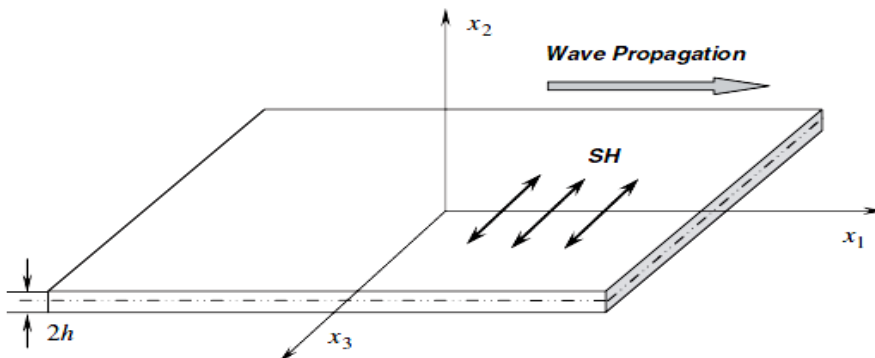


Figure 2.3: Horizontal shear (SH) mode in composite laminate [8].

Anisotropic properties of composite structures introduce many interesting but somewhat complex phenomena in wave propagation, such as direction-dependent speed, and

difference between phase and group velocities. In an N-layered composite laminate, the Lamb wave can be generally described using its displacement field, u , by satisfying Navier's displacement equations within each layer [8]

$$\mu^n \nabla^2 u^n + (\lambda^n + \mu^n) \nabla(\nabla \cdot u^n) = \rho^n \frac{\partial^2 u^n}{\partial t^2} \quad (n=1,2,\dots,N) \quad (2.3)$$

where ρ^n and λ^n, μ^n are density, Lamé constants for the i -th layer, respectively. Attenuation in magnitude, variation in propagating velocity and change in wavenumber are commonly observed, referred to as dispersion. Table 2.1 details experimentally measured attenuation coefficients of Lamb waves in different composite structures [11]. Also tabulated is the distance of propagation before decaying to 10% of its original amplitude. It is clear that in general Lamb waves are able to propagate a relatively long distance even in the composites. A longer propagation distance is normally observed in the carbon fiber-based materials than in the glass fiber reinforced materials. The introduction of stiffening members (such as T-stringers) can increase the attenuation but not substantially. The most serious effect on attenuation is the presence of surface coating materials which may cause very significant damping [11]. On the other hand, applying boundary conditions at N-1 interfaces and free surfaces to Eq. (2.3) leads to a comprehensive dispersion equation [8]

$$|A(\omega, k, \lambda^n, \mu^n, h_n)| = 0 \quad (2.4)$$

where Lamb wave frequency ω is related to the wavenumber k and plate geometry (h_n), for a given material (λ^n, μ^n). In an implicit expression, the dispersion equation has infinite roots, corresponding to the dispersive curves of infinite Lamb modes, respectively.

Materials	Lamb mode	Excitation frequency (kHz)	Attenuation coefficient (mm^{-1})	10% amplitude distance (mm)
CFRP woven 8-ply	S_0	250	0.0014	1700
CFRP woven 10-ply	A_0	285	0.027	85
CFRP woven 10-ply with T-stringers				
<i>Parallel to stringers</i>	S_0	250	0.00078	3000
<i>Perpendicular to stringers</i>	S_0	250	0.0016	1500
GFRP random	S_0	220	0.0035	660
CFRP/GFRP hybrid (RTM) sandwich foam core	S_0	250	0.013	182
CFRP/GFRP hybrid (RTM) sandwich honeycomb core	S_0	250	0.0036	640
	S_0	150	0.0015	1600
GFRP filament wound pipe	S_0	250	0.015	150
	S_0	150	0.011	210

Table 2.1: Attenuation coefficients of Lamb waves in various composite materials [11]

2.3 Generation of Lamb waves

2.3.1. Actuator/sensor for Lamb waves

Lamb waves can be actively excited and collected by a variety of means, roughly grouped under five categories, summarized in Table 2.2 and compared with other NDE transducers.

2.3.2. Ultrasonic probe

Notable for excellent precision and controllability, ultrasonic probes coupled with adjustable-angle perspex wedges [12, 13] or Hertzian contact transducer [14] have been widely used to actively generate and collect a pure Lamb wave, in accordance with Snell's law. Without the complexity of multi-mode, it permits explicit signal interpretation. During manipulation, couplant, directionality and contact are issues that may influence effectiveness.

Non-contact innovations, such as air-coupled [15, 16], and fluid-coupled [17] transducers and electro-magnetic acoustic transducers (EMATs) [18, 19] have therefore been introduced. In particular, EMAT is an effective way to generate shear horizontal mode [20], although their applications were normally limited to metallic structures.

However, these transducers can suffer from the large difference in mechanical impedance between air/fluid and objects under detection, resulting in low precision.

Downtime of the system to be inspected is usually required and the system must be accessible from both sides.

Moreover, such methods may be less efficient for detecting near-surface damage, where reflections from a defect are limited within the wavelength of the transmitted ultrasonic pulse [20]. In addition, the non-negligible mass/volume of the probe and limited access to complex geometry often reduce the practical applications.

2.3.3. Laser

Non-contact excitation of Lamb waves via laser-based ultrasonics (LBU) and acquisition using laser interferometer are reputable methods for high precision [18, 21, 22]. A LBU can be flexibly designed to be broadband or narrowband depending on an actual application, to satisfy different spatial resolution requirements.

The exact detection that LBU can offer ranges from apparent defects to small cracks. Such an approach is also exceptionally effective for curved surfaces or complicated geometry, where access is unfeasible. Additionally, by using a short laser pulse it is possible to excite a broad bandwidth signal with several Lamb modes in a single measurement, providing more opportunities to selectively generate the desired modes [23]. Nevertheless, the cost of equipment can limit broad application.

Sensor	Applications/features	Available style
Ultrasonic probe	Flaw, distance and thickness detection, exact and efficient	Contact, air/ fluid-coupled
Laser interferometer	Derivation or displacement measurement, high precision, expensive	Contactless
Piezoceramics	Active sensor, vibration detection, high-frequency response, low driving force, cheap	Attaching, embedding
Piezoelectric paint and PVDF	Vibration and/or crack detection, easy application for non-flat shapes, cheap	Attaching, embedding
EMAT	Narrow band, avoidance of physical contact	Contact, attaching
Accelerometer	Acceleration detection, high-frequency response	Attaching
Shape memory alloy	Active sensor, deformation detection, active control, large force, low-frequency response	Attaching, embedding
Magnetic sensor	Crack or large deformation with magnetic leakage, soft magnetic piece, magnetic field required	Contact, attaching
Optical fibre	Deformation, temperature and location detection, line sensing, high precision, conformable, expensive	Embedding
AE sensor	Changes in physical property only, location detection, passive sensor	Attaching, embedding
Eddy-current transducer	Electromagnetic impedance detection, good for composites, too complicated, expensive	Attaching
Strain gauge	Deformation detection, low-frequency response, possible to use in hostile environments, cheap	Attaching

Table 2.2 Comparison of Lamb wave transducers with other NDE transducers

2.3.4. Piezoelectric element

Piezoelectric lead Zirconate Titanate (PZT) elements (Figure 2.4 a), deliver excellent performance in Lamb wave generation and acquisition, and are particularly suitable for integration into a host structure as an in-situ generator/sensor, for their neglectable mass/volume/thickness, easy integration, excellent mechanical strength, wide frequency responses, low power consumption and acoustic impedance, as well as low cost. With regard to thickness selection, it has also been observed that the maximum voltage applied on a PZT, without depolarizing it, is 250–300 V/mm [24]. PZT-generated Lamb waves unavoidably contain multiple modes. Sophisticated signal processing is accordingly required. Moreover, a PZT element usually reveals certain nonlinear behavior and hysteresis under large strains/voltages or at high temperature. Small driving force/displacement, brittleness, low fatigue life, etc., may be some other concerns limiting application [25].

2.3.5. Interdigital transducer

Novel interdigital transducers, such as polyvinylidene fluoride (PVDF) piezoelectric polymer film (Figure 2.4 b), have been increasingly introduced to accommodate more versatile applications with reduced cost [26, 28]. Compared with piezoelectric ceramics, PVDF features better flexibility, higher dimensional stability, more stable piezoelectric coefficients over time and greater ease of handling [29]. PVDF is able to produce Lamb waves with controllable wavelength by adjusting the space between interdigital electrodes [27]. Soft and flexible, it can be variously shaped to cope with curved surfaces. PVDF is mainly used as a sensor due to its weak driving force, though it has been used as an

actuator in a few studies [39,40], to find that PVDF actuators work in a very low frequency range only (up to 500 Hz).

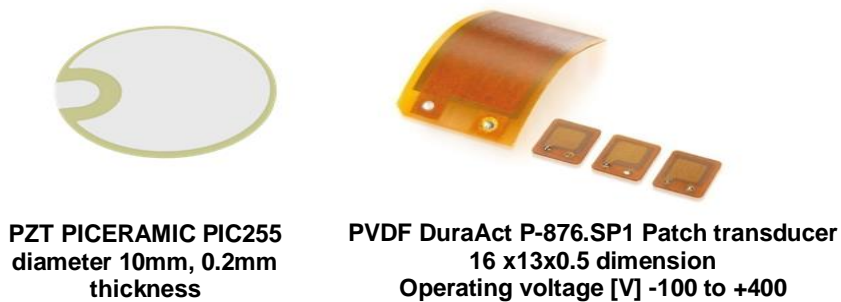


Figure 2.4: (a) Piezoelectric lead Zirconate Titanate; (b) polyvinylidene fluoride (PVDF) piezoelectric polymer film

2.3.6. Optical fiber

With light weight, immunity to electromagnetic interference, wide bandwidth, good compatibility, long life and low power consumption and cost, optical fiber sensors have been increasingly adopted in damage identification [30]. In most approaches, fiber optic devices are used for capturing static or quasi-dynamic strain, with the capacity to measure strain at two-to-three orders of magnitude better resolution than conventional electrical resistance strain gauges [31]. However, applications as a sensor to monitor dynamic Lamb wave signal in the ultrasonic range are rare [32, 33], because of the low sampling rate of the normal optical spectrum analyzer (OSA). One solution to accommodate this concern is the use of a fiber Bragg grating (FBG) filter connected with a photodetector [34], with which the light intensity induced by the Lamb wave, rather than strain itself, can be recorded at a high sampling rate. It has been demonstrated [35] that the amplitude of a Lamb wave captured by a FBG sensor perpendicular to the wave propagation can be 100 times less than that measured by a FBG sensor paralleling the propagation, indicating strong directivity of FBG sensors in collecting Lamb wave signal. In another study [36] on the effectiveness of surface-bonded and embedded FBG sensors in acquiring Lamb waves, it was concluded that an embedded FBG sensor is 20 times more sensitive to Lamb waves than a surface-bonded FBG sensor, although the surface-bonded sensor is more practical because embedding an optical fiber into composite materials often lowers structural mechanical properties, with consequent difficulty in repair and replacement [37].

2.4 Ultrasonic Guided Waves Inspection

Ultrasonic testing represents one of the most prevalent inspection techniques for NDE and SHM [38]. The work in this dissertation makes use of frequencies in the range of 20-100 kHz, although for other applications either higher or lower frequencies may be warranted.

As previously presented, the ultrasonic waves when guided by the boundaries of a one dimensional (1D) or two-dimensional (2D) propagation medium, they belong to a unique class known as ultrasonic guided waves (UGWs) or Lamb waves. Guided waves are formed by the resonance of waves in the material as they reflect off the boundaries. Although the number of modes, in each class symmetric or antisymmetric, is infinite, higher modes can only exist at higher excitation frequencies. Therefore, below a certain cut-off frequency-thickness product, only the fundamental antisymmetric (A_0) and fundamental symmetric (S_0) modes exist. All of the experiments considered in this dissertation are below the cut-off frequency-thicknesses product of their respective media, and therefore these are the only two modes generally discussed. Which mode is dominant for a particular application primarily relates to the transducer design, although the so-called “mode ratio” may be influenced by other factors as well.

Guided waves are of particular interest in SHM for a number of reasons. Among nondestructive testing methods, UGW inspection offers relatively large coverage areas per sensor with appropriate system design, particularly considering the corresponding sensitivity to small damage [39]. UGW inspection is often still feasible when access to the part is limited. The transducers used for generating UGW are easily embeddable and relatively inexpensive [40].

The propagation of UGW is governed by several parameters, most notably material properties (especially elastic moduli and density), the product of excitation frequency and plate thickness, temperature, material stresses, and boundary conditions. In general, the velocity of UGW is a frequency-dependent parameter, giving rise to the well know phenomenon of dispersion. Because of the dispersive character of these waves have a distinct group and a phase velocity. As previously said, the group velocity is the speed at which the envelope of the wave packet propagates, while the phase velocity is the speed of the particles within the wave packet.

For monitoring of damage, the wavelength of interrogation is the most critical parameter. In order to maintain sensitivity to a particular form of damage, the wavelengths must be of the same order as the damage scale [41, 42]. The efficacy of UGW as an inspection technique is ultimately dependent on the fact that the wave scattering changes when damage is present. One of the most significant challenges associated with the UGW SHM approach is that all geometric irregularities (stiffener elements, material changes, boundaries, etc.) cause changes in the wave propagation. Most of these geometric features represent impedance mismatches that cause waves to scatter in the same way as the target damage, which further complicates the accurate inspection of geometrically-complex structures.

2.5 UGW Signal processing for damage detection

The data obtained from dynamic testing and frequency response of structures need further processing and are not always easy to interpret and handle. Signal processing is the core for any damage identification system. Figure 2.5 summarizes the overall intelligent chain of processing for a multi-sensor architecture. As a first step, data preprocessing has to be implemented, which involves signal correction, according to the data acquisition unit, mean value calculation, time synchronous averaging, and filtering. It includes also data normalization which helps to generalize amplitude levels of different data [43]. Main next step is the feature extraction, which is a key point since the determination of damage-sensitive features is not always evident (ToF, Group Velocity, Transmission Factor, Signal Level, etc.). Damage indices can be obtained from analysis in time domain, in frequency domain or simultaneously in the time-frequency domain via special transforms such as the wavelet or short time Fourier transform. After data fusion, the separation and clustering of the data correspondingly to their damage state and/or location utilizes pattern recognition techniques. The basic idea is to recognize the behavior of the undamaged structure as well as its behavior under various damage states. When the implemented analysis system receives any data from the dynamic response of the structure it should be able to correspond it to a specific damage (or non-damage) state [44].

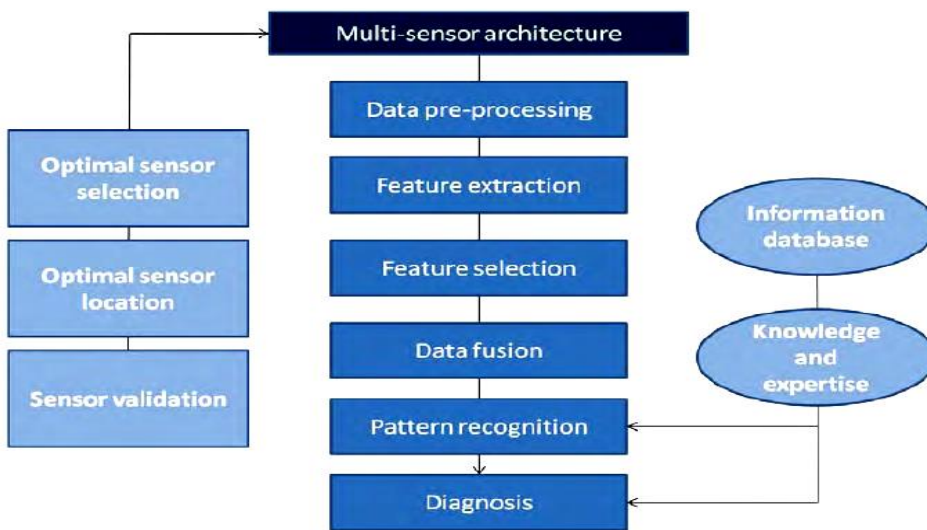


Figure 2.5: Signal processing for a multi-sensor architecture

2.6 References

1. M.J.S. Lowe, Matrix techniques for modelling ultrasonic waves in multilayered media, *IEEE Transactions on Ultrasonics, Ferroelectrics and Frequency Control* 42 (4) (1995) 525–542.
2. D.E. Chimenti, Guided waves in plates and their use in materials characterization, *Applied Mechanics Reviews* 50 (5) (1997) 247–284.
3. D.C. Worlton, Experimental confirmation of Lamb waves at megacycle frequencies, *Journal of Applied Physics* 32 (1961) 967–971.
4. J.L. Rose, A vision of ultrasonic guided wave inspection potential, *Proceedings of the Seventh ASME NDE Topical Conference, NDE-Vol. 20 (1–5)*, 2001.
5. K. Worden, G. Manson, D. Allman, Experimental validation of a structural health monitoring methodology: Part I. Novelty detection on a laboratory structure, *Journal of Sound and Vibration* 259 (2) (2003) 323–343.
6. E.A. Birt, Damage detection in carbon-fibre composites using ultrasonic Lamb waves, *Insight* 40 (5) (1998) 335–339.
7. W.J. Percival, E.A. Birt, A study of Lamb wave propagation in carbon-fibre composites, *Insight* 39 (1997) 728–735.
8. J.L. Rose, *Ultrasonic Waves in Solid Media*, Cambridge University Press, New York, 1999.
9. M. Lemistre, D.L. Balageas, Structural health monitoring system based on diffracted Lamb wave analysis by multiresolution processing, *Smart Materials and Structures* 10 (2001) 504–511.
10. Z. Su, L. Ye, X. Bu, A damage identification technique for CF/EP composite laminates using distributed piezoelectric transducers, *Composite Structures* 57 (2002) 465–471.
11. S.G. Pierce, B. Culshaw, G. Manson, K. Worden, W.J. Staszewski, The application of ultrasonic Lamb wave techniques to the evaluation of advanced composite structures, *Proceedings of SPIE* 3986 (2000) 93–103.
12. D.N. Alleyne, P. Cawley, The interaction of Lamb waves with defects, *IEEE Transactions on Ultrasonics, Ferroelectrics and Frequency Control* 39 (3) (1992) 381–397.
13. N. Guo, P. Cawley, Lamb wave reflection for the quick nondestructive evaluation of large composite laminates, *Materials Evaluation* 52 (1994) 404–411.
14. F.L. Degertekin, B.T. Khuri-Yakub, Lamb wave excitation by Hertzian contacts with application in NDE, *IEEE Transactions on Ultrasonics, Ferroelectrics, and Frequency Control* 44 (1997) 769–779.
15. M. Castaings, P. Cawley, The generation, propagation, and detection of Lamb waves in plates using air-coupled ultrasonic transducers, *Journal of the Acoustical Society of America* 100 (5) (1996) 3070–3077.

16. M. Castaings, B. Hosten, Lamb and SH waves generated and detected by air-coupled ultrasonic transducers in composite material plates, *NDT & E International* 34 (2001) 249–258.
17. T. Ghosh, T. Kundu, P. Karpur, Efficient use of Lamb modes for detecting defects in large plates, *Ultrasonics* 36 (1998) 791–801.
18. Z. Guo, J.D. Achenbach, S. Krishnaswamy, EMAT generation and laser detection of single Lamb wave modes, *Ultrasonics* 35 (1997) 423–429.
19. S. Legendre, D. Massicotte, J. Goyette, T.K. Bose, Wavelet-transform-based method of analysis for Lamb-wave ultrasonic NDE signals, *IEEE Transactions on Instrumentation and Measurement* 49 (2000) 524–530.
20. J.D. Achenbach, Quantitative nondestructive evaluation, *International Journal of Solids and Structures* 37 (2000) 13–27.
21. S. Yoshimura, G. Yagawa, A. Oishi, K. Yamada, Neural network based inverse analysis for defect identification with laser ultrasonics, *Key Engineering Materials* 145-149 (1998) 443–452.
22. W. Gao, C. Glorieux, J. Thoen, Laser ultrasonic study of Lamb waves: determination of the thickness and velocities of a thin plate, *International Journal of Engineering Science* 41 (2003) 219–228.
23. M.Z. Silva, R. Gouyon, F. Lepoutre, Hidden corrosion detection in aircraft aluminium structures using laser ultrasonics and wavelet transform signal analysis, *Ultrasonics* 41 (2003) 301–305.
24. C.S. Wang, F.-K. Chang, Diagnosis of impact damage in composite structures with built-in piezoelectrics network, *Proceedings of SPIE* 3990 (2000) 13–19.
25. M.J. Schulz, P.F. Pai, D.J. Inman, Health monitoring and active control of composite structures using piezoceramic patches, *Composites, Part B* 30 (1999) 713–725.
26. R.S.C. Monkhouse, P.W. Wilcox, M.J.S. Lowe, R.P. Dalton, P. Cawley, The rapid monitoring of structures using interdigital Lamb wave transducers, *Smart Materials and Structures* 9 (2000) 304–309.
27. R.S.C. Monkhouse, P.D. Wilcox, P. Cawley, Flexible interdigital PVDF transducers for the generation of Lamb waves in structures, *Ultrasonics* 35 (1997) 489–498.
28. P. Blanas, D.K. Das-Gupta, Composite piezoelectric sensors for smart composite structures, *Proceedings of the 10th International Symposium on Electrets, Athens, Greece, 1999*, pp. 731–734.
29. S. Hurlaus, L. Gaul, Smart Layer for Damage Diagnostics, *Journal of Intelligent Material Systems and Structures* 15 (2004) 729–736.
30. C. Boller, Ways and options for aircraft structural health monitoring, *Smart Materials and Structures* 10 (2001) 432–440.
31. A. Guemes, Optical fibre sensors, Presentation on the First European Pre-Workshop on Structural Health Monitoring, 9 July 2002, Paris, France, 2002.

32. W.J. Staszewski, S.G. Pierce, K. Worden, B. Culshaw, Cross-wavelet analysis for Lamb wave damage detection in composite materials using optical fibres, *Key Engineering Materials* 167-168 (1999) 374–380.
33. A. Gachagan, G. Hayward, A. McNab, P. Reynolds, S.G. Pierce, W.R. Philp, B. Culshaw, Generation and reception of ultrasonic guided waves in composite plates using conformable piezoelectric transmitters and optical-fiber detectors, *IEEE Transactions on Ultrasonics, Ferroelectrics and Frequency Control* 46 (1) (1999) 72–81.
34. H. Tsuda, N. Toyama, K. Urabe, J. Takatsubo, Impact damage detection in CFRP using fiber Bragg gratings, *Smart Materials and Structures* 13 (2004) 719–724.
35. D.C. Betz, G. Thursby, B. Culshaw, W.J. Staszewski, Acousto-ultrasonic sensing using fiber Bragg gratings, *Smart Materials and Structures* 12 (2003) 122–128.
36. S.G. Pierce, W.R. Philp, A. Gachagan, A. McNab, G. Hayward, B. Culshaw, Surface-bonded and embedded optical fibers as ultrasonic sensors, *Applied Optics* 35 (25) (1996) 5191–5197.
37. G. Zhou, L.M. Sim, Damage detection and assessment in fibre-reinforced composite structures with embedded fibre optic sensors review, *Smart Materials and Structures* 11 (2002) 925–939.
38. P.J. Shull, editor, *Nondestructive Evaluation: Theory, Techniques, and Applications*, CRC Press, Boca Raton, 2002.
39. P.D. Wilcox, M.J.S. Lowe, P. Cawley, Mode and Transducer Selection for Long Range Lamb Wave Inspection, *Journal of Intelligent Material Systems and Structures*. 12, 8; 2001, 553–565.
40. V. Giurgiutiu, J. Bao, W. Zhao, Piezoelectric wafer active sensor embedded ultrasonics in beams and plates, *Experimental Mechanics*. 43, 4; 2003, 428–449.
41. K. Worden, C.R. Farrar, G. Manson, G. Park, The fundamental axioms of structural health monitoring, *Proc. R. Soc. A*. 463, 2082; 2007, 1639–1664.
42. D.N. Alleyne, P. Cawley, The interaction of Lamb waves with defects, *IEEE Transactions on Ultrasonics, Ferroelectrics and Frequency Control*. 39, 3; 1992, 381–397.
43. Staszewski, W.J. *Intelligent Signal Processing for Damage Detection in Composite Materials*. In *Composites Science and Technology*. 62 (7-8), 941-950, 2002.
44. Staszewski, W.J., Worden, K. *Signal Processing for Damage Detection*. In *Health Monitoring of Aerospace Structures: Smart Sensor Technologies and Signal Processing*. John Wiley & Sons Inc., West Sussex, United Kingdom, 2004.

Chapter 3

Structural Health Monitoring System

Design and Testing

3.1 Introduction

The extensive use in modern design of composite materials for primary structures of civil and military aircraft requires continuous verification of their integrity through effective programs of non-destructive inspections and investigations, both in the case of "anomalous events "(safe life criterion), both when they are an integral part of the design philosophy and then already scheduled (damage tolerance criteria) in maintenance programs. However, the "inspection and maintenance" operations represent more than 25% of operating costs of an aircraft and the certification authority for composites requires the adoption of high safety factors: the result is a significant increase in terms of weight and costs.

The degradation of critical structural components is controlled through careful and expensive regularly scheduled inspections in an effort to reduce their risk of failure. However, the increasing cost of scheduled, often unneeded, maintenance make imperative the implementation of an intelligent real-time monitoring of the structures conditions to guarantee their safe and affordable continuing operation.

An SHM system able to interrogate a structural sub-component with accuracy and reliability of a consolidated Non Destructive Technique (NDT) would permit immediately to substitute the actual level inspection approach based on visual inspection followed eventually by NDT analysis with a single-level inspection highly automated based on sensors permanently and not invasively installed on the structure to monitor [1].

In this chapter is presented a detailed description of the many technological and methodological aspects related to the design of a SHM system based on guided waves with reference to the application to a wing box small structural element made of Graphite Reinforced Plastics.

The main issues that will be described include: sensors selection, hardware and software systems design, numerical tool aimed at system design and sensors location optimization and functionality check [2].

The proposed procedure is conceived to detect interlaminar defects (delaminations, debonding and/or inclusions) in a typical CFRP laminate. A damage index (DI) approach for damage detection and localization based on high frequency wave propagation data is presented. Improved ultrasonic test setup, consisting of distributed high-fidelity piezoelectric sensors, data acquisition boards, signal conditioning and dedicated software have been implemented.

Using the initial measurements performed on an undamaged structure as baseline, damage indices are evaluated from the comparison of the dynamic response of the monitored structure with an unknown damage.

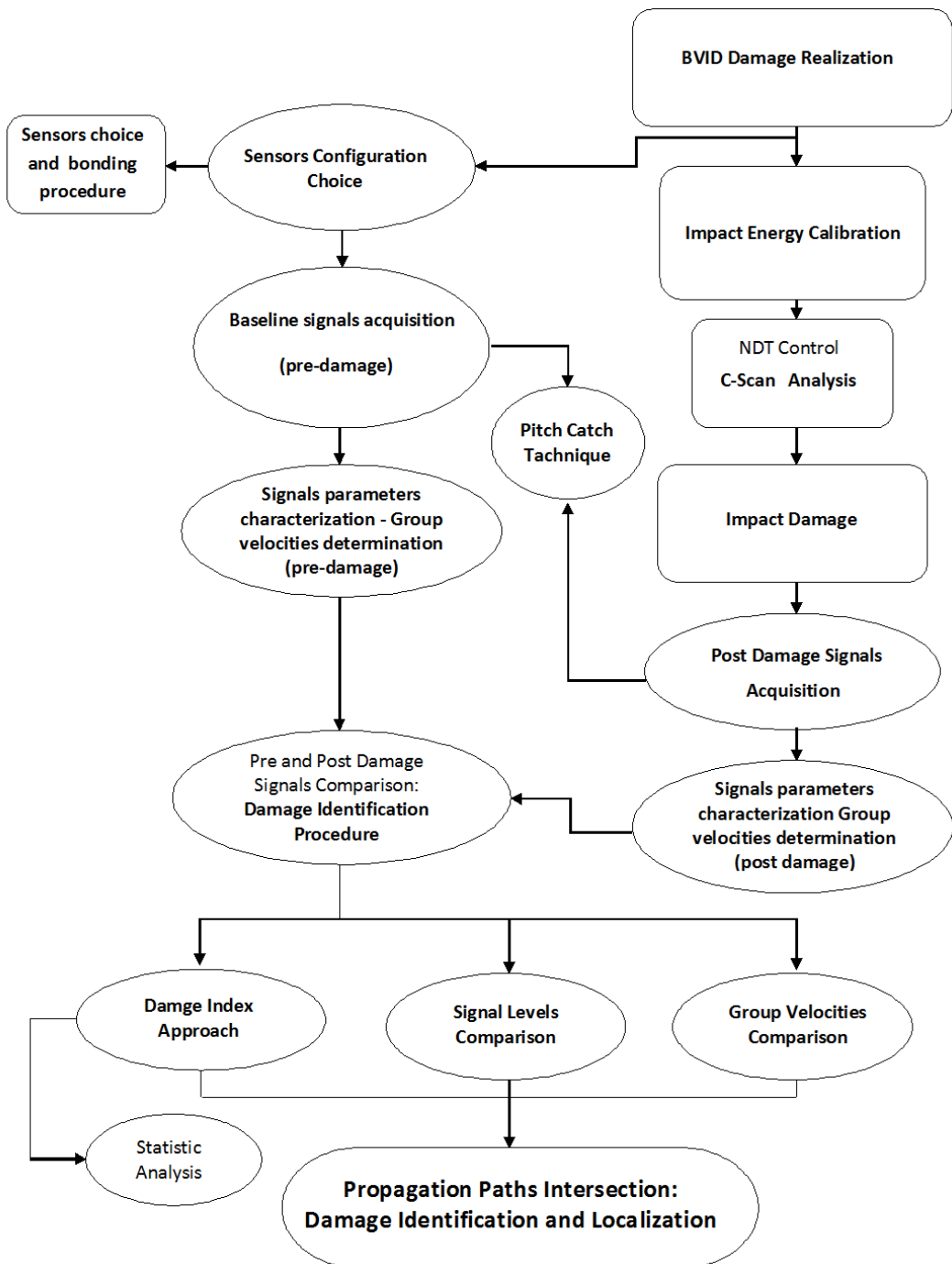
In case of wave propagation measurements, a damaged/undamaged paths recognition mechanism is used to approximately locate the damage using the correlations obtained between Damage Index, wave propagation velocities or Time of Flight (TOF) and energy levels damaged/undamaged differences.

In this approach, a DI comparing the measured dynamical response of two successive states of the structure is introduced as a determinant of structural damage. The index can, in principle, be defined for a generic structural parameter including displacement, velocity, acceleration, strain, or voltage measured by embedded or secondary bonded sensors.

The DI returns non-zero values only if any change in the measured dynamical response of the structure occurs, and it will return zeros if the experimental measurements are identical. The damage presence modifies certain ultrasonic waves characteristics, so changes in the measured dynamic response of the structure are analyzed to reveal the presence of damages.

Elastic waves with known properties are launched by broadband transducers located on the surface of the structure. The dynamic response induced by the source is acquired by multiple sensors conveniently located on the surface of the structural component.

Design of SHM systems



3.2 Sensor technology

SHM application transducers have to be small, light, cheap and suitable for aerospace applications, where the requirements of weight and cost are stringent. In this regard, the PWAS sensor (Piezoelectric Wafer Active Sensors) satisfy most of these characteristics and are the most widely used sensor for actuator or sensor applications. Based on the piezoelectric effect and originally used for surveys and inspections of vibrational nature, nowadays the application field of PWAS sensors is divided into three main areas: the modal analysis, the electro-mechanical impedance and the wave propagation parameters analysis.

It is worth to note that the sensors typology has gone through a continuous development over the research activity following a building block approach (Figure 3.1). Starting from commercial piezoelectric sensors, brittle ceramic or flexible, individually controlled by laboratory devices such as signal generators, oscilloscopes and data acquisition systems Lab View based, the sensor evolution has moved toward flexible piezoelectric sensors, with a customized omnidirectional shape, driven by a dedicated multiplexing channel acquisition systems.

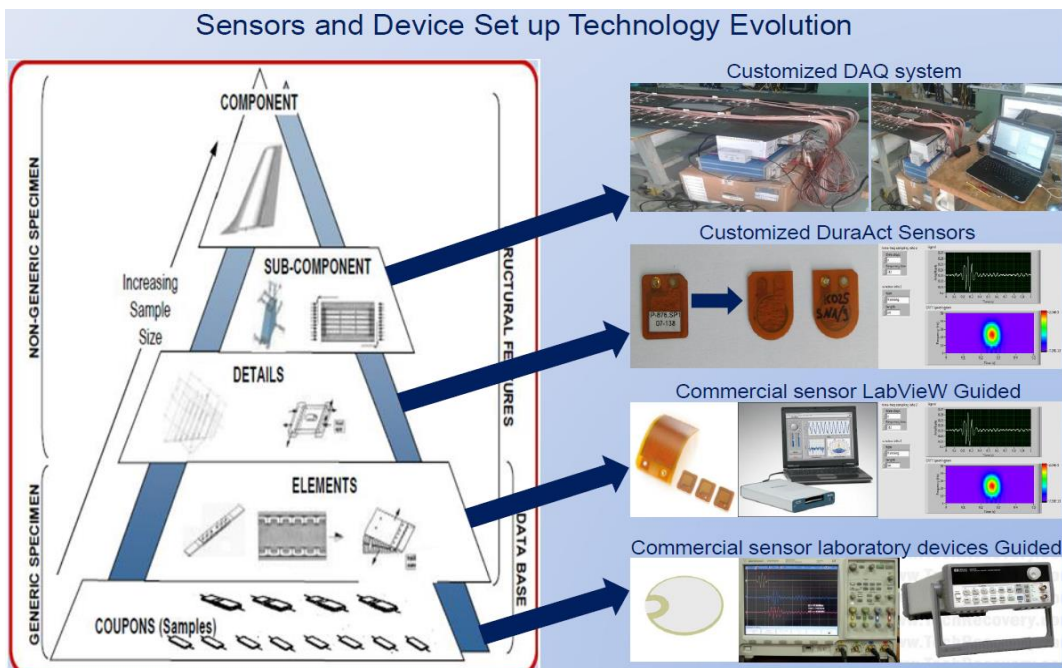


Figure 3.1: Sensors evolution

The above mentioned, piezoelectricity is the property of some materials to convert electrical energy into mechanical energy and vice versa. In 1880 Jacques and Pierre Curie discovered that pressure generates electrical charges in a number of crystals such as Quartz and Tourmaline [3]. This phenomenon was called “piezoelectric effect”. Later they noticed

that electrical fields can deform piezoelectric materials, this effect was called “inverse piezoelectric effect”. The piezoelectric effect of natural monocrystalline materials such as Quartz and Tourmaline is relatively small. Polycrystalline ferroelectric ceramics such as Barium Titanate (BaTiO₃) and Lead Zirconate Titanate (PZT) exhibit larger displacements or induce larger electric voltages.

The first kind of sensors used in this work are PIC255 (PI Ceramic GmbH) (Figure 3.2 a), a thin disk having a diameter of 10 mm, a thickness of 0.2 mm and a density of 7.80 g/cm³. These sensors are a modified Lead Zirconate – Lead Titanate (Soft-PZT) with radial mechanical deformation, very high Curie temperature (about 350 °C), high permittivity, high coupling factor, high charge coefficient, low mechanical quality factor, low temperature coefficient and low-power consumption.

The second kind of sensors tested are DuraAct P-876.SP1 (Figure 3.2 b) having dimensions 16x13x0.6 mm, active area of 0.64 cm² and a mass of 0.5 g. DuraAct patch transducers (commercial rectangular or customized circular shape) are based on a thin piezoceramic foil between two conductive films, all embedded in a ductile composite-polymer structure. In this way, the brittle piezoceramic is mechanically pre-stressed and electrically insulated, which makes the transducers more robust and therefore applicable on curved surfaces.



Figure 3.2: a) PIC255 PZT, b) DuraAct P-876.SP1

3.2.1. Sensors bonding procedures

After the sensors choice, fundamental is the bonding procedure selection and the correct surface treatment in order to allow the best sensor-surface integration. The adopted sensor bonding procedure consists of the following main steps:

1. Preparation of position and alignment;
2. Surface preparation;
3. Mixing of adhesive;
4. Application of adhesive;
5. Application of sensor.

Usually, once defined the sensor position, it is necessary to mark the intended position with some hairlines and mask the surrounding surface in order to ensure the correct sensor

alignment. Then a slightly roughing of the surface protection layer of CFRP substrates is practiced in order to activate the surface.

Removed the abrasion dust and degreased the substrate and the sensor bottom with a clean lint-free cloth moistened with an adequate cleaning solvent like Isopropanol, a thin film of a bi-component cold curing epoxy adhesive, Hysol EA9394 (by Loctite) (Figure 3.3 and Table 3.1) [4], is applied on the substrate and on bottom of the sensor. Finally, the sensor is set its intended position and permanently fixed employing a vacuum based secondary bonding procedures.

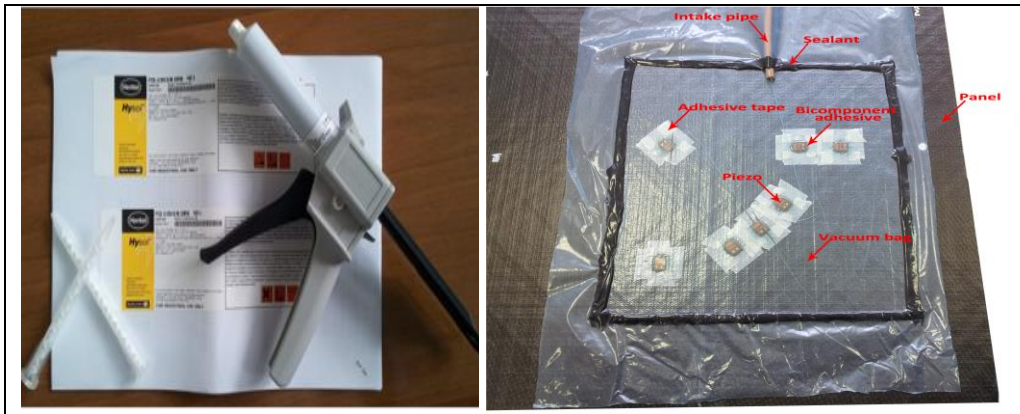


Figure 3.3: (left) Hysol EA9394 bi-component cold curing epoxy adhesive applicator, (right) vacuum based secondary bonding procedures

Mixing ration	Part A (Base)	Part B (Hardener)
By weight	100	17

Table 3.1

3.3 Laboratory device actuation and sensing technology

3.3.1 Acquisition System

A typical UT inspection system consists of several functional units, such as the pulser/receiver, transducer, and display devices. A pulser/receiver is an electronic device that can produce high voltage electrical pulses. Driven by the pulser, the transducer generates high frequency ultrasonic energy. The sound energy is introduced and propagates through the materials in the form of waves. When there is a discontinuity (such as a crack) in the wave path, part of the energy will be reflected back from the flaw surface.

In the applet below (Figure 3.4), the reflected signal strength is displayed versus the time from signal generation to when an echo was received. Signal travel time can be directly related to the distance that the signal traveled. From signal analysis, information about the reflector location, size, orientation and other features can sometimes be gained.

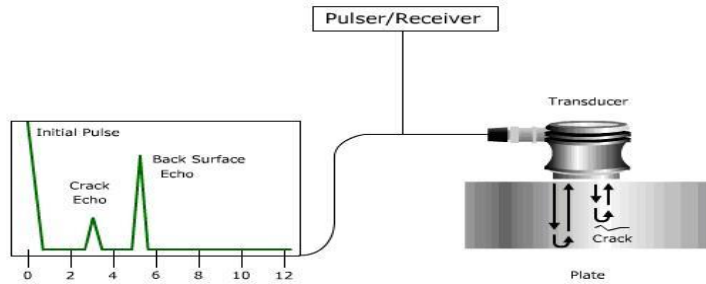


Figure 3.4: pulse echo acquisition technique

3.3.2 Power amplifier

The voltage amplifier, placed between the signal generator and the piezoelectric sensors, performs the task of increasing the amplitude of the excitation signal. The voltage amplifier is used with a constant gain and allows to increase the amplitude of the input signal up to 8 times. Since, during the tests, the amplitude of the input signal is typically set to a constant value of 10 volts, the excitation signal to the actuator can assume amplitudes between 10 and 80 volts.



3.3.3 Signal generator

The excitation of the piezoelectric sensors has been realized by a signal generator HP/AGILENT 33120A. This device, in addition to being equipped with a stock of more than ten forms standard waveform, gives to the user the possibility to create arbitrary waveform by the use of a simple software. It is also possible to generate signals having very high frequencies, up to 15 MHz, by choosing the appropriate burst rate. The main features are tabulated below:

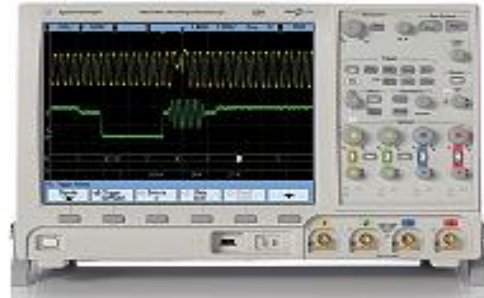


Standard Waveforms	Sine, square, triangle, ramp, noise, sin(x)/x, exponential rise exponential fall, cardiac, dc volts.
Frequency range	100 μ Hz- 15 MHz
Dimensions	254.4mm x 103.6mm x 374mm
Weight	4kg
Operating Environment	0°C to 55°C

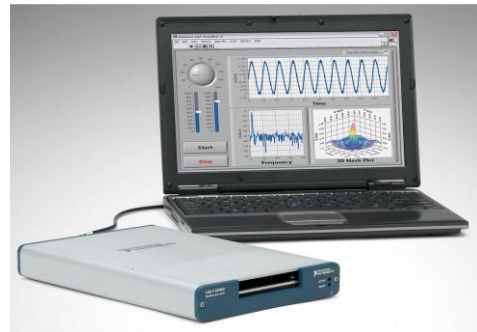
Table 3.2 – Main characteristics of the HP/AGILENT 33120A generator

3.3.4 Data storage

The signals emitted and/or received by the piezoelectric sensors were displayed, processed and stored on a USB device with a AGILENT oscilloscope, model InfiniiVision DSO7014A, engineered with advanced technology that allows to see subtler signal detail and more infrequent events. Such a device, provided with four channels of analog acquisition, presents a high speed update (up to 100,000 waveforms per second) and a sampling rate equally high (up to 2 GSa/s). The 12.1" XGA display with 256 levels of color allows accurate visualization of the signal, with a maximum of 8 Mpt zooming.

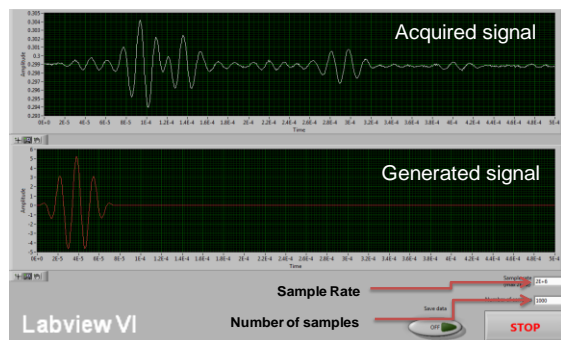


In parallel with the oscilloscope, it was used a USB Multifunction Data Acquisition (DAQ) System X USB-6366 model. NI X Series USB devices are the most advanced data acquisition devices of National Instruments. They feature significant improvements in onboard timing and triggering and optimizations for use with multi-core PCs. X Series integrate high-performance analog, digital, and counter/timer functionality for the most common types of static and waveform measurements, making them well-suited for a broad range of applications from basic data logging to control and test automation. With LabVIEW SubVI it is possible easily acquire and view data on a wide variety of graphs and displays. It is possible use configuration-based wizards called Express VIs to take measurements and perform signal processing with minimal programming.



The device has eight input channels and a sample frequency of 2 Ms/s. The advantages of its use compared with the oscilloscope are:

- eight input channels;
- by Virtual Instrument (VI) it is possible to change the time window improving the time resolution of the signal;
- the signal is stored directly on the computer and ready for analysis and manipulation;
- is a lightweight and portable.



3.4. Signal acquisition

Impact damage assessment using integrated ultrasonic sensors is performed by signal analysis, so a common understanding of the actuation signal, of the main signal parameters (features) and of the possible feature extraction methods (decomposition algorithm) is required.

From a practical point of view, the acquired signals carry important information on defects that may be present in their propagation path. However, these signals are also affected by the material characteristics, including the level of anisotropy, rivets, stringers and geometric discontinuities (such as thickness variation) and boundaries due to scattering, diffraction and reflection of the waves [5].

Three main parameters are necessary to characterize a signal response of a wave-packet: time of arrival, frequency and amplitude. The aim of signal processing is the extraction and identification of the main wave packages that constitute the signal, for analysis, denoising or compression. A method particularly interesting for decomposition and compression will not be necessarily the best for analysis of Guided waves since we do not want a general form of the signal but more the details that it contains.

If a pair of transducers is bonded on one surface of the plate, knowing the distance between the two transducers, the time of flight can be used to get the group velocity of the wave, and then, by its position in the group velocity versus frequency, namely, from the dispersion curves identify the wave mode.

That is the primary reason that justify the need of a good method. There are numerous Time-Frequency Representation methods and several detailed studies about this subject [6]. In the following the most commonly Time-Frequency-Representations used for the data analysis.

3.4.1 Choice of excitation signal

The first problem to be addressed in the signal choice is the reduction of the side harmonics. Limiting the number of sinus-cycles let a dominant central frequency but cannot avoid harmonics as it is possible to see in Figure 3.5.

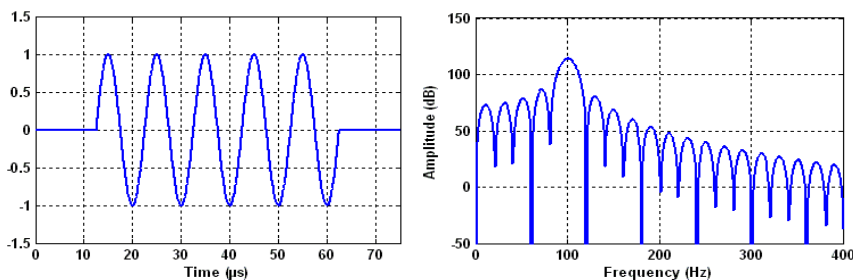


Figure 3.5: 5 sinus signal (left) of 100kHz and its FFT-spectrum (right)

Even if a stronger central frequency is obtained, sidebands have to be lowered. The ratio between the amplitude of the central frequency and the first sidebands has to be increased. The figure below shows an Hanning window and its frequency spectrum. This window offers the least “spill-over” from neighboring frequencies.

The Hanning window equation is:

$$x(t, T) = 0.5 \cdot \left(1 - \cos\left(\frac{2\pi \cdot t}{T}\right) \right) \quad (3.1)$$

where T represents the period of the window. The Hanning windowed n -cycles sinus signal thus obtained is usually referred as "Burst".

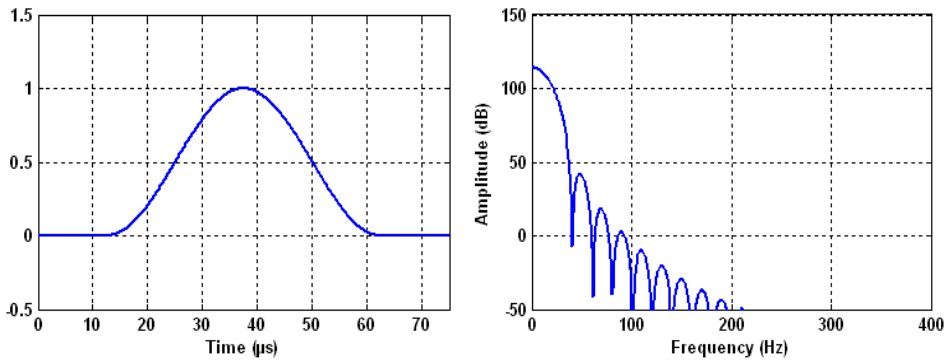
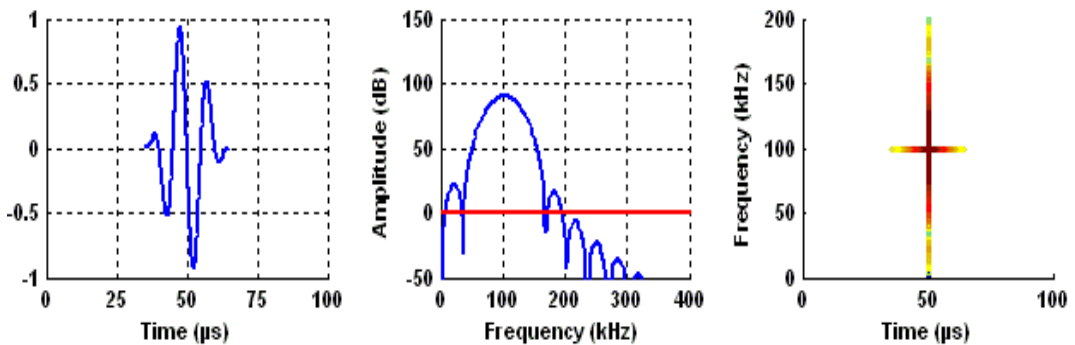


Figure 3.6: Hanning-window (left) and its FT-spectrum

Special attention deserves the definition of the number of the cycles in the incident wave. It is one of the most important parameters, because it has direct influence on the frequency content of the signal. A greater “central to sideband frequencies ratio” requires a great number of cycles which leads to a long lasting excitation signal. Typical used signals vary from 3.5 to 13.5 cycles per actuating pulse [7]. Figure 3.7 represents different burst with the same frequency of 100kHz but with different number of cycles.



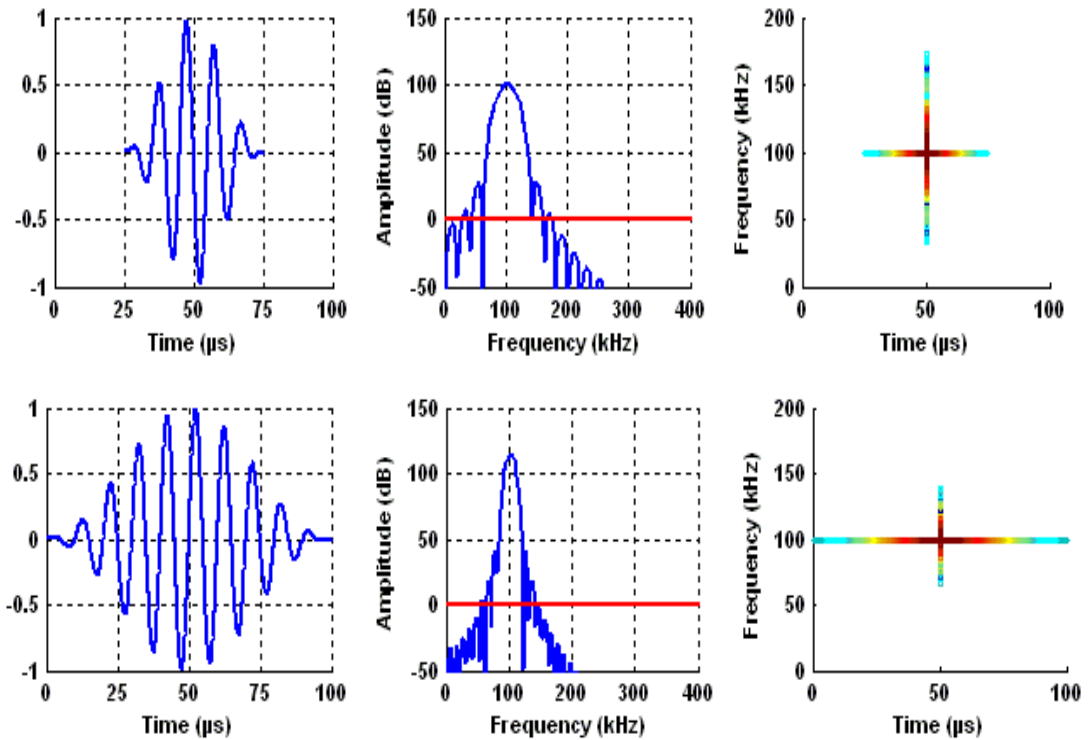


Figure 3.7: Tone-burst with different number of cycles (left), their FFT-spectra (center) and the time-frequency localization (right)

As we have reciprocity for time versus frequency resolution, it is therefore important to well define the number of cycles. The most used signal during this project is a 4,5-cycles burst, since it gives a good balance between time and frequency resolution (Figure 3.8).

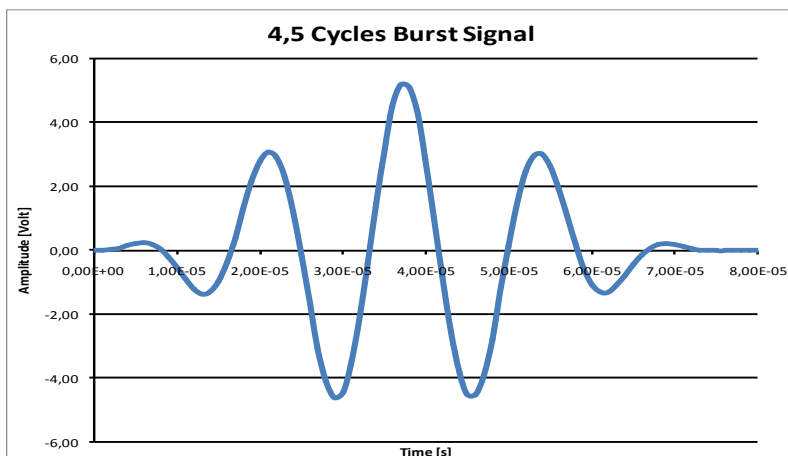


Figure 3.8: 4,5 Cycles Burst Signal

3.5 Signal Acquisition Parameters (Sampling Frequency, Windowing...)

3.5.1 Time of flight (TOF)

The time of flight is the time needed for an emitted wave-packet to travel on the distance between two transducers. There are different ways to measure it, as shown in Figure 3.9 below.

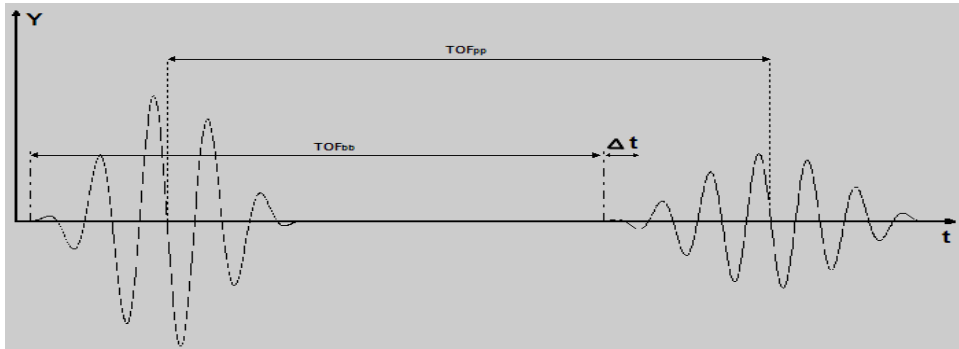


Figure 3.9: TOF: beginning of the wave, peak of the wave

TOF_{pp} is for time of flight peak to peak and TOF_{bb} is for beginning to beginning. Δt is for the difference $TOF_{pp} - TOF_{bb}$. As a wave-packet can be dispersive, the use beginning of the incoming wave is not a good choice. Therefore, the TOF will be calculated assuming that the peak arrives with the central frequency of the actuation. The reference is then the maximum amplitude of the actuation signal calculated with the same Time-Frequency Representation (TFR) method. Given dispersive character of Lamb waves, a change in the structure can affect the time of flight. An impact delamination causes Lamb waves to propagate in a different thickness condition thus this has an effect in wave propagation velocity. A shift in the arrival time of A0 mode can be observed on the raw signal (Figure 3.10) [8].

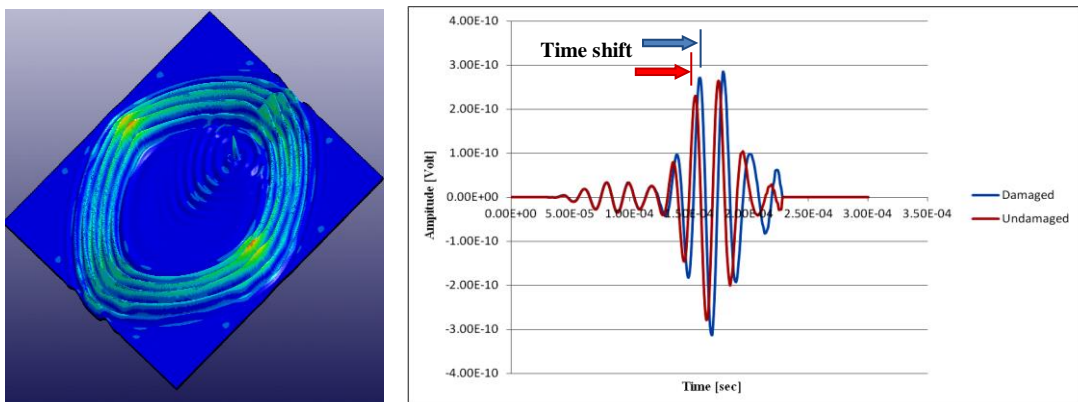


Figure 3.10: Left: Numerical simulation of waves propagation across an impact delamination. Right: Acquired signal with pristine state (red) and after delamination (blue)

3.5.2 Central Frequency

The choice of the excitation frequency is an important consideration in defects detection [9]. It's necessary to take into account three basic requirements. The mode number of the Lamb waves should be as low as possible to limit the complexity of the received signals; the modes should be as non-dispersive as possible so that the waveform is independent of the propagation distance and the wavelength should be equal to or smaller than the size of the damage to be detected. To meet these requirements, the dispersion curves for the group velocity must be examined. To satisfy the first requirement, only the zero-order modes, S_0 and A_0 , should be generated. The second condition implies that, at the driving frequency, the slope of the dispersion curves should be nearly zero, so that the group velocity is almost frequency independent, and the dispersive effect of the propagation distance can be avoided. The third condition requires the frequency to be as large as possible without affecting the first two conditions.

So, to identify a mode, once the TOF is found, the wave packet frequency is needed in order to compare it with the corresponding dispersion curves. The central frequency of the actuation is a fingerprint of a mode, for example as a “sweet-spot” in excitability. This frequency will be defined as the one corresponding to the maximum amplitude of a detected peak. The group and phase velocity of Lamb waves depends on the product of thickness and frequency. A change in thickness can have an influence in frequency and the dispersion curves.

3.5.3 Amplitude

To check the influence of a defect, the main effect seen will be an attenuation or an absorption of a wave energy (Figure 3.11). To quantify this effect and maybe correlate it with the size of the delamination, the amplitude must be precisely determined. The changes in the amplitude of wave packages is widely used to detect damages [8].

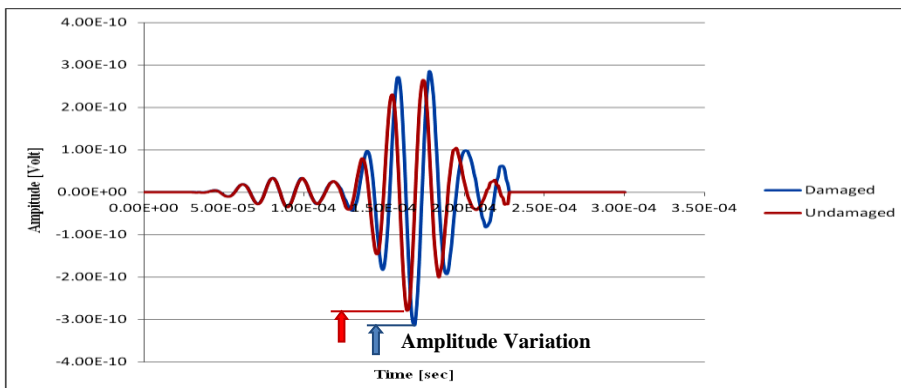


Figure 3.11: Acquired signal with pristine state (red) and after delamination (blue)

3.6 Signal analysis

3.6.1 Signal analysis technique aimed at damage patterns extraction (STFT, Wavelet, Damage Indices...)

Guided waves are created by the constructive interference of the bulk waves reflected between the surfaces of the plate; these waves have a number of characteristics that are different from those of the bulk waves. First, they are, in general, multimodal and dispersive; the particle motion (symmetric or extensional and antisymmetric or flexural) and the velocity of each mode depends upon the thickness and material properties of the plate, as well as the frequency of the excitation of the wave. Second, they can propagate a much larger distance than the bulk waves without significant decay in their amplitude. Third, and most important, they are extremely sensitive to the presence of discontinuities in their path, and carry information on certain properties of the flaws as they propagate away from the flaws. Finally, it is relatively easy to generate and record the guided waves using (PZT) actuators and sensors that require very little power, and are therefore suitable for online structural health monitoring.

From this point of view, the approach that currently is investigated is a local approach whereby changes in the characteristics of ultrasonic waves propagating across existing defects or created by emerging defects are measured and analyzed. This approach based on ultrasonic wave propagation techniques is highly effective in detecting very small local defects in a variety of structural components. Typical signals analysis techniques based on wave propagation are Damage Index Approach and STFT (Short Time Fourier Transform) Approach while Pitch Catch and Pulse Echo Technique are the typical methods for signals acquisition.

3.6.2 Damage Index (DI) Approach

The DI approach [10] is designed to overcome the complexity and variability of the signals in the presence of damage as well as the geometric complexity of the structure. It relies on the fact that the dynamical properties of a structure change with the rise up of a new damage or the growth of an existing damage. Using measurements performed on an undamaged or partially damaged structure as baseline, the DI is evaluated by comparing the changes in the frequency response of the monitored structure as a new damage occurs or an existing damage grows. Thus, unless the environment undergoes significant changes between the two sets of measurements (which can occur within a very short time frame), noise, in general, will have no effect on the results. Moreover, the proposed algorithm does not require extensive rigorous signal processing, but it computes a single damage parameter (namely, *DI*) with a high confidence level which makes its very fast and automatic. The DI vanishes if there is no change in the structure and its value increases with the severity and proximity of damage to the sensor locations. Thus if damage is initiated at a location within or near the sensor array, then its location and severity can be determined by the autonomous scheme. The method is applied to identify several types of

defects in both metallic and composite panels for different arrangements of the source and the receivers.

A DI comparing the measured dynamical response of two successive states of the structure is introduced as a determinant of structural damage. The dynamic state involved in the definition of the DI at a given sensor location (control point) is the frequency spectrum of the signal in the wave propagation test. The presence of damage modifies certain characteristics of the ultrasonic waves. The changes in the measured dynamic response of the structure are analyzed to reveal the location and degree of damage. Wave propagation tests are performed in the reference and damaged states of the structure. Elastic waves with known properties are launched by broad band transducers located on the surface of the structure. The motion induced by the source is acquired by multiple sensors located on the surface of the structural component.

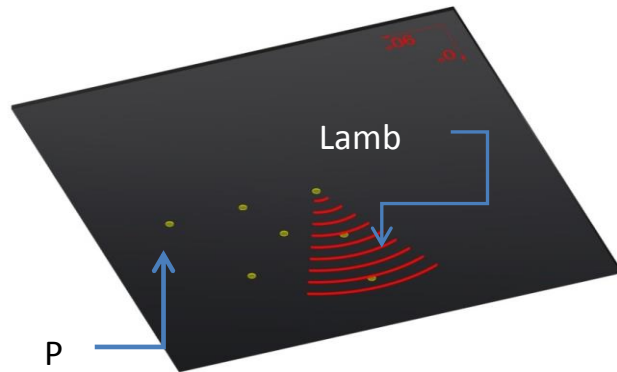


Figure 3.12 – Lamb waves propagation

The damage index, DI, is defined as follows:

$$DI = \left| 1 - \frac{\sum_{f_k=0}^{f_s/2} FD^2(f_k)}{\sum_{f_k=0}^{f_s/2} FI^2(f_k)} \right| \quad (\text{Eq. 3.2})$$

where f_k are the frequencies where the spectra are evaluated, FI and FD the magnitudes of the frequency response functions or spectra for the undamaged and damaged structures respectively, and f_s the sample rate.

The index can, in principle, be defined for a generic structural parameter including displacement, velocity, acceleration, strain, or voltage measured by embedded or attached sensors. The DI defined in Eq. (3.1) returns non-zero values only if any change in the measured dynamical response of the structure occurs, and it will return zeros if the experimental measurements are identical.

The reliability of the damage detection procedure is strongly dependent on the reliability of the measured dynamic response of the structure in the reference and damaged states. However, the measurements can be affected by random errors or environmental noise, leading to false or inaccurate results for the DI values. Thus, the tests are repeated several times under the same conditions. In order to correlate the DI values to the presence and

degree of damage with a high confidence level, either the collected data are averaged a number of times or a statistical analysis is carried out.

3.6.3 STFT Approach

The primary basis of this method is that any signal can be expressed as a sum of sine and cosine functions. *FFT (Fast Fourier Transform)* transforms the raw signal in the time domain into a frequency domain, it serves to evaluate the frequency spectrogram of the signal. FFT formulation is:

$$X(f) = \frac{1}{\sqrt{2\pi}} \int_{-\infty}^{+\infty} x(t)e^{-i\omega t} dt \quad (\text{Eq. 3.3})$$

With FFT it is possible to determinate the window width of the actuation burst: at low frequencies the frequency range of the burst is narrow and excites only the required frequency and at higher frequencies the burst excites a more and more wide range of frequencies, loosing frequency resolution (Figure 3.13).

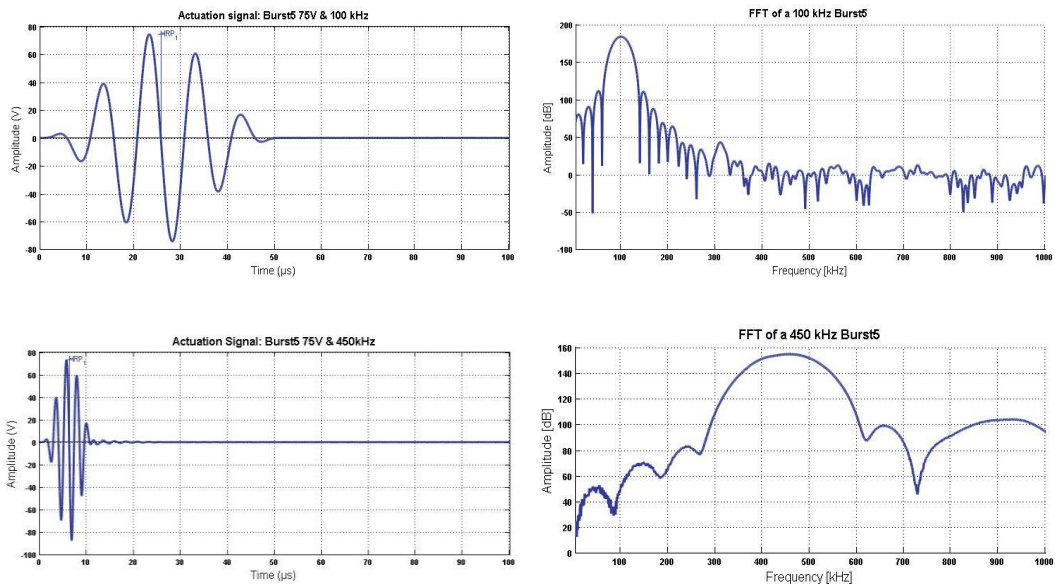


Figure 3.13 - Actuation 5-peak Burst signal (left) and respective FFT representation (right)

With FFT all the time information is lost, limiting the signal analysis. To keep the time information of the signal following the Fourier Transform method, the signal is divided in intervals, where a Hanning window is applied in order to avoid numerical problems at extremes and afterwards the FFT is applied to each one of these intervals (*STFT – Short Time Fourier Transform*). The width of the window has to be a compromise between the time and the frequency resolution: a narrower window will improve the time resolution and

will worsen the frequency one, and vice versa, a wider window will have a better frequency resolution but it will be detrimental to time resolution.

3.6.4 Pitch catch and pulse echo technique

For signals detection two different techniques may be used: pitch catch (Figure 3.14) and pulse echo (Figure 3.15). The first technique employs the attenuation of the ultrasonic beam due to the defects allowing the identification of the heading angle of the damages. In this case were used opposing probes, with the function of actuators and receivers respectively.

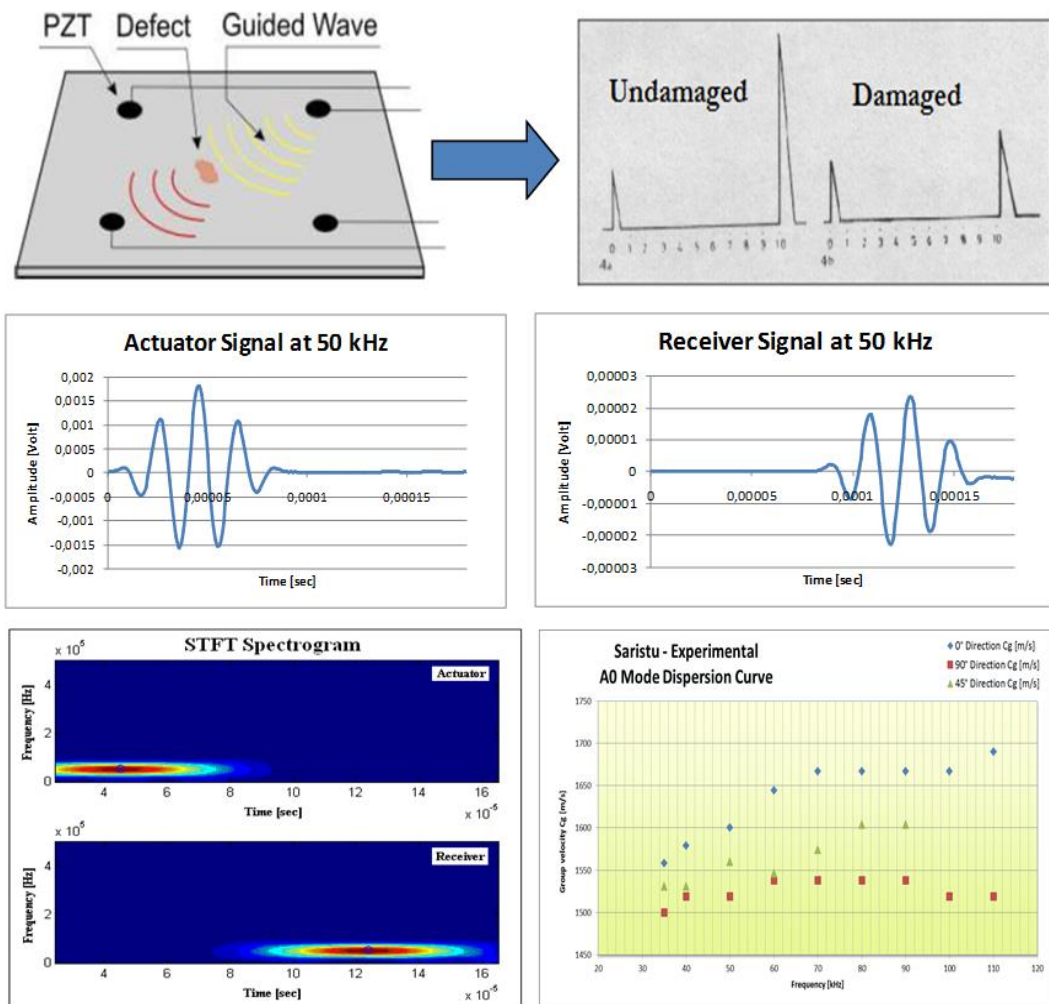


Figure 3.14 –Pitch Catch Technique

The second technique is based on the detection of the signal reflected from any discontinuity surface. By signal analysis it's possible to define the time of flight between

the signal and its echo (TOF) and so the distance of the damage from the probe. In this case, each probe is used both as transmitter and as receiver.

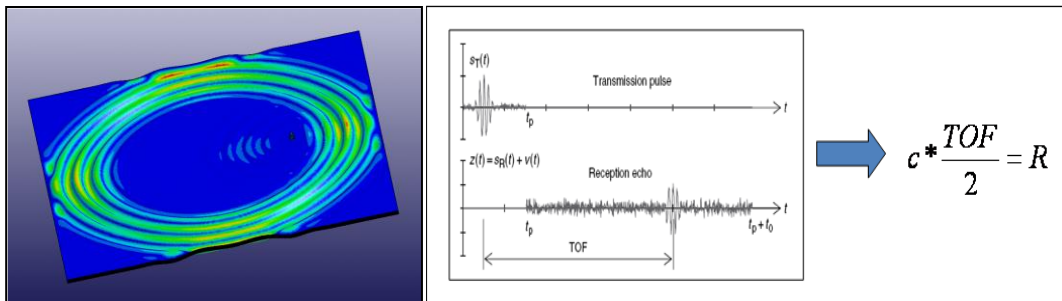


Figure 3.15 – Pulse Echo Technique

3.7 Damage scenario

The main objective of the dissertation is the definition of guided wave based algorithms for damages identification that, starting from the stress waves signals acquired by piezoelectric sensors, permit to identify the location and size some Barely Visible Damages (BVID) artificially induced through impact tests on a composite wing structural elements.

Like sensor (section 3.2) also the test articles dimension and complexity have gone through a continuous development over the research activity following a building block approach from flat small panels up to a full scale reinforced wing panel as final test article of the SARISTU project (Figure 3.16). [11 - 12]

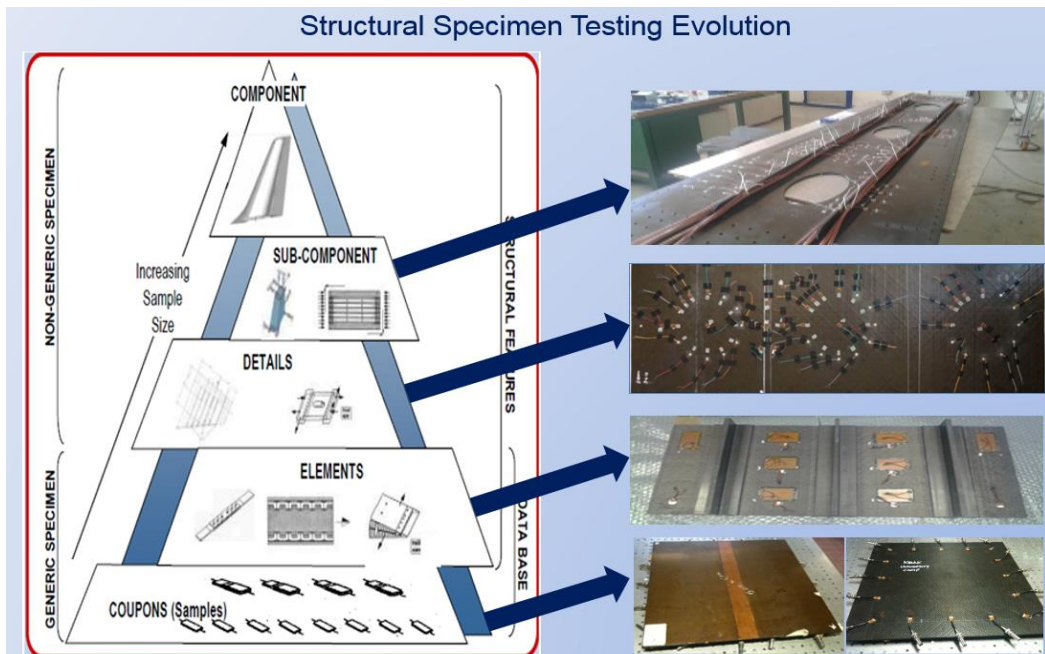


Figure 3.16: structural specimen testing evolution

Depending on the test article dimensions and structural complexity, the impact testing setup used was a modified Charpy Pendulum, having a striker with a 12.7 mm diameter, or a spring gun, pneumatically actuated, equipped with a hemispherical nose 1 inch in diameter (Figure 3.17).



Figure 3.17: impact test set up

To impact the several specimens various fixing plates have been implemented to support specimen different shapes and sensors set up applied on them (Figure 3.18).

Taking into account the thicknesses, materials and lay-ups of different test articles, a preliminary impact energy calibration activity has been carried out, for each of them, in order to find the minimum impact energy producing a consistent delamination dimension to each selected impact position.

Impact energy threshold and induced damages dimension have been assessed with the aid of thermography (Figure 3.19) and phased array C-scan analysis.

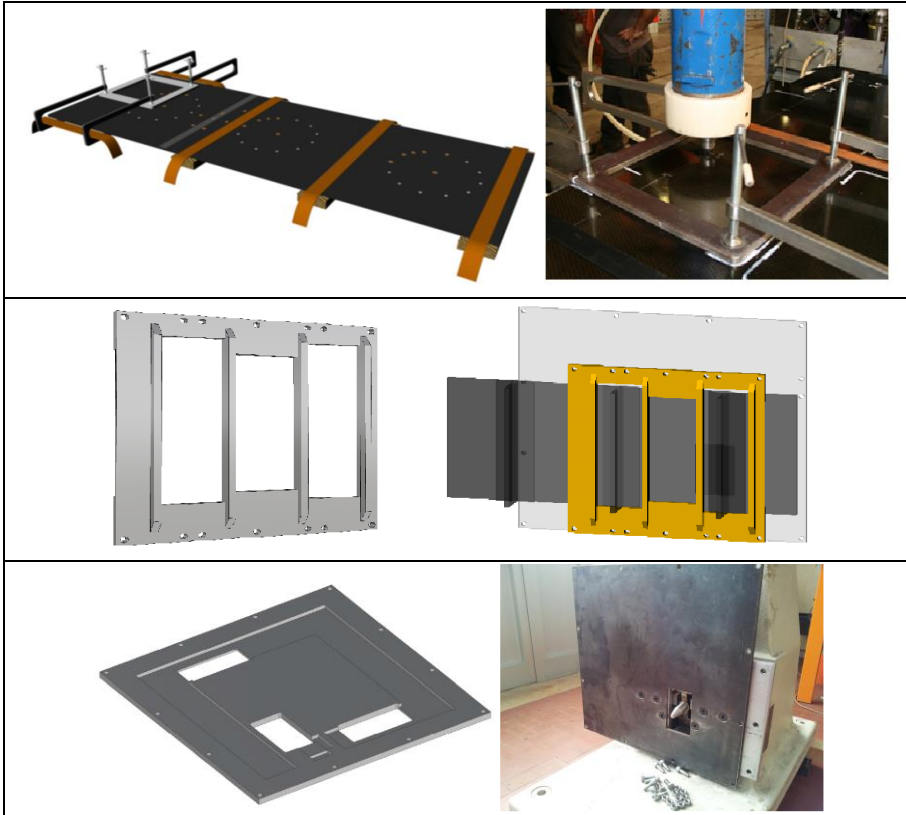


Figure 3.18: impact test fixing plates

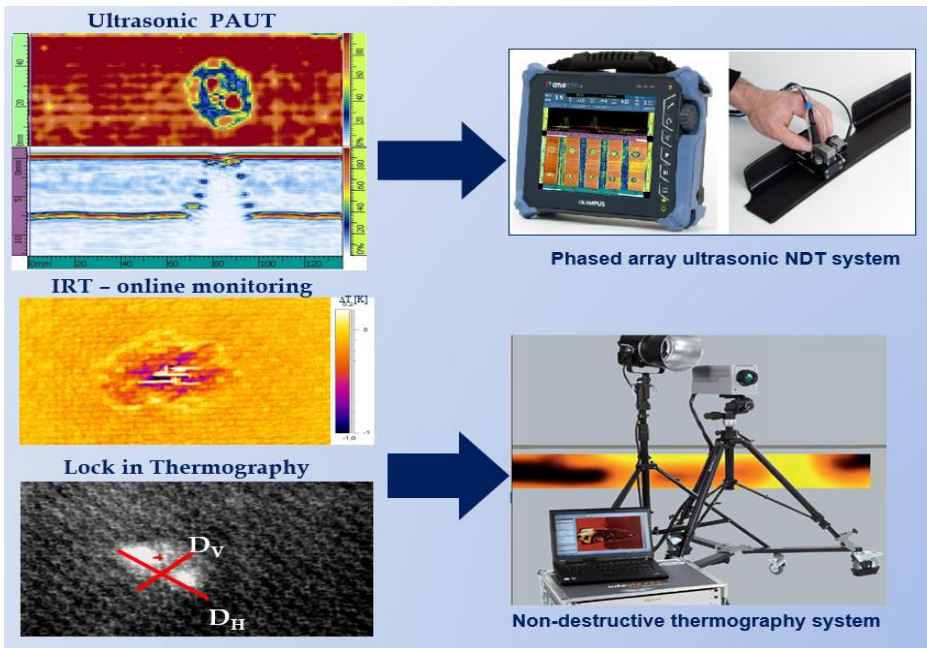


Figure 3.19: NDT control set up

3.8 Guided waves based SHM methodologies

The methodologies, developed and employed to detect delaminations and disbonds in flat composite unstiffened and stiffened panels (Figure 3.20) via ultrasonic guided waves, can be classified within the family of tomographic methods (TMs). The operating principle of TMs is based on DI approach [10], namely, on the comparison of the wave signal actuator-sensor detected on a pristine condition of the component (baseline signal), with the same signal detected after damage (current signal). Differences in the two signals are used to denote the presence of the defect in the actuator-sensor path.

All the considered test articles have been subjected to a preliminary C-Scan analysis in order to define the initial state of health and then permanently sensorized with PI255 or DuraAct PZT employing a vacuum based secondary bonding procedures (see 3.2.1. Bonding procedures section).



Figure 3.20: preliminary flat and stiffened panel analyzed

Employing an array of sensors, a network of propagation path can be built considering all the possible combinations actuator-sensor. Then it is possible to associate to each path one or more DI formulation and its associated statistic parameter to select the most perturbed path and their intersections. (Figure3.21).

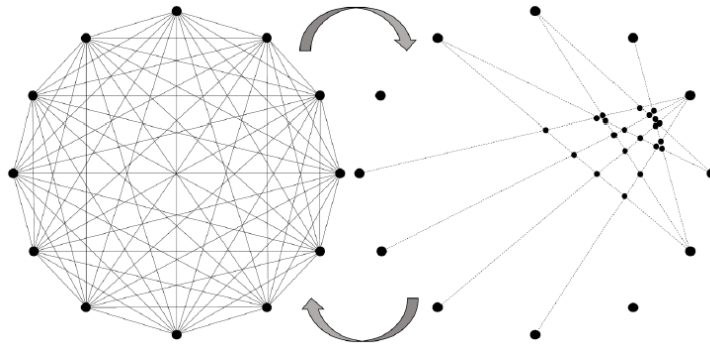


Figure 3.21: Network of the propagation paths for a circular array of piezo and selected paths obtained with DI approach [13]

Increasing the number of actuators and sensors, and so the waves paths, and combining the indicators of all paths allows to detect and locate the defect.

After impact energy calibration (Figure 3.22) and BVID damage replication, all tests articles have been subjected to a second NDI control to obtain the damage characteristics references for the SHM assessment.

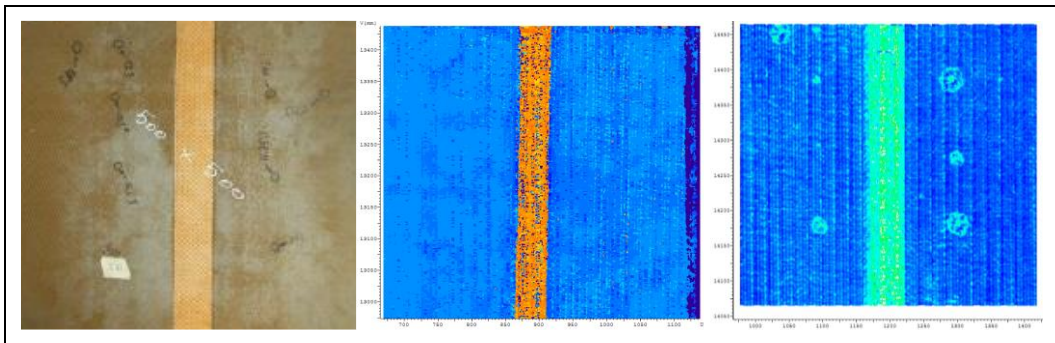


Figure 3.22: C-Scan analysis after impact energy calibration testing

3.8.1 Damage patterns definition

For the positioning of the sensors have been essentially followed two strategies. The first approach provided for the positioning of sensors in order to allow some preliminary considerations such as the definition of the Tuning curves and Dispersion curves in the main fibers directions (0 °, 45 °, 90 °) and the effect, when present, of the anti-lightning protection system on the waves propagation. The latter usually leads a local slowing of the wave propagation velocity, as shown in the Figure 3.23.

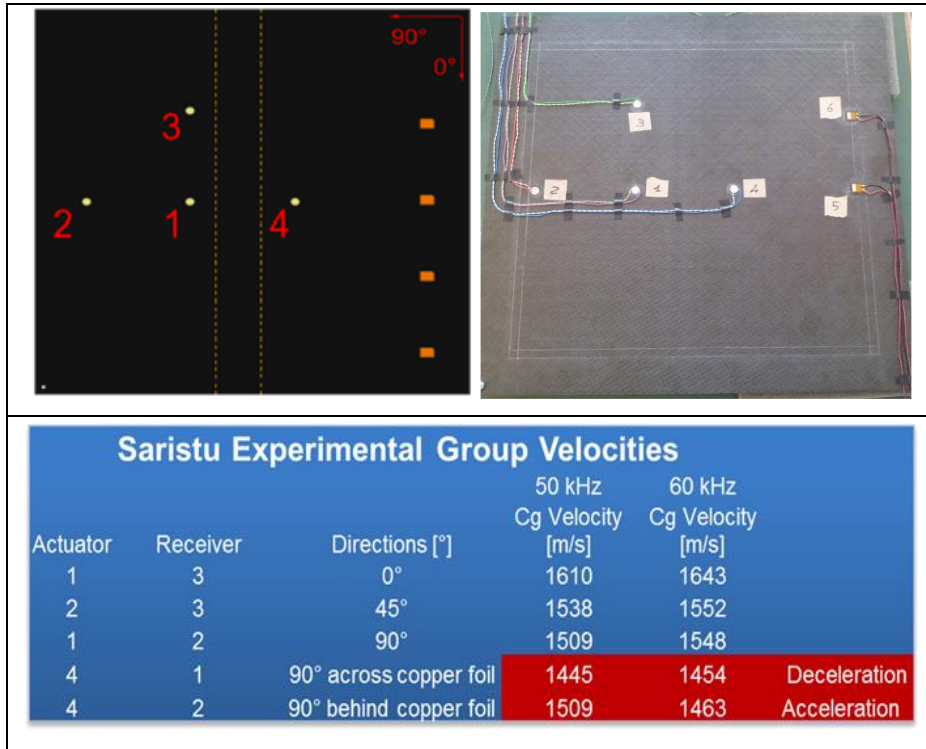


Figure 3.23: Copper foil effect on group velocity

The second approach was designed to allow the scanning of the largest possible sensors delimited area, using the fewest number of sensors. In particular, on the inner surfaces of each panel was placed a set of piezoelectric sensors, arranged along the edge for the flat panel or properly defined area and within each bay for the stiffened panels (Figure 3.24). Generally it is considered appropriate to leave at least 50 mm between the sensors and the edges of analyzed area, in order to avoid or mitigate the edge reflections effects.

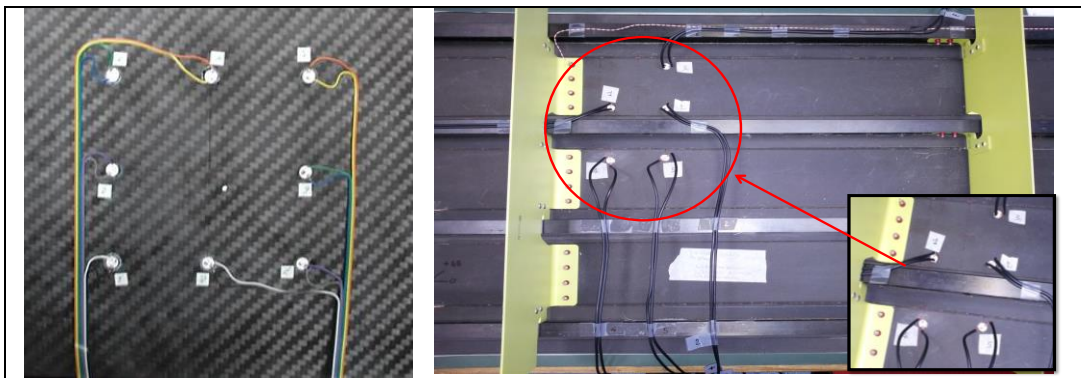




Figure 3.24: Test articles sensor configuration

3.9 Signal algorithm evolution

Structural Health Monitoring (SHM) based on ultrasonic guided waves is one of the most promising tool for improving maintenance strategies of composite structures. However, wave propagation in composite structures presents several difficulties for effective damage identification due to the anisotropic behavior of material and the complexity of the signal analysis required to extract useful and reliable information on the state of health.

To alleviate these problems, various signal transformation techniques and tools have been developed and used to detect structural damage by extracting the parametric information regarding damage from complex signals.

For each step forward on the test-articles pyramid, seen in previous section, a corresponding step has been done by the methodologies and algorithms employed for detecting and localizing the damages (Figure 3.25) [13 – 14 - 15].

The signals analysis consisted in a mathematical part as well as in a graphical post processing. Both components of the analysis went through some evolutions during the last years: the mathematical part consisted in extracting from the rough signals, related to each propagation path connecting an actuating piezo to a receiving one, some metrics (namely Damage Index) characterized by different formulations and approaches based on the evaluation of signal intensity or propagation velocities variations due to flaws; the graphical post processing consisted in selecting propagation paths filtering them on the basis of DIs values or of their statistical causality [13] and evaluating the damage envelope by plotting the most perturbed path.

The analysis evolved from a “Single Path Wave Propagation Based Analysis Codes – Single DI Approach” and “Propagation Paths Intersection Based Damage Detection” (Figure 3.25) to, last status presented within this work, a modular analysis code able to perform a “Statistical Multi-Parameter Analysis” combined with a contour plot representation of damage envelop obtained, thanks to a dedicated Graphical User Interface, by fusing images related to the evaluated parameter at propagation paths intersection [11].

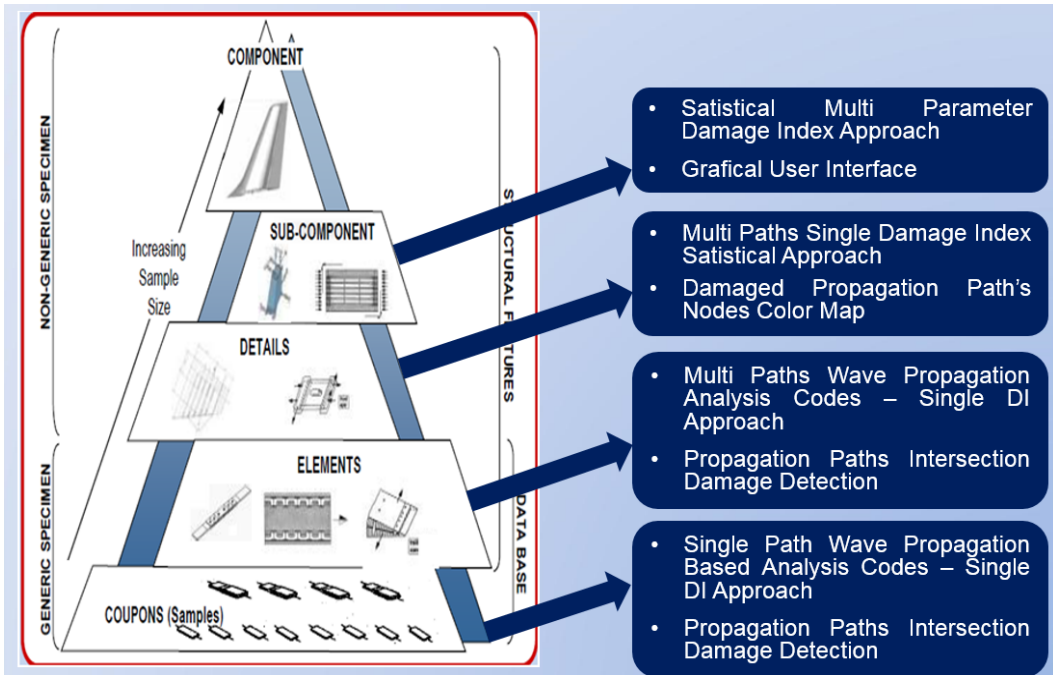


Figure 3.25: Analysis methodologies and software technology evolution

Before presenting the results of SHM system implementation on the main test article, namely, the Saristu Project Full Scale Ground Wing Demonstrator, below a brief overview of the preliminary signals analysis codes evolution and their experimental and numerical implementation for damage detection on composite wing coupon or elements will be presented.

3.9.1 Preliminary damage analysis software

At the beginning of the research activity, preliminary signal analysis software were made of simple Matlab or Lab View customized script, able to carry out the analysis of a single source-receiver propagation paths per times and to extract the main propagation characteristics of the considered wave packet. For each actuator-receiver propagation path were evaluated the differences relating to the flight time (ToF), signal level (EL), group velocity (Vg) and the damage indices (DI). Exploiting the intersection of the propagation paths characterized by higher values of such differences, relatively to the average value, was possible to delimit on flat panels a circumscribed area around the imposed damage which allowed an approximated identification of the same in terms of position and surface extension.

All the acquired signals, both before (pristine status) and after the impact (current status), have been treated with a STFT based script that, for each of them, calculates the ToF and the Group velocity (Figure 3.26).

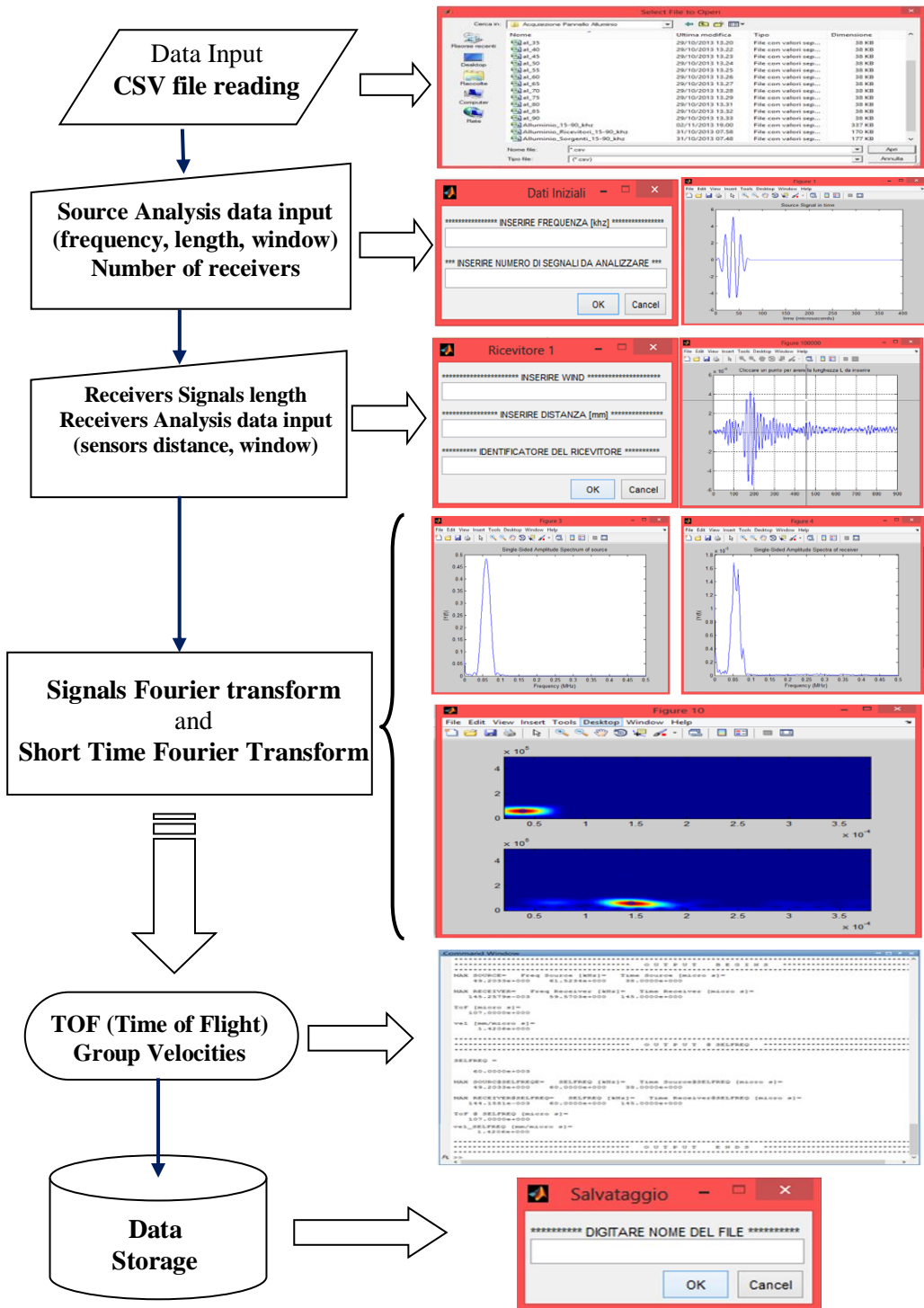


Figure 3.26: Matlab signal analysis code logical flow chart

Code steps can be easily summarized as:

- signals matrix reading by csv file. This matrix was provided directly by the acquisition system (oscilloscope or National Instrument NI 6366 USB board) and consists of n columns of which the first is the time vector, the second the source vector and all the other the receivers vectors;
- Short Time Fourier Transform and the Fourier Transform calculation of the source signal and receivers signals;
- determination of source and receivers maximum point;
- Time of Flight (TOF) and group velocities determination.

The parameters that affect the code operations and that are required in the input, before analysis performing, are:

- **Source frequency**;
- **signal length** (time history length);
- **size of STFT window**;
- **actuator/receiver distance**.

After signals processing the script generates a set of diagrams representative of source/receivers time history, Fourier Transform and STFT spectrogram (Figure 3.23).

In the Matlab Command window a table with ToF and Group Velocities, calculated for each source-receiver sensors couple, is displayed and it is possible to save the elaboration results in a xls file.

Then, with the aid of further matlab script, signal levels and damage indices in the pristine and damaged status are compared with each other (Figure 3.27).

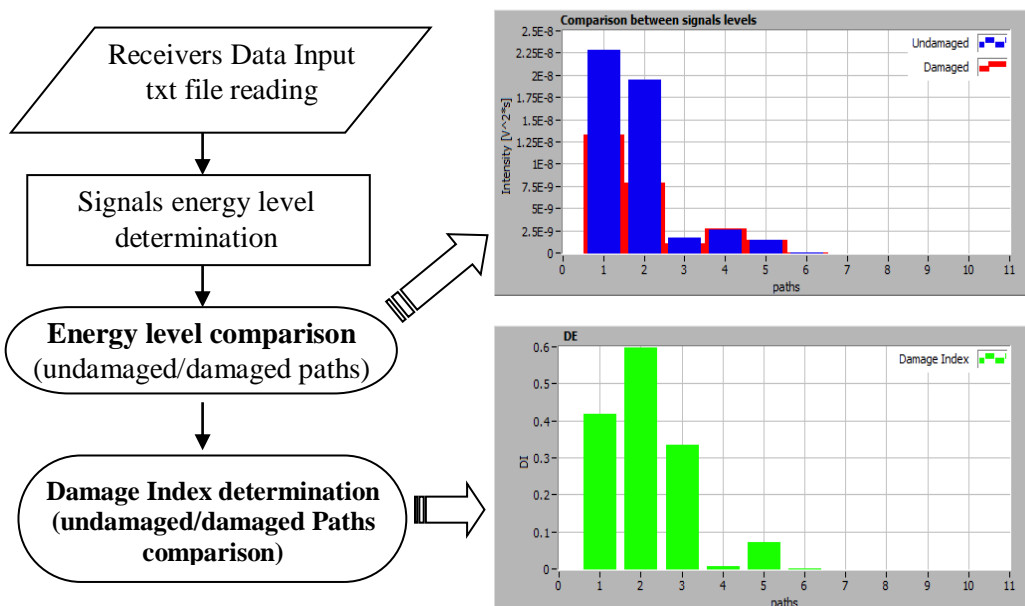


Figure 3.27: signal levels and damage indices comparison

3.9.2 Matlab damage analysis code testing

Below are reported the early experimental results obtained, with preliminary SHM Matlab code seen above, for a 500x500 mm panel including Non-Crimp Fabrics (NCF), Multiaxial Reinforcements (MR) and 5 Harness Satin Weave (HSW) with a thickness of 5 mm. The panel was also equipped, on the outer surface, with a copper anti-lightning protection system. On the inner surface of the panel a set of 16 piezo DuraAct were placed along the perimeter of a square 400x400 mm with a step of 100 mm from each other and 50 mm from panel edges. The piezos have been used to acquire the signals generated by further two piezos bonded in the central area of the panel. The choice of using two central piezo as generators is derived by the need to avoid, at least initially, paths that were mostly affected by the copper strip placed on the panel, as shown in the Figure 3.28.

In order to implement damage localization, source-receiver paths with greatest variations of damage indices, signals levels, group velocity (time shift) and maximum amplitude have been considered. Plotting the obtained variations as a paths function it is possible to have a fairly clear idea of mostly disrupted area by damage presence (Figure 3.29 and 3.30).

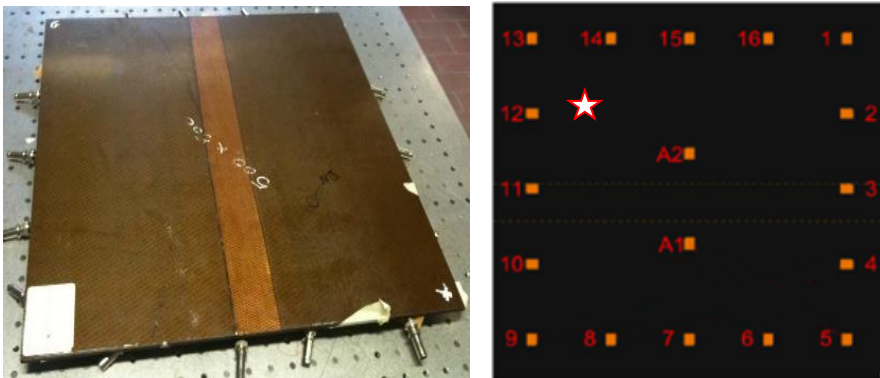


Figure 3.28: (left) outer view of composite flat panel, (right) piezo sensor s configuration

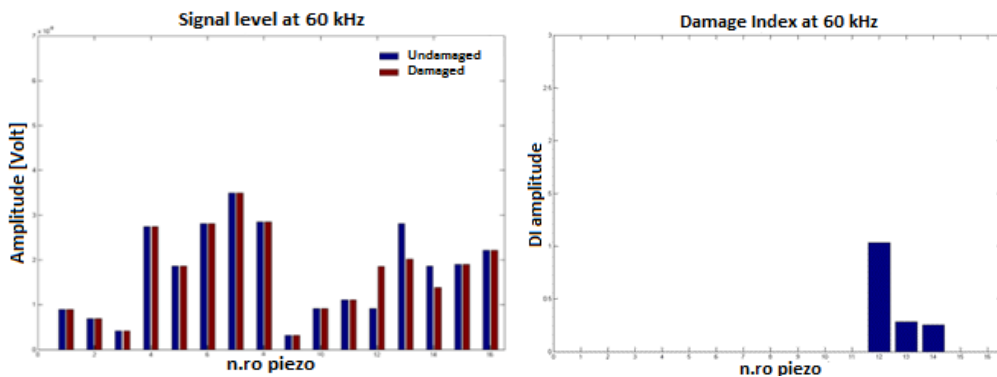


Figure 3.29: (left) Undamaged/damaged signals levels comparison using central piezo, (right) Damage Indices using central piezo

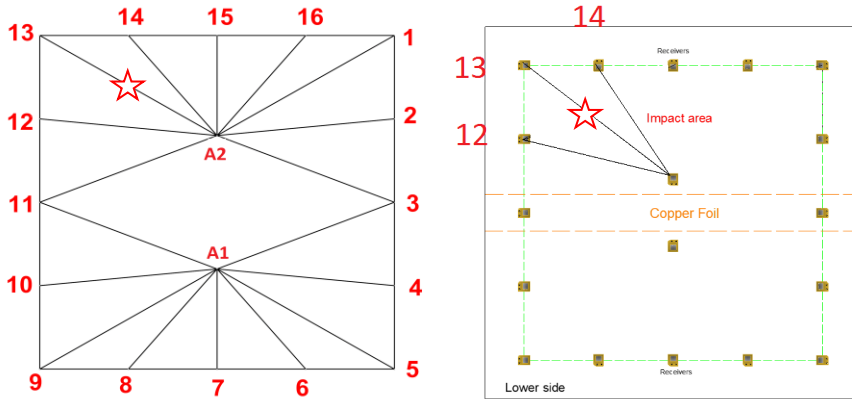


Figure 3.30: (left) analyzed path, (right) mostly perturbed code selected paths

After damage area identification, to more accurately determinate the damage position, one more analysis has been carried out using the piezo 12th on the side as actuator (Figure 3.31 left). This has allowed to a better delineation of the damaged area.

Obviously, the use of only two actuators, located in the central area, was found to be not adequate for an accurate analysis of damage position. In fact, using this strategy (Figure 3.30 left) only a few paths could be generated, at most 32.

To create a denser paths network, the whole array of 16 piezo set around the edges should be used as actuators. So, additional 120 paths would be achieved (Figure 3.31 right), that probably would be sufficient for the damage detection in the whole area of the panel within sensors square.

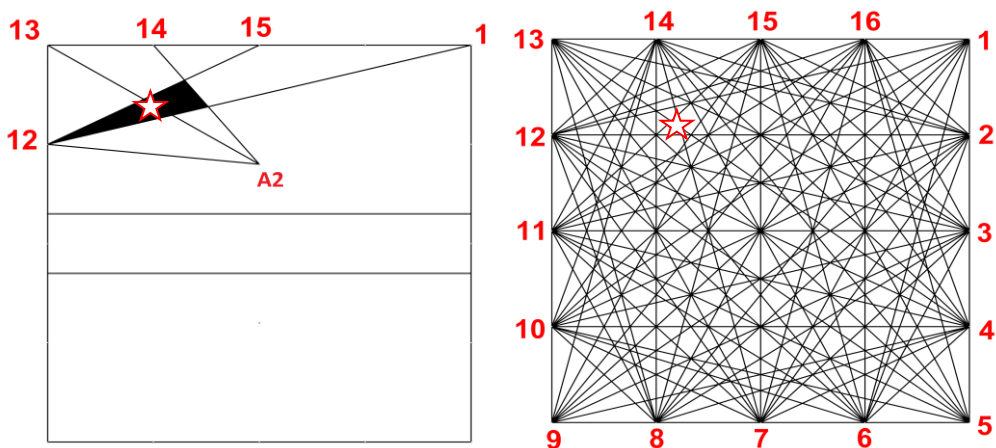


Figure 3.31: (left) Paths required to the detection of delamination, (right) further propagation paths

3.9.3 LabVIEW damage analysis code design and testing

Below will be presented the identification and localization of a structural damage by the use of a LabVIEW® code able to show the real time response of a composite panel excited through piezoelectric transducers. The analyzed specimen was a 550x550 mm flat panels, 3 mm thick, composed of prepreg woven fabric, 2/2 twill layers, with the following stacking sequence $[(0,90), (0,90), (+/-45)]_2s$.

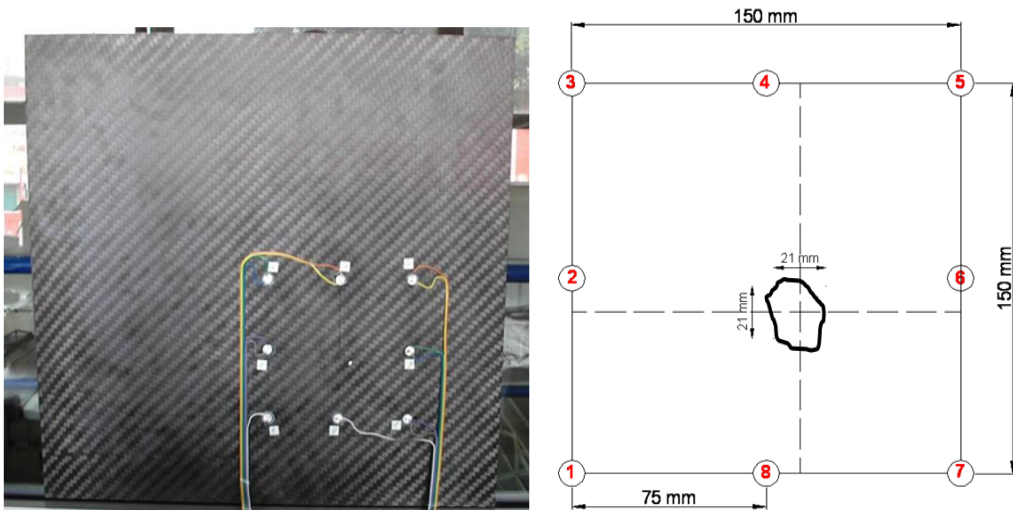
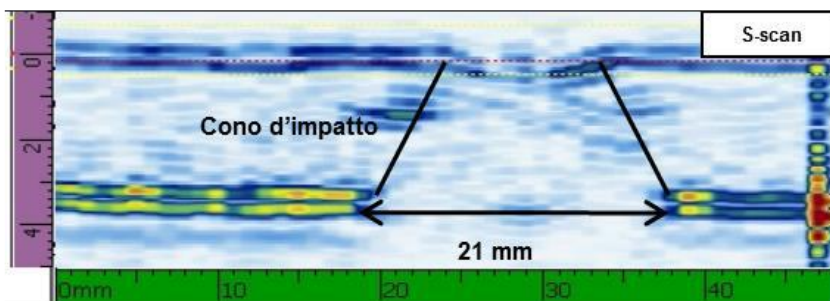


Figure 3.32: (left) sensors configuration, (right) damage location

For the test purpose, 8 PIC255 sensors type have been secondary bonded on the inner surface of the test article along a square perimeter with 150mm length side. The sensors have been arranged with a minimum distance of 75mm from each other. On the specimen outer surface an impact, that has produced a delamination of 21x21mm, has been experimentally imposed. Damage dimensions have been assessed with the aid of Ultrasonic C-Scan NDT control (Figure 3.33).



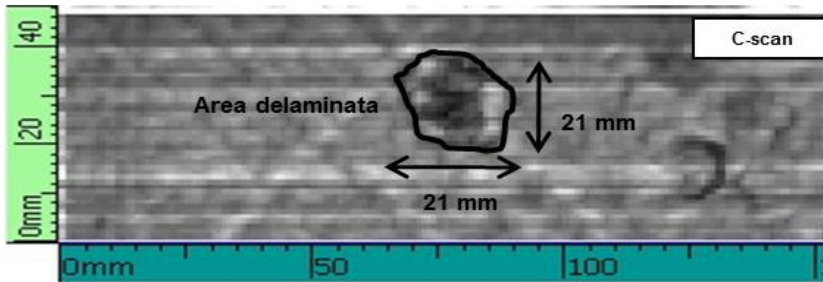


Figure 3.33: (upper) S_scan analysis, (bottom) C_scan analysis

Looking at the code user interface, is showed in Figure 3.34, it is possible to see, on the left side of the front panel, the key parameters for the correct signals acquisition:

- **Average:** represents the number of arithmetic averages performed on the acquired signals;
- **Channels:** allows the user to choose the channels from which acquire the signals;
- **Samples per channel:** Allows the user to set the number of samples acquired;
- **Sample mode:** specifies whether the channels acquire in a continuous or discrete mode;
- **Rate:** represents the sampling frequency of the acquired signals.

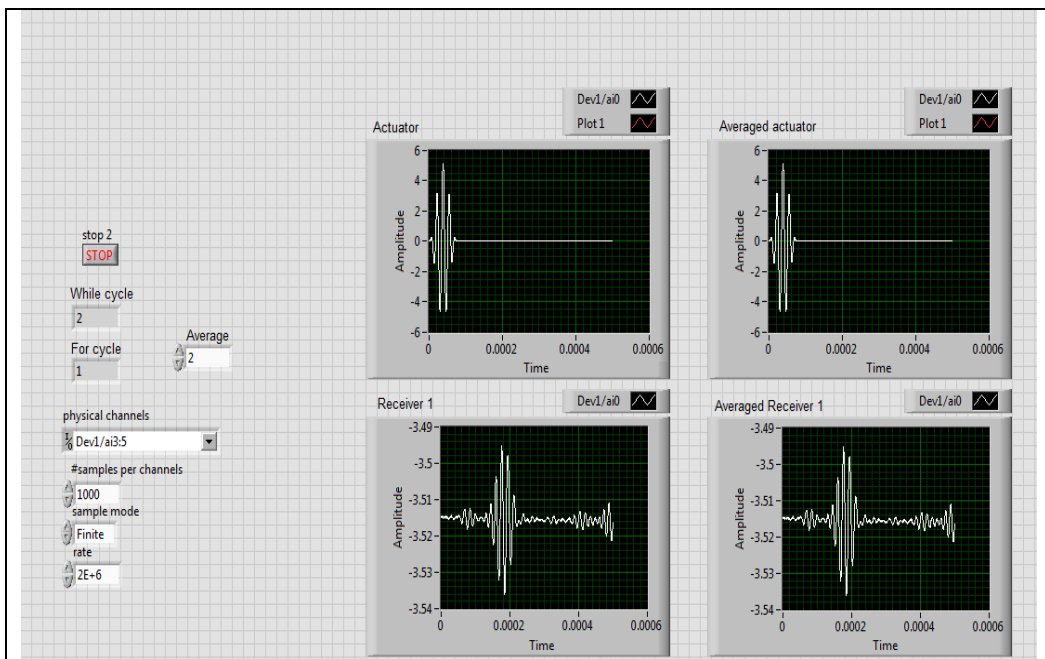


Figure 3.34: Lab VIEW Analysis Code Front Panel

The signal processing has been focused on the TOF (time of flight) determination and, in particular, on the extraction and the identification of major wave packets constituent the

signals. Like Matlab code, seen in the previous section, the data analysis has been aimed to preserve the temporal and frequency signals content through the Short Time Fourier Transform (STFT) methodology implementation.

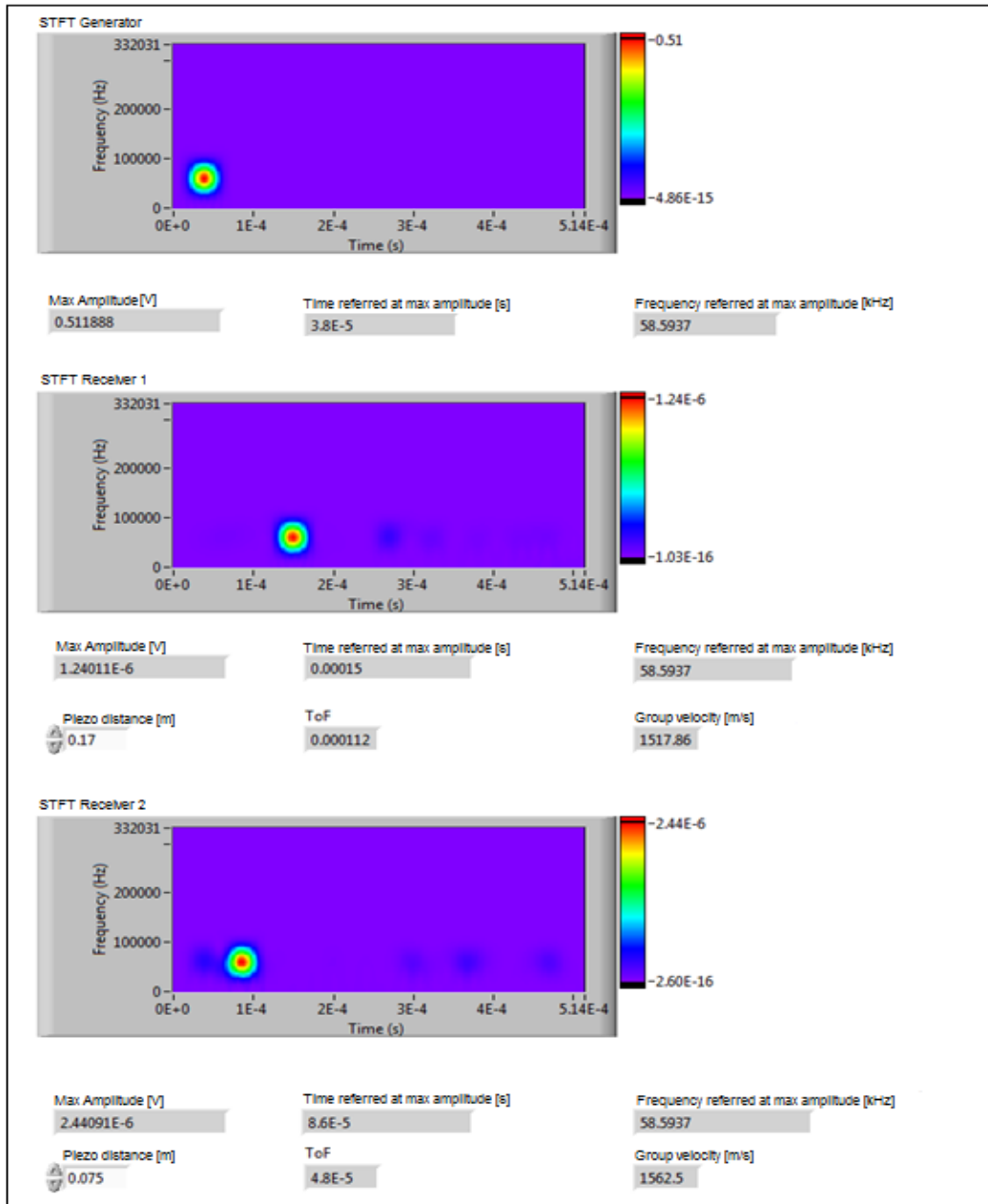


Figure 3.35: Frequency and time detection.

In order to, in real time, evaluate the STFT of the acquired signals, a dedicated LabVIEW SubVI (sub Virtual Instrument) (Figure 3.36) for time-frequency spectrogram elaboration has been developed. The SubVI allows to extract the value of the frequency and the time at maximum amplitude detected on the spectrogram (Figure 3.35). The input parameters that have to provide to SubVI are the distance between the piezo (actuator-receiver path length) and the central frequency of the source signal. In the output, the SubVI provides the maximum amplitude of the signals, the time and the frequency related to the maximum amplitude, the TOF and the group velocity related to the selected path.

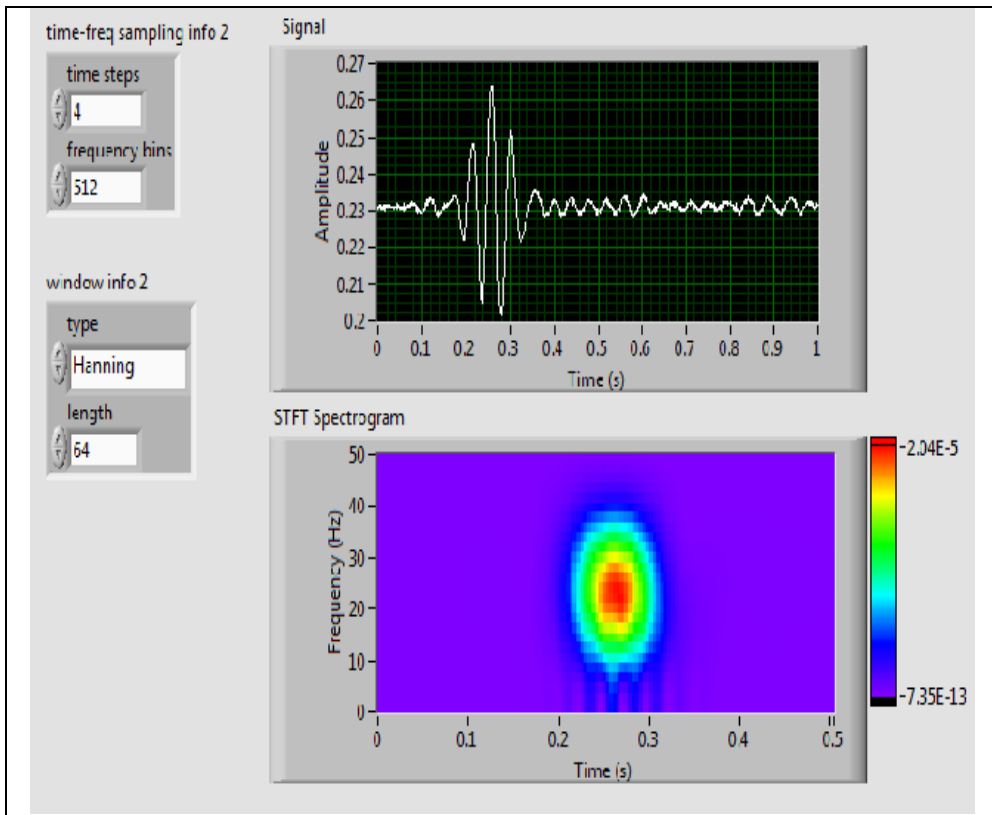


Figure 3.36: Spectrogram of a received signal

After signal data saving with a quickly and easy SubVI specifically designed, the next step has been the creation of a code able to import the test article geometry and the sensors configuration on a XY Graph. In order to import the panel geometry and sensors configuration three text files (txt) have been created: the first text file contain the coordinates of the piezoelectric used as an actuator, the second the coordinates of the edges of the panel and the third the coordinates of the remaining piezoelectric used as receiver (Figure 3.37).

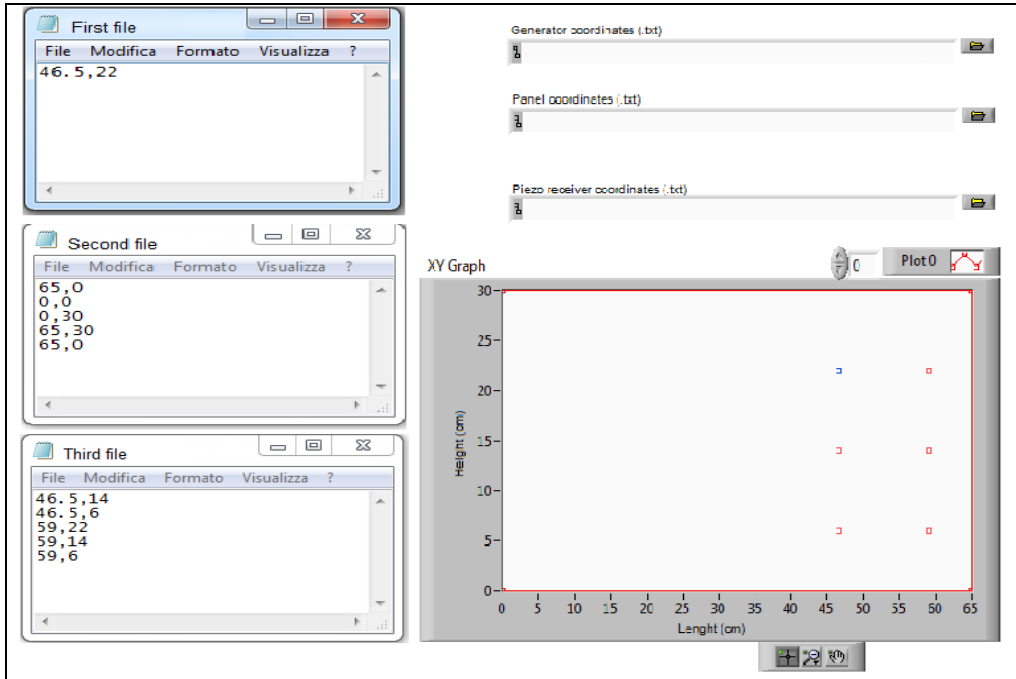
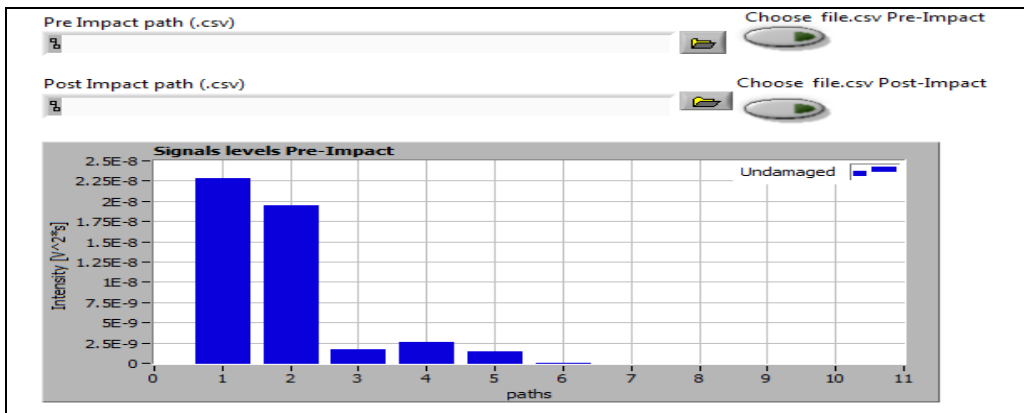


Figure 3.37: (left) input coordinate files, (right) test article and sensors geometry

In order to implement damage identification a code that allow "Damage Indices (DI)" assessment has been developed. Using the initial measurements performed on an undamaged structure as baseline, damage indices will be evaluated from comparison of the signals levels of the monitored structure with an unknown damage.

Provided to the DI SubVI a csv input file related to pristine and post damage acquired signals, Front Panel displays four graphs (Figure 3.38): signal levels relative to pre impact baseline (blue histograms), signal levels related to the post-impact signals (red histograms), comparison between to pristine and post damage status signal levels and, finally, histogram of the "Damage Indices "in green.



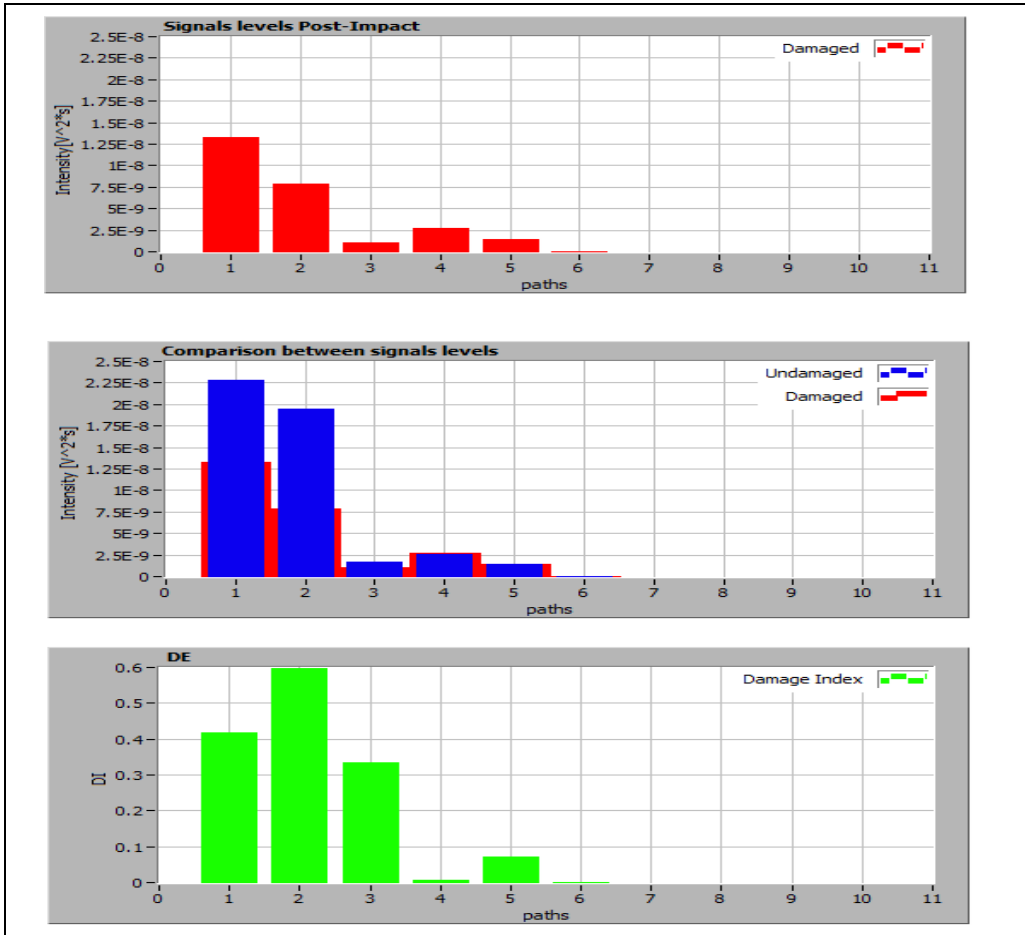


Figure 3.38: Signals levels and damage indices

To easily identify the paths mostly affected by damage presence a dedicated SubVI has been implemented. The code identifies the "path related damage indices" that exceeds a certain DI threshold (usually DI mean value) and extracts the related piezo sensors coordinates in order to rebuild the paths fields concerned by the damage (Figure 3.39)

Matrice delle coordinate

46.500	46.500	59.000	59.000	46.500	46.500	46.500	46.500
22.000	6.000	22.000	6.000	14.000	14.000	14.000	14.000
46.500	59.000	59.000	46.500	46.500	46.500	46.500	46.500
14.000	22.000	14.000	6.000	6.000	6.000	6.000	6.000
46.500	59.000	59.000	46.500	46.500	46.500	46.500	46.500
6.000	22.000	14.000	14.000	14.000	14.000	14.000	14.000
59.000	46.500	46.500	46.500	46.500	46.500	46.500	46.500
22.000	22.000	22.000	22.000	22.000	22.000	22.000	22.000
59.000	46.500	59.000	46.500	46.500	46.500	46.500	46.500
14.000	6.000	6.000	14.000	14.000	14.000	14.000	14.000
59.000	46.500	59.000	59.000	46.500	46.500	46.500	46.500
6.000	6.000	22.000	14.000	14.000	14.000	14.000	14.000

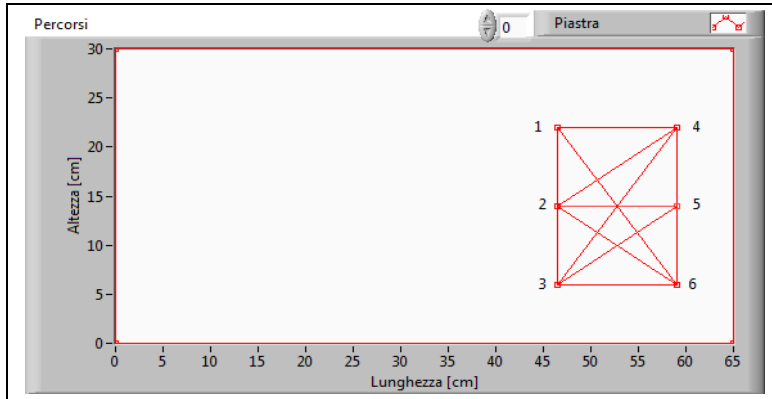


Figure 3.39: Damaged path fields reconstruction

For each actuator-receiver propagation path are evaluated differences, before and after the damage, relating to group velocities (Figure 3.40), signals levels and damage indices (Figure 3.41). Exploiting the intersection of the propagation paths characterized by higher values of such differences, relatively to the average value, it is possible to delimit, on flat panel surface, a circumscribed area around the imposed damage which allows a good identification of the same in terms of position and surface extension.

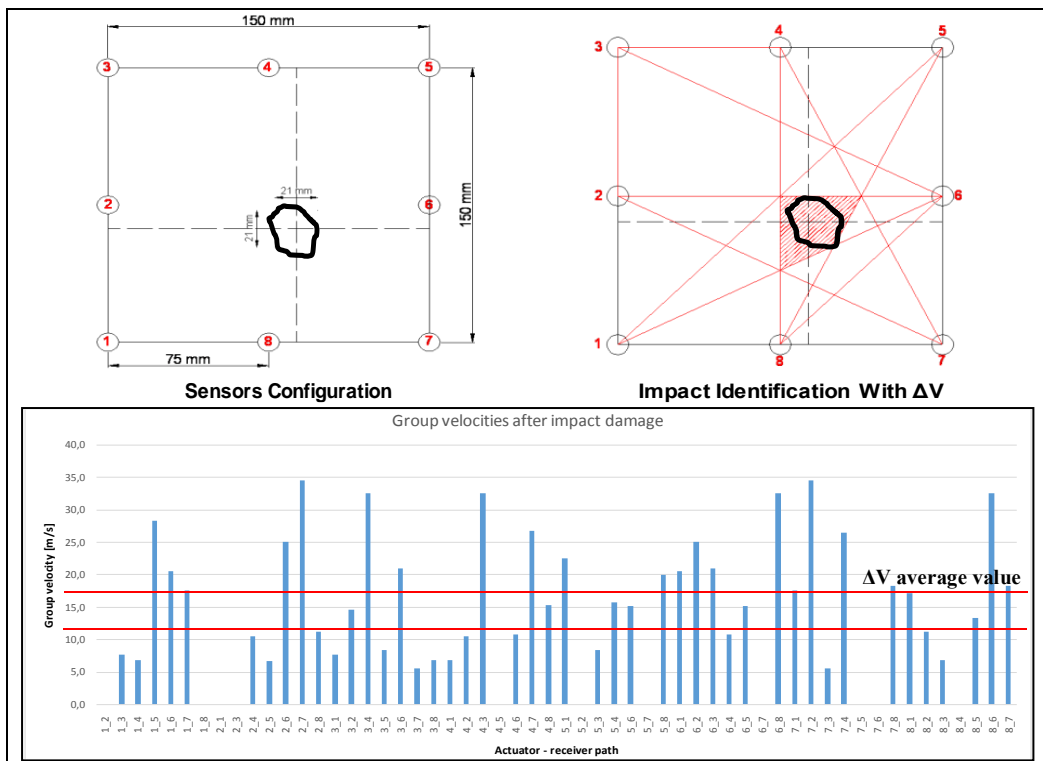


Figure 3.40: damage identification on flat panel: sensors configuration and group velocities comparison.

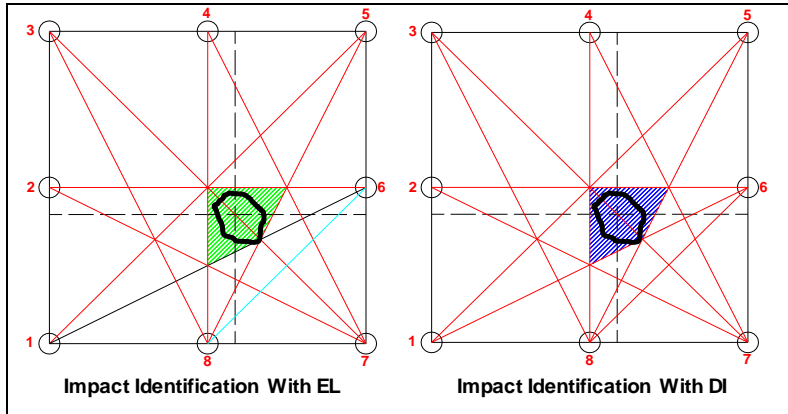


Figure 3.41: damage identification on flat panel: (left) signal level comparison, (right) damage indices.

The same procedure has been followed for debonding and middle bay damages in the case of a stiffened panel. Unfortunately, in this case the fewest number of sensors used has allowed only the identification of damages position while no assessment is possible for their surface extension (Figure 3.42 and 3.43 right). Like in the previous test article, also in the stiffened panel, the damage assessment after impact has been made with the aid of C_scan NDT control (Figure 3.42 and 3.43 left).

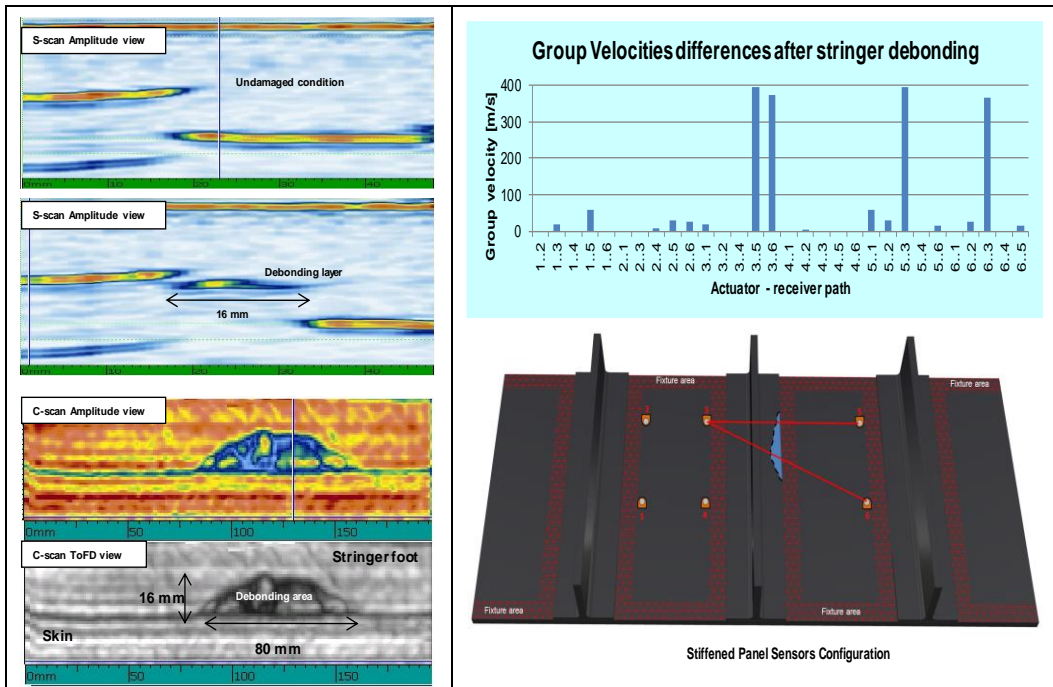


Figure 3.42: Under stringer debonding identification on stiffened panel: (left) post impact C_scan damage assessment, (right) group velocities comparison.

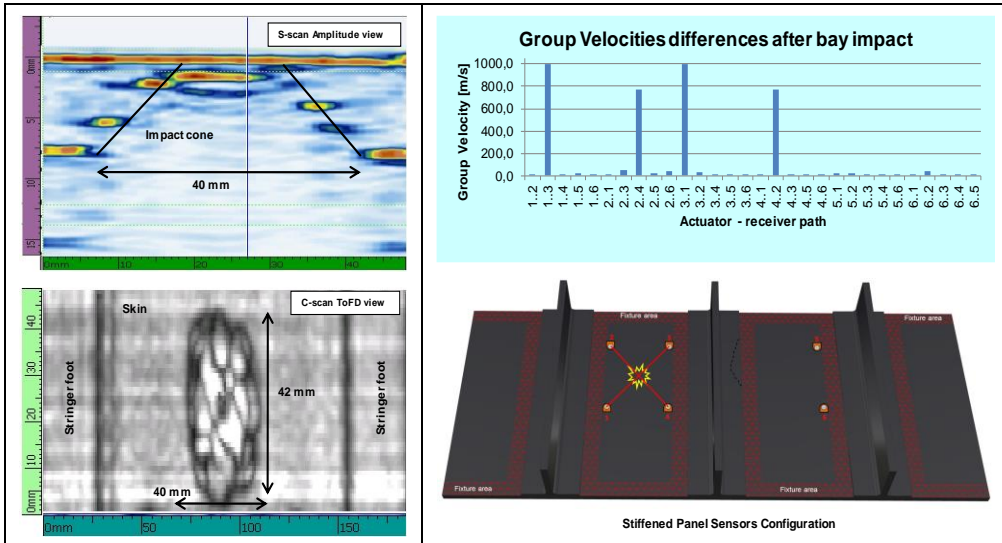


Figure 3.43: Middle bay impact identification on stiffened panel: (left) post impact C_scan damage assessment, (right) group velocities comparison.

3.10 Numerical modeling approaches for SHM system design

The material inhomogeneity, anisotropy and the multi-layered construction of composite materials lead to significant dependence of wave modes on laminate layup configurations, direction of propagation, frequency, and interface conditions.

The finite element method (FEM) is a versatile tool to analyze this class of problems. Comprehensive numerical (finite element) approach [16 - 17], including experimental results assessment, have been used to determine the interaction of ultrasonic guided waves with a crack-like defect in a composite plate and a disbond at skin-stringer interface in a stiffened panel [18].

The test article under consideration is a stiffened composite panels of a wing-box of a typical regional turboprop aircraft. The damages considered have been taken by the specifications given at certification level: a delamination and skin-stringer disbonding originated by a low velocity impact simulating a tool drop. Then the energies involved, the damage type and dimension are those that typically occur in an actual scenario of aircraft operations and are of great interest from an inspection point as they produce BIVID or hidden damage.

Numerical 2D and 3D simulations have been carried out, by the LS-DYNA explicit Finite Element (FE) code, with the aim to evaluate the models capability to determinate group velocities at different frequencies and directions, to identify Lamb ways and frequencies most suitable for damage detection, understand the stiffener effect on wave propagation.

In 3D model the piezoelectric actuator has been modeled employing 8 knots, arranged with constant angular pitch of 45° along a circle with a diameter of 10 mm (Figure 3.43 left). In

each node has been applied a pair of in plane orthogonal forces in order to reproduce the characteristic deformation of a circular piezoelectric actuator excited by an electrical impulse. In the 2D model the piezoelectric actuator has been modeled like a normal load located in a single node on the top side of the model (Figure 3.44 right).

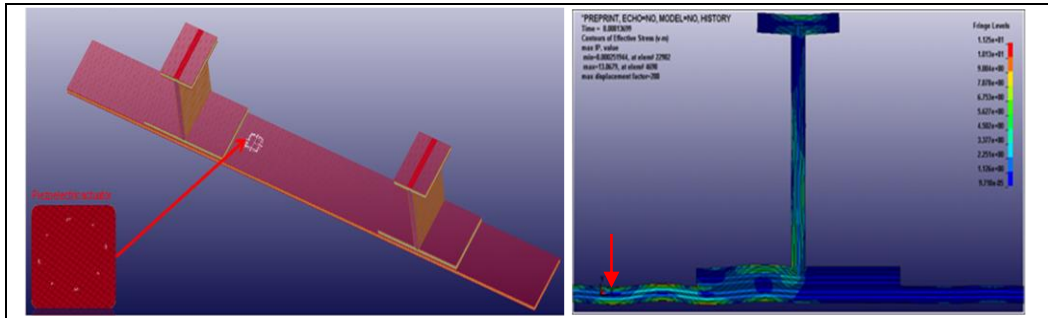


Figure 3.44: 3D (left) and 2D (right) sensor modeling

In order to develop a good understanding of the properties of the guided waves as they interact with a delamination, first a simple model of a composite flat plate with a crack-like discontinuity parallel to its faces has been considered (Figure 3.45).

3.10.1 Composite flat panel model

The test article under consideration was a composite laminate flat panel, about 550 by 550, mm 2.6 mm thick, obtained by ten woven plies overlapping according to the stacking sequence [(0.90)], [(0, 90), (± 45)] 2s, [(0.90)].

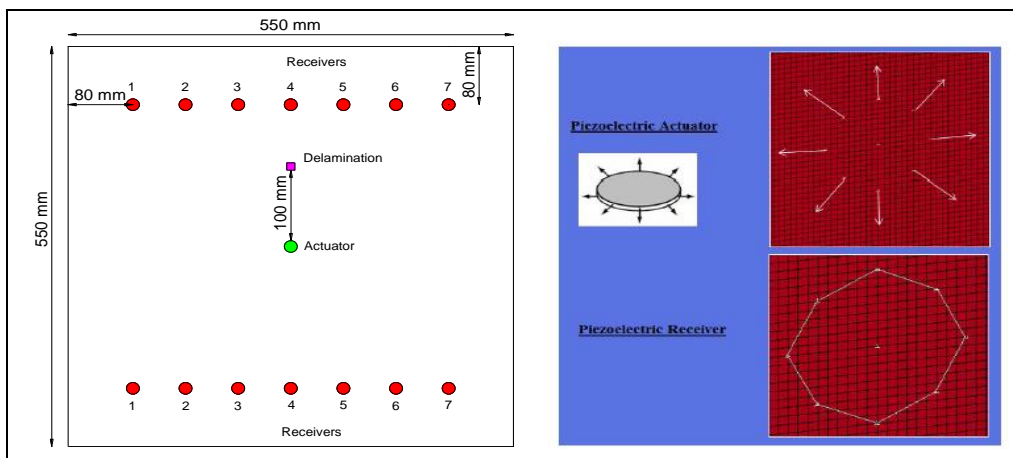


Figure 3.45: Flat panel and sensors (actuator/receiver) models

On the upper surface of the panel were placed 15 piezoelectric sensors, 14 of which, as receivers, positioned along the upper and lower edges and 1, with the function of actuator,

at the center of the panel. On the midplane of the panel, at a distance of 10 cm from the geometrical center and at a heading angle of 90°, a 20 by 20 mm square delamination has been reproduced (Figure 3.45 left).

Purpose of the tests is to evaluate the model's capability to represent the elastic waves propagation, to fix group velocity at different frequencies and directions, to identify the most appropriate Lamb mode and frequency for damage detection. The range frequency analyzed is between 50-250 kHz and a Hanning windowed five-cycle sinusoidal tone burst has been used. Analyzing the contour plots of deformed models, provided by the LS-Dyna solver, it is possible to draw some interesting considerations (Figure 3.46).

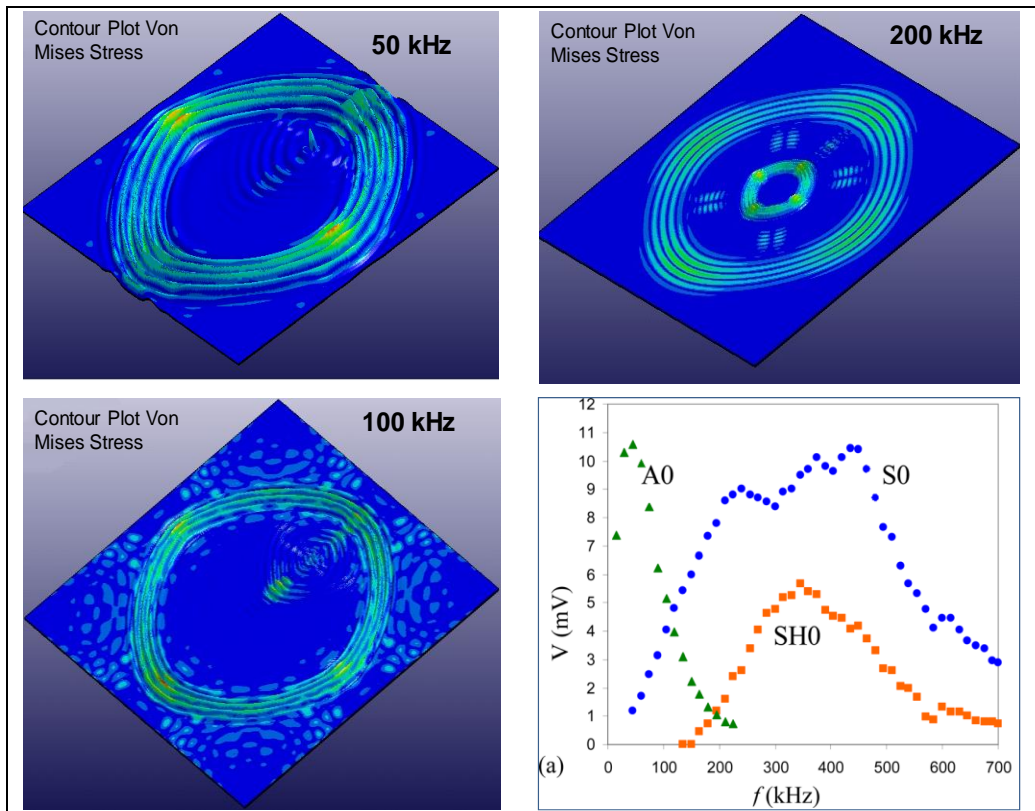


Figure 3.46: FE simulation - contour plots of deformed models

First, for all the different frequencies analyzed, it is possible to detect a wave front distortion which is not circular but slightly stretched along the main directions of the panel, i.e. 0° and 90°. This distortion was probably due to material orthotropy rather than to numerical effects.

The highest concentration of [(0/90)] plies on the external surfaces of the plate made dominant elastic moduli at 0° and 90° with higher propagation speeds in the same directions. Moreover, by increasing excitation frequencies, the model loses its capability to

detect the presence of damage, so the antisymmetric mode and low frequency values, 50 – 60 kHz range, can be considered as the most suitable for damages detection. Again, piezoelectric sensors located downstream of the most damage perturbed area shown signal levels greater than of their homologues located in the undamaged area. This is justified by the fact that, in the damaged area, the out of plane displacements enrolled a time shift, due to a speed wave reduction, and also an increase of amplitude that is especially evident for antisymmetric waves (Figure 3.47). This effect could be explained by assuming that the reduced thickness seen by the waves leads to an energy dissipation or a shift of the thickness frequency towards values most exciting for A0 modes [5].

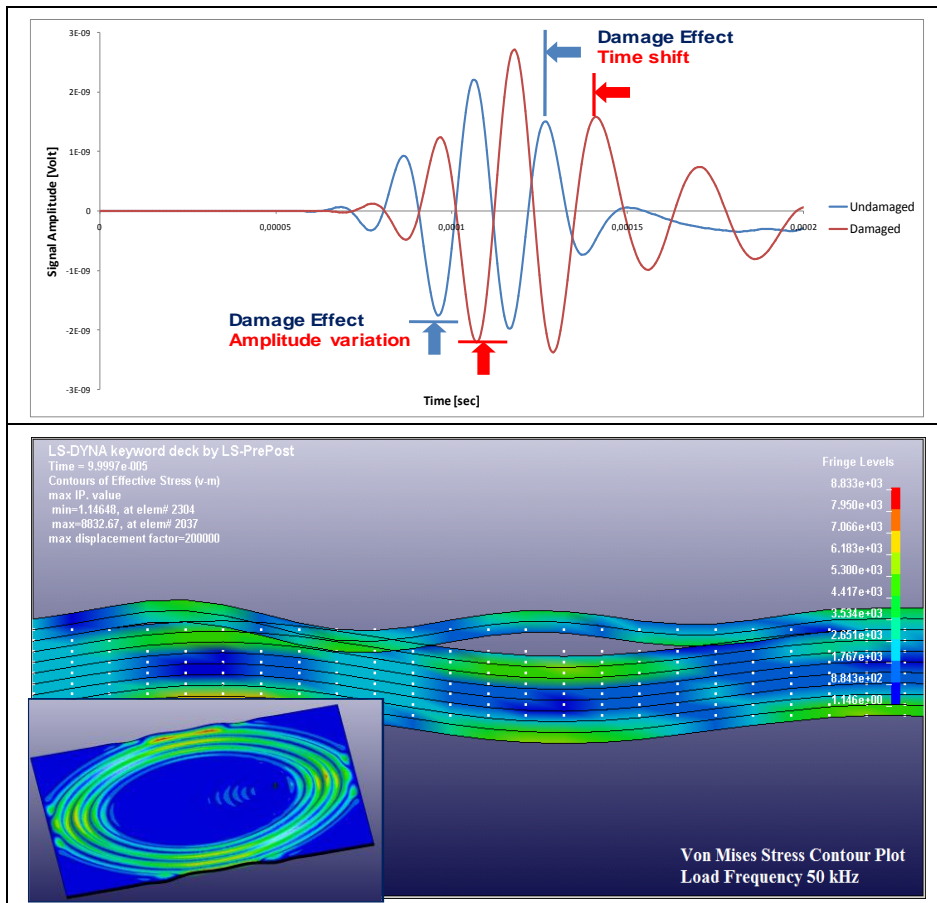


Figure 3.47: FE simulation of damage effect on Z_displacements

3.10.2 Composite stiffened panel model

The second test article analyzed was a stiffened composite panel of a wing-box of a typical regional turboprop aircraft. The panel was 3.8 mm thick with I shaped stringers that were 1.9 mm thick and 45.8 mm high with a pitch of 120.0 mm.

A finite element simulation of wave propagation in the intact and disbanded configuration has been carried out to analyze the effect of the damage on the waves in the stringer-panel bond region. In all simulations and experiments a five-cycle sinusoidal excitation in a Hann window with a central frequency of 60 kHz is used [5].

Analyzing the contour plots of deformed models, it is possible to see that the wave-path is strongly affected by the presence of the stringers. When the stringer is perfectly bonded to the panel (Figure 3.48), the waves travelling from the bay adjacent to a stringer (zone 1) enter the stringer travelling through the web up to the flange (zone 2), and only a small portion of the wave energy crosses the stringer travelling in the panel (zone 3). This is due to the mismatch in the acoustic impedance between zones 2 and 3, as explained in [19].

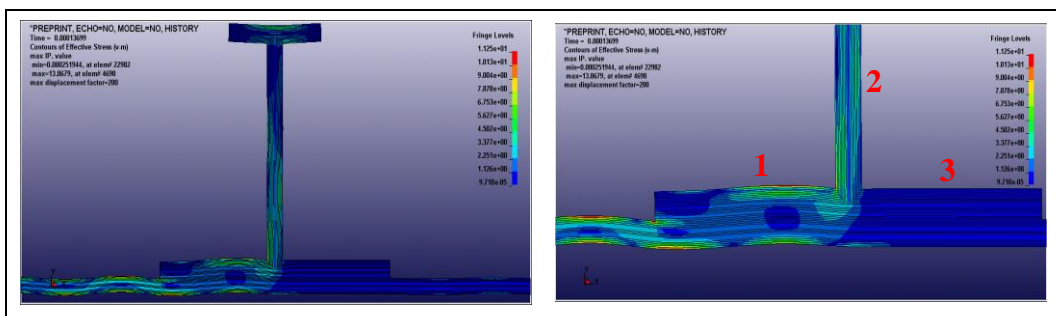


Figure 3.48: FE simulation of the waves path in the damage free configuration of the stiffened panel (left) and a close-up (right)

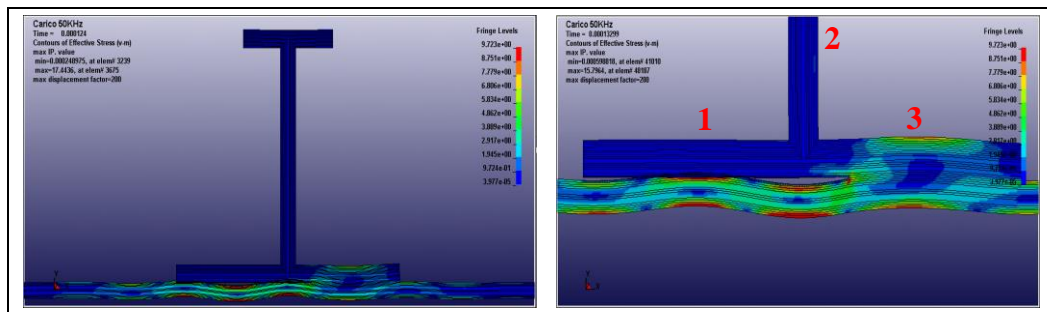


Figure 3.49: FE simulation of the wave-path in the disbanded configuration of the stiffened panel (left) and a close-up (right).

Furthermore, the presence of a disbanded region between the panel and the stringer (Figure 3.49) modifies the path of the wave that now travels mostly in the panel crossing the stringer below the disbanded region (from zone 1 to 3) when the stringer to plate bonding is lost after impact.

The same behavior observed in the finite element simulations is found in the experiments. Some preliminary experimental tests have been carried out on a defect free configuration (Figure 3.50), i.e. stringer perfectly bonded to the skin, to examine how the propagation characteristics change when the waves encounter the stringer.

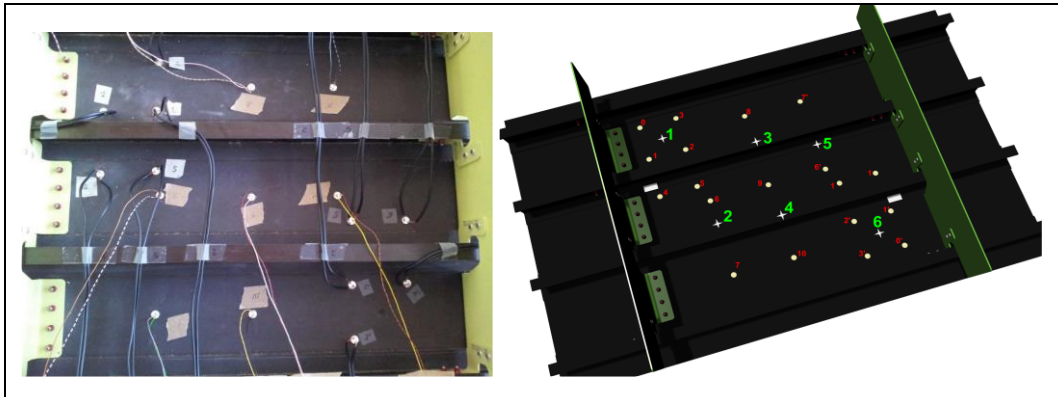


Figure 3.50: experimental sensors set up on stiffened panel

In Figure 3.51 (right) the stringer with two adjacent panel bays and the locations of three piezo patches are sketched. The PZT #10 works as a source and PZTs #7 and #9, placed on the opposite sides of the stringer, work as receivers.

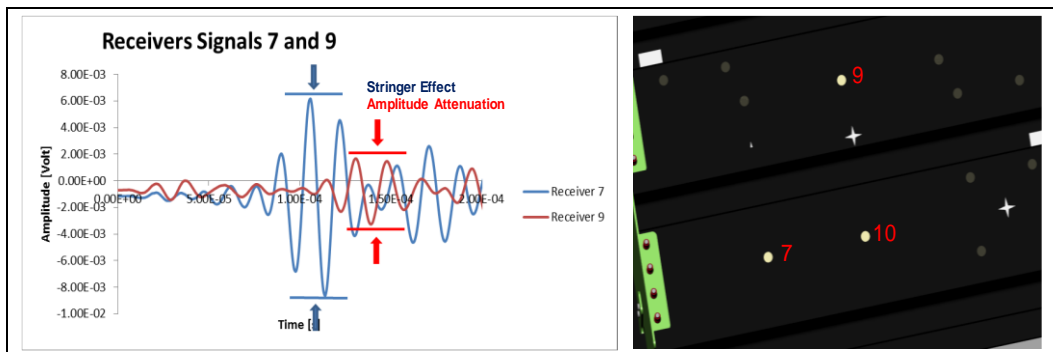


Figure 3.51: amplitude attenuation of the guided waves due to the stringer effect [5].

From the waveforms presented in Figure 3.51 (left) it can be seen that a substantial loss of amplitude of the waves travelling across the stringer (path 10-9) occurs as compared to the amplitude recorded by receiver 7 in the bay path (10-7). In fact, referring to Figure 3.48, the waves generated at the point 10 propagate to zone 1 and then is split into two propagation paths, to zone 2 and 3, respectively. As the thickness in zone 2 (stringer web) is smaller than that in zone 3 (panel and stringer base), most of the A0 wave energy will go up to the stringer web instead of crossing the stringer to travel to zone 3.

The stiffened panel has been impacted at the Alenia Aermacchi aerstructures laboratories in Pomigliano d'Arco (Napoli-Italy) using a calibrated pre-loaded spring gun causing the stringer-panel disbonding (Figure 3.52 right). Wave propagation tests have been conducted before and after the impact using an array of sources and receivers. In Figure 3.52 a sketch

of the stiffened panel, with source and receiver PZT patches and impact locations is shown.



Figure 3.52: stiffened panel source and receiver PZT patches and impact locations (left), Alenia Aermacchi experimental impact test (right)

Although multiple impact damages at different impact energies have been produced in the test article, in the present work we will focus on the impact location 5 (pointed out by a circle) for which a stringer disbonding of 40 mm x 80 mm has been achieved, as assessed by a C- Scan (Figure 3.53).

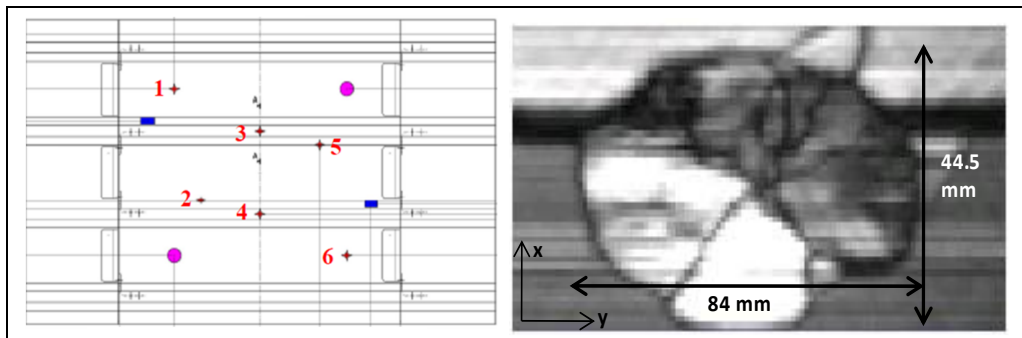


Figure 3.53: stiffened panel impact locations (left), under stringer feet impact C_scan assessment (right)

The amplitudes of the signals received from PZT #7' with the source at #6' (Figure 3.52) is about 3 times higher in case of disbonding, as showed in Figure 3.54.

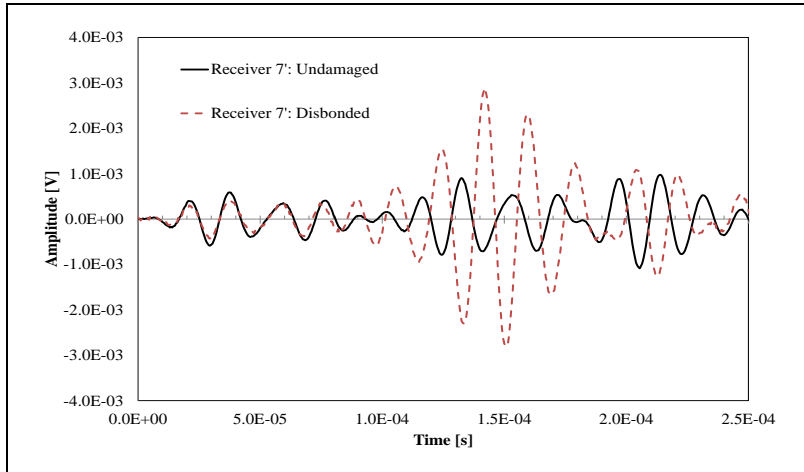


Figure 3.54: Influence of the stringer-panel disbonding on the A_0 waves travelling in the panel and transmitted across the stringer: source is in $6'$, receiver in $7'$ (ref. Figure 3.52).

Moreover, the group velocity of the A_0 waves through the stringer region is about 14% smaller than in the case of disbonding (see Table 3.3). This is due to the fact that the acoustic impedance is lower for the reduced overall thickness in the disbonded region.

	Intact	Damaged	Comparison
Path	v	v [m/s]	Δv %
	[m/s]		
$6' - 7'$	1604	1376	14.2
$7' - 6'$	1596	1376	13.8

Table 3.3: The influence of disbonding on A_0 waves group velocity at 60 kHz [5].

3.11 Statistical evaluation of experimental noise: threshold value definition

The aim of SHM applications, that is the Damage Identification, can be treated as a statistical event; damage is detected if some damage “metrics” evaluated from signals acquired on the structure overcome a “threshold value” by a fixed confidence level. Nevertheless, the noise, signal response containing no useful flaw characterization information, prevents to consider as useful each signal response. Experimentation could provide a statistical trend of noise in order to establish more accurately threshold value. It can be considered as the signal output below which the response can be considered as mixed in the noise and no assumptions can be made on the concreteness of the experimental result. In fact, the real issue is the definition of the least damage information that allows to identify an alteration in the structure, decision value, which is equal to or larger than threshold value [20].

Determination of threshold level is a prime parameter both for damage identification itself and assessing of a statistical reliability of an SHM system. The POD function, that allow to assess the capability of an NDE/SHM system, is strongly dependent from threshold level because by that we can distinguish hit data (damage is identified) from miss data (damage is not identified) in order to define a statistical data collection.

From the above definition, each result below the decision value is automatically censured. Determination of a threshold is substantially a statistical problem and there are two different ways to proceed, parametric and non-parametric statistics.

Parametric statistics is a branch of statistics which assumes that the data has come from a type of probability distribution and makes inferences about the parameters of the distribution. Most well-known elementary statistical methods are parametric (e.g.: Student Test). Generally speaking, parametric methods make more assumptions than non-parametric methods. If those extra assumptions are correct, parametric methods can produce more accurate and precise estimates. They are said to have more statistical power [21 - 22]. However, if assumptions are incorrect, parametric methods can be very misleading. For that reason, they are often not considered robust. On the other hand, parametric formulae are often simpler to write down and faster to compute. The most accepted hypothesis on the distribution of measurements noise is the Gaussian trend. However, when mathematical elaborations or data analysis are carried out after experimentation, Damage Index (DI) is calculated as:

$$DI = \frac{\text{Normalized}(\text{current signal} - \text{baseline signal})}{\text{baseline signal}} \quad (3.3)$$

and the Gaussian trend of a DI population is not obvious. Repeated signal acquisition is necessary to understand the statistical properties of DI population and its distribution. Taking into account repeatability, sensor’s relative position, direction of propagation, DI

formulation, signal amplitude and carrier frequency of signal, the analysis of DI population comparing different baseline signals could produce an important consciousness of DI distribution. Knowing all the necessary information about statistics distribution, a lower confidence level can be developed in order to obtain a threshold value. In this way we have the possibility to understand if a DI value obtained considering the current signal could belong to the baseline structure configuration or to a different one, with a certain confidence level. There are two possible procedures, evaluating if only a current signal (first case) or a current signal population (second case) belong to baseline signal population. The former approach is based on the determination of a threshold in term of DI. If current DI exceeds DI decision value, we are in presence of a different structure configuration with a certain confidence level.

The second approach consists in the comparison of two populations (current and baseline) that have proper distribution. A statistical test variable (e.g.: t Student) is considered to understand if the populations refer to different structure configurations or to the same one. In this case a threshold value is defined in term of the test variable.

In the case of non-parametric statistics, the first, simplest, approach became very complex and the second one results in a non-parametric test. However, considerations made up above have to be verified for take advantage of parametric statistics.

As a consequence, it is fundamental to verify the normality distribution of DI population.

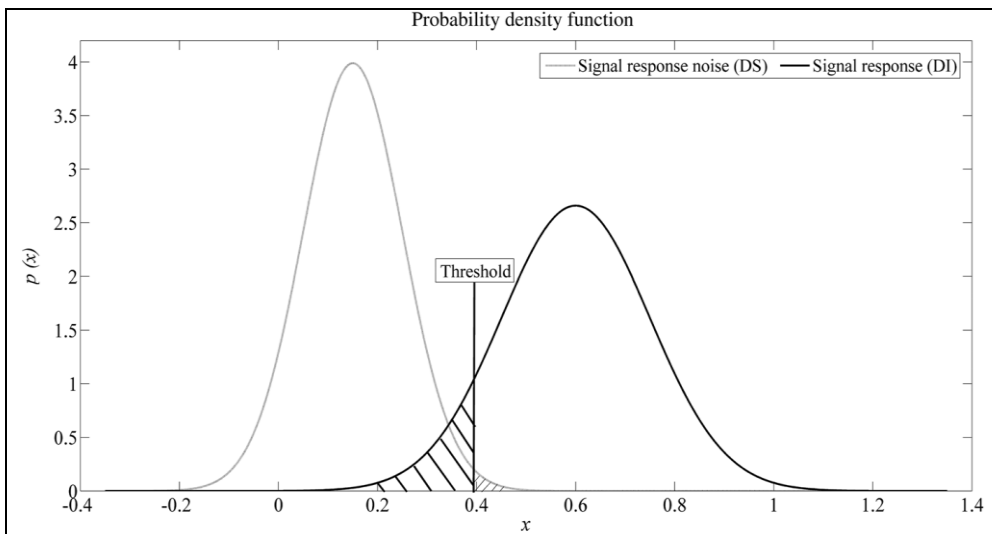


Figure 3.55: Typical overlap between the normal distributed noise of the signal response and the system signal response. The threshold defines the separation line between compound events of a damage detection system.

In order to consider the noise resulting from operating conditions, that produces the overlap in Figure 3.55, the value of Damage Sensibility (DS) is carried out from the several acquisitions of the same representative signal:

$$DS = \frac{\text{Normalized}(\text{current signal} - \text{current signal})}{\text{current signal}} \quad (3.4)$$

In DS function the current signal could be either the baseline signal or current signal (signal after operating life). DS Population represents the noise level of a certain signal, referred from its definition to a certain direction of propagation.

Kolmogorov-Smirnov Test is used to define the characteristic of statistical population. Such as every statistical hypothesis test, it is used in determining what outcomes of a study would lead to a rejection of the null hypothesis for a pre-specified level of significance; this can help to decide whether results contain enough information to cast doubt on conventional wisdom, given that conventional wisdom has been used to establish the null hypothesis. The critical region of a hypothesis test is the set of all outcomes which cause the null hypothesis to be rejected in favor of the alternative hypothesis. The null hypothesis consists in the non-Gaussian trend of the population under study. If the hypothesis is not confirmed after testing, the population can be considered a Gaussian type. This is always true if we consider the same reference signal (denominator in DS formulation) to compute the DS value. From n different signals, we have a combination of n*(n-1) DS values. Considering all data collection as a unique DS population, the null hypothesis is satisfied and the population could not be considered as Gaussian type. Nevertheless, considering n different populations with the same reference DS value, we have n-1 occurrences for each family, and the null hypothesis is false; all the n populations could have Gaussian trend.

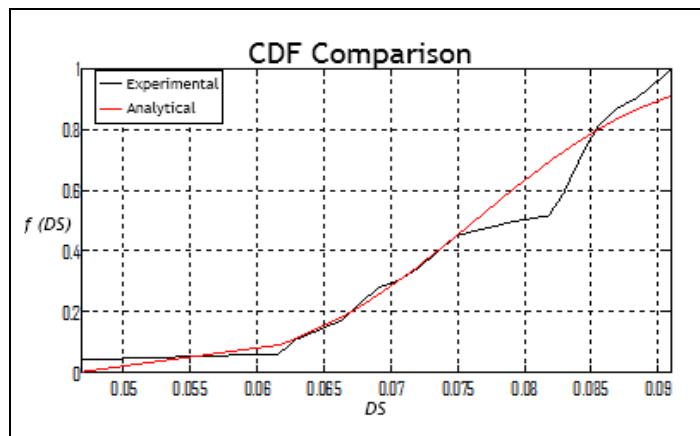


Figure 3.56: Kolmogorov-Smirnov test: comparison of cumulative functions to verify the null hypothesis.

From the mentioned procedure, for each direction of propagation we have n different Gaussian populations. For each of those, we can define the mean value μ , the standard deviation of the DS population σ and the relative normalized Gaussian function. From the definition of a confidence level (0.95, 0.99, ...) a threshold value for each DS Population can be easily found:

$$l_{th} = \mu + k * \sigma \quad (3.5)$$

where k can be obtained from the significance level chosen.

<i>Significance α</i>	<i>Factor k</i>
0.10	1.65
0.05	1.96
0.01	2.58

Table 3.4: Significance levels and confidence bounds of the standardized Gaussian distribution

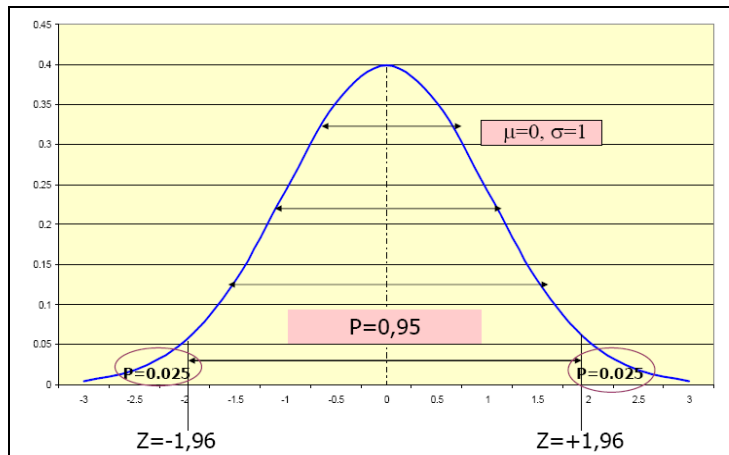


Figure 3.57: Confidence Level of a Gaussian distribution.

It should be noted that increasing in the confidence level, namely increasing the k factor, the probability of false alarm of the system decreases but at the same time the probability of detection decreases [23].

From the collection of the n threshold values for each couple of sensors, the maximum value could be considered the more accurate definition of the threshold because experimentation showed that the values obtained from the collection data given by l_{th} formulation are of the same order of magnitude and no statistical assumptions could be do again.

The above mentioned methodology has been adopted for a typical wing composite layered panel with tapered thickness (RAMP panel). The thickness variation has been obtained through two ramp links between three bays with constant thickness respectively of 10, 8 and 6 mm. Thus, each bay can be considered as an independent structure and no interferences phenomena between them are taken in consideration.

The source signal, generated by an arbitrary waveform generator (HP/Agilent 33120A), consists in a 4.5 sine cycles signal, 60 kHz central frequency, with 10V peak-to-peak tension Hanning windowed. An amplifier has been used to burst the PZT sensors with up to 80V peak to peak signal in the experiments.

The ultrasonic signal has been digitized and recorded directly in a four channel digital oscilloscope with 100MHz sampling rate (Agilent InfiniiVision DSO7104A). The digital ultrasonic signals are then downloaded to a personal computer and post processed. The methodology exploited for damage detection is based on a multiple propagation paths approach [24].

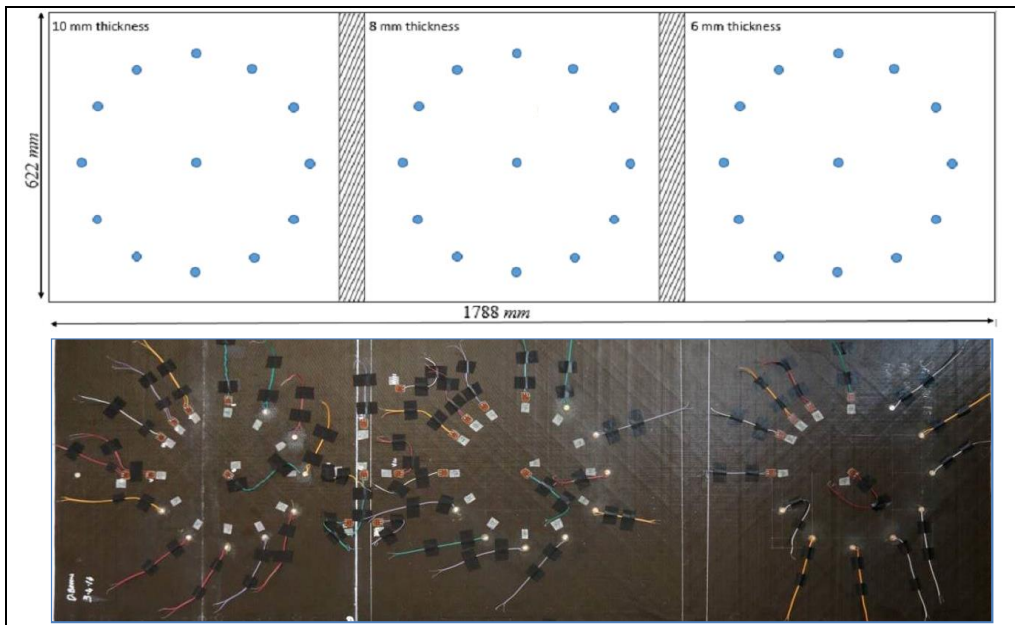


Figure 3.58: Sensors configuration of the tapered wing panel

Thirty-nine PZTs sensors, thirteen for each bay, have been permanently bonded on the structure employing a vacuum based secondary bonding procedures of common use by aircraft industries. The radial sensors pattern is adopted for an optimal monitoring of the enclosed surface of the plate. In order to check the correct operation, an additional PZT disk is installed at the circle center to perform a propagation velocity analysis. The overall configuration of the instrumented panel is shown in Figure 3.58.

Systematically, each sensor has been actuated and the signals at the other PZT locations are acquired using the classic pitch-catch method. So the baseline signals corresponding to 156 different actuator and sensor paths, for each panel bay, were recorded at a known intact condition of the plate. The measurements were repeated ten times with the same methodology in order to characterize the collected populations with the above mentioned approach. For each path, ten thresholds were obtained computing a 0.5% significance level; the maximum is considered as path detection threshold. Thus, for every bay 156

threshold values have been obtained, one for each path. Again, the maximum value has been considered as reference threshold of the single system (Table 3.5). Then each bay is subjected to low velocity impact damage tests. A calibrated pre-loaded spring gun impact machine have been used with a 1-inch striker (Figure 3.59).

Bay Thickness “t”	6 mm	mm 8	mm 10
Bay Threshold “Ith”	39 .0	45 .0	22 .0

Table 3.5: statistical detection thresholds of the bays with 0.5% significance level.

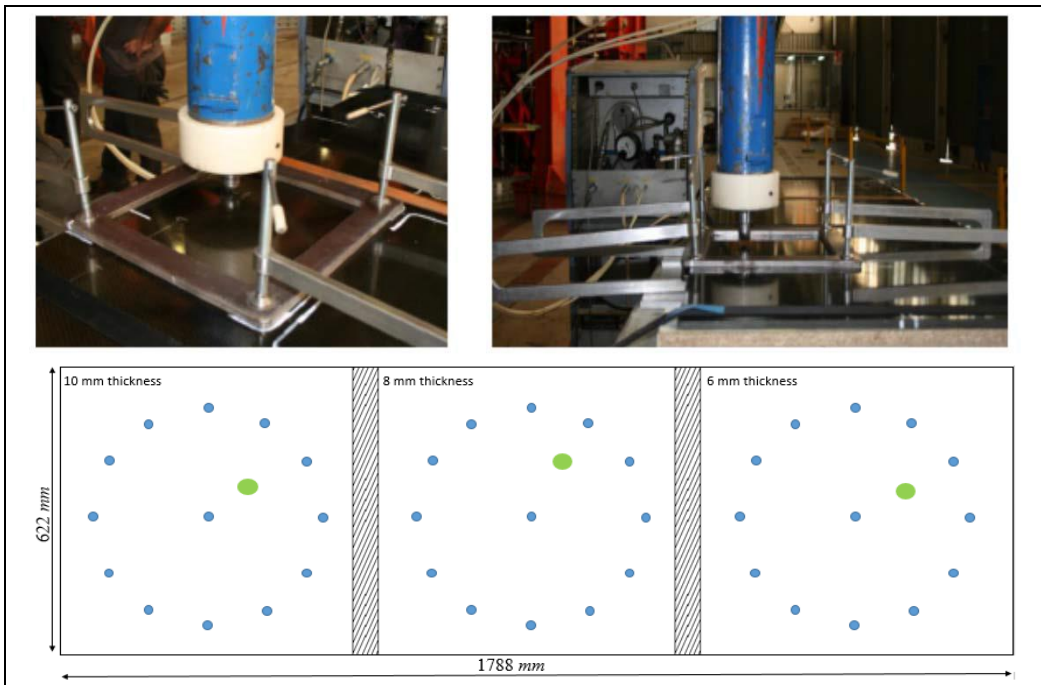
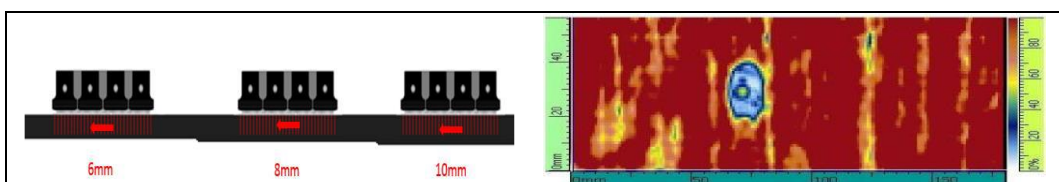


Figure 3.59: (upper) Alenia Aermacchi impact test setup, (lower) overall configuration of the tapered wing panel. The green area is the impact zone

To be sure to overcome the damage energy threshold for each thickness section, several energy values were imposed after a specific impact calibration. In order to induce a consistent damage, the three bays of 6, 8 and 10 mm are pushed with 85, 110 and 150 Joules, respectively. The exterior surface of the plate was then inspected with C-scans around the impact locations. The performed C-scan images, reported in Figure 3.60, clearly show the appearance of delaminations.



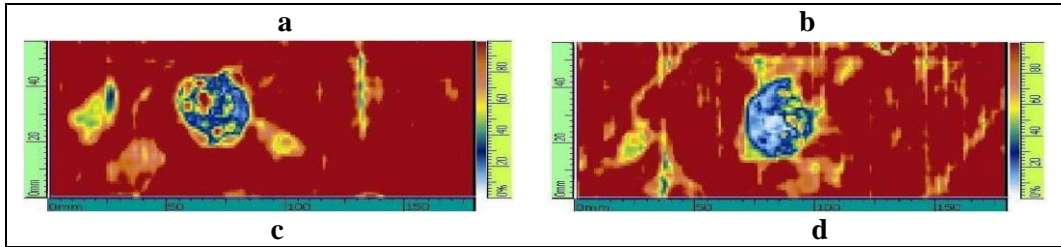


Figure 3.60: Calibrated Impact Longitudinal C Scan. Scan direction (a), 10mm Thickness Section (b), 8mm Thickness Section (c), 6 mm Thickness Section (d).

Finally, measurements were repeated after the low velocity impact has been carried out. Impact position was randomly chosen in the monitored area to test the system configuration without taking advantage of favorable locations for damage detection. Measurements were taken again for the damage indices computation. Only those that overcome the defined threshold were considered for damage detection. The correlated paths were considered to be damaged paths and displayed in a mixed arrow-space graphical representation.

The tip of the arrow indicates the source to receiver direction. From the plot of the measurement paths shown in Figure 3.61, it is envisioned that the damages appear always in the region with the maximum number of damaged paths. Hence, the combination of a very simple representation with the statistical definition of detection threshold has the potential to detect damage and the area of interest.

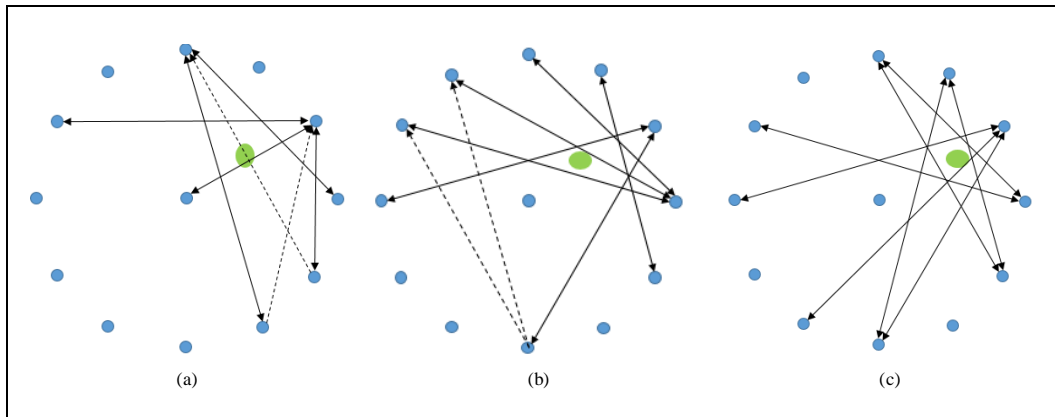


Figure 3.61: Arrow based graphical representation of damaged paths performed on 10 mm thickness (a), 8 mm thickness (b) and 6 mm thickness (c) bays. Threshold significance level 0.5%

3.12 Tomographic analysis

Starting from the statistical definition of the threshold level, for each bay only the damaged paths are selected. Each path is associated with a damage index that defines the damage condition intercepted. Each pair of intersecting paths defines a node inside the space enclosed by the ultrasonic sensors, which contains the structural condition of its surrounding area. In this way it is possible to identify several points forming a grid of nodes affected by the damage occurrence, the above mentioned damage grid. Considering the damage grids of the three bays, impact locations fall exactly inside the correspondent grid. To confine the damage a surface is fitted on the scattered data using a triangulation-based cubic interpolation. A color mapped 2D image is obtained and considered as a damage report. Then the damage location is detected considering an equivalent system of concentrated masses situated at the location of the grid points. Each node of the constructed grid represents a discrete body whose mass is identified by the damage index of the damaged node. Thus, greater the mass, the worse the condition of the surrounding area. A health mass system is generated and its pseudo-center of gravity is estimated first via a geometric weighted averaging and then considering its arithmetic weighted average. The damage location is so defined as the point $CG = (X_G; Y_G)$ in the Cartesian reference system of the health mass system. The geometric extrapolation of the coordinate is carried out from (Eq. 3.5):

$$X_G = \left(\sum_{i=1}^n f_i \right) \sqrt[3]{\prod_{i=1}^n x_i^{f_i}} \quad Y_G = \left(\sum_{i=1}^n f_i \right) \sqrt[3]{\prod_{i=1}^n y_i^{f_i}} \quad (3.5)$$

while the arithmetic coordinates are given by (Eq. 3.6):

$$X_G = \frac{\sum_{i=1}^n x_i f_i}{\sum_{i=1}^n f_i} \quad Y_G = \frac{\sum_{i=1}^n y_i f_i}{\sum_{i=1}^n f_i} \quad (3.6)$$

where the f_i is the weight of the i -th node, corresponding to the defined equivalent mass. Comparing the colormap image with the impact location it is possible to understand the goodness of the first methodology. On the other hand, the distance between the pseudo-center of gravity and impact location allows to quantify the reliability of the second methodology. In Figures 3.62(a), 3.63 (a) and 3.64 (a) the results of the three bays considered are shown, respectively. For the 6 mm thickness bay, the geometric and arithmetic definitions of the pseudo-center of gravity are very close to the impact location. However, even if the most critical area is near the damage location, some ghost damaged area can be shown in the map. As far as the 8 mm thickness bay (Figure 3.63 (a)) is

concerned, the position defined with the pseudo-center of gravity definition is again very close to the impact location. Finally, about in the 10 mm thickness bay (Figure 3.64 (a)) it can be observed that this time the pseudo-centers of gravity are not very close to the impact location. However, it falls exactly inside the most critical area obtained with the damage map.

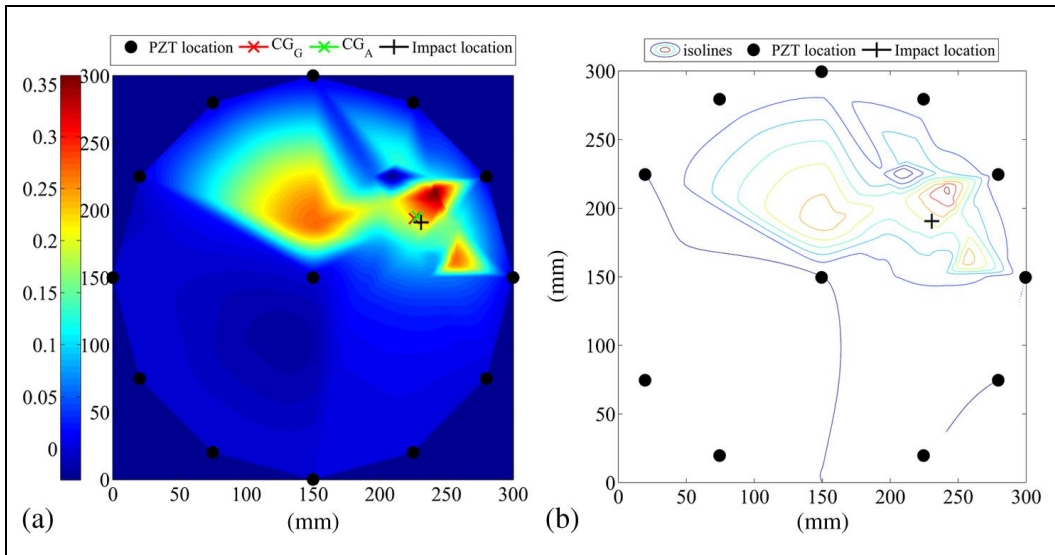


Figure 3.62: Tomographic analysis of the 6 mm thick bay. (a) Map of damage and (b) contour of isolevel.

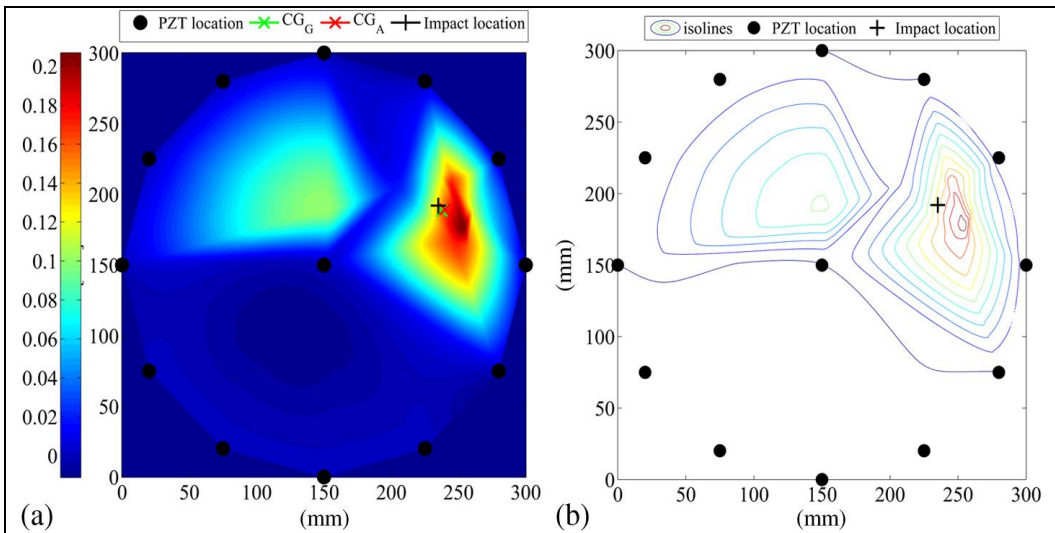


Figure 3.63: Tomographic analysis of the 8 mm thick bay. (a) Map of damage and (b) contour of isolevel.

In order to perform a detailed analysis with the methodology proposed, the surfaces interpolated on the scattered data of damage grid are sectioned in order to display the isolevel with a contour plot. In Figure 3.62 (b), 3.63 (b) and 3.64 (b) the contour plots of the three bays are shown. The graphic representation allows to better understand the health condition reconstructed via the interpolation. Similar conclusions made up for the maps can be again underlined, with a good agreement between impact location and the damaged area individuated by the isolevel.

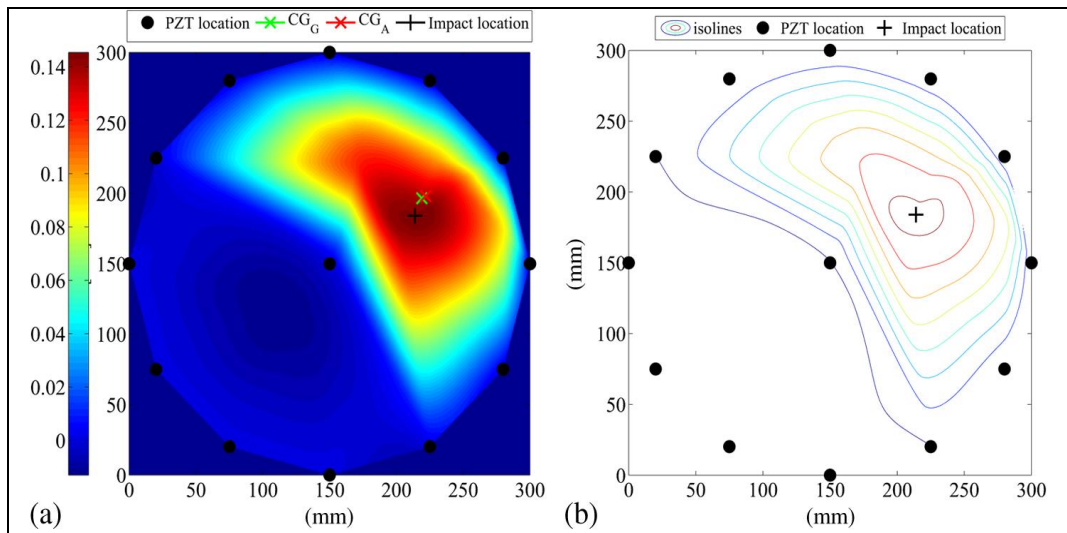


Figure 3.64: Tomographic analysis of the 10 mm thick bay. (a) Map of damage and (b) contour of isolevel.

To improve the methodology proposed and to eliminate any indecision when ghost damages appear in the map, the damage index is corrected with a densification factor. From Figure 3.65 it can be noted that the most critical area in the damage map corresponds to the area with the largest number of neighboring damaged nodes.

It can be envisioned that the condensation of damaged nodes may be a damage parameter; the greater the number of damaged points, the greater the probability of damage occurrence in the concerned area. This consideration relies on the fact that the occurrence of an isolated spot with a high damage index may originate a false alarm of the health monitoring system. Conversely, the presence of a large number of points with a certain index of damage provides a higher system response reliability. Figure 3.65 shows that the ghost damages are located in a sparsely populated area. This means that the hypothesis is well founded.

However, a better justification can be achieved considering the methodology proposed, based on the intersections of the propagation paths affected by the damage occurrence. It may happen that two damaged paths that are strongly affected by the hidden failure, namely have a high index of damage, intersect each other in an area far away from the real damage location. In this case, an isolated spot arises due to a shortcoming of the proposed

methodology, generating a lack of reliability. To reduce the probability that the damage prediction may be affected by this sort of false alarm, the condensation of damaged nodes in a specific area of the monitored structure can be considered once again. In this case, the probability of a false alarm due to the occurrence of ghost damage may rapidly decrease. To take into account this aspect, the condensation of damaged nodes is considered by dividing the monitored area in several parts of finite dimension.

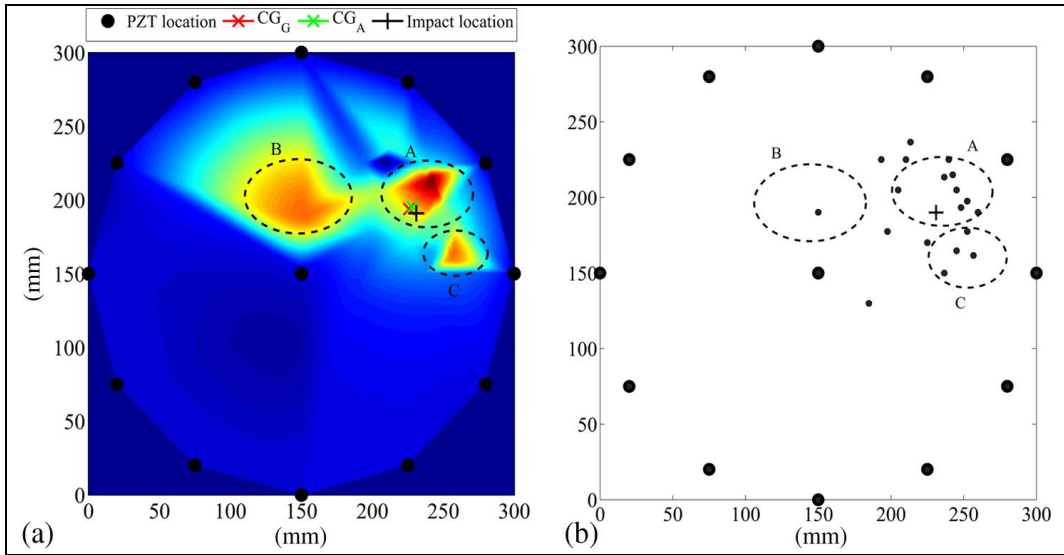


Figure 3.65: The 6-mm-thick bay. Concentration of damaged nodes and damaged area occurred in the damage map.

So, the area enclosed by the sensors is divided in nine parts, considering a constant mesh along the spatial coordinates. For each selected sub-area, only the damaged nodes that fall there are considered, assuming a new index of damage also depending upon a densification factor. The damage index already calculated is simply weighted with the factor f following the Eq. (3.7):

$$f = \frac{n \cdot A_{tot}}{N \cdot A} \quad (3.7)$$

Two effects are considered simultaneously; n/N is the densification parameter, where n represents the number of damaged nodes that fall inside the selected sub-area and N the number of all detected damaged nodes. Another parameter A_{tot}/A is included in the formulation to take into account the size of the selected area, making possible the division of the monitored area in parts of variable size. The dimension parameter takes into account the size of the selected area related to the total area enclosed by the sensors A_{tot} . Obviously to make absolute the nodes densification parameter, the greatest the area the largest the

number of nodes that is expected to have the same weight. Thus the inverse ratio A_{tot}/A is considered in the correction factor. The new index of damage associated with i -th node is thus obtained from Eq. (3.8):

$$(DI)_i^w = f_i \cdot (DI)_i \quad (3.8)$$

Considering the new map of damage of the 6 mm thickness bay, shown in Figure 3.66 (a), it can be noted that the introduction of a weighted damage index leads to two simultaneously results. The critical area appears more evident as the number of damaged nodes in that location is remarkable. Furthermore, the ghost damaged area are shaded with a reduction of their definition. This result is even more evident considering the isolevel in Figure 3.66 (b), obtained from the interpolating surface.

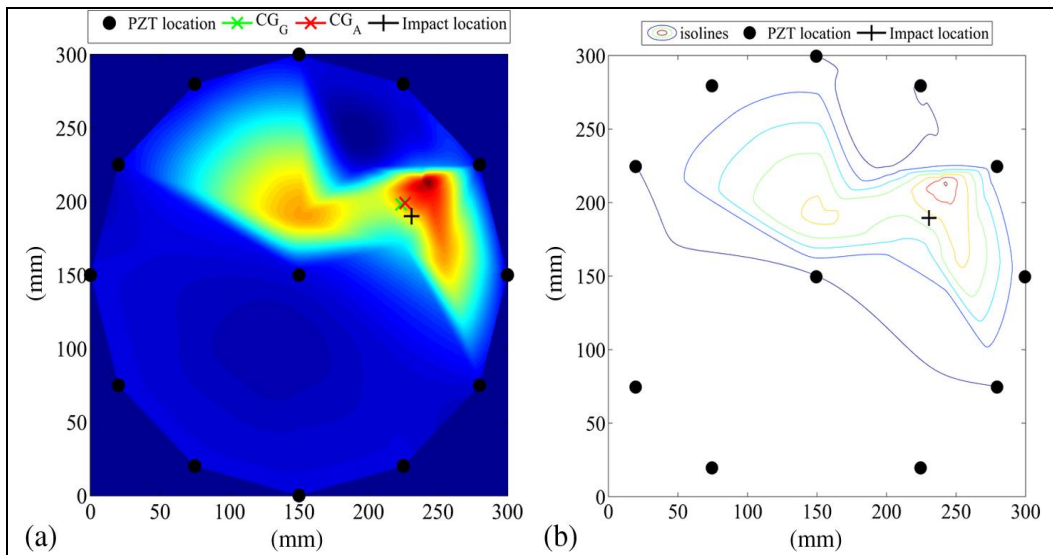


Figure 3.66: Tomographic analysis of the 6 mm thick bay improved with the densification correction. (a) Map of damage and (b) contour of isolevel.

The use of a weighted damage index calculation is carried out only for the 6 mm thickness bay, since for this bay the appearance of single nodes in the damage grid is particularly remarkable. When only a spot of damaged nodes is obtained, the weighting procedure does not induce any change on the map of damage. Obviously, this result makes reliable the technique because it acts effectively when different areas are affected by the damage occurrence but irregularly. Furthermore, the densification factor proposed in Eq. (3.7) takes into account also the size of the area selected through the definition of the dimension parameter introduced in the formulation. Thus, the user can select areas with different dimension in order to correctly separate the several spots emerging in the damaged grid. Furthermore, variable meshing along x and y direction in the space can be implemented. However, it must be emphasized that reducing the dimension of the selected areas leads to

an inconsistent correction; when the area of the finite elements is less than the minimum distance between the damaged spots, at most one node is included in a selected area and the correction results in a simple multiplication factor that is the same for all nodes.

3.12 References

1. Kudva, J. N, Grace, M. J., Roberts, M. M., “Aircraft structural health monitoring and other smart structures technologies – perspective on development of smart aircraft,” Proc. Of the 2nd International workshop on structural health monitoring, 122-32 (1999)
2. Saristu - Smart Intelligent Aircraft Structures D52.1: Methodologies for identification and localization of structural damages
3. Fundamentals of Piezo Technology - <http://www.piceramic.com>
4. Henkel application-technologies - <http://na.henkel-adhesives.com>
5. Fabrizio Ricci, Ajit K. Mal, Ernesto Monaco, Leandro Maio, Natalino D. Boffa, Guided waves in a stiffened composite laminate with a delamination, Structural Health Monitoring - 2016
6. Niethammer M., Jacobs L.J., Q. Juanmin, Jarzynski J., “Time-frequency representations of Lamb waves”, Journal of the Acoustical Society of America, Vol. 109, No. 5, 2001
7. Seth S Kessler, S Mark Spearing and Constantinos Soutis, Damage detection in composite materials using Lamb wave methods - SMART MATERIALS AND STRUCTURES (2002)
8. N. D. Boffa, L. Lecce, E. Monaco, F. Ricci, Application of the beam-forming technique for damage detection in composite plate - American Society of Mechanical Engineers, Noise Control and Acoustics Division (Publication) NCAD - pp. 489-495 - August 2012
9. Grondel S, Paget C, Delebarre C, et al. Design of optimal configuration for generating A0 Lamb mode in a composite plate using piezoceramic transducers. J Acoust Soc Am 2002; 12(1): 4–90.
10. Sauvik Banerjee, Fabrizio Ricci, Ernesto Monaco, Ajit Mal, A wave propagation and vibration-based approach for damage identification in structural components, Journal of Sound and Vibration 322 (2009) 167–183
11. Monaco E., Boffa N. D., Memmolo V., Ricci F., Testoni N., De Marchi L., Marzani A., Hettler J, Tabatabaeipour M., Delrue S., Van Den Abeele K., “Methodologies for Guided Wave-Based SHM System Implementation on Composite Wing Panels: Results and Perspectives from SARISTU Scenario 5”, [Smart Intelligent Aircraft Structures (SARISTU)], Springer International Publishing Switzerland, 495-527 (2016).
12. Marzani A, Testoni N., De Marchi L., Monaco E., Sharif Khodaei Z., Aliabadi M.H, Viana J., “Implementation of a Structural Health Monitoring system for a Composite Wing Box skin”, [Smart Intelligent Aircraft Structures (SARISTU)], Springer International Publishing Switzerland, 883-908 (2016).

13. Memmolo, V., Maio, L., Boffa, N. D., Monaco, E., and Ricci, F., "Damage detection tomography based on guided waves in composite structures using a distributed sensor network," *Optical Engineering*, 55(1), 011007, (2016).
14. Maio, L., Memmolo, V., Ricci, F., Boffa, N. D., Monaco, E., Pecora, R., "Ultrasonic wave propagation in composite laminates by numerical simulation," *Composite Structures*, 121, 64–74 (2015)
15. Ricci, F., Mal, A. K., Monaco, E., Maio, L., Boffa, N. D., Di Palma, M., Lecce L., "Guided waves in layered plate with delaminations, EWSHM 7th European workshop on structural health monitoring, Nantes, France, July 8-11, 2014.
16. Guo N and Cawley P. The interaction of Lamb waves with delaminations in composite laminates. *J Acoust Soc Am* 1993; 94(4): 2240–2246.
17. Su Z and Ye L. Identification of damage using Lamb waves (Lecture notes in applied and computational mechanics). London: Springer, 2009.
18. Ricci F, Monaco E, Baid H, et al. Guided waves in a disbanded honeycomb composite structure. In: Proceedings of the 9th international workshop on structural health monitoring, Stanford University, Stanford, CA, 11 September 2013, pp. 910–916.
19. Schaal C, Samajder H, Baid H, et al. Rayleigh to Lamb wave conversion at a delamination-like crack. *J Sound Vib* 2015; 353: 150–163.
20. USA Dept of Defense Handbook, "MIL-HDBK-1823, NDE system reliability assessment," April 2009.
21. Freedman, D. (2000) *Statistical Models: Theory and Practice*, Cambridge University Press, ISBN 978-0-521-67105-7.
22. Geisser, S.; Johnson, W.M. (2006) *Modes of Parametric Statistical Inference*, John Wiley & Sons, ISBN 978-0-471-66726-1.
23. E. Monaco, V. Memmolo, F. Ricci, Boffa N. D. and L. Maio, "Guided waves based SHM systems for composites structural elements: statistical analyses finalized at probability of detection definition and assessment," in *Health Monitoring of Structural and Biological Systems 2015*, Tribikram Kundu, Ed., Proc. SPIE 9438, 11 pp (2015) [doi: 10.1117/12.2084334].
24. S. Banerjee, F. Ricci, E. Monaco and A. K. Mal "A wave propagation and vibration-based approach for damage identification in structural components," *Journal of sound and vibration* 322, 167-183 (2009) [doi: 10.1016/j.jsv.2008.11.010].

Chapter 4

SHM System Implementation on a Full Wing

Ground Demonstrator

4.1 Introduction

A full-scale lower wing panel, of a wing box ground demonstrator, made of composite material has been designed, manufactured and sensorized within the European Funded research project named SARISTU. The research activity, conducted during the whole doctoral thesis, has seen the contribution to the overall development of the system, from design to implementation as well as to the impacts campaign phase where Barely Visible and Visible Damages (BVID and VID) have been artificially induced on the panel external surface by a spring gun impact machine. The work summaries experimental results related to damages production, their assessment by C-SCAN as reference NDT method as well as damage detection by a guided waves based SHM [1].

The implemented SHM system, based on Electromechanical impedance (EMI) and Guided Waves (GW), is made by customized piezoelectric patches secondary bonded on the wing plate acting both as guided waves sources and receivers.

The system is capable to control a network of up to 160 piezoelectric transducers and to perform both Electromechanical Impedance (EMI) measurement at each transducer, to check the reliability as well as their bonding strength, and to perform an active guided waves screening [2].

The research activity, here described, will deal mostly about of the experimental impact campaign and of the signal analysis carried out to extract the metrics more sensitive to damages induced. Image reconstruction of the damages dimensions and shapes will be also described based mostly on the combination of metrics maps over the plate partial surfaces.

4.2 Full Scale Ground Test Wing Demonstrator experimental investigations

One of the most relevant Saristu objective is the structural Integration of morphing and Structural Health Monitoring (SHM) devices on an outer wing demonstrator. Morphing technology target is to implement seamless structural concepts able to control the wing aerodynamic loads and enhance its performance, reducing drag and high intensity forces.

SHM technology objective is to demonstrate the possibility to carry out robust monitoring devices, based on ultrasonic and optical fiber sensors, able to detect in service damages.

For these purposes, two full scale ground test, 4,5 m span, outer wing demonstrators have been manufactured and tested. The first one has been testes in a low speed wind tunnel (at TsAGI) to validate the functionality and the system integration of the morphing devices; the second one, to validate the Structural Monitoring System (SHM) integration and functionality, to perform static strength, fatigue and dynamic Tests on ground (at Alenia Aermacchi).

Below a brief overview of the second ground test demonstrator tests setup is presented. Static and fatigue tests were performed by Alenia technicians while damage replication and assessment, SHM implementation and testing have been performed by Federico II University of Naples (Unina) and Bologna University (Unibo) researchers.

The tested wing box demonstrator consisted of a main box realized as a composite pristine parts in terms of Panels, Stringers, Ribs, Rear & Front Spar. Fairing (tip, cuff,...), Leading & Trailing Edge and also Actuator, Winglet, Pipes, Movable Surface have not been integrated into test article, only main box components was tested (Figure 4.1).

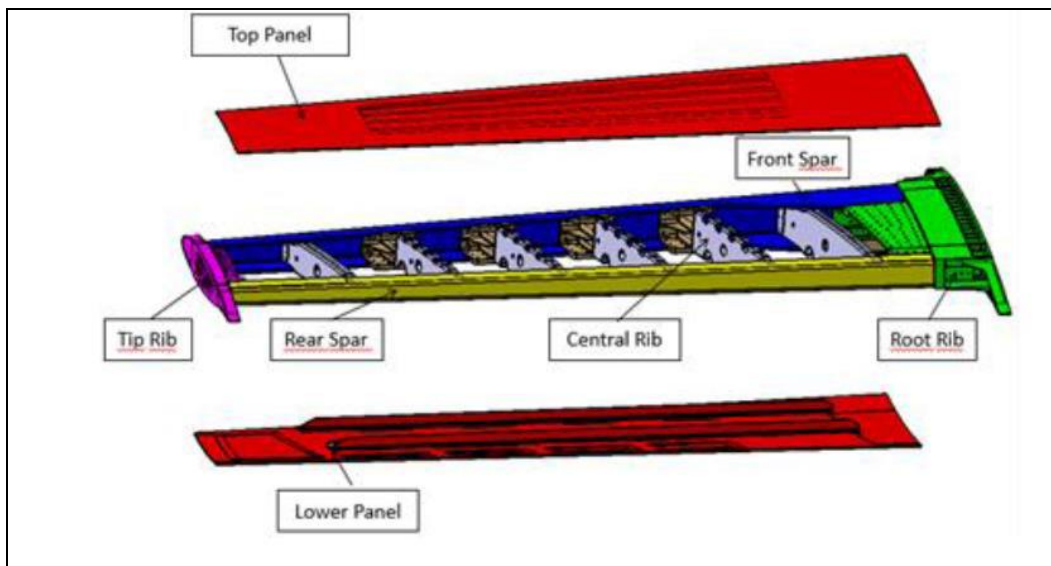


Figure 4.1: full scale wing box ground demonstrator main components exploded view.

Scope of the wing box demonstrator test activities is to summarize the analyses that have been performed on preliminary test articles and coupons to substantiate the structural integrity on SARISTU demonstrator.

The tests can be considered as a “Full-Scale” static tests. The objective of the tests were to validate analytical predictions as well as to demonstrate compliance with the SHM system. So, for the validation of the main box, two distinct phases have been performed:

Phase 1: application Static Limit Loads, Ultimate Loads, all accounting for environmental conditions.

Phase 2: application of 20000 FC of Fatigue loading, inflict BVID impact for SHM damage detection.

The test purposes were:

1. demonstrator verification;
2. substantiate the capability of the SHM system;
3. demonstrate the Ultimate static capability after a fatigue cycle on skin panels in presence of manufacturing damages and BVID’s under compressive loads.

In order to verify the points above mentioned, a loads distribution, along the wing main box, have been applied to rebuild typical Real Flight Load Cases (Figure 4.2).

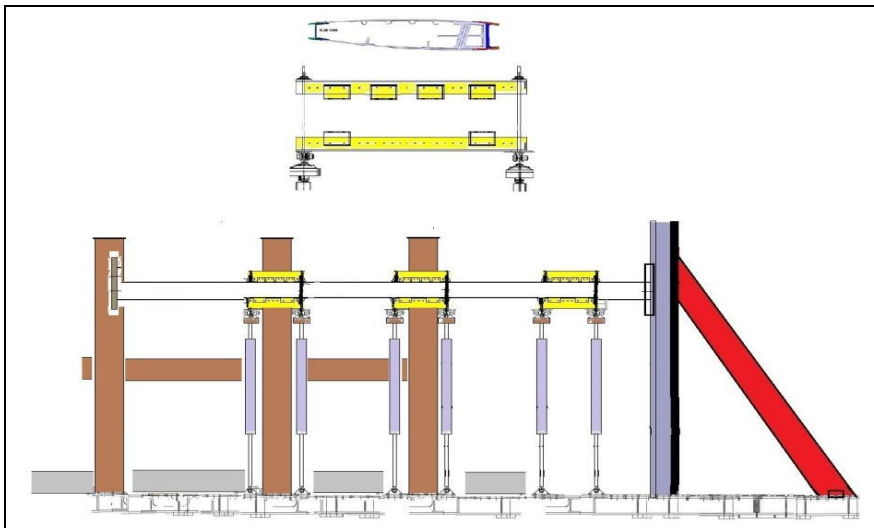


Figure 4.2: Main box support for fatigue and static tests

No damages (disbonding, tool drop, hail, stone, debris ...) have been inflicted to the test article before or during Calibration, Static & Fatigue Test.

Damages for SHM evaluation and behavior have been inflicted on the outer surface of the wing box lower wing panel only after Fatigue Test.

The test article has been fixed to a dedicated test strong back fixture by a metallic root rib interfacing. The test loads have been introduced by means of three saddle whiffletree (4 pads each ones) on front and rear spars, all of them loaded by hydraulic jacks (Figure 4.3).

Each actuator has been fitted with a hinged constraint in both side. The lower constraint is fixed on the ground test platforms, while the upper part of each actuator is free to move together with the load cell keyed in axis.

Pre-test checks and inspections have been performed before the test starting in order to certify the test article configuration, status and test set-up conformity to lab design requirements. Functional test are performed to verify the installation of the automated load control system and to prevent unexpected trouble during the test.

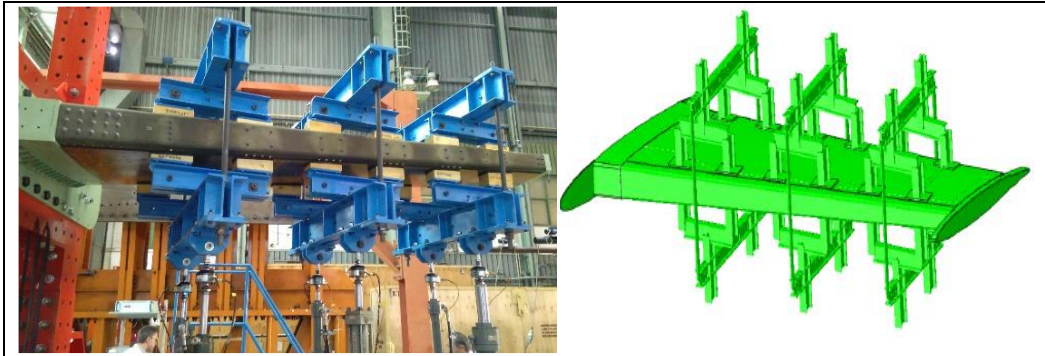


Figure 4.3: Application of loads during ground calibration tests (left), finite element model endowed with load application saddles (right)

4.2.1 Static tests

A total of 13 flight condition have been numerically analyzed (Table 4.1), although for experimental static test, only worst load condition has been considered (gust case - LC5). Load has been applied perpendicularly on the saddles, along the z direction (Figure 4.4).

Flight conditions for structural box sizing:											OLOAD RESULTANT "saristu_demo_fine_r14"						
N°	Case	W [Kg]	W (ID)	Mach	V [KEAS]	V [m/s]	ZFt [kft]	Pdyn [Kpa]	nz (g)	CL	alpha [deg]	FX [N]	FY [N]	FZ [N]	MX [Nmm]x10 ³	MY [Nmm]x10 ³	MZ [Nmm]x10 ³
1	Cruise	60000	MTOW	0.484	320.0	164.7	0	16615.0	1	0.322	0.24	-217	1856	24303	-377947	-131724	6842
2	Vc Nz Max	60000	MTOW	0.484	320.0	164.7	0	16615.0	2.5	0.800	5.50	-10566	10326	101031	-1592716	-520095	-107170
3	Vc Nz Min	60000	MTOW	0.484	320.0	164.7	0	16615.0	-1	-0.315	-6.68	-6055	-15548	-73289	1169203	343155	-177268
4	Vd Nz Max	60000	MTOW	0.605	400.0	205.9	0	25961.0	2.5	0.512	1.84	-3331	9031	83815	-1317480	-437455	-2180
5	gust_1	60000	MTOW	0.484	320.0	164.7	0	16615.0	3	0.959	7.49	-16891	12378	127152	-2007136	-654395	-194624
6	STGust (gust_2)	55000	MLW	0.484	320.0	164.7	0	16615.0	3.2	0.926	7.05	-15529	11974	121893	-1923491	-627332	-175493
7	Va Nz Max*	60000	MTOW	0.388	256.6	132.0	0	10672.0	2.5	1.230	13.00	-21501	8833	107321	-1696825	-555685	-286130
* Va was computed using the CLmax value obtained from the aerodynamic analyses performed on the reference wing																	
Flight conditions for morphing device performances evaluation:											OLOAD RESULTANT "saristu_demo_fine_r14"						
N°	Case	W [Kg]	W (ID)	Mach	V [KEAS]	V [m/s]	ZFt [kft]	Pdyn [Kpa]	nz (g)	CL	alpha [deg]	FX [N]	FY [N]	FZ [N]	MX [Nmm]x10 ³	MY [Nmm]x10 ³	MZ [Nmm]x10 ³
8	Cruise MTOW	60000	MTOW	0.750	240.0	222.4	35	9387.9	1	0.569	1.270	-890	4155	34546	-545692	-182158	8813
9	Cruise MLW	55000	MLW	0.750	240.0	222.4	35	9387.9	1	0.522	0.921	-630	3528	30162	-475827	-159970	9512
10	Climb 0k	60000	MTOW	0.400	264.6	136.1	0	11348.0	1	0.470	2.041	-1454	3358	32843	-515186	-170894	-4062
11	Climb 20k	60000	MTOW	0.600	270.0	189.6	20	11734.0	1	0.455	1.294	-932	3261	31394	-492643	-165072	3439
12	Climb 30k	60000	MTOW	0.700	252.3	212.2	30	10321.0	1	0.517	1.336	-987	3718	33225	-523005	-174699	5006
13	Low Speed V Max**	60000	MTOW	0.250	165.0	85.1	0	4433.0	1	1.197	11.293	-9166	3277	43813	-691373	-228021	-123959

Table 4.1: static tests flight conditions

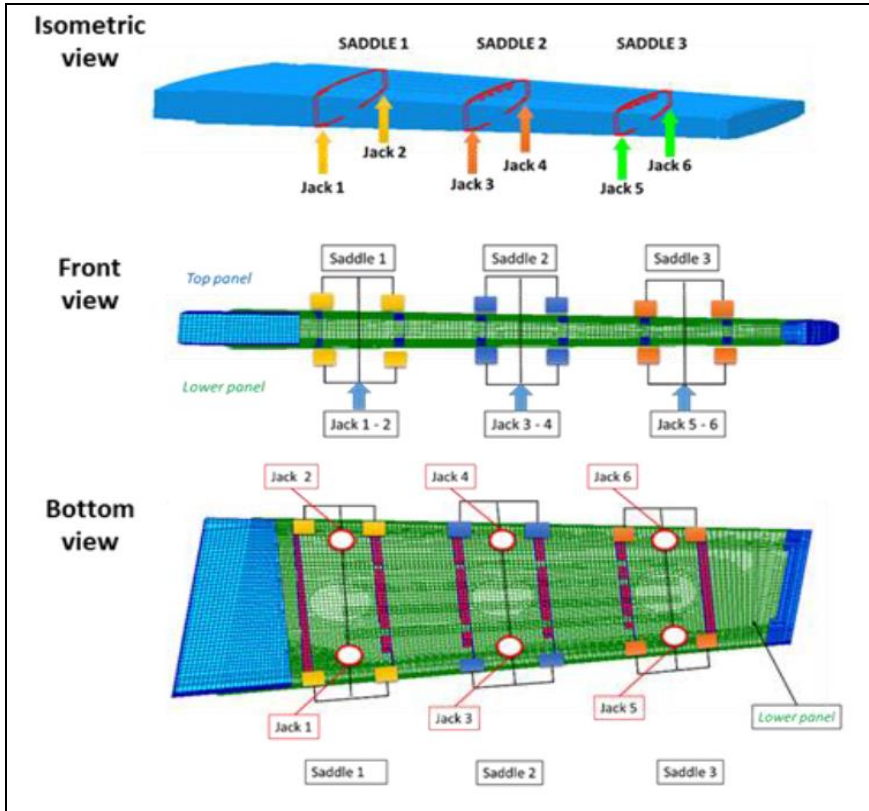


Figure 4.4: Saddles and jacks position

Preliminary 10 static calibration tests have been performed: the first 5 with the only Tip Saddles, while the second 5 with all the 3 Saddles. This Last condition has been then applied to Static and Fatigue Test (Table 4.2).

Reference Vertical shear, bending Moment, Torsion (VMT) values for worst load condition LC5 were:

SADDLE	SHEAR (Fz)	TORQUE(My)
No1	27283,6[N]	6680500[Nmm]
No2	27960,9[N]	505000[Nmm]
No3	29523,3[N]	3180100[Nmm]

Table 4.2: LC5 Reference Vertical shear, bending Moment, Torsion (VMT) values

Starting from reference VMT load and taking into account mass, geometry and positions of the saddles, the discretized applied loads were:

TARE LOAD (only Saddles Pre-Load)	F1	[N]	100%	+1912
	F2	[N]	100%	+1912
	F3	[N]	100%	+1863
	F4	[N]	100%	+1863
	F5	[N]	100%	+1814
	F6	[N]	100%	+1814
NET LOAD (without Saddles Pre-Load)	F1	[N]	100%	+22213
	F2	[N]	100%	+5071
	F3	[N]	100%	+40296
	F4	[N]	100%	+8119
	F5	[N]	100%	+31911
	F6	[N]	100%	-2388
GROSS LOAD (with Saddles Pre-Load)	F1	[N]	100%	+24125
	F2	[N]	100%	+6983
	F3	[N]	100%	+42160
	F4	[N]	100%	+9982
	F5	[N]	100%	+33725
	F6	[N]	100%	-573

Table 4.3: Discrete Static Gross Load applied saddles jacks

4.2.2 Fatigue Test

The test article has been tested according to Load Case 10 (Table 4.1) that corresponding at 33% of limit load for worst load condition for static test LC5.

The Fatigue Test has been applied to all 3 Saddles configuration by a fatigue cycles cross “0” with Rstress = -1. The following table shown the load condition applied to fatigue test.

			TARE LOAD (only Saddles Pre-Load)	NET LOAD (without Saddles Pre-Load)	GROSS LOAD (with Saddles Pre-Load)
F1	[N]	100%	+1912	+12298	+14210
F2	[N]	100%	+1912	-4654	-2742
F3	[N]	100%	+1863	+11653	+13516
F4	[N]	100%	+1863	-4207	-2344
F5	[N]	100%	+1814	+10471	+12285
F6	[N]	100%	+1814	-3676	-1862

Table 4.4: Discrete Fatigue Gross Load applied saddles jacks

As above reported for static tests, also for fatigue test 10 preliminary calibration tests have been performed. First 5 Load Calibration Case were carry out with only one SADDLE at Tip, while second 5 Load Calibration Case were carry out with all three SADDLES.

The fatigue test, implemented by a traction-compression fatigue cycles, has been performed with a cycle frequency of 0,27 Hz for about 20 hours and 20000 applied cycles. No damage was detected during the fatigue and static tests.

4.2.3 Ground Test Demonstrator SHM experimental tests setup

Before fatigue and static tests and still before wing box demonstrator assembly, the wing box lower panel (LWP), produced by Bombardier and including three different thicknesses zones and transition areas, has been sensorized for SHM system implementation.

Unina and Unibo researchers agreed a sensors configuration and a test matrix for signal acquisition in order to provide a preliminary signals baseline for SHM system (Figure 4.5) and to test the bonding procedure effectiveness (see chapter 3, section 3.2.1).

The panel has been sensorized by Alenia technicians in coordination with Unina researchers.

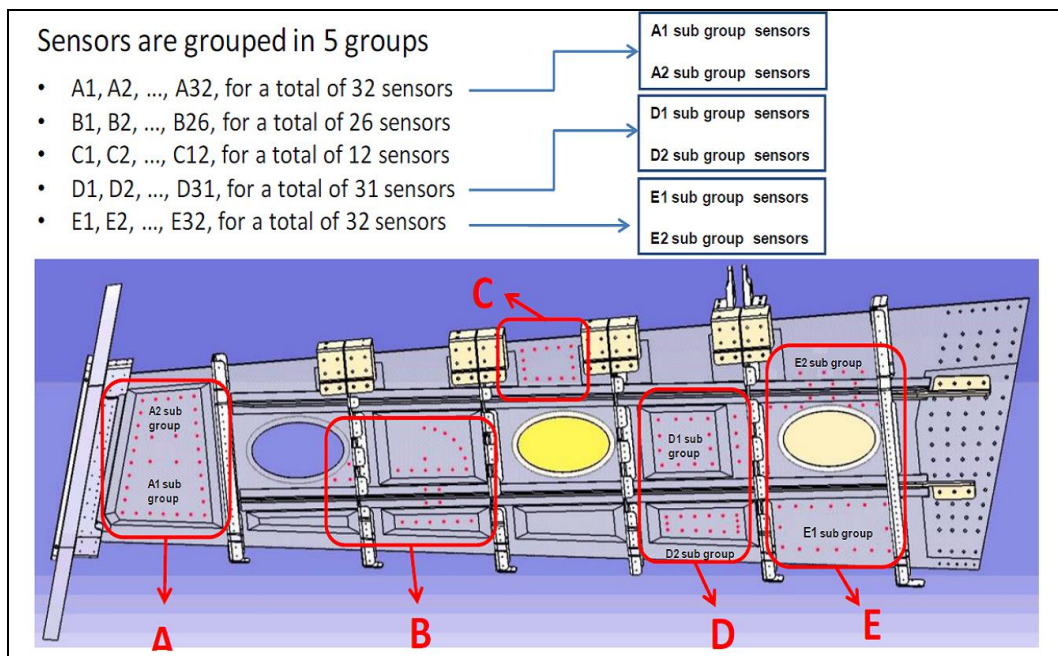


Figure 4.5: LWP Sensors tags

UNIBO have oversaw the sensors wiring and carried out the measurements with a dedicated DAQ System using the same methodologies, pitch catch technique, used for preliminary test articles, Ramp Panel, Flat and Stiffened panels, described in the previous chapter.

A set of 133, customized shape, flexible smart layer sensors (DuraAct sensors) have been secondary bonded, with a vacuum based procedures, on the internal surface of the LWP and organized in 5 different groups (groups: A, B, C, D, E) representative of 5 different bays (Figure 4.5).

The sensors distribution, for each group and for each bay, was defined taking into consideration the potential impact locations, settled in the project phase, (Figure 4.6) and the wave propagation directionality analysis.

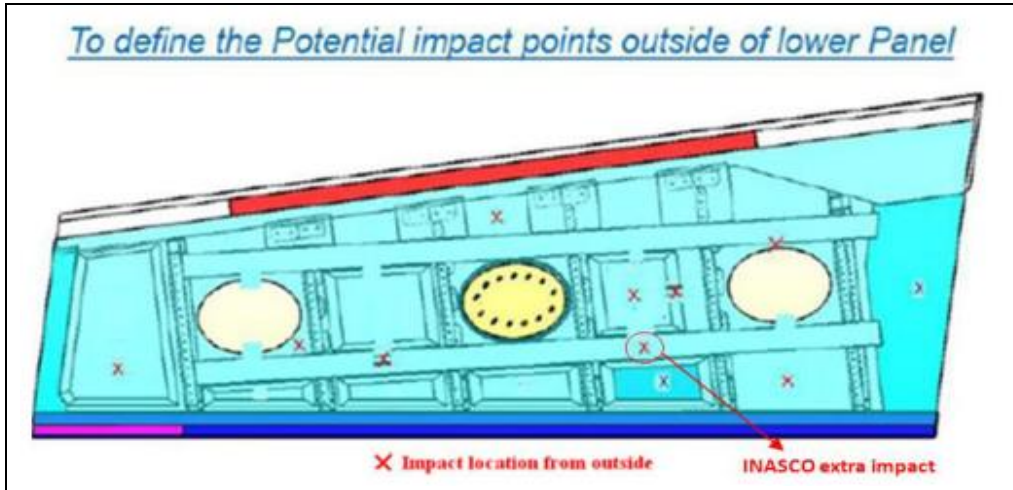


Figure 4.6: LWP potential impact points

To reduce electro-magnetic interference on the recorded signals generated by external sources as well as crosstalk between the actuated sensors and the ones used for recording the incoming signals, the proposed transducer cabling assembly make use of shielded cables, as an alternative solution to the usage of twisted pairs. To further increase the crosstalk attenuation, the mini coax cables type RC178 (M17/93-RG178, see Figure 4.7) have been preferred. The impedance of this cable is 50Ω , which is optimal for delivering the maximum amount of power from the amplifier to the transducers used as actuators, less than 6.2 dB attenuation over 4 m at 1 MHz, and to reduce to the minimum the attenuation of the received signals on the path from the sensors to the acquisition equipment, less than 5.5 dB over 4 m at 1 MHz

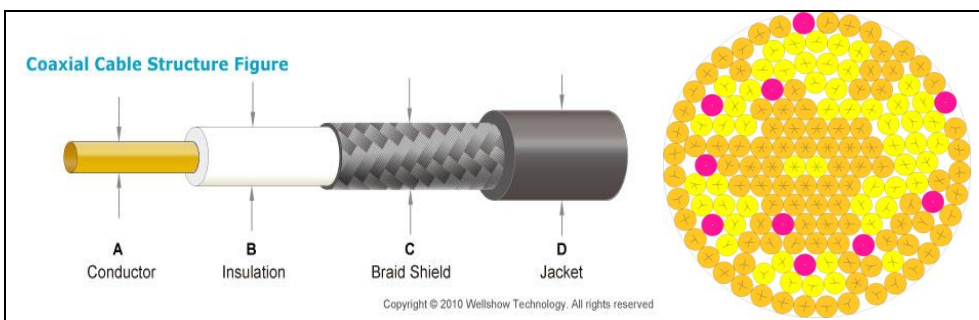


Figure 4.7: (left) mini coax cable type RG178 (M17/93-RG178), (right) minimum size packing of the 160 cables for a circular hole.

As for bonded sensors, the cables have been grouped in 5 bundles (group A for a total of 32 cables, group B for a total of 26 cables, group C for a total of 12 cables, group D for a total of 31 cables and group E for a total of 32 cables). The bundles had a free length (outside of the demonstrator) of about 1 meter.

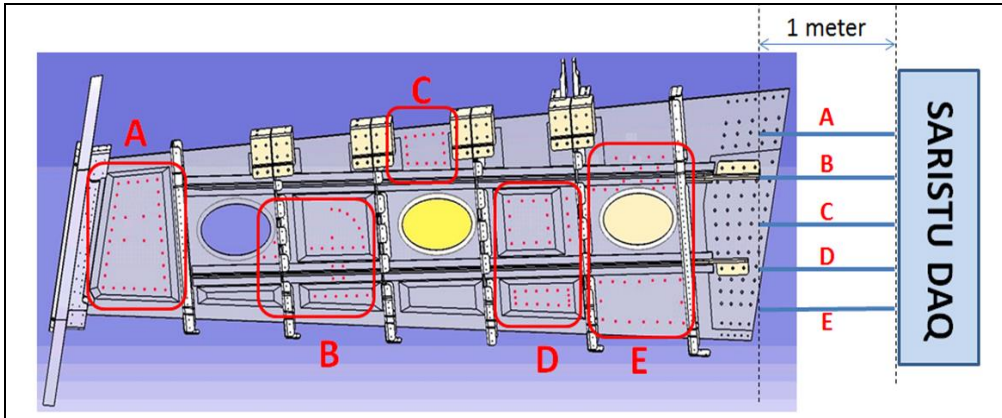


Figure 4.8: Cabling implementation on the lower wing panel.

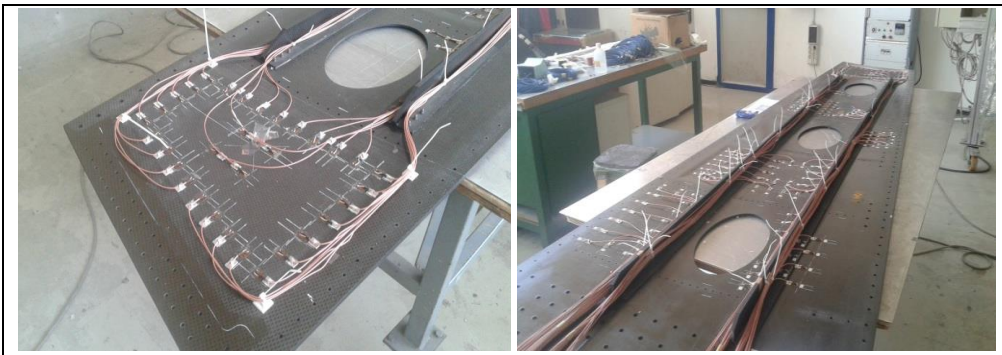


Figure 4.9: Cabling implementation on the lower wing panel.
(left) group A and (right) overall view.

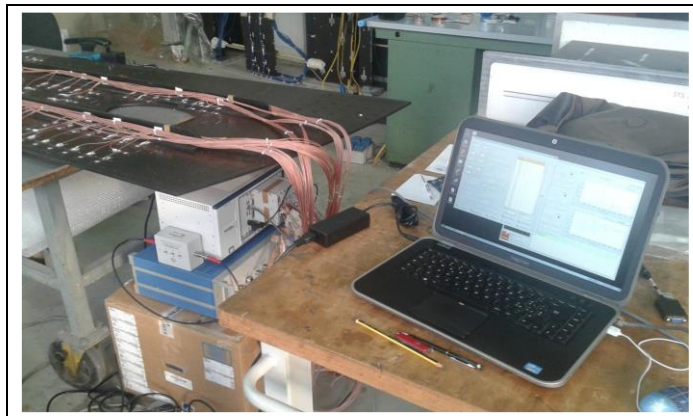


Figure 4.10: Sensors system final configuration testing

Then the distributed sensors system was tested in its final configuration (Figure 4.10); the cabling underwent a full electrical test highlighting no shorts neither opens; all sensors were electrically tested as well as the electronic equipment, which was tested up to 150%

of the maximum voltage required for SHM implementation. The calibration test was used as well to collect data from the lower wing panel, as to assess the environmental conditions and the machine time for the collection of the baseline and SHM signals.

4.3 Data Acquisition System (DAQ)

Basically, guided waves based SHM systems consists in a network of tiny and low weight piezoelectric transducers, bonded or embedded into the structure (generally the skin), driven by a proper Data Acquisition System (DAQ). The DAQ is capable to actuate guided waves from one or more transducers (actuators) and receive from some others (sensors), when it operates in active manner, or simply to record waveforms at sensors when operates in passive mode [3, 4]. In both cases, the guided waves signals acquired at the sensors are next treated with signal processing tools with the aim of assessing the existence of damage, to localize the damage, and also aim at characterizing the shape of the damage.

Compared to other SHM approaches, SHM systems based on guided wave have some potential being characterized by the following peculiar and positive aspects:

- allow to monitor and inspect large areas from few accessible points of the structure (the transducers positions); including hidden parts of the structure as long as they can be well reached by the guided wave propagation;
- guided waves are characterized by an high speed of propagation (impacts and delaminations can be detected and located in almost real-time), have limited attenuation and are sensitivity to multiple types of damage (see chapters 2 and 3) including those hidden in the structure [3, 4];
- allow to develop a permanently embedded monitoring system that can potentially operate in flight with no disturbance for the standard operations;
- are characterized by low weight equipment.

However, today SHM approaches based on guided waves because of some methodological and technological limitations hardly meet the standards of the aerospace industry and their integration in the manufacturing process seems still far to come. Among the several, major limitations are:

1. the developed methodologies for impact/damage detection, localization and characterization allow to operate properly on regular geometries made of isotropic materials whereas their reliability on composite structures with the presence of stiffeners, rivets, manholes, and other geometrical anomalies has still to be proven; in addition the majority of the developed methodologies need baseline measurements (it is proven that the baseline might change because of temperature, moisture, operative loads, ageing, etc.);
2. the scalability from laboratories to aircrafts of the SHM system technology is still unproved (open issues related to weight, hardware power consumption, complex circuitry, life duration, bulky signal processing);
3. absence of means to assess the SHM cost/benefit analysis.

Doubtless, the SARISTU project, within which falls the research activity presented here, has contributed to advance the state-of-art of all points above by increasing the Technology Readiness Level (TRL) of guided waves based SHM in aeronautics thus shortening the gap from demand and supply.

The proposed experimental DAQ platform, developed in collaboration with the Department of Electrical, Electronic and Information Engineering of Bologna University and with the Fraunhofer Institute (FhG), is designed to operate guided waves based methodologies aimed at detecting defects, mainly delaminations, in structural components. Thus, as mentioned above, the experimental apparatus must be able to actuate and receive stress guided wave signals from the network of piezoelectric transducers bonded to the structure under inspection, whereas the processing phase, meant to translate the acquired signals into damage metrics, will be performed on a personal computer.

Since the adopted piezoelectric transducers are capacitive by nature their use adds extra challenges in the development of a proper hardware system. For instance, common signal amplifiers used in standard ultrasonic applications are not suitable for this purpose due to the fact that the impedance of the transducers changes with frequency. A special amplifier is therefore needed to handle piezoelectric transducers used to actuate guided waves.

Furthermore, when the transducers are used as sensors, care must be taken because the low impedance inputs or high value capacitive inputs change the behaviour of the sensors. Basically there are two modes of reading piezoelectric sensors: voltage and charge. When the sensor is read as a voltage source, care must be taken on the parasitic capacitance of the cables and the input DAQ impedance. Input impedance must have high value of resistance and a low value of capacitance in order not to degrade the signals. The DAQ inputs must handle values of some micro volts to hundreds of volts. A major advantage in reading the voltage of sensors is that any universal analogue input can be used to handle this kind of signals. Alternatively, reading the charge of the sensors has also some advantages, such as the elimination of the capacitive effect of the cable, but a major drawback that each input must have a charge converter circuit and this is the reason why this approach is not popular on data acquisition systems and modular instruments. In addition, currents could be high on the cables compared with the voltage mode.

In guided wave analysis, each piezoelectric transducer acts sometimes as an actuator and other times as a sensor. This gives extra complexity to the system because the actuation and sensing architecture must be designed to handle both these operative modes. Also, care must be taken on the selection of the cables because they must handle big voltages and currents up to one Ampere (Amp). The use of very thin section cables, in fact, could be sufficient to read the signals but not to excite the piezoelectric actuators. In addition, all cables should be shielded to reduce interference between channels (crosstalk).

All these issues have been taken into account in the development of the DAQ and will be described in the following.

4.3.1 DAQ Hardware

The proposed DAQ systems is composed by:

- a PXIe-1078 9-slot chassis unit from National Instrument (NI) embedding:
- a NI controller PXIe Express-Card 8820;
- a PXI-6115 S Series Multifunction DAQ Module;
- a 5x PXIe-2529 High-Density Multi-Configuration Matrix;
- a TB-2636 Screw Terminal Block for NI PXI-2529 4 x 32 Matrix;
- an external Electromechanical Impedance measurement device (EMILIA);
- an external high voltage amplifier.

The DAQ exploits LabVIEW Full Development System and it is controlled by Matlab.

The DAQ can be used to control at least 160 piezoelectric transducers to perform the guided wave based screening. Each transducer is connected to the DAQ via proper cabling. Technically, the switching matrix will allow for dynamically selecting the transducer that will act as actuator and the ones (up to 3) which will be used as sensors to acquire the propagating waves. Thus, in the proposed architecture the DAQ operates on 4 transducers at the same time instant. Every time it is necessary to read a new group of 3 transducers, the switching matrix is reprogrammed. By means of the proposed architecture all the transducers can be controlled by the DAQ system, so that the entire network of transducers can be considered as a whole, whereas the cost of the apparatus is controlled since it's not necessary to have multiple dedicated actuating and sensing devices connected to the transducers. The DAQ is connected to an external Personal Computer with proper software (Matlab) for the signal processing and damage metrics phase (Figure 4.11).

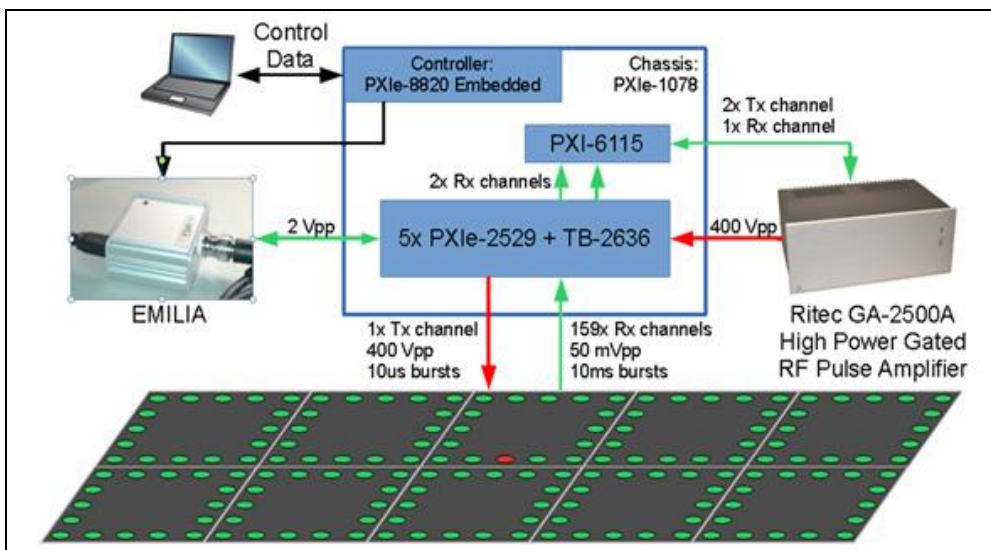


Figure 4.11: proposed DAQ architecture.

The DAQ control system integrates four main modules (Figure 4.1) an impedance analyser (EMILIA), a 6 channel acquisition card (NI TB-2708), a high voltage amplifier (RITEC) and an array of five switching matrixes.

Emilia modulus

The EMILIA (EMI) modulus, developed by FhG Institute, is used to measure the impedance of one PZT. The EMI estimation procedure has been developed to measure the piezoelectric transducer impedance as a function of the frequency in order to detect partial and/or total detachment of the transducer from the structure as well as transducer malfunctioning.

Acquisition card (NI TB-2708)

The NI TB-2708 used card has four analogue inputs (only three are used) and 2 analogue outputs. The acquisition card is responsible to control and monitor the amplifier output voltage and to read the response of the PZT's

High voltage amplifier

This device must be able to provide at least 400 V_{pp} to the transducers at a frequency of 350 kHz by delivering a current of at least 1.8 A. To this purpose an arbitrary waveforms generator from NI (PXI-6115 S Series Multifunction DAQ Module) will be used to feed a high voltage amplifier. A Ritec GA-2500A High Power Gated RF Pulse Amplifier is adopted. This one channel amplifier features an output voltage range in excess of 600 V_{pp}, an output current of 3.6 A, a slew rate of 6600 V/ μ s and a maximum RF Pulse Power of 400 kW over a full power frequency range of 30 kHz to 2.5 MHz.

The source signal used consists of a 4.5 sine cycles signal, 60 kHz central frequency, with 10V peak-to-peak tension Hanning windowed.

Switching matrix

In order to connect each transducer in the outer wing to the signal generation and acquisition equipment (DAQ), and to automate the baseline generation as well as the damage detection, a switching matrix (5x PXIe-2529 High-Density Multi-Configuration Matrix) with five TB-2636 cards switching has been employed.

The primary benefit in using a switching matrix consists in a simplified wiring since the overall test system can easily and dynamically change the internal connections path without any external manual intervention. This capability eliminates the need to duplicate instruments and thus reducing testing cost.

4.3.2 DAQ Data Storage

The acquired data will be retrieved from the DAQ system by means of a DAQ control software based on LabVIEW and Matlab. This software features a Graphical User Interface (GUI) to ease the filling of the required data (Figure 4.12). Since the GW-based methodologies are implemented in Matlab, a Matlab based Application Program Interface (API) has been developed for seamless information retrieval and automated interfacing with the stored data.

The Saristu DAQ control system is composed of three parts: the DAQ application, the control application and the remote viewers (Figure 4.12).

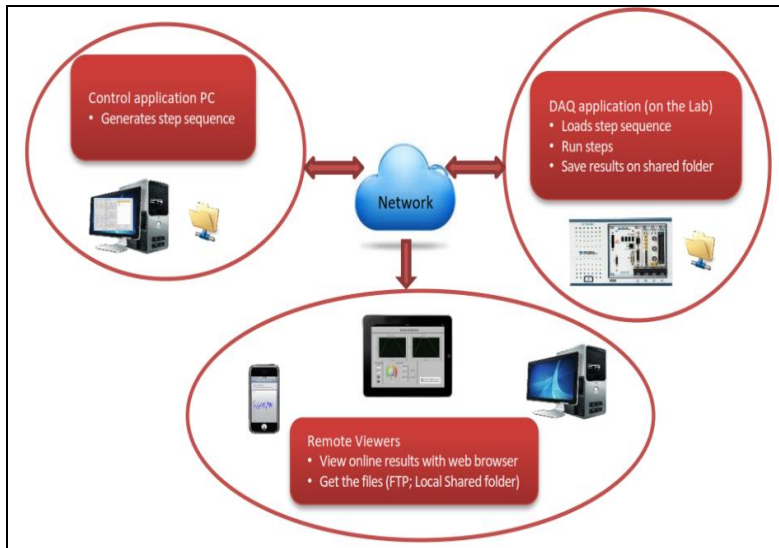


Figure 4.12: SARISTU DAQ control system

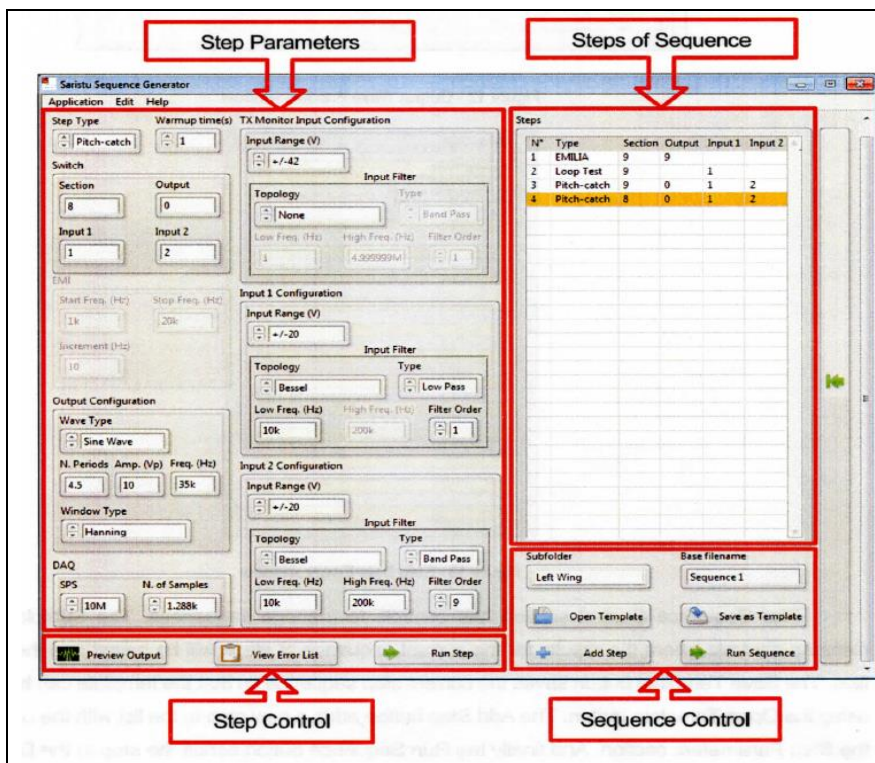


Figure 4.13: SARISTU DAQ main window

- The DAQ application is responsible to control of the hardware installed, acquiring and pre-processing all the data from the DAQ hardware.
- The control application, called Saristu Sequence Generator, allows to define the test sequence acquisition to be run on the DAQ.
- The data viewer is a WEB based page that can be viewed in a web browser (CHROME, FIREFOX...). It presents the configuration parameters, the resulting waves and the historic of the warning messages of the last acquisition step. The data files created from each acquisition step can be accessed remotely via a network shared folder on the computer running the DAQ application.

The application main window is show in Figure 4.13, indicating different sections of the application. This window has the information of the last acquisition step, status of the DAQ system and a list of messages. In the section Step Parameters, the user can see the configuration of the last acquisition step and a warning for each of the input channels.

The Status section displays the current hour, an indicator signaling if the application is running or not an acquisition step or not, and the sequence number of the last step.

In the Graphs section is shown the results for the last step.

The resulting data acquisition file is a tab separated text file using the system decimal separator. In the top of the file are a set of parameters used on the acquisition step followed by the results of the measurement.

The output filename will depend on four parameters, the filename, the step number within the sequence, the step type and a four-digit number. The resulting filename will be “Base filename”_“four digit number”_“Step number”_“step type”.txt. The parameters for the file name are as follows:

- Base filename — This is defined in the Base Filename parameter of the configuration window.
- Four-digit number — The next available number within the selected folder.
- Step number — Step number in the sequence.
- Step type — Step type. Will add “pc” for pitch-catch, “lp” for loop test and “emi” for EMILIA.

4.4 Damage scenario

As already mentioned in the previous section 4.2.3, the LWP sensors distribution, for each group and for each bay, was defined taking into consideration impact locations (Figure 4.5 & 4.6). The LWP thickness analysis has showed slightly different thickness values from those measured on the preliminary test articles LWP like, namely ramp panel specimen (10, 8 and 6 mm tick) (see section 3.11), with an inhomogeneous distribution inside each bay. The identified thickness values (12.5 mm, 10 mm, 8.3 mm and 6.4 mm) and their distribution on LWP are represented in the following figure (Figure 4.14).

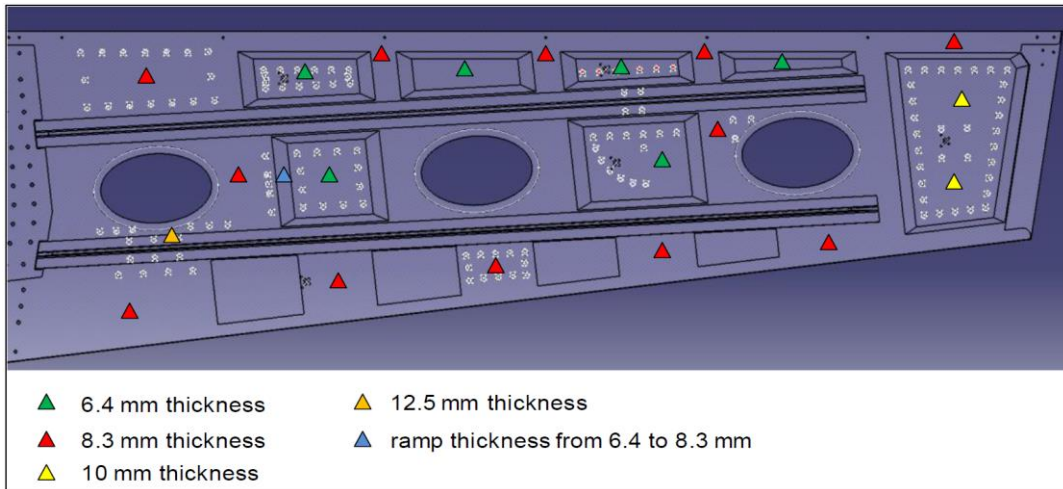


Figure 4.14: LWP Thickness distribution

The different test article constrain system, the inhomogeneous distribution and the slight thickness differences compared with the ramp panel suggested to perform impact energy calibration tests starting from the impact energy values identified in the ramp panel tests (see 3.11).

To this purpose four impact tests areas have been identified on the LWP surface (Figure 4.15) and an energy range (about +/- 20J) has been suggested for the calibration tests starting from ramp panel impact energy values.

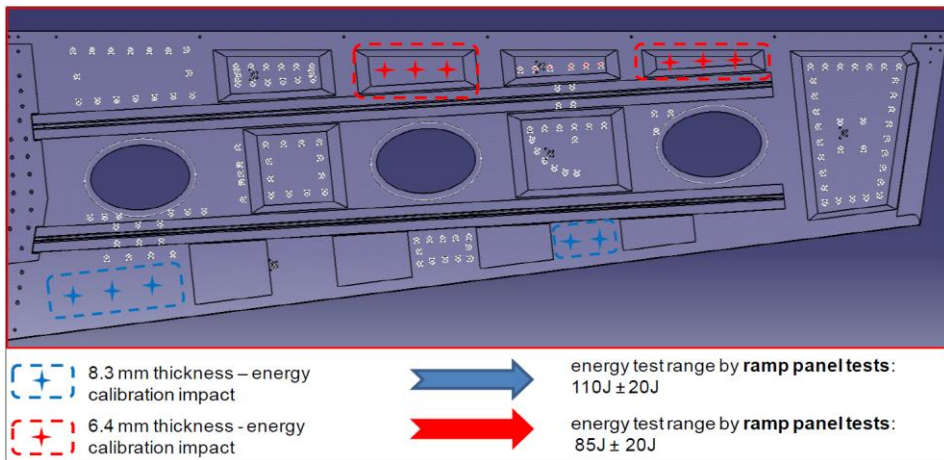


Figure 4.15: LWP impact energy test Calibration areas



Figure 4.16: LWP impact energy test calibration

4.4.1 Ground test demonstrator impact survey

Multiple impacts have been imparted on the outer side of the LWP, in its final assembly on wing box ground demonstrator (Figure 4.16), in order to evaluate the structure response through the SHM system and a traditional non-destructive testing assessment of the imparted damages has been effectuated. Impact tests have been first carried out on the free sensors calibration areas in order to calibrate the BVID energy threshold for the 6.4 and 8.3 mm thickness identified on the LWP.

After impact energy calibration, scheduled impacts have been imparted inside each sensorized bay area (see LWP Sensors tags and potential impact points, Figure 4.5 & 4.6). Each impact has been inspected with non-destructive ultrasonic C_scan in order to detect damage presence and to evaluate delamination area dimensions (Figure 4.17). The impacts have been made orthogonally to the bottom side of the test article and the impact gun was equipped with a hemispherical nose 1 inch in diameter.

The experimental calibrated energy found are:

- 60 J for 6.4 mm thickness;
- 80 J for 8.3 mm thickness;
- 120 J for 10 mm thickness.



Figure 4.17: LWP damages NDT assessment by Olympus C_scan

4.4.2 LWP calibration impacts NDT inspection

In the following the LWP calibration impacts assessment performed by Unina researchers with NDT device Olympus Omniscan SX (Figure 4.18, 4.19, 4.20, 4.21, 4.22).

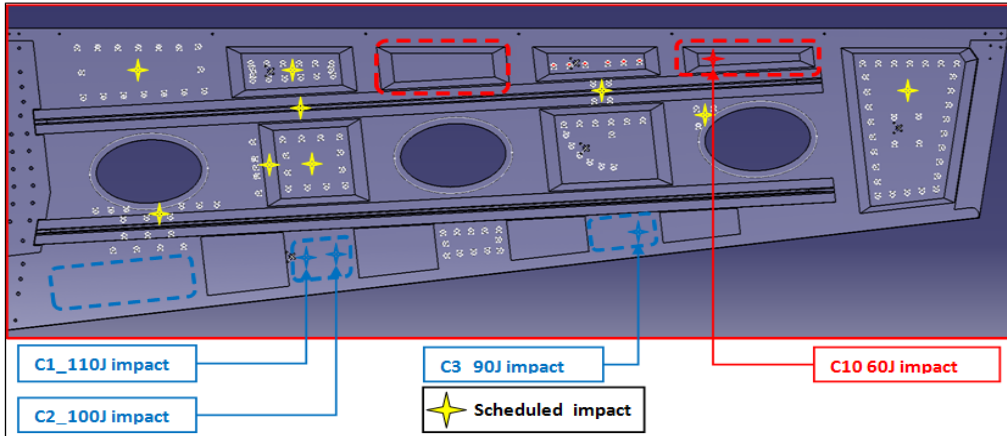


Figure 4.18: LWP calibration impact positions and energies (8.3 and 6.4 mm thickness)

C1 110 Joule calibration impact:

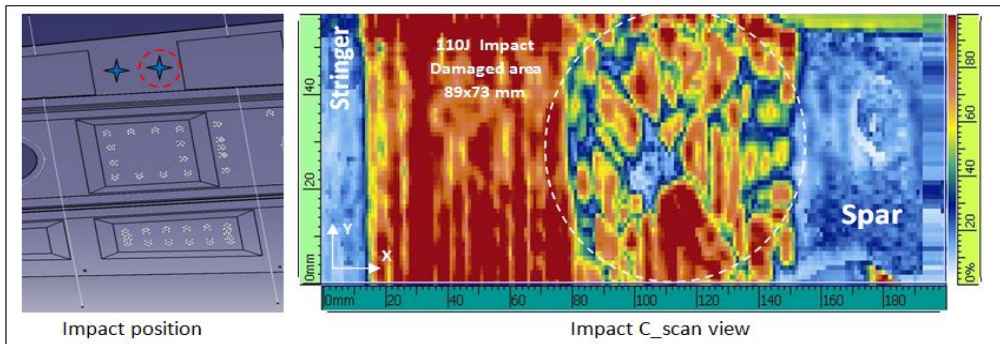


Figure 4.19: LWP 110J impact NDT evaluation

C2 100 Joule calibration impact:

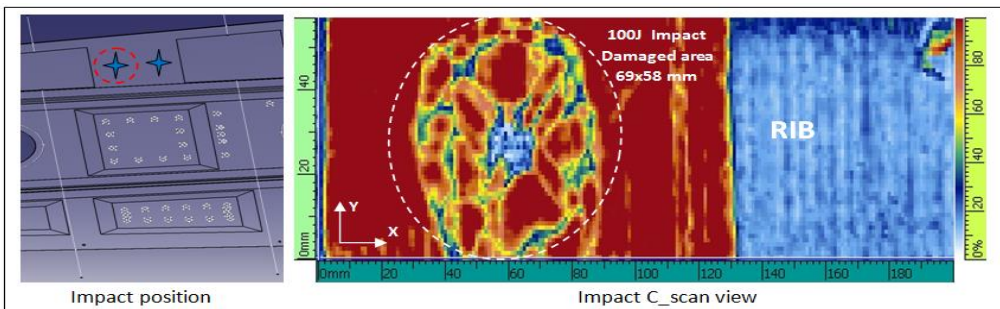


Figure 4.20: LWP 100J impact NDT evaluation

C3 90 Joule calibration impact:

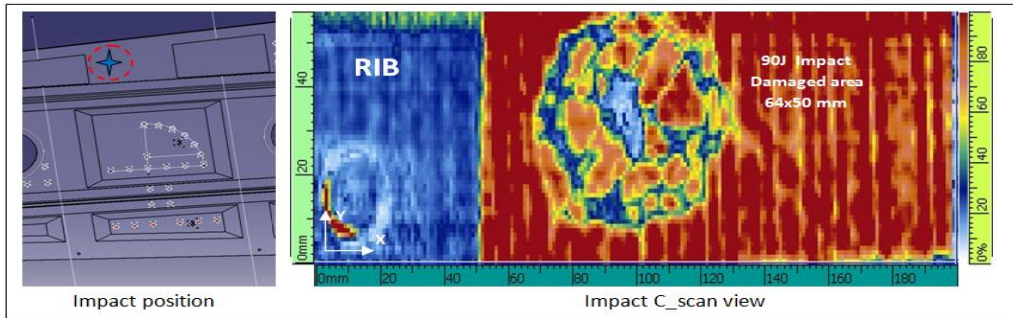


Figure 4.21: LWP 90J impact NDT evaluation

C10 60 Joule calibration impact:

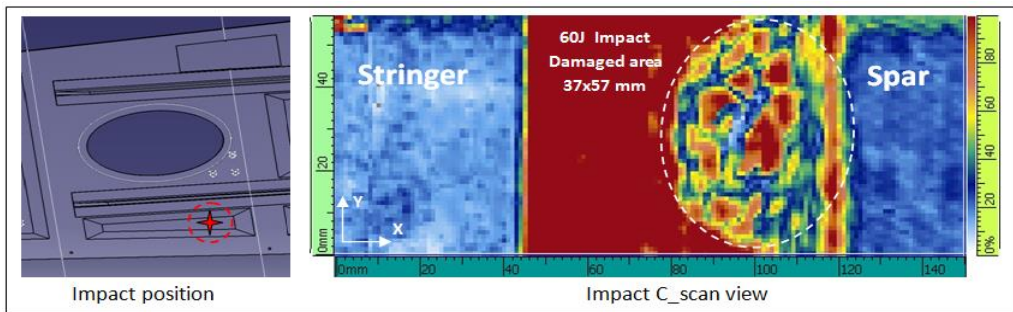
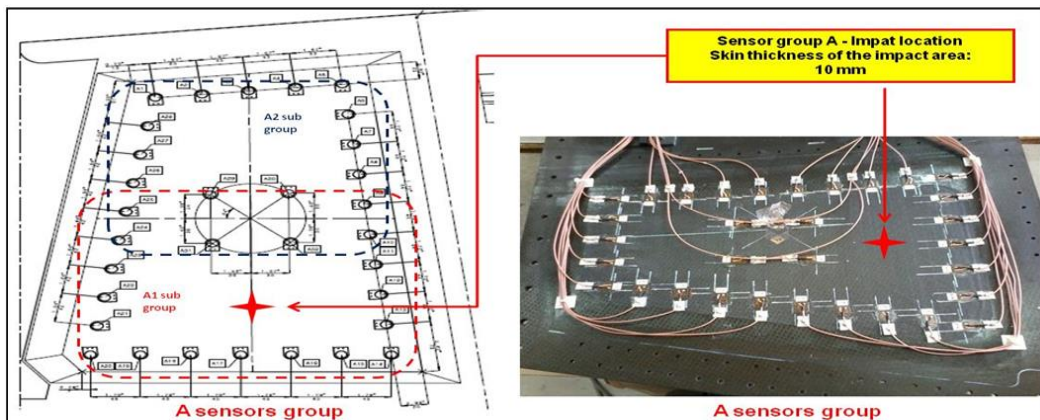


Figure 4.22: LWP 60J impact calibration NDT evaluation

4.2.3 LWP scheduled impacts NDT inspection

Listed below the NDT inspection of scheduled impact imparted inside bays sensors configuration collected in group or sub-group (groups: A, B, C, D1, D2, E1, E2 – see section 4.2.3 Figure 4.5).

A group impact inspection: central position with respect to A1 sub group sensors (impact energy 130J).



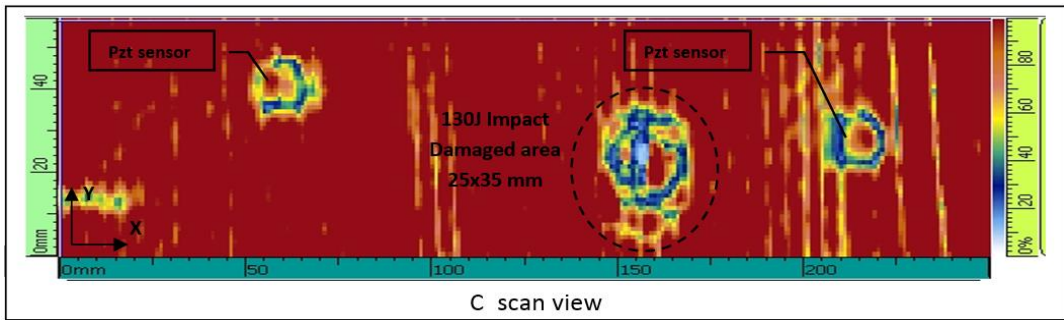


Figure 4.23: LWP A sensor group impact NDT inspection

B group impacts inspection: under stringer web (impact_1 - 120J) and close to corner of the inspection hole (impact_2 - 80J).

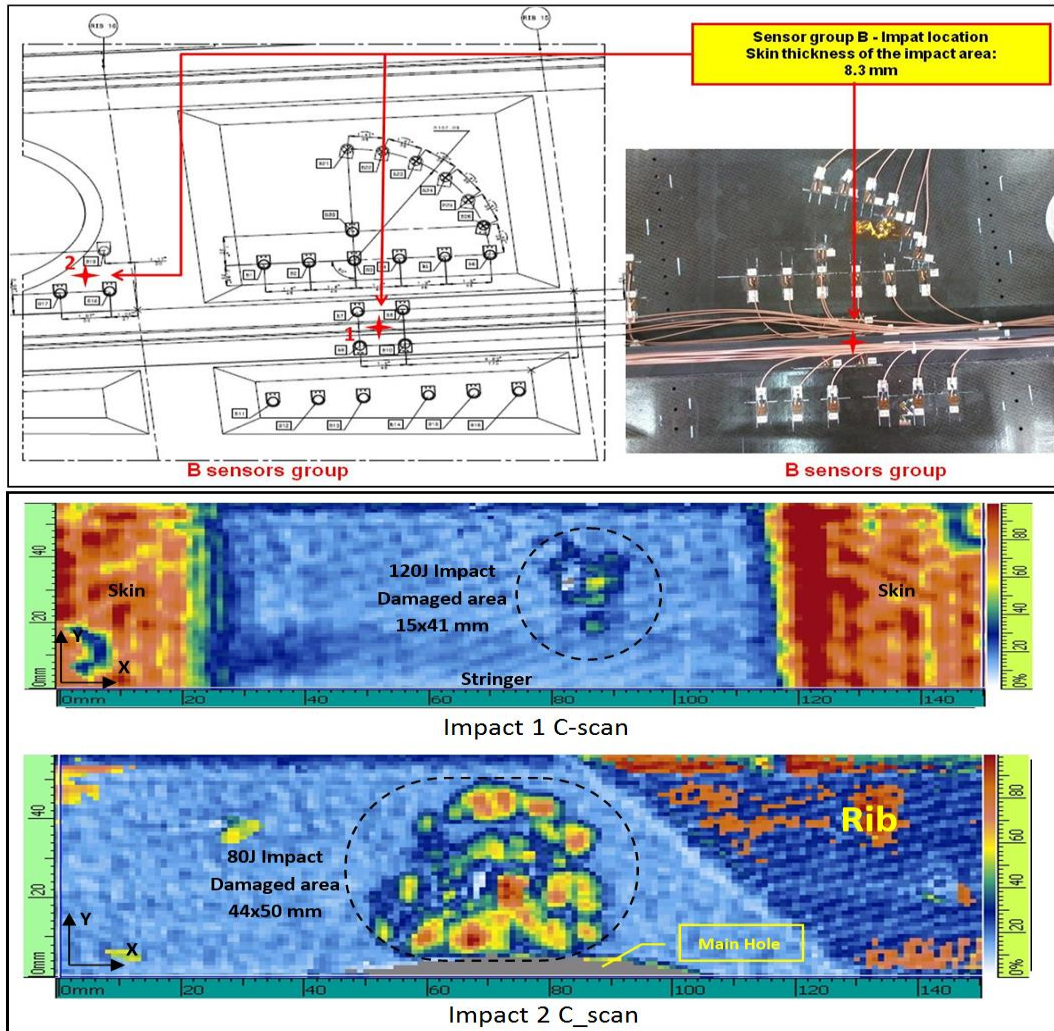


Figure 4.24: LWP B sensors group impacts NDT inspection

C group impact inspection: central position (energy 80 J).

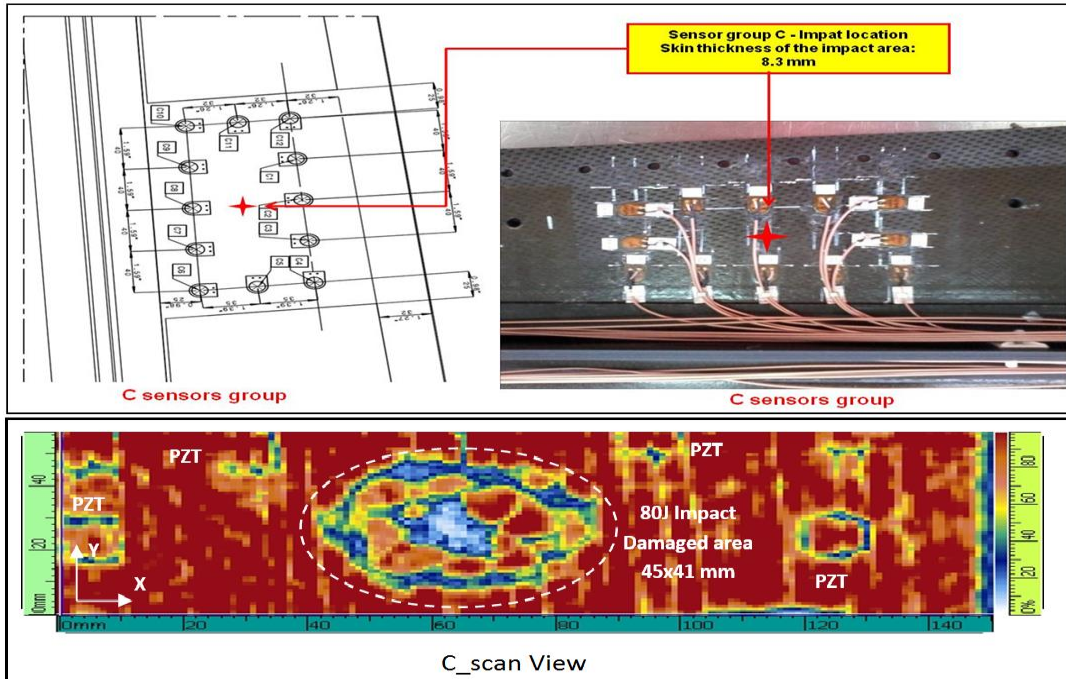


Figure 4.25: LWP C sensors group impact NDT inspection

D1 sub group impacts inspection: central position with respect to the subgroup D1 (impact_1 - 60J) and central position with respect to the thickness ramp (impact_2 - 70J).

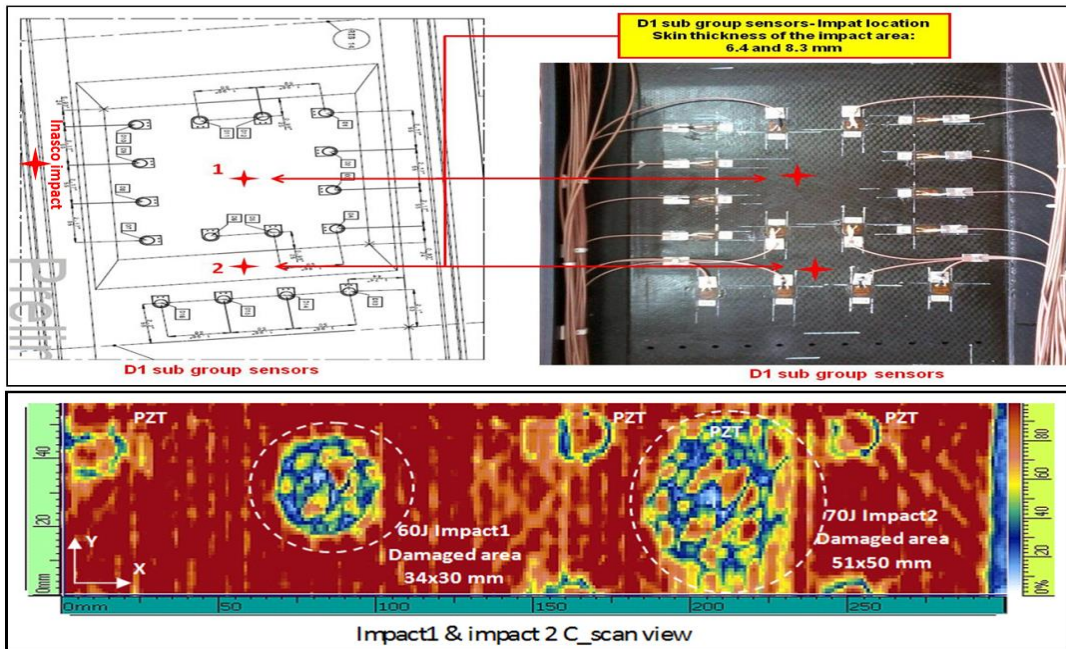


Figure 4.26: LWP D1 sensors sub-group impacts_1 and impact_2 NDT inspection

D2 sub group impact inspection: central impact (energy 60J) and Inasco under stringer web impact (energy 120J).

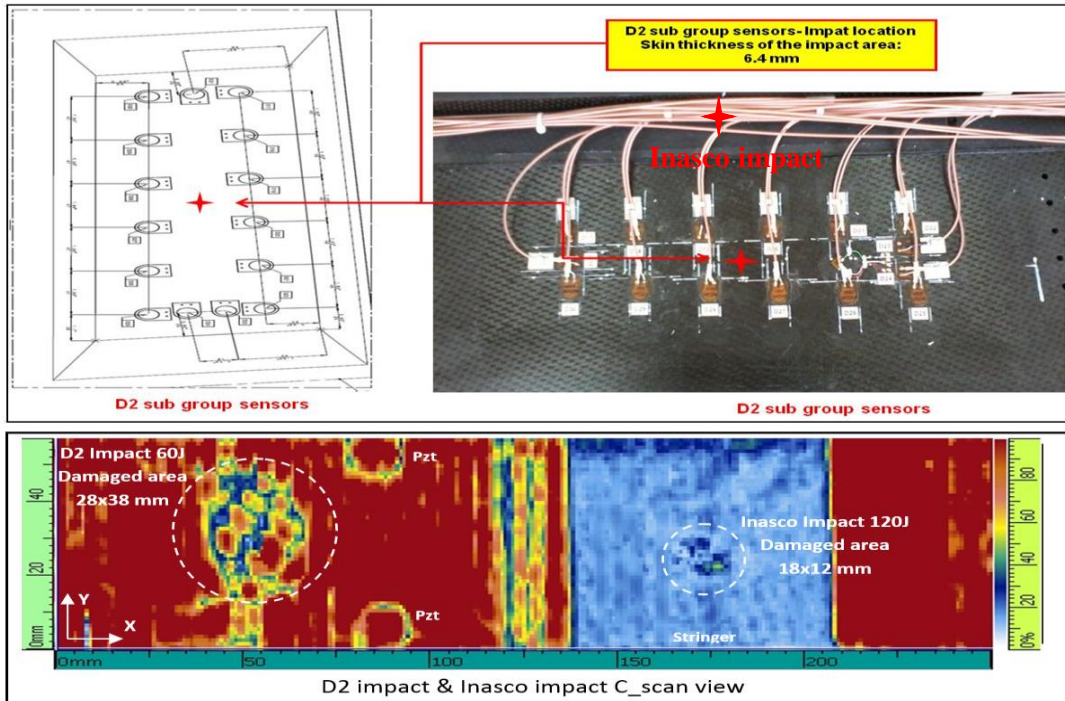


Figure 4.27: LWP D2 sensors sub-group impact NDT inspection

E group impact inspection: central position impact (energy 95J).

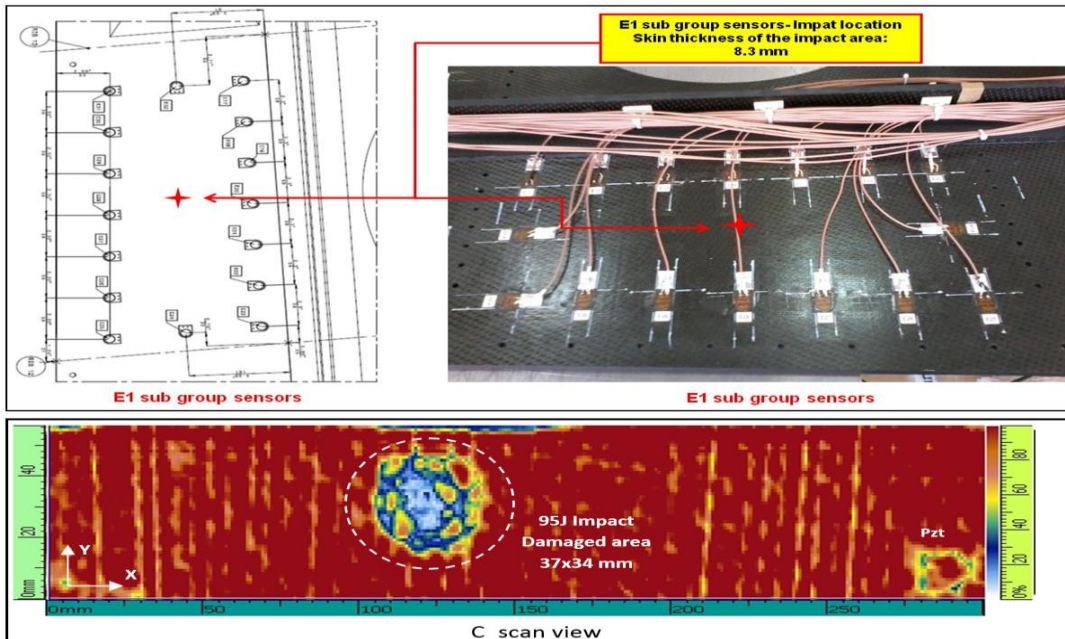


Figure 4.28: LWP E1 sensors sub-group impact NDT inspection

E group impact inspection: under stringer foot (internal side of subgroup E2 - impact energy 80J).

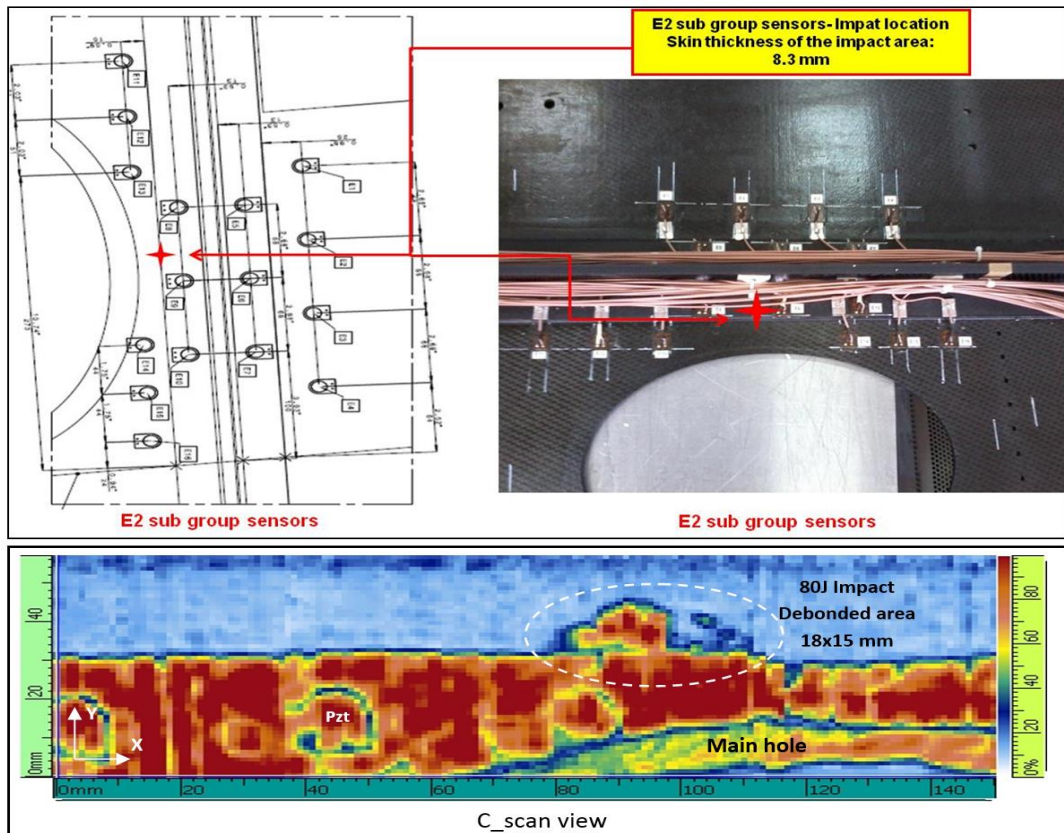


Figure 4.29: LWP E2 sensors sub-group impact NDT Inspection

4.5 SHM system data acquisition

The ground test was performed in different phases. For what concerns the PZT-based SHM, the test was subdivided into three different phases.

During the first phase, as soon as the strongback required for holding the wingbox was ready, the wingbox was suspended in floating condition by means of its own fixtures (Figure 4.30) as the elastic properties of the test article were enough to guarantee the orthogonally to the strongback (maximum deflection at tip was measured to be less than 5mm). The DAQ system was then be reassembled, placed on its final position with respect to the test article, and tested: no faults were found neither in the software nor in the hardware. The terminal blocks employed to connect the PZT sensors to the DAQ were tested in order to check for faults occurred during or before the final assembly stages. Two sensors were eliminated from the pool due to damages occurred to the piezos, while another has been dropped because a cut-off in the cables causing a short.



Figure 4.30: wingbox demonstrator in floating condition

Once the system passes all electrical, HW and SW tests, EMI pristine baseline was acquired in two different sets: one for the low frequency, acoustic range (1k-20kHz) and one for the high frequency, ultrasound range (20k-100kHz). EMI measurements highlighted different static loads on the piezos. This is most probably due to the fact that calibration measurements were taken when LWP was positioned on a table before its final assembly, while first baseline measurements were taken in floating condition on a stiffened test article by spar and rib installation. Guided waves group velocity profile was then recorded exploiting pitch-catch configuration using at least two different paths for each bay in the frequency range 50k-350kHz. Finally, the pitch-catch pristine baseline for the tomographic method was acquired for the 50kHz to 100kHz frequencies range with steps of 10kHz. Once the pristine baseline recording was completed, the DAQ system has been disassembled.

The second phase occurred in the time lapse between the mechanical stress tests campaign and the impact session. The stress tests saddles were dismantled and actuators detached and folded below the wingbox; the wingbox itself was again suspended in floating condition by means of its own fixtures. The DAQ system was then reassembled and tested: no faults were found neither in the software nor in the hardware. All the PZT sensors were then checked against disbonding by acquiring an EMI second baseline and comparing it with first EMI baseline. No sensor was found debonded: capacitive and resistive measurements were comparable to first baseline with a deviation of 2% or less with few exceptions.

Guided waves group velocity second profile was then recorded exploiting pitch-catch configuration using the same configuration of the first group velocity profile, in order to assess for material properties alterations due to mutated environmental conditions. A slight variation due to a decreased room temperature was observed. Finally, the pitch-catch second baseline for both tomographic method was acquired for frequencies from 50kHz to 100kHz with steps of 10kHz. Acquired data were compared with the pristine baseline: alteration of the scattering field was observed and tested thoroughly by means of an Olympus C-Scan machine. The alteration was found to be due to deformations in the copper net forming the anti-lightning protection layer.

Once the second baseline recording was completed the wingbox underwent impacts on different locations.

The third and final phase occurred as soon as the impact session was terminated. All the PZT sensors have been checked against disbonding by acquiring EMI SHM profiles and comparing it with second EMI baseline. No sensor was found debonded: capacitive and resistive measurements were comparable to pristine baseline with a deviation of 5% or less. Capacitive deviations in excess of 2% were recorded and are most probably due to the impacts imparted to the test article in each bay.

Group velocity third profile was then recorded exploiting pitch-catch configuration using the same configuration of the pristine group velocity profile, in order to assess for material properties alterations due to mutated environmental conditions or impacts. Several variations in the anisotropy profiles were observed in the bays whose sensors are closer to the impacts. Finally, the pitch-catch SHM third profile for tomographic method was acquired for frequencies from 50kHz to 100kHz with steps of 10kHz in order to assess and locate damages generated by the impacts.

4.6 Guided wave based Graphic User Interface (GUI)

The pitch-catch data sets, downloaded from DAQ system, have been then analyzed by tomographic method implemented in an Interactive Graphical User Interface (GUI) [1], developed in Matlab® environment, including a multi parameter damage algorithm integrated with a material characterization utility as well. Experimental and/or numerical data can be processed by means of structured algorithms in a fast processing and then used to reconstruct a damage maps. With an advanced geometric tool, any complex structure can be investigated by means of a specific txt file containing geometry vertices coordinates.

The main GUI interface (Figure 4.31), able to present a fast overview of the obtained results at the end of signals elaboration, allows the user, by functional buttons, to easily recall all the different parameter SHM methodologies implemented, namely, Signal Energy Level or Transmission Factor evaluation as well as wave propagation velocities elaboration by Short Time Fourier Transform.

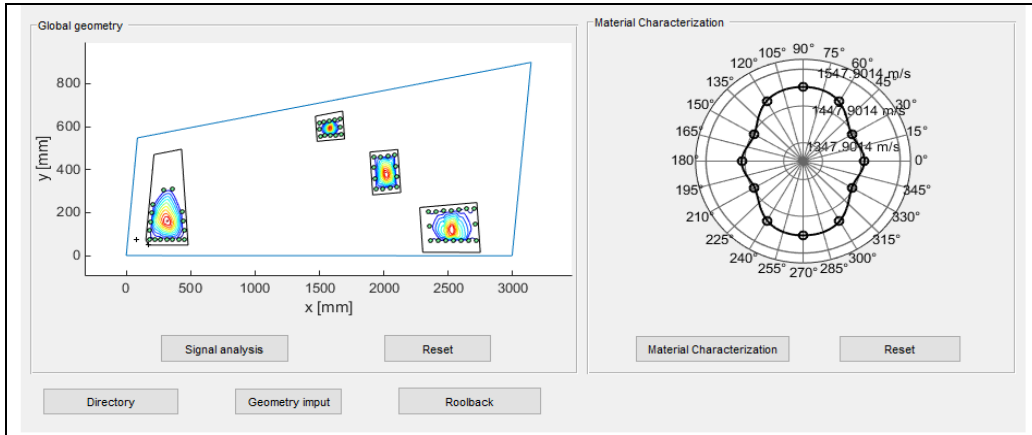


Figure 4.31: Interactive Graphical User Main Interface

4.6.1 Signal analysis GUI sub interface

Three different parameters are analyzed to determine the damaged area: Signal Energy Level, Time of flight and Transmission factor. The monitoring is then operated through a signal interrogation (Figure 4.32).

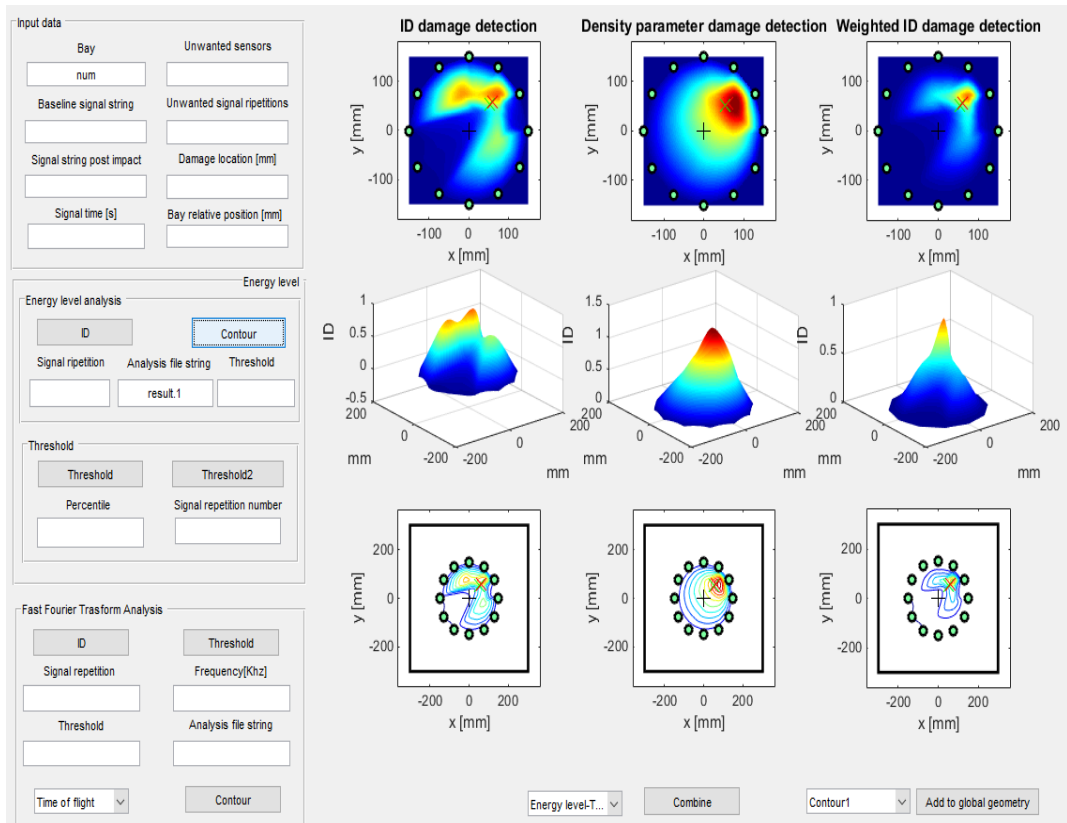


Figure 4.32: multi parameter signal analysis GUI sub interface

As fully described in previous chapter, DI (damage index) formulation is computed for each sensor pair and provides the comparison between the current state and the baseline one. Comparing the result with a specific threshold level each path is classified as healthy or damaged.

The intersections of the damaged paths define the nodes that compose the damage grid [5]. For each node a damage index is calculated by averaging the ones belonging to the intersecting paths.

These “damaged nodes” can be calculated though the two ID buttons present in the signal analysis GUI sub interface (Figure 4.32). The one linked to the signal intensity analysis will create a xlsx file in which specific information will be stored; the one linked to the FFT analysis create the same xlsx file for both the time of flight and the transmission factor parameters. All the xlsx files contain the information arranged in a specific format (Figure 4.33).

Report File				
x	y	z(DI)	threshold	z'(DI-threshold)
0	150	0	0	0
20.09619	225	0	0	0
75	279.9038	0	0	0
150	300	0	0	0
225	279.9038	0	0	0
279.9038	225	0	0	0
300	150	0	0	0
279.9038	75	0	0	0
225	20.09619	0	0	0
150	0	0	0	0
75	20.09619	0	0	0
20.09619	75	0	0	0
150	150	0	0	0
153	199	0.66245	0.39	0.27245
214	216	0.62348	0.39	0.23348
246	226	0.71334	0.39	0.32334
252	228	0.74165	0.39	0.35165
255	216	0.71049	0.39	0.32049
265	208	0.55716	0.39	0.16716
257	202	0.58547	0.39	0.19547
216	178	0.505	0.39	0.115
267	169	0.6596	0.39	0.2696

Annotations in the figure:

- Piezo**: Points to the first 18 rows of the table.
- Damaged nodes**: Points to the last 10 rows of the table.
- Optional**: Points to the last 5 columns of the table.
- N.B.: Select the opportune column**: Points to the 'z'(DI-threshold)' column.
- Original index of Damage**: Points to the 'z(DI)' column.
- Estimated Threshold**: Points to the 'threshold' column.
- Scaled index of Damage**: Points to the 'z'(DI-threshold)' column.

Figure 4.33: Format file of the xlsx file created by the ID script containing information obtained from the “ID” script that can be processed to obtain a graphical representation.

Three input are required for this script: the specified step repetition, the name with which save the, afore mentioned, xlsx file and the threshold level that can be casually given or obtained through the GUI. Specific to the time of flight parameters and the transmission factor is the input frequency. This because the two parameters are obtained by analyzing the signal Fast Fourier transform. In particular, the time of flight (ToF) parameter is evaluated as the time values at which the Fourier transform reach it max, while the

transmission factor can be considered as the ratio between the receiver and actuator Fast Fourier transform max value.

Energy levels data are obtained as:

$$energy\ level = \int_0^t s_p^2 dt \quad (4.1)$$

where s_p is the signal intensity at the specific time. Since the collected data are clearly a discrete set of values, the energy level are calculated as a summation.

The threshold evaluation function (Figure 4.32) for energy level allows the user to implement two different methods to quantify the noise for the intensity parameter: the first one is obtained by assuming a normal distribution of signal noise, the second one by working on the mean values and error of the signal energy level.

Energy level threshold

The first threshold value, obtained by assuming a normal distribution of signal noise as already discussed in the section 3.11 of previous chapter, is defined as:

$$l_{th_{ij}} = \mu_{ij} + k * \sigma_{ij} \quad (4.2)$$

where μ_{ij} is the estimated mean value and σ_{ij} the estimated standard deviation of a $n(n-1)$ population, where n is the signal repetition number, the k values define the confidence bounds and depends on the significance level chosen.

The final Threshold can be obtained as:

$$Threshold = \max(l_{th_{ij}}) \quad (4.3)$$

$$Threshold = \frac{\sum_{i=1}^s \max(l_{th_{ij}})}{s} \quad (4.4)$$

$l_{th_{ij}}$ is the threshold level obtained from equation above for the receiver j -th and i -th actuator sensor, s is the sensors number.

In the following Figures 4.34 and 4.35 are presented the typical energy levels and sensibility indexes for all signal repetition related to each receiver and for a fixed actuator sensor. In the Figure 4.36 are showed the averaged sensibility indexes for each receiver related to a fixed actuator. The displayed histograms give a useful device in detecting the quality of the signal repetition or acquisition. The threshold values obtained from Eq. 4.3 and Eq. 4.4 are displayed through a message box (Figure 4.36 upper right).

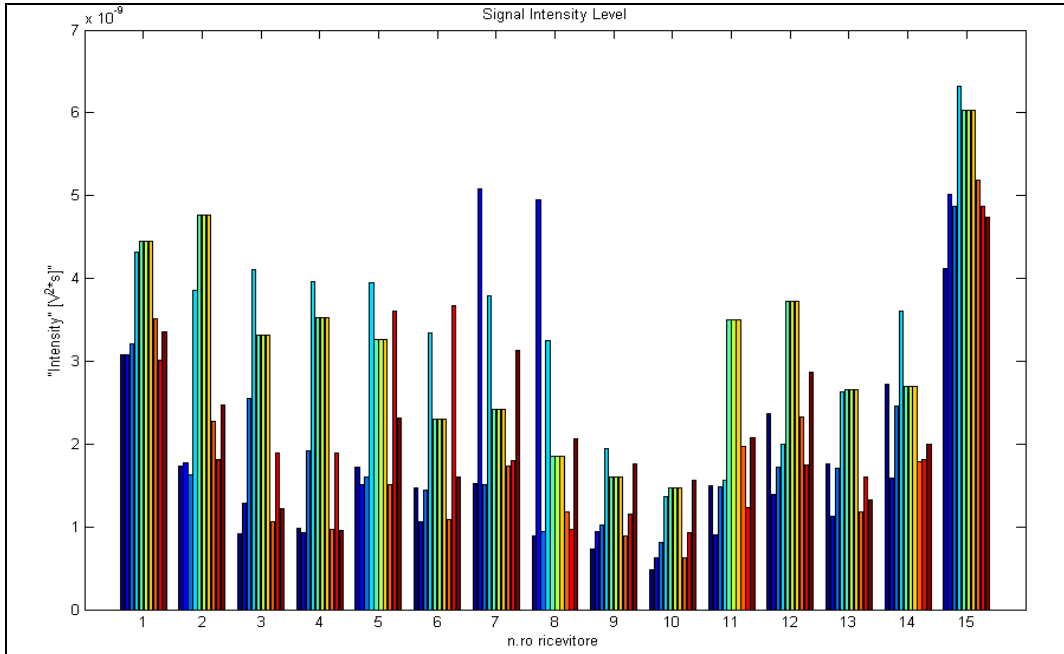


Figure 4.34: Signal intensity level for each repetition of a specific actuator signal (16th)

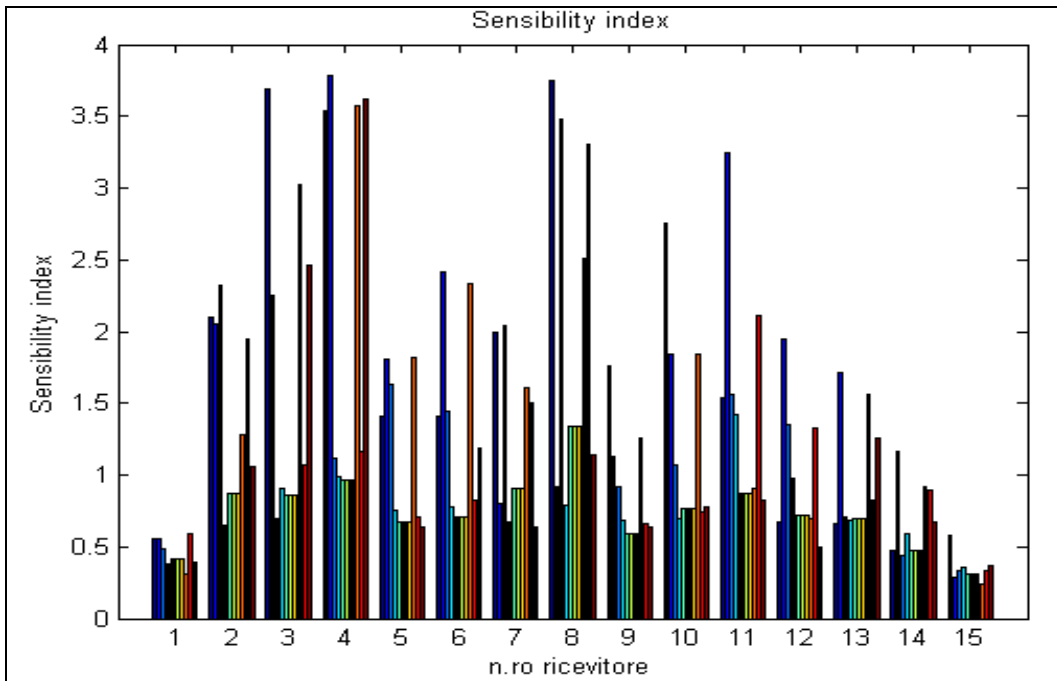


Figure 4.35: Sensibility indices for each repetition of a specific actuator signal (16th)

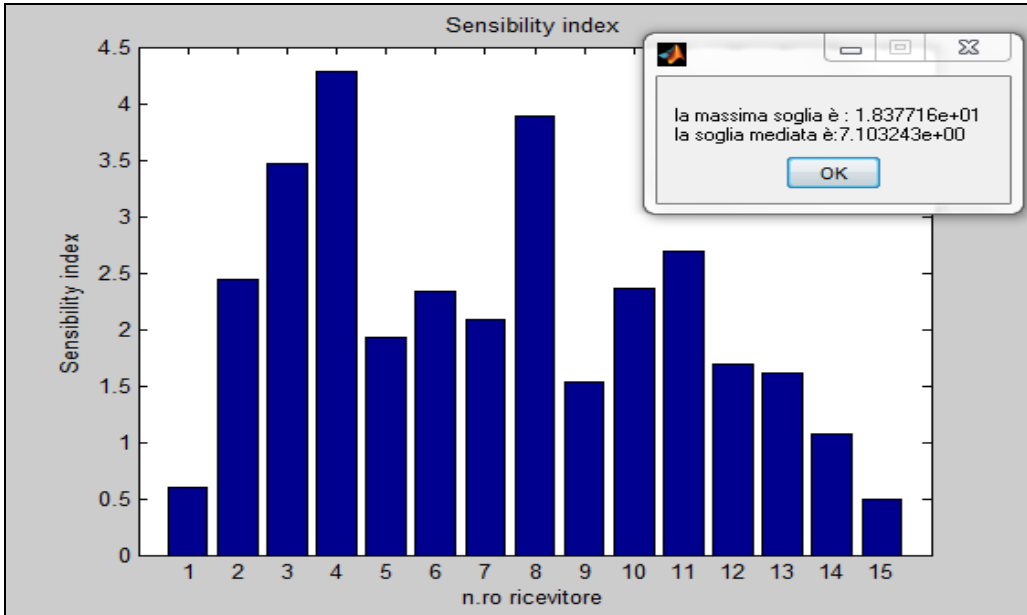


Figure 4.36: (upper right) estimated threshold values, (bottom) receiver sensibility indexes for fixed actuator sensor.

The second method to quantify the noise, linked to *Threshold2* button, has been implemented for the eventuality in which the signal repetitions are not enough similar to each other. This practically means that the values obtained with the previous threshold evaluation are totally wrong.

Various threshold values are calculated; it is expected that only some of them are able to better quantify the noise. Fundamental, in this threshold definition, is the error committed by deviating from the normal distribution hypothesis:

$$error = \frac{\sigma}{\sqrt{n}} \quad (4.5)$$

The five value are calculated considering the following formulations:

$$\frac{\sum \mu}{s(s-1)} + \max(error) \quad (4.6)$$

$$\frac{\sum \mu}{(s-1)} + \frac{\sum error}{(s-1)} \quad (4.7)$$

$$\frac{\sum \mu}{(s-1)} + \max(error) \quad (4.8)$$

$$\max \left(\frac{\sum \mu}{(s-1)} + \frac{\sum error}{(s-1)} \right) \quad (4.9)$$

$$\max \left(\frac{\sum \mu}{(s-1)} + \max(error) \right) \quad (4.10)$$

Apparently two of these five values define a range, while the other three are concentrated around the possible threshold value. However, a little tweaking is needed to obtain a clean graphical representation.

Time of Flight or Transmission Factor thresholds

Thresholds are obtained by considering the difference of the ToF or TF in reciprocal path (example path 2-1 and path 1-2). For each parameter, starting from a population of $s*(s-1)$ signals, the absolute maximum value (Eq. 4.11) and the mediated one (Eq. 4.12) are evaluated.

$$Threshold = \max \left(\frac{TOF_{ij} - TOF_{ji}}{TOF_{ij}} \right) \quad (4.11)$$

$$Threshold = \left(\frac{\sum_{i,j=1}^s \frac{TOF_{ij} - TOF_{ji}}{TOF_{ij}}}{s^2 - s} \right) \quad (4.12)$$

Obviously, Eq. 4.11 and Eq. 4.12 can be equivalently applied to the Transmission Factor parameter.

Contour Function

The “Contour” button allow the user to process the *xlsx* file created through the ID analysis to obtain a graphical representation of the damaged area. The graphical representation can be a color map, a surface or a contour, however different methods are employed to obtain them:

- the ID damage detection (section. 1 of Figure 4.37) is obtained by simply considering the damage index associated to each damaged node.
- the Density parameter damage detection (section. 2 of Figure 4.37) is obtained by considering the node density parameter calculated with the following Eq. 4.13:

$$density_i = \frac{\left(\frac{1}{\sum_{j=1, j \neq i}^n dist(i, j)} \right)}{\max(density_i)} \quad (4.13)$$

where (i, j) represent a specific damaged node. Obviously, as many nodes are concentrated in a given area greater the associated density will be.

- the Weighted ID damage detection (section 3 of Figure 4.37) is obtained by weighting the damaged index associated at each nodes with the density parameter (Eq. 4.14). Where W_{ID_i} is the weighted damage index of the i-th node.

$$W_{ID_i} = ID_i \cdot density_i \quad (4.14)$$

Finally, in order to improve the damage detection accuracy, the Combine Contour Function (Figure 4.37 bottom center) allows the user to perform a graphical multi-parameter analysis consisting in a graphical overlapping of the different damage reconstructions.

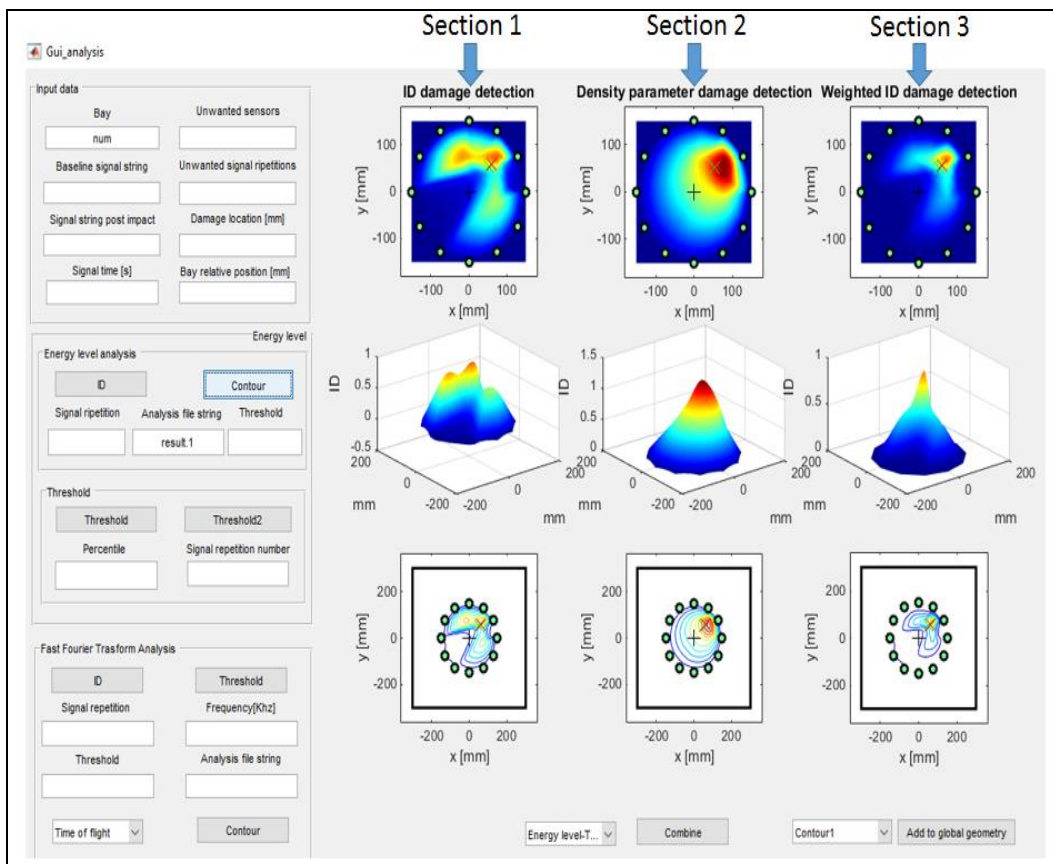


Figure 4.37: Different damage graphical reconstruction by Contour Function

4.6.2 Material Characterization GUI sub interface

As asserted at the beginning of this section, the Interactive Graphical User Interface (GUI) is equipped with a material characterization utility aimed to estimate the material's wave propagation characteristics.

Based on Fast Time Fourier Transform method, signals analysis is implemented in order to obtain the frequency tuning and the group velocity dispersion curves for a fixed material direction (Figure 4.38). Multi direction dispersion curves data are then gathered in a group velocities polar plot.

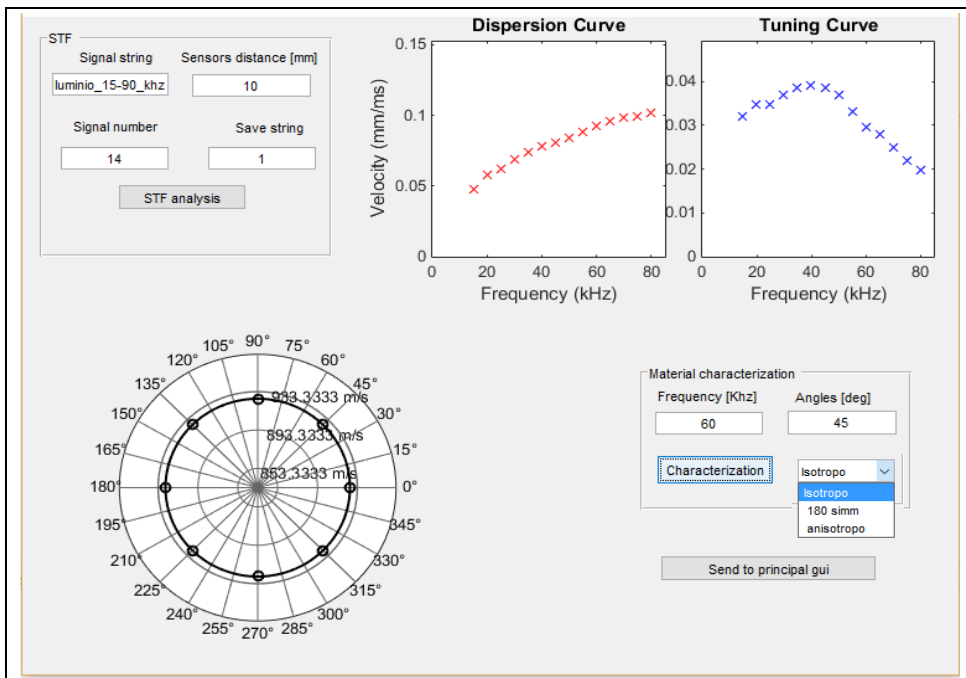


Figure 4.38: Material characterization dedicated GUI sub interface

Fundamental for the STFT analysis are the input data that have to be arranged in a specific txt file (Figure 4.39). The first column of the txt file contains information about the time vector, the second about the source sensor signal and the third about the receiver signal. The third row contain information about the signal frequency only in the receiver columns. The specific sensors setup, both in an experimental set up or numerical simulation, need only a couple of sensor set in a specific direction and at an appropriate distance. Needed input for the script are the signal file string, sensors distance, number of different signal frequency contained in the txt input file, and the save file string name (Figure 4.38 upper left). This latter also has a specific format (Figure 4.40) and must be saved with a specific name carrying sensors heading angle information.

	Time	Receiver									
	A	B	C	D	E	F	G	H	I	J	K
1	x-axis	Source 1	Receiver 1	Source 2	Receiver 2	Source 3	Receiver 3	Source 4	Receiver 4	Source 5	Receiver 5
2	second	Volt	Volt								
3	0	0	15	0	20	0	25	0	30	0	35
4	0	-0.02539	-0.0008	-0.03516	-0.0002	-0.03516	0.000156	-0.03516	0.000273	-0.03516	-2E-05
5	0.000001	-0.02539	-0.0008	-0.03516	-9.8E-05	-0.03516	0.000234	-0.03516	0.000332	-0.03516	-5.9E-05
6	0.000002	-0.02539	-0.00086	-0.03516	-0.00012	-0.03516	0.000195	-0.02539	0.000215	-0.03516	-0.00012
7	0.000003	-0.02539	-0.0007	-0.02539	-0.00018	-0.02539	0.000137	-0.02539	0.000215	-0.01563	-7.8E-05
8	0.000004	-0.02539	-0.00078	-0.02539	-0.00014	-0.01563	0.000215	-0.00586	0.000352	0.003906	-3.9E-05
9	0.000005	-0.02539	-0.00088	-0.01563	-0.00012	-0.00586	0.000215	0.013672	0.000273	0.033203	-9.8E-05
10	0.000006	-0.01563	-0.0008	-0.00586	-0.00016	0.013672	0.000156	0.042969	0.000215	0.072266	-7.8E-05
11	0.000007	-0.01563	-0.00076	0.003906	-0.00012	0.033203	0.000137	0.072266	0.000313	0.111328	-7.8E-05
12	0.000008	-0.00586	-0.0008	0.023438	-0.00012	0.0625	0.000215	0.111328	0.000273	0.160156	-5.9E-05
13	0.000009	0.003906	-0.0008	0.042969	-0.00012	0.091797	0.000195	0.150391	0.000215	0.189453	-9.8E-05
14	0.00001	0.013672	-0.00088	0.0625	-0.00012	0.121094	0.000156	0.189453	0.000313	0.21875	-3.9E-05
15	0.000011	0.033203	-0.0007	0.091797	-0.00016	0.160156	0.000195	0.208984	0.000254	0.208984	-5.9E-05
16	0.000012	0.042969	-0.00076	0.111328	-0.00016	0.189453	0.000195	0.21875	0.000254	0.179688	-7.8E-05
17	0.000013	0.0625	-0.00096	0.140625	-7.8E-05	0.208984	0.000215	0.208984	0.000254	0.111328	-7.8E-05
18	0.000014	0.082031	-0.0008	0.169922	-0.00016	0.21875	0.000176	0.179688	0.000273	0.003906	-5.9E-05
19	0.000015	0.091797	-0.00072	0.189453	-0.00018	0.21875	0.000156	0.130859	0.000352	-0.13281	-9.8E-05

Figure 4.39: xlsx version of the txt file needed for the Fast Time Fourier Transform.

	A	B	C	D	E	F
1	Frequenza	Ampiezza	Velocità [mm/ms]	Distanza	Wind	Lunghezza
2	15	0.031992	1184.6	100	75	559
3	20	0.034805	0.574712644	100	75	495
4	25	0.034727	0.621118012	100	70	378
5	30	0.036758	0.694444444	100	70	347
6	35	0.038418	0.735294118	100	70	351
7	40	0.039004	0.769230769	100	65	320
8	45	0.038418	0.81300813	100	65	310
9	50	0.036895	0.840336134	100	55	271
10	55	0.033027	0.884955752	100	55	273
11	60	0.02959	0.925925926	100	50	233
12	65	0.027793	0.961538462	100	45	252
13	70	0.024961	0.980392157	100	40	258
14	75	0.021973	0.99009901	100	40	250
15	80	0.019687	1.020408163	100	30	240
16	85	0.0175	1.030927835	100	20	237
17	90	0.015117	1.052631579	100	15	204
18						

Figure 4.40: Xlsx file containing the resulting information of the Fast Time Fourier Transform analysis

4.6.3 GUI results

Interesting results have been obtained by analyzing the pitch-catch data by means of the tomographic method implemented in the Interactive Graphical User Interface. In particular, the different graphical damage reconstruction methods have been performed on the A1, C, D and E1 bays or sub bays (ref. Figure 4.5). All the pristine signals baselines acquired have been analyzed trying to assess the right threshold values for the best damage detecting evaluation. In the following the results obtained for each bay, after a threshold tweaking, are presented.

A1 LWP bay sensors Sub Group damage detection after 130J impact

Below the color maps obtained with the signals energy level analysis (Figure 4.41). From the color map all the damage indices appear able to determine the damaged location, even though some ghost areas (yellow/green) are present in which the methods find high damage index. This is due to the falling of some intersection nodes far away from the real damage location. A visual validation of the damaged area can be obtained by the isolevel map. It can be seen how the damaged area is contained in the 90% energy level isoline.

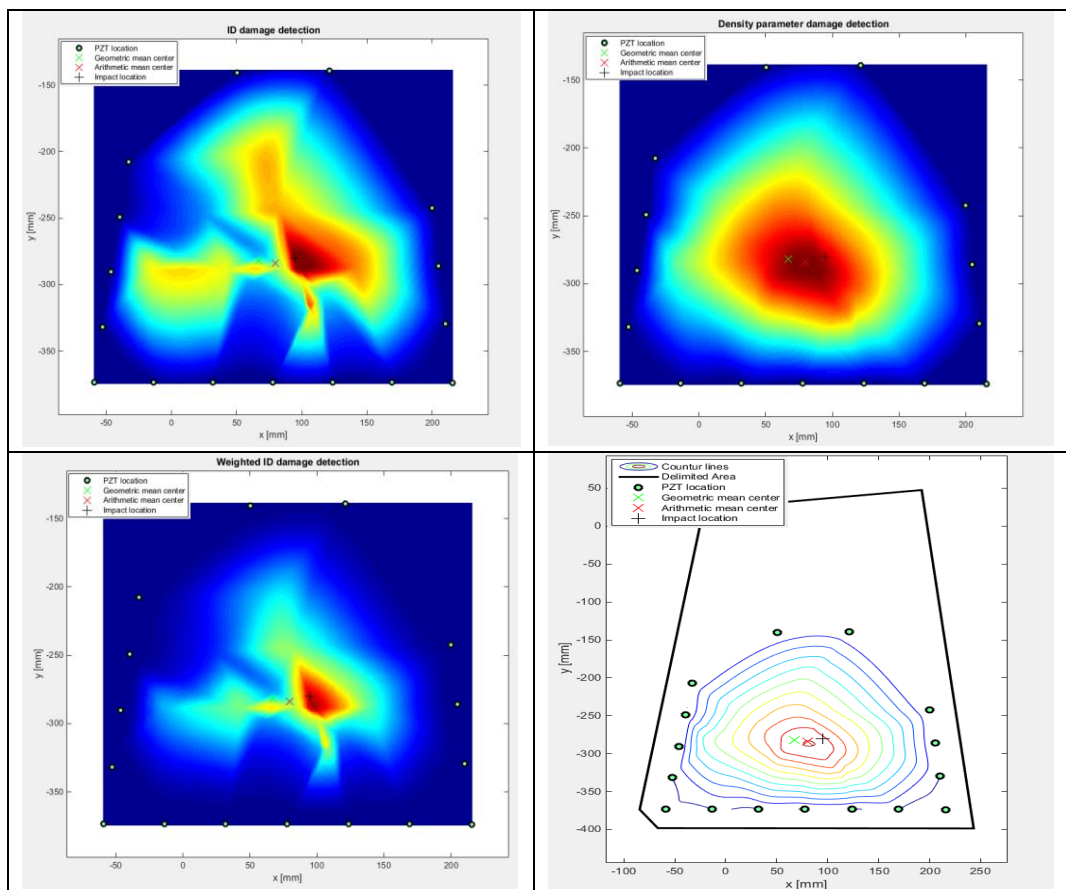


Figure 4.41: energy level ID color and isolevel maps

Better results are obtained with the multi-parameter analysis (Figure 4.42) by combine the various damage parameter graphical reconstructions. In the figure below the results obtained by overlapping the weighted ID damage color map of the different parameters. It is worth noting that the best results are obtained by the overlapping all the three different damage parameters (Figure 4.42 d).

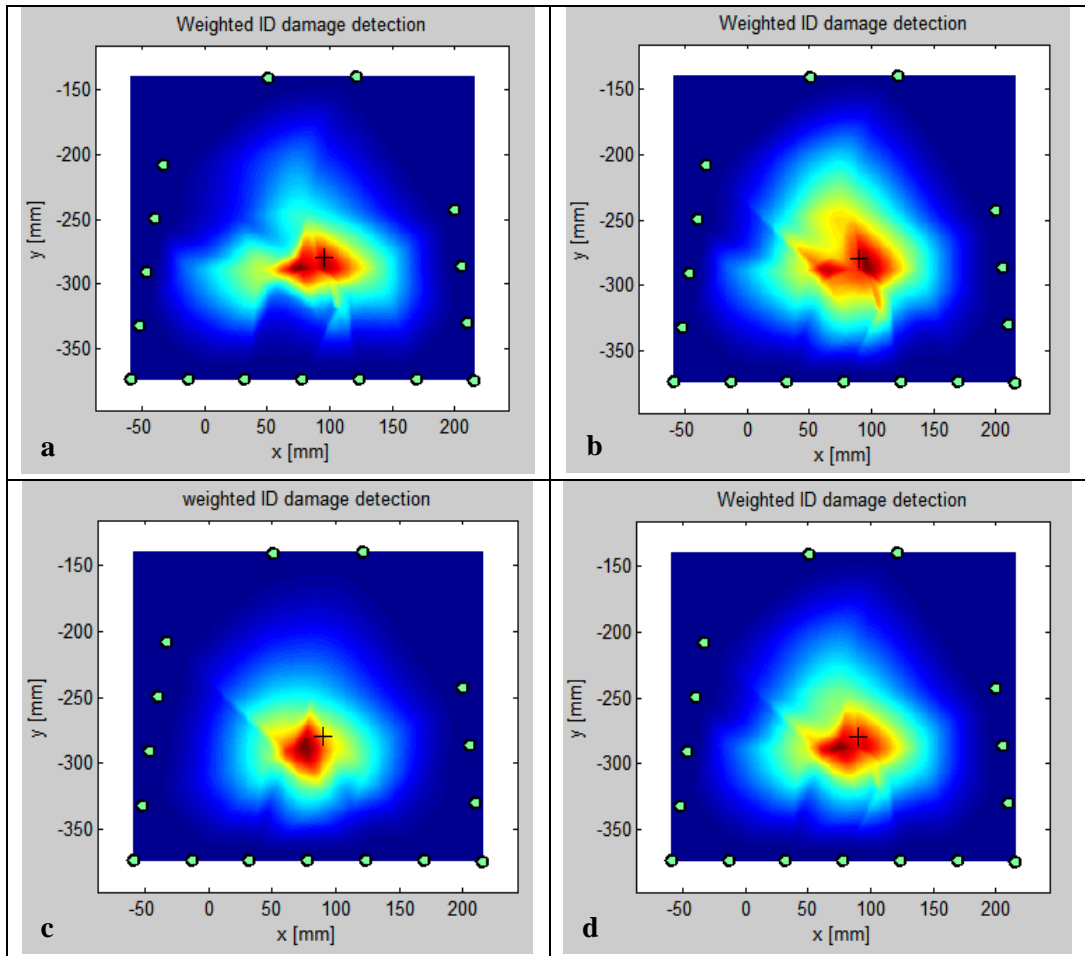


Figure 4.42: A1 bay energy level and time of flight combine (a), energy level and transmission factor combine (b), transmission factor and time of flight combine (c), energy level, time of flight and transmission factor combine (d)

In the following the results obtained for the remaining bays C, D1 and E1 in terms of multi-parameter analysis. Since the best representation has been found to be the one associated at the 3 parameter analysis (multi-parameter), the results for the remaining bays are given by applying the aforementioned method.

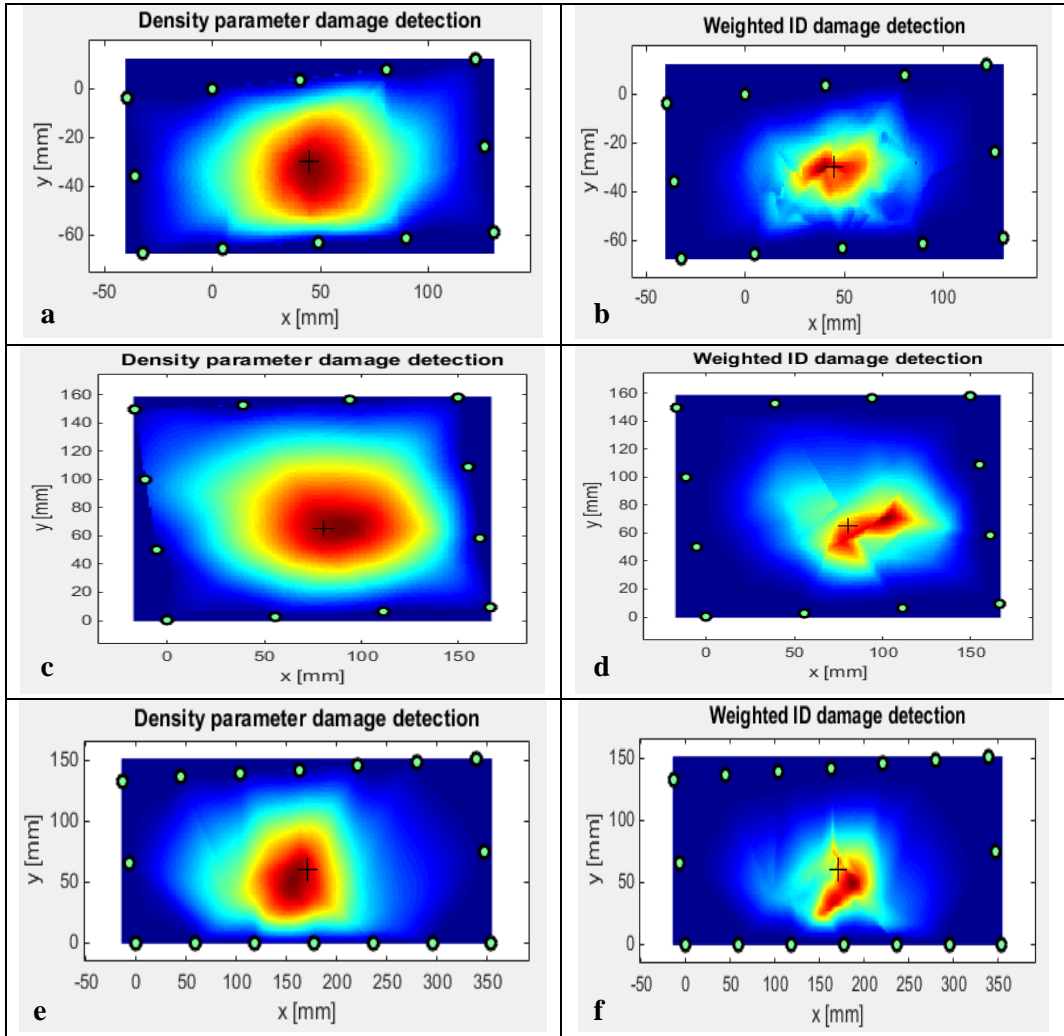


Figure 4.43: (a, b) C bay energy level, time of flight and transmission factor combine; (c, d) D bay energy level, time of flight and transmission factor combine; (e, f) E1 bay energy level, time of flight and transmission factor combine

At the end of each bay analysis, the color map or contour results can be sent to the main GUI interface and allocated in its relative position in the test article CAD model. In Figure 4.44 the wing box demonstrator's analysis results displayed on the LWP geometry.

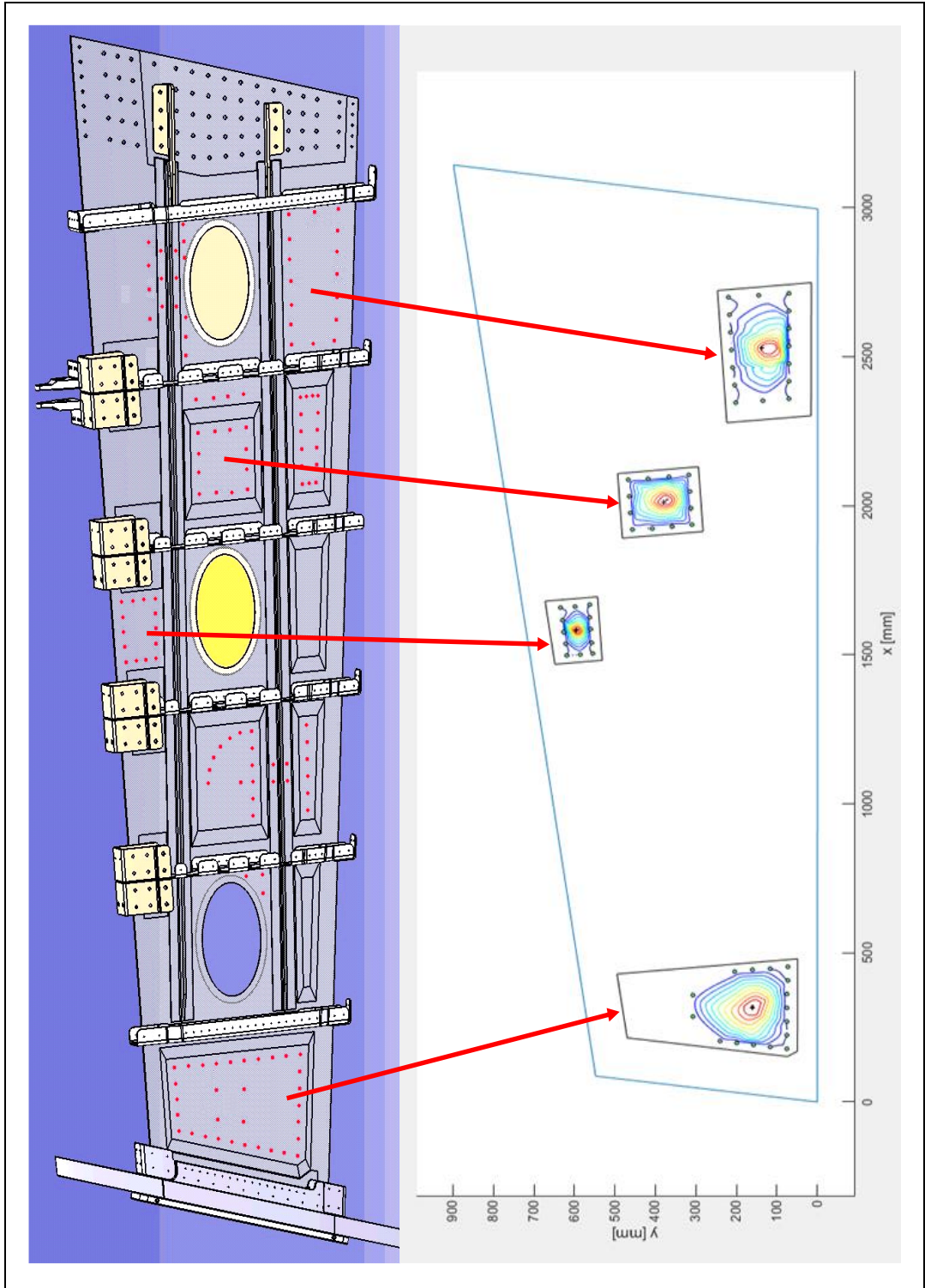


Figure 4.44: Complete analysis of the Test Article

4.7 References

1. E. Monaco, N. D. Boffa, V. Memmolo, F. Ricci, L. Maio, Detecting delaminations and disbondings on full-scale wing composite panel by guided waves based SHM system, SPIE Smart Structures/NDE - Las Vegas, NV, United States 20 - 24 March 2016
2. A. Marzani, N. Testoni, L. De Marchi, E. Monaco, Z. Sharif Khodaei, M.H. Aliabadi, J. Viana, Implementation of a Structural Health Monitoring system for a Composite Wing Box skin, Smart Intelligent Aircraft Structures (SARISTU) Proceedings of the Final Project Conference (May 2015) - Springer International Publishing Switzerland 2016
3. Zhongqing, S., Lin, Y., Ye, L.: Guided lamb waves for identification of damage in composite structures: a review. *Journal of Sound and Vibration* 295, 753-780 (2006).
4. Staszewski, W.J., Mahzan, S., Traynor, R.: Health monitoring of aerospace composite structures: active and passive approach. *Composites Science and Technology* 69(11), 1678-1685 (2009).
5. Memmolo, V., Maio, L., Boffa, N. D., Monaco, E., and Ricci, F., "Damage detection tomography based on guided waves in composite structures using a distributed sensor network," *Optical Engineering*, 55(1), 011007, (2016).

Conclusions

A comprehensive and detailed investigation of a structural health monitoring system based on ultrasonic guided wave propagation has been presented. The obtained results confirm the effectiveness of the SHM system in the assessment of the structures health condition and prove that Lamb waves can be efficiently used for fast damage monitoring in order to identify and locate structural failures. Several features and parameters, that appear to be effective for damage detection, can be extracted from wavefield signals and almost any type of structural change can be intercepted, especially when composite materials are considered. All aspects of the system implementation have been explained and the measurements are presented after a comprehensive analysis of signal processing.

The first antisymmetric mode of Lamb waves (A0) has been found very effective in detecting through thickness delamination and disbonding in layered plates. The interaction of this mode with hidden defects in structural components provides important information on the location of the damage. The finite element simulations carried out in the two and three-dimensional model have provided a good understanding of the interaction process.

A good agreement between simulations and experimental results has been achieved. Using inexpensive and easy to install piezoelectric patches, it has been possible to monitor complex realistic structures, such as composite stiffened panels, to detect delaminations and disbondings produced by overstress or low velocity impact during aircraft service.

The statistical damage index approach adopted to interpret the recorded signals demonstrate the effectiveness of the developed tomographic technique with the aim to investigate the presence and location of damage using simple imaging reports and a limited number of measurements.

Some parameters affecting the methodology have been firstly investigated using CFRP coupons or structural elements with increasing dimensions and complexity. Then, following a building block approach, its effectiveness has been tested on a real full scale reinforced wing panel, characterized by bays with different thickness and structural complexity, each one subjected to impact loads with different impact energies.

The proposed approach, based on concurrent acquisitions of the same system response, allows to exclude healthy paths from detection algorithms and thus to reduce the time of the detection process. The damaged area can be localized by considering the intersection of remaining damaged paths (i.e., damaged nodes) via several graphical techniques. The

interpolation of health data coming from damaged node data on the entire area monitored appears to be an interesting tomographic approach.

Measurements and data signal processing demonstrate that the damage is always detectable and the damaged area is localized. Furthermore, the isolevel map allow to detect the area with the same failure probability and to detect with precision the location of the expected most critical area.

When ghost damages appear, due to the falling of some intersection nodes far away from the real damage location, the condensation correction allows to clarify if several real damages or also some ghost damages have been occurred. The correction allows increasing the reliability of the methodology simply by taking into account the number of damage calls per area of the system. Moreover, this correction is well conditioned because it does not alter the damage detection algorithm when a single spot of nodes is found from the data processing.

Finally, the fusion image of different results, by the GUI multi-parameter combine contour function, further optimize the accuracy of the damage detection and localization as well.

It is worth to note that the implemented methodology can be extended to every structural condition monitoring system, by simply changing the parameter to be considered for the damage sensitivity. In fact, the entire system proposed can be fashioned time to time using different damage index formulations.

Future Developments

In the presented work only a single-damage occurrence has been considered. A multi damage scenario should be investigated to better understand the reliability of the detection system in a real failure event. A correlation between damage dimensions and system response should be carried out in order to allow a continuous monitor after damage, that is in view of a condition-based monitoring maintenance. In fact, practical implementation of the technique in real structures requires additional investigations, involving numerical simulations, to understand some aspects that could be hidden by the noise in the laboratory tests.

Furthermore, since a variation of the propagation characteristics and of the technique effectiveness has been found depending on sensors configuration, the SHM system effectiveness and reliability should be statistically demonstrated by a Probability of Detection function definition. A real implementation of an SHM system requires, in fact, the clearly targets definition. It is desirable to know what type and dimension of flaw can be detected with a certain probability and confidence level. Only by a rigorous probability of detection (POD), the system performances can be assessed, but often this requires a very complex setup arrangement and many coupons. So, starting from this consciousness, a rigorous POD Model Assisted function definition and evaluation is under investigation.

Appendix

Infrared thermography and ultrasonics

in carbon epoxy materials

I. Introduction

The availability of techniques able to perform effective non-destructive evaluation of composites is of great concern in the today era in which composites are increasingly used in aircraft primary structural components. The heterogeneous nature of composite materials as well their continuous evolution entails a continuous upgrading of non-destructive evaluation methodologies to fulfil with safety criteria.

In parallel to the research activities concerning the development of a SHM system, a secondary research activity, summarized below, based on nondestructive techniques comparison has been conducted and used for SHM system damage scenario assessment.

The attention of the activity has been focused on the suitability of two techniques, infrared thermography and ultrasonics, to evaluate impact damaged carbon/epoxy specimens. The obtained results have been compared by highlighting advantages and disadvantages of each technique, as well their limits in view of an integrated use.

In this context, the assessment of delamination extension, caused by an impact event, has been considered as a crucial task, which may ask to guess between sound and damage at the edge of instrument noise threshold. To help fixing this problem, results obtained with either lock-in thermography, or an ultrasonic phased array system, have been analysed with the aid of thermographic data collected during impact tests.

The visualization of thermal signatures, caused by local dissipation of impact energy, allows gaining information which is useful for understanding the material response to impact. In particular, the two techniques allow for estimation, in a reliable way, of the

overall delamination extension which is of utmost importance for material design purposes.

II. Techniques overview

Carbon Fibre Reinforced Polymers (CFRP) are increasingly used in aircraft primary and secondary structural components [1]. However, as most types of composites, they exhibit different problems when compared to metallic materials. A main weakness is their vulnerability to low velocity/energy impact [2]. In particular, important damage may arise inside the material thickness without any perception on the impacted side; this may compromise the performance of the part with substantial reduction of its fatigue life. Then, the availability of non-destructive evaluation techniques (NDE) is of fundamental importance to ascertain the soundness of a part. Different techniques are today available, but not all are very effective to detect the slim delamination caused by low energy impact. On the other hand, the heterogeneous nature of composite materials as well their continuous evolution entails a continuous upgrading of non-destructive evaluation methodologies to fulfil with safety criteria.

Since the research activity has been focused only on ultrasonics (UT) and infrared thermography (IRT) techniques to estimate the damage capability and both of the two methodologies are well known, only some basics are here recalled.

Ultrasonic technique

Ultrasonic testing is, of course, the most commonly used non-destructive testing technique [3]. It is based on the principle that an ultrasonic wave, of frequency higher than 20 kHz (above human hearing range), is modified by passing through a material. In particular, the wave undergoes both amplitude variation and reflection at interfaces between parts of different acoustic impedance. This method is effective in the detection of most of the common CFRP defects, (such as porosity, slag inclusions and delamination) but has the disadvantage of a needed contact with the part to be inspected. This entails some problems since the test article surface must be smooth enough to assure good contact, a coupling medium (e.g. oil, ultrasound gel, water, glycerine) is necessary and time is needed to scan large surfaces. In recent years the advent of phased array ultrasonics (PAUT) [4] has solved some of the problems of conventional ultrasonics. The main advantage of using PAUT technology lay in the ability to modify electronically the acoustic probe characteristics. Probe modifications consist in introducing time shifts (beam forming) in the signals sent to (pulse) and received from (echo) individual elements of an array, allowing generation of multiple transducer paths within only one probe and the creation of an image of the inspected zone, which increases the ability to visualize. Phased array imaging provides the user with the ability to see relative point to point changes and multi-angular defect responses, which can assist in flaw discrimination and sizing [5]. However,

from one side, the PAUT allows for the inspection of complex geometries in a faster way, on the other side, it poses the problem of the custom-built reference blocks which must be fabricated, used and stored following specific rules [5].

Infrared thermography technique

Infrared thermography IRT bases its principle on the thermal energy radiated from objects in the infrared band of the electromagnetic spectrum [6]. It is very attractive since it offers noncontact and fast inspection of wide areas. Non-destructive evaluation (NDE) with IRT can be performed with different approaches which allow for detection of defects and reconstruction of their position in plane and in depth within the thickness of the inspected component. It is worth mentioning flash thermography [7] that has emerged as the most valuable method to account for the presence of porosity in composites. Infrared thermography, apart from its use as non-destructive evaluation technique, can be also used to take a video during an impact event. In fact, visualization of thermal signatures, caused by local dissipation of impact energy, allows gaining information about the material response to impact.

III. Experimental investigation

Infrared thermography and a phased array system have been used to detect low energy impact damage in carbon fibre reinforced polymers for aeronautical applications. However, rather than discovering impact damage, resulting from the in-service life of a structure, for maintenance purposes, the main interest is to ascertain, in a rapid and effective way, the damage caused by an impact of given energy for materials design purposes.

Many test articles of SARISTU project have been inspected for damage assessment with both techniques but here, for sake of simplicity and brevity, only the results of a single specimen will be discussed.

The material considered is a thermoset matrix reinforced with carbon fibres, which has been mainly used as skin material in the Saristu wing box ground test demonstrator. More specifically, it is a 7,8 mm thick plate including: Non-Crimp Fabrics (NCF), Multiaxial Reinforcements (MR) and 5 Harness Satin Weave (HSW). It has been fabricated by the hand lay-up technology and appropriate curing cycle in autoclave. The panel has been first non-destructively evaluated with both lock-in thermography (LT) and PAUT, then impacted with a modified Charpy pendulum from one side while an infrared camera watched the rear side. A sequence of thermal images has been taken, which allows monitoring the material thermal behaviour under impact. After impact, the specimen has been again non-destructively evaluated with both LT and PAUT.

IV. Impact tests

Impact tests have been carried out with a modified Charpy pendulum (Figure 1 left), which allows enough room for positioning of the infrared camera (Figure 1 right) to view the rear specimen surface (i.e., opposite to that struck by the hammer). The hammer has a hemispherical nose 12.7 mm in diameter. The impact energy E is in the range 50-70 J, chosen to produce only barely visible damage without perforation and is set by suitably adjusting the falling height of the Charpy arm.



Figure 1: Impact tests setup. (left) Charpy pendulum , (right) specimen lodge and position of the infrared camera

The used infrared camera was the SC6000 (Flir system), which is equipped with a QWIP detector, working in the 8-9 μm infrared band, NEDT < 35mK, spatial resolution 640x512 pixels full frame with the pixel size 25 μm x 25 μm and with a windowing option linked to frequency frame rate and temperature range.

Sequences of thermal images have been acquired during impact tests at 84 Hz. To allow for a complete visualization of thermal effects evolution with respect to the ambient temperature, the acquisition starts few seconds before the impact and lasts for some time after. To better analyse the material's thermal behaviour, the first image ($t = 0$ s) of the sequence, i.e. the specimen surface temperature (ambient) before the impact, has been subtracted to each subsequent image so as to generate a map of temperature difference ΔT :

$$\Delta T = T(i, j, t) - T(i, j, 0) \quad (1)$$

where i and j representing lines and columns of the surface temperature map.

Some ΔT images are shown in Figure 2 for varying the impact energy and the acquisition time.

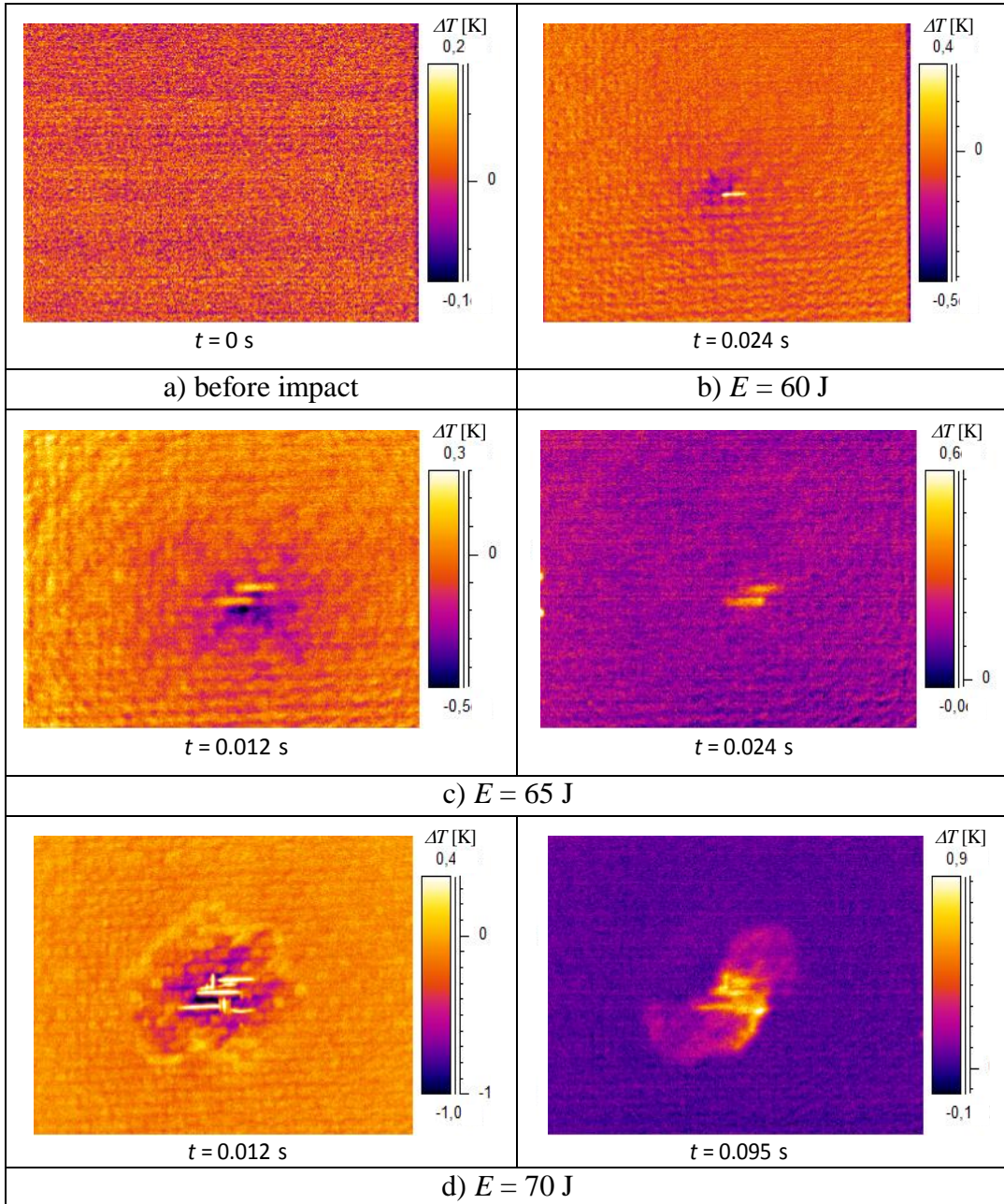


Figure 2: ΔT images taken before (a) and after impact at 60 J (b), 65 J (c) and 70 J (d)

The temperature scale is not maintained constant for all the images, but it is fine-tuned for each image to highlight any thermal signature induced by the impact. The specimen surface, which is initially (before the impact) at an almost constant $\Delta T = 0$ K (Figure 2a), displays sudden at the impact, temperature variations which strongly depend on the impact

energy (Figure 2b-d). In particular, at $E = 60$ J (Figure 2b) the specimen surface displays a local cooling down ($t = 0.024$ s), due to thermo-elastic effects, and a short hotter line, accounting for local delamination. By increasing the impact energy to $E = 65$ J the cooling down effect becomes stronger (Figure 2c) and two hot lines appear to account for some expansion in delamination. However, the maximum ΔT remains below 0.5 K meaning that no important damage occurred. To a further increase of the impact energy to $E = 70$ J the temperature variations strengthen up and the warm area enlarges (Figure 2d). In particular, thermal signatures display a more complex evolution in time and in space meaning that more important delaminations occurred at different layers through the material thickness. Of course, quantitative data can be obtained by applying ad hoc post-processing procedures to the sequences of thermal images recorded during impact tests.

V. Non-destructive evaluation with lock-in thermography

The test setup includes the specimen, the infrared camera and halogen lamps (1 kW each) for thermal stimulation of the specimen. The infrared camera is the same SC6000 used to monitor the impact, but now is equipped with the IrNDT^(R) (AT technology) lock-in option which includes both hardware and software to allow setting up of test parameters, handling of thermal images, visualization and processing of phase (or amplitude) images. Lock-in thermography basic relationship is reported, which links the thermal diffusion length μ to the material thermal diffusivity α and to the heating frequency f :

$$\mu = \sqrt{\frac{\alpha}{\pi \cdot f}} \quad (2)$$

The depth range for the amplitude image is given by μ , while the maximum depth p , which can be reached for the phase image, corresponds to 1.8μ . In general, it is preferable to reduce data in terms of phase image because of its insensitivity to both non uniform heating and local variations of emissivity over the monitored surface. The material thickness, which can be inspected, depends on the wave period (the longer the period, the deeper the penetration) and on the material thermal diffusivity. According to Eq.2, the knowledge of the thermal diffusivity α is fundamental to evaluate the depth at which any detected anomaly is located, or to choose the frequency value to check the material conditions at a given depth. To this end, the overall thermal diffusivity evaluated with the lockin technique has been found to be equal to $\alpha = 0.03$ cm²/s.

Each impacted specimen is inspected by viewing both sides, the impacted and the opposite one, and by varying the heating frequency f . No damage is detected for impacts at $E = 50$ and 60 J. A light stain may be recognized for $E = 65$ J, which could be ascribed to the indentation, but the contrast is very poor making difficult any deduction. Instead, some

damage is clearly visualized for the impact performed at $E = 70$ J as can be seen from the phase images shown in Figure 3 and which were taken, for varying f , from the impacted side.

Starting from the impacted surface (Figure 3), it is possible to follow the evolution of the damage at the different layers as depicted by the white stain. In particular, considering the thermal diffusivity, $\alpha = 0.03$ cm²/s, it is also possible to estimate the corresponding depth. Then, for $f = 0.88$ Hz the white stain may correspond to the surface indentation. Going more in depth, for $f = 0.53$ Hz ($p = 2.4$ mm), the white stain enlarges and strengthens accounting for some damage there. It is possible to see a two-lobed structure, evolving along the fibres direction, and surrounded by a lighter elliptic-shaped stain, which becomes even more pronounced as f is decreased to 0.36 Hz ($p \cong 3$ mm), to 0.26 Hz ($p \cong 3.4$ mm), to 0.19 Hz ($p \cong 4$ mm). Such a lobed structure for $f = 0.15$ Hz ($p = 4.6$ mm) tends to merge into a unique structure, which becomes well consolidated for $f = 0.12$ Hz ($p = 5$ mm). To a further reduction of f (going further deep inside the material thickness) it is possible to see again a split up into a two-lobed appearance (Figure 3h and i).

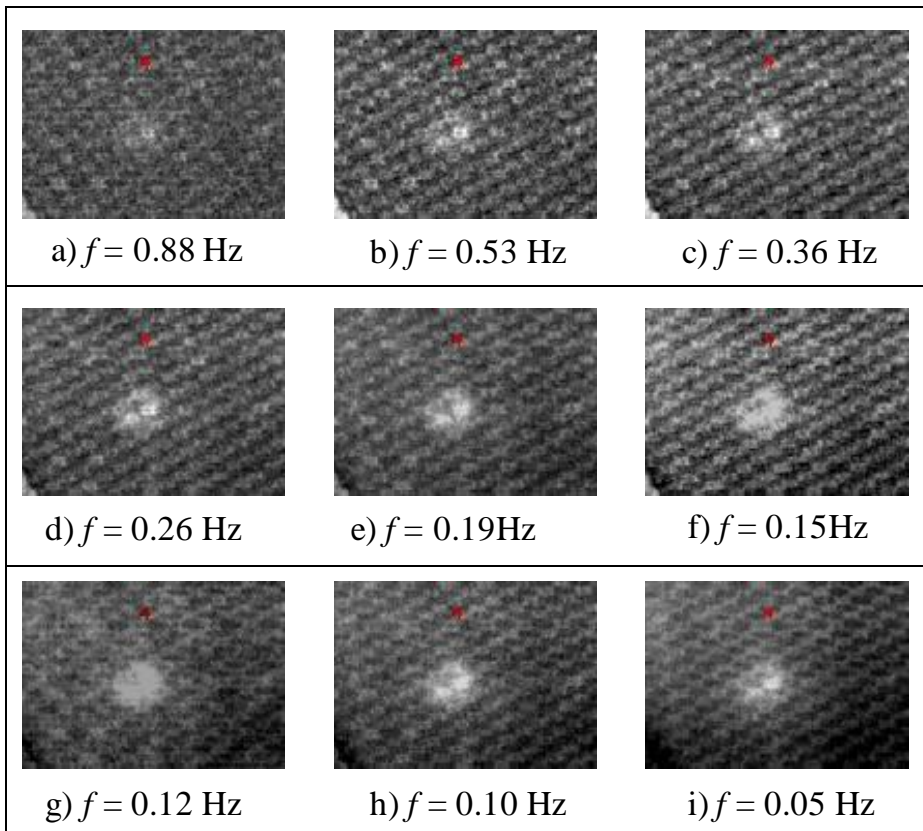


Fig. 3 Phase images taken for varying f on the side impacted at $E = 70$ J

The size of the damaged zone can be easily evaluated by contouring the white stain and computing its area A_D . A representation of A_D with the depth p is shown in Figure 4. However, one main requirement is to set the boundary between sound and damaged materials; this is done owing to a previous established criterion [8]:

$$\frac{\phi_m - \phi}{\phi_m - \phi_c} \cong 0.5 \quad \text{for} \quad \phi_m - \phi > \Delta\phi_s \quad (3)$$

where ϕ is the phase angle in a generic point, ϕ_m is the average phase value for sound material, ϕ_c is the value above the centre of the discontinuity, $\Delta\phi_s$ is the average deviation of ϕ over the sound material. With this approach the overall delamination may be underestimated because delamination propagates between fibres and matrix in a rather tortuous way and in a very thin delaminated zone, the variation of the phase angle gets confused with the background. Of course, this problem becomes more important with the increase of the thickness.

On the other hand, if tests are carried out by viewing the rear side (Figure 5), the two-lobed structure appears already for $f = 0.88$ (close to the surface) even if of low-contrast, and strengthens up as f is decreased to 0.36 Hz ($p \cong 3$ mm). For $f = 0.15$ Hz ($p \cong 4.6$ mm) a larger stain appears, which encloses the two-lobed structure. For the sake of accuracy, it is worth nothing that the used thermal diffusivity was measured on the sound material, while the occurred damage may affect the local thermal diffusivity entailing some variations on the effective depth at which the visualized damage is located.

$A_D(\text{mm}^2) = 203$ $P(\text{mm}) = 2.37$	1 	$A_D(\text{mm}^2) = 182$ $P(\text{mm}) = 5.10$	5 
$A_D(\text{mm}^2) = 209$ $P(\text{mm}) = 3.06$	2 	$A_D(\text{mm}^2) = 251$ $P(\text{mm}) = 5.74$	6 
$A_D(\text{mm}^2) = 188$ $P(\text{mm}) = 3.71$	3 	$A_D(\text{mm}^2) = 198$ $P(\text{mm}) = 6.42$	7 
$A_D(\text{mm}^2) = 188$ $P(\text{mm}) = 4.36$	4 	$A_D(\text{mm}^2) = 227$ $P(\text{mm}) = 7.04$	8 

Figure 4: Damaged area and corresponding depth for $E = 70$ J

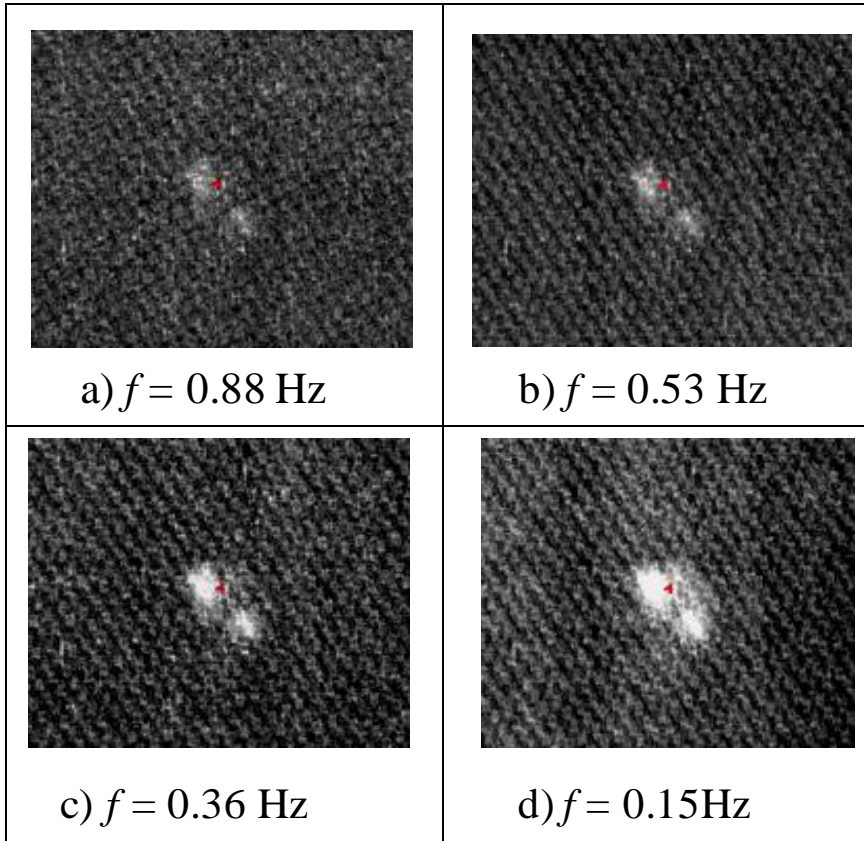


Figure 5: Phase images taken for varying f on the rear side, for $E = 70$ J

VI. Non-destructive evaluation with ultrasonic phased array

Phased array ultrasonic testing (PAUT) is performed with a recently released model by Olympus the OmniScan SX flaw detector with a 16:64PR phased array unit equipped with a conventional UT channel for pulse-echo (PE), pitch-catch or time-of-flight diffraction (TOFD) inspections. Phased array elements are pulsed in such a way to allow multiple beam components to combine with each other and form a single wave front travelling in the desired direction. Similarly, the receiver merges the signals coming from multiple elements into a single representation.

Any ultrasonic instrument typically records two fundamental parameters of an echo: amplitude and pulse transit time. The basic output is in the form of an A-scan, or waveform display, in which echo amplitude is plotted against time. Another data representation mode is in terms of cross sectional B-scan, which provides a detailed end view of a test piece along a single axis. Successive A-scan plots over elapsed time, or actual encoded transducer position, supplies pure cross-sections of the scanned line. This allows visualization of both near and far surface reflectors within the sample. The Linear Straight Scan (S-scan) option allows, through electronic scanning along the length of a linear array probe, to create a cross-sectional profile without moving the transducer. As each focal law is sequential, the associated A-scan is digitized and plotted. Successive gate apertures are "stacked" creating a live cross sectional view. Another data presentation is the C-scan, a two dimensional presentation of data displayed as a top, or planar, view of the test piece. The probe is typically moved physically along one axis while the beam electronically scans along the other one, according to the focal law sequence. Signal amplitude or depth data are collected within gated regions of interest and plotted with each focal law progression, using the programmed beam aperture.

In the present work, tests have been carried out using an encoded 5 MHz, 64 elements linear array probe with a straight wedge and by using a specific gel as coupling medium. No specific calibration blocks have been used, the instrument calibration has been obtained by the ultrasonic wave propagation velocity measurement through the test article thickness; it is worth noting that it is difficult to fabricate reference blocks reproducing the CFRP specimen. Tests have been carried out with the phased array positioned over the smooth surface, which coincides with that impacted. B, S and C scans in amplitude view are presented in Figure 6, referring to the specimen region including two impacts at 60 J and at 65 J, and in Fig.7, referring to the region involving one impact at 70 J.

From Figure 6 it is possible to see, in the C-scan image, two blue-yellow contoured zones in correspondence of the two impacts at 60 and 65 J. From the B-scan images it is possible to see some millimetric lenticular delaminations confined exclusively in the first layer of the laminate. This type of damage underlines an indentation process of the material surface occurred during the impact. However, the indentation damage is too small and below the axial resolution of the B-scan analysis (PAUT limited detection zone, or dead zone). In fact, the time delay between the first interface echo (first surface echo) and the indentation

echo is so small that the two impulses are practically superimposed, so it is impossible to detect the imperceptible shallow defect for a correct interpretation. Then, it is possible to infer that not significant damage has occurred, but only a negligible indentation.

Conversely, more important damage occurred under the impact at 70 J as it is possible to see from C, B and S-scans shown in Figure 7. In fact, the articulated and colourful C-scan image bears witness for remarkable damage occurred at the different layers through the thickness. The C-scan amplitude view (Figure 7a) shows the presence of a wide intense surface damage; in particular, the central red areolas, indicates significant indentation damage with presence of impact surface penetration and surface cracks. The surrounding yellow/blue areas, with a lower signal amplitude, immediately suggest the presence of more wide delaminations of different orientations and at different depths through the thickness.

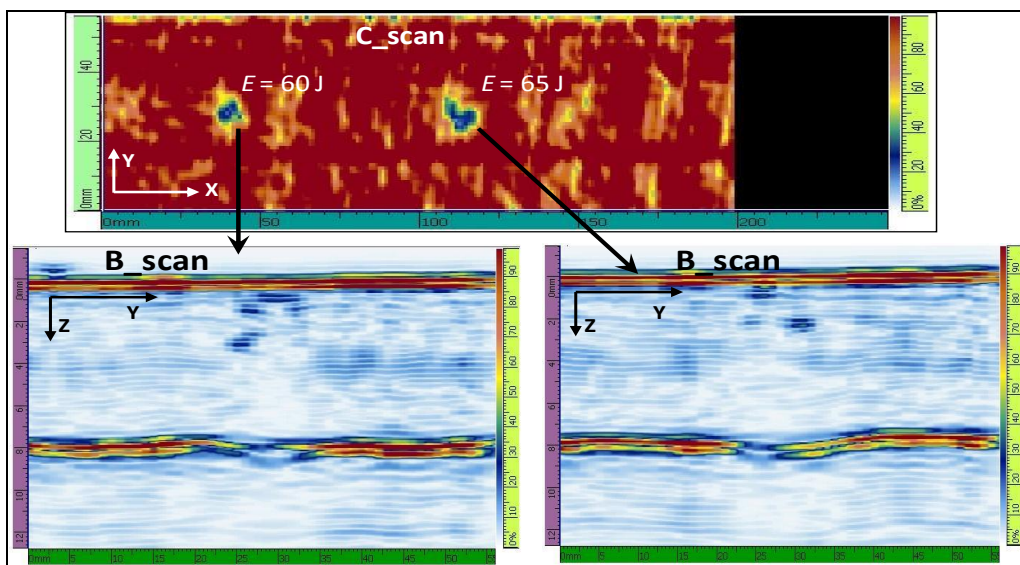


Figure 6: C-scan and B-scan of the zone with impacts at E = 60 and 65 J

In particular, the Time of Flight Diffraction, or TOFD C-scan, displays (Figure 7d), in gray scale (where white means near the impact surface) the presence of characteristic lenticular delaminations that tend to propagate between adjacent laminae and to assume the classical peanut shape with the major axis parallel to the fiber direction of the foil underlying the interface. Such lenticular delaminations increase in size, by moving along the thickness away from the impact point, and describe the characteristic well known truncated-conical path. Such a damage behaviour is confirmed by the B and S scans images shown in Figure 7b and c, which prove the truncated-conical development of the delaminations through the thickness and supply information about the position in depth of the damage along x and y directions; in particular, it seems some important damage being located at a depth of about 6 mm. Of course, for a complete reconstruction of the position of the observed lenticular

structures along the impact cone, many scans are necessary with varying the position of the probe along B-scan and S-scan directions.

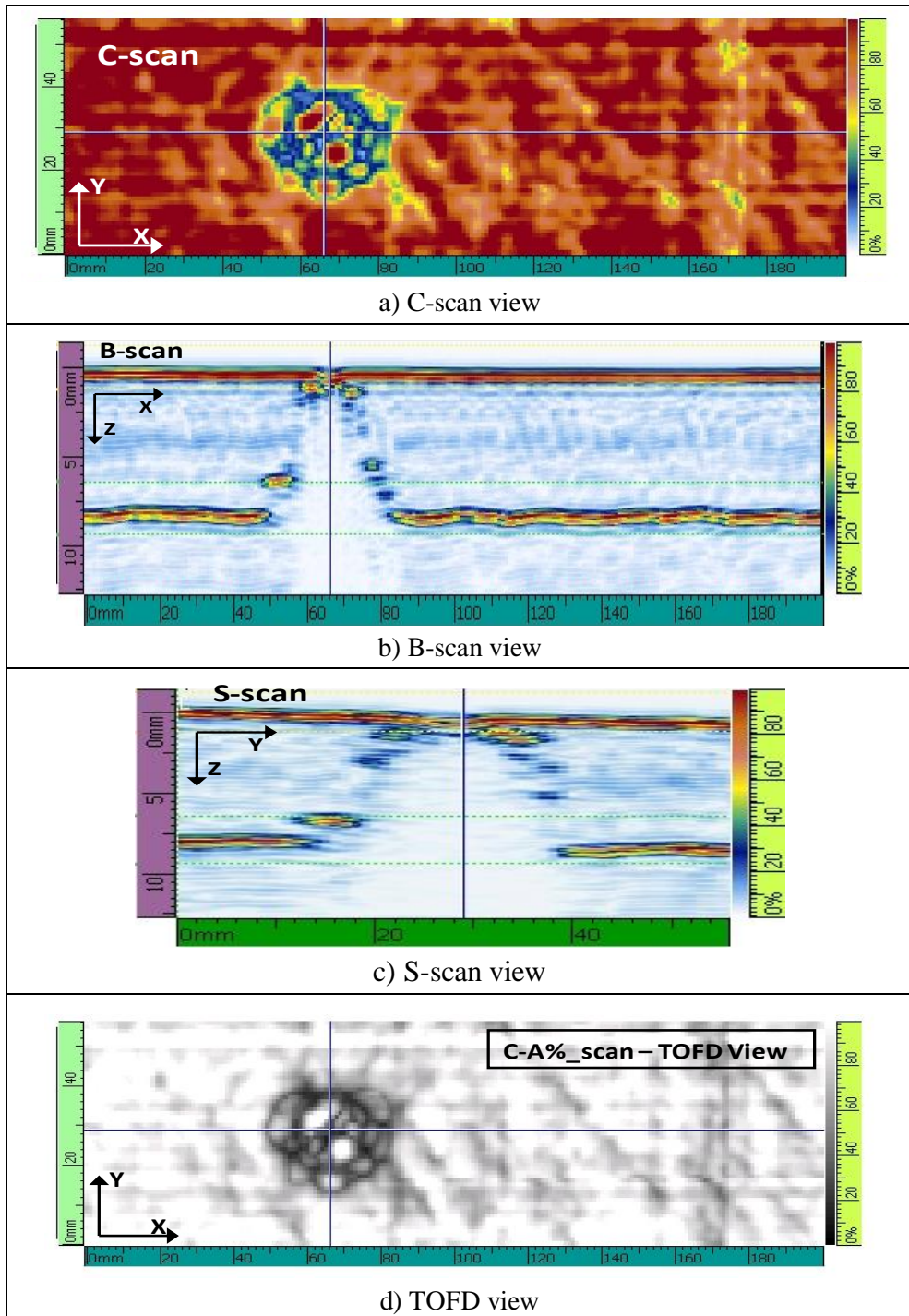


Figure 7: C, B and S scans of the specimen region impacted at $E = 70$ J

VII. Data comparison and discussion

From a general comparison between data coming from LT and PAUT, a general agreement is found. However, to a close view of results obtained for the different impact energies some important comments can be derived.

The first observation is that no damage occurs for $E \leq 65$ J, but only surface indentation. In fact, there is no temperature rise (online monitoring) meaning that the absorbed fraction of the impact energy is very small. On the other side, what PAUT detects is a very superficial discontinuity caused by local indentation. Such a small surface concavity is not detected by LT because the signal gets confused within the noise induced by the material texture. The impact at $E = 70$ J causes more important damage, which becomes detectable with all the three means: online monitoring, LT and PAUT. A greater fraction of the impact energy is now absorbed which entails more significant rise in temperature as shown in Figure 2d. On the other hand, phase images visualize some damage at the different layers through the thickness (Figure 3). This occurrence is in general validated by the PAUT output (Figure 7) even if a detailed comparison is difficult due to the superposition of all the damage structures at any depth in the C-scan image.

Nevertheless, the two central ovals, which appear (dark-red) in the C-scan (Figure 7a) and (white) in the TOFD (Figure 7d) images, well match the two-lobed structure which appears in some phase images (e.g. Figures 3b-e and Figures 5a-d), also the lenticular structures over the border in the C-scan and in the TOFD images can be recognised in the phase images of Figures 3b-e. Most probably the two-lobed structure corresponds to the oblong hot zone displayed by the second thermal image in Figure 2d, which appeared later because it was located deeper and not over the external layer. Of course, the sequence of phase images allows for the reconstruction of the impact damage through the thickness (Figure 4).

In addition, it seems that the largest damaged zone detected by PAUT (Figure 7a and d) is similar to the largest damaged area detected by LT (Figure 4). With regard to the location of the damage in depth, the PAUT seems more effective since one test is sufficient to supply information about the presence of damage at any depth through the entire thickness (B-scan, S-scan). The LT, instead, requires more tests with close variation of the heating frequency.

For a quantitative comparison, the C-scan image of Figure 7a is proposed again in Figure 8 together with the phase image of Figure 5d and the first thermal image of Figure 2d. In each image is measured the maximum extension of the damaged area along two directions D_H and D_V . These values are collected in Table I.

Image	D_H (mm)	D_V (mm)
Thermal	40	35

Phase	34	25
C-scan	35	27

Table I: Extension of the damaged zone along two directions

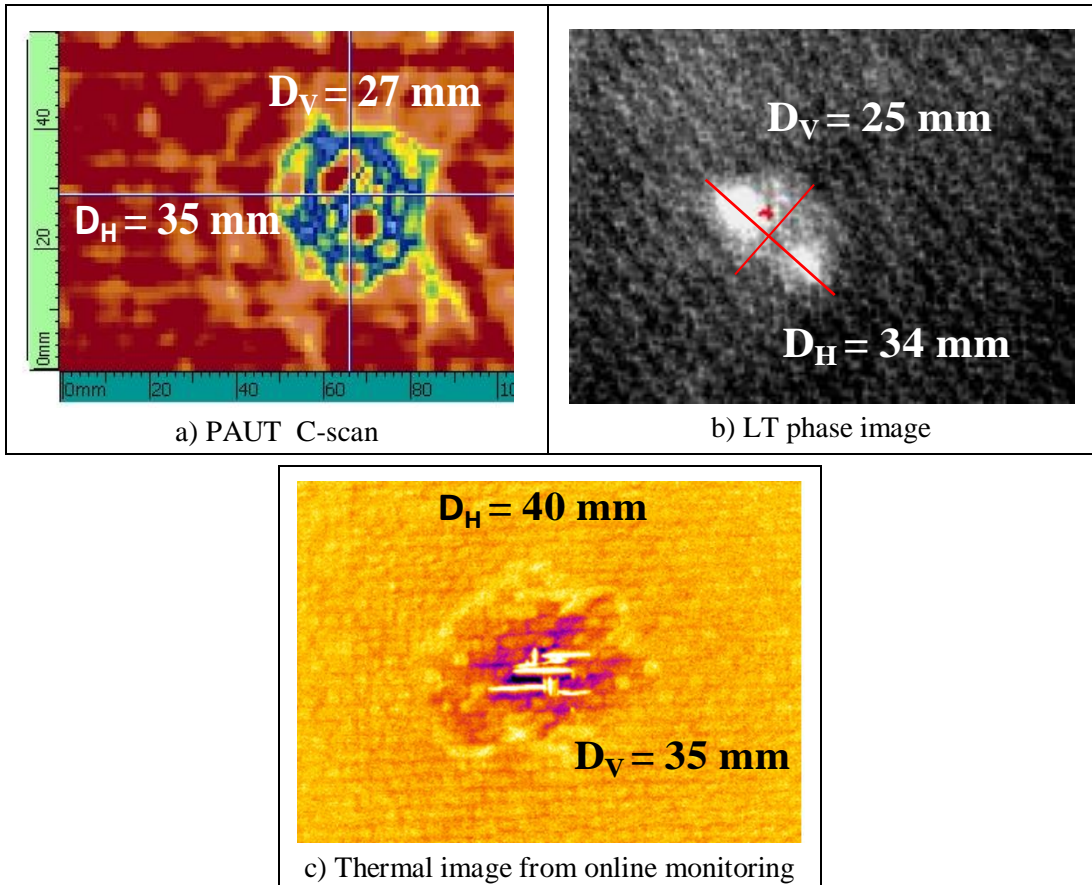


Figure 8: Phase image for $f = 0.15$ Hz
(ref. Figure 2d)

The obtained results highlight that both LT and PAUT are effective in detecting the impact damage; LT is fast and more effective to map large surfaces, conversely PAUT is better to get information along the thickness especially in presence of thick parts. Then, an integrated use would be advantageous. However, both techniques are characterized by some uncertainty in the discrimination of very thin delamination in comparison with the thermal signature visualized during monitoring of the impact event especially in presence of composites with complex stacking sequence.

VIII. References

1. C Soutis, "Fiber reinforced composite in aircraft construction", *Progr Aerosp Sci*, Vol 41, pp 143–151, 2005.
2. M O W Richardson and M J Wisheart, "Review of low-velocity impact properties of composite materials". *Composites Part A*, Vol 27, pp 1123-1131, 1996.
3. Standard Practice for Ultrasonic Testing of Flat Panel Composites and Sandwich Core Materials Used in Aerospace Applications ASTM E2580-07 2007.
4. T J Batzinger, W Li, R S Gilmore, E J Nieters, W T Hatfield, et al. "Phased array ultrasonic inspection method for industrial applications" US6789427 (2004).
5. Olympus manual: Advances in phased array ultrasonic technology applications.
6. C Meola and G M Carlomagno, "Recent advances in the use of infrared thermography" *Meas Sci Technol*, Vol 15, pp 27-58, 2004.
7. C Meola and C Toscano, "Flash thermography to evaluate porosity in CFRP", *Materials*, Vol 7, N 3, pp 1483-1501, 2014.
8. C. Meola, G.M. Carlomagno Application of infrared thermography to adhesion science, *Journal of Adhesion Science and Technology* (review) vol.20, n.7, 589-632, 2006.